UNIVERSITÄT DUISBURG ESSEN

Offen im Denken

Dissertation

Synthesis and characterization of Fe/Si-based functional nanostructures

zur Erlangung des akademischen Grades
Doktor der Naturwissenschaften
an der Fakultät für Physik
der Universität Duisburg-Essen

vorgelegt von

Tatiana Smoliarova

aus
Sretensk, Russische Föderation

Tag der Abgabe: 1. August 2023
Tag der Disputation: 28. November 2023

Mitglieder der Prüfungskommission:
1. Gutachter: Prof. Dr. Ulf Wiedwald
2. Gutachter: Prof. Dr. Lambert Alf
Prüfer: Jun. Prof. Dr. Michael Farle
Vorsitzender: Prof. Dr. Peter Kratzer

Kurzfassung

Im Bereich der Mikroelektronik werden neue Materialien und Bauelementearchitekturen benötigt, um die Leistung der Bauelemente zu kontrollieren und zu steigern. Diese Arbeit konzentriert sich auf die Herstellung von Fe/Si-Nanostrukturen mit Bottom-up- und Top-down-Nanofabrikationsverfahren.

Ein Bottom-up-Nanofabrikationsansatz, der die Selbstorganisation einschließt, wurde verwendet, um Ensembles von α-$FeSi_2$ und β-$FeSi_2$ Eisensilizid-Nano- und Submikron-Kristallen auf goldaktivierten und goldfreien Si(001)-, Si(110)- und Si(111)-Oberflächen bei verschiedenen Si/Fe-Flux und unterschiedlichen Substrattemperaturen herzustellen. Die Studie zeigt, dass die Verwendung von Gold die Morphologie der resultierenden Kristallite und die bevorzugte Orientierungsbeziehung (OR) der α-$FeSi_2$(001)-Gitterebene parallel zur Si-Substratoberfläche reguliert. Der Widerstandswert des α-$FeSi_2$/Si-Systems nimmt zu, wenn der Winkel zwischen den Leitfähigkeitskanälen in α-$FeSi_2$ und den Leitfähigkeitstälern in Si zunimmt. Das präparierte α-$FeSi_2$/Si-System kann als ein System von rückwärts geschalteten Schottky-Dioden betrachtet und verwendet werden, wenn der ohmsche Kontakt durch einen anderen Schottky-Kontakt mit niedrigerer Barrierenhöhe in Halbleiterbauelementen ersetzt wird.

Es wurde ein Top-Down-Nanofabrikationsansatz eingesetzt, um Silizium-Nanodrähte (Si NW) als Indium-Back-Gate-Feldeffekttransistoren (FET) mit Schottky-Kontakten auf Silizium-auf-Isolator-Substraten (SOI) mit Fe-Source- und Drain-Kontakten und unterschiedlichen Si-NW-Breiten herzustellen. Aufgrund von Änderungen im technologischen Verfahren bildete sich unter der Fe-Schicht eine Fe/Si-Kontaktfläche, was dazu führte, dass die hergestellten Bauelemente eine relativ niedrige Schottky-Barriere-Höhe von 0,05-0,1 eV aufweisen.

Die Bauelemente zeigen ein ambipolares Verhalten unabhängig von der Gate-Polarität, und der Strom wird durch die von Source (S) und Drain (D) gebildete, rückwärts geschaltete Schottky-Dioden beeinflusst. Die resultierenden Bauelemente werden für den Nachweis von Biomolekülen durch Messung der Source-Drain-Charakteristik eingesetzt. Die Funktionalisierung der Si-NW-Oberfläche wurde dafür mit einem Dip-Pen-Nanolithographieverfahren durchgeführt.

In dieser Arbeit werden die Faktoren vorgestellt, die wesentlich zum Verhalten des elektrischen Widerstands im $FeSi_2$/Si-System beitragen und die für die Vorhersage der elektrischen Eigenschaften des Systems und die Gestaltung von Kontakten in mikroelektronischen Bauelementen wichtig sind. Die vorgeschlagene Version des Si-NW-FET mit Fe-S/D-Kontakten ist ein vielversprechender Prototyp zur Detektion biologischer Verbindungen.

Abstract

In the field of microelectronics, new materials and device architectures are required to control and improve device performance. This work focuses on the preparation of Fe/Si nanostructures using bottom-up and top-down nanofabrication approaches.

A bottom-up nanofabrication approach involving self-assembly was used to prepare the ensembles of α-$FeSi_2$ and β-$FeSi_2$ iron silicide nano- and submicron crystallites on gold-activated and gold-free Si(001), Si(110), Si(111) surfaces at different Si/Fe flux ratios and different substrate temperatures. The study reveals that using gold-assisted growth regulates the morphology of the resulting crystallites and preferred orientation relationship (OR) of the α-$FeSi_2$(001) lattice plane parallel to the Si substrate surface. The resistivity value of the α-$FeSi_2$/Si system increases as the angle between the conductivity channels in α-$FeSi_2$ and the high-conductivity directions in Si increases. A prepared $FeSi_2$/Si system can be considered as a system of back-to-back connected Schottky diodes and used when another Schottky contact with lower-barrier height in semiconductor devices may substitute the ohmic contact.

A top-down nanofabrication approach was used to prepare silicon nanowire (Si NW)-based Indium-back-gate field-effect transistors (FET) with Schottky contacts on silicon-on-insulator (SOI) substrates with Fe source and drain contact pads and varied Si NW widths. Due to modifications in the technological procedure, an Fe/Si contact area was formed under the Fe film, which led to prepared devices demonstrating relatively low Schottky barrier heights of 0.05-0.1 eV. The devices exhibit ambipolar behavior independent of the gate polarity, and the current is influenced by the back-to-back Schottky diodes formed by the source (S) and drain (D). Based on the source-drain current changes, the resulting devices are applied for biomolecular detection. The functionalization of the Si NW surface was performed using a dip-pen nanolithography process.

This thesis introduces the factors that significantly contribute to the electrical resistivity in the $FeSi_2$/Si system and are important to consider for predicting the electrical properties of the system and designing contacts in microelectronic devices. The proposed version of Si NW FET with Fe S/D contacts is a promising prototype for the realization of detectors and sensors for biological compounds.

Contents

Chapter 1
Introduction 13
1.1 Motivation and research objectives 13
1.2 Metal/semiconductor interface 18
1.2.1 Low-barrier Ohmic contacts 18
1.2.2 High-barrier Schottky contacts 20
1.2.3 Metal/semiconductor contacts in field effect transistors 24
1.3 Fe/Si-based materials properties and fabrication 29
1.3.1 Si nanowires 29
1.3.2 $FeSi_2$ iron silicides 31
1.4 Applications of Fe/Si-based materials 38
1.4.1 Iron silicides in electronics 38
1.4.2 Si nanowires in electronics 40
Chapter 2
Experimental methods 45
2.1 Fabrication techniques 45
2.1.1 Electron-beam lithography 46
2.1.2 Thermal evaporation in ultrahigh vacuum 47
2.2 Characterization techniques 50
2.2.1 Characterization of morphology 50
2.2.2 Structural characterization 57
2.2.3 Electron transport investigation 64
Chapter 3
Self-assembled $FeSi_2$ crystallites on Si surfaces 69
3.1 Fabrication procedure 69
3.2 Morphology of $FeSi_2$ crystallites 71
3.2.1 $FeSi_2$ on Si(001) 71
3.2.2 $FeSi_2$ on Si(110) 80
3.2.3 $FeSi_2$ on Si(111) 89
3.3 Structure of fabricated $FeSi_2$ crystallites 97
3.3.1 $FeSi_2$ on Si(001) 99
3.3.2 $FeSi_2$ on Si(110) 105
3.3.3 $FeSi_2$ on Si(111) 111
3.4 Discussion of the growth mechanism of $FeSi_2$ crystallites on Si 117
3.5 Temperature-dependent resistance of $FeSi_2$/Si system 124
3.6 Summary and discussion 137

Chapter 4
Si nanowire Schottky barrier FETs with Fe source/drain contacts 139

4.1 Fabrication procedure 139

4.2 Morphology of Si NWs and Fe contact pads 142

4.3 Electron transport in Si NW FETs 145

4.4 Si NW surface functionalization 148

4.5 Biosensing performance 150

4.6 Summary and discussion 158

Conclusions and outlook 161

List of publications 165

List of conference contributions 166

Symbols and Abbreviations

$\bar{A}$	*average crystallite area*
A_d	*diode area*
A_M	*metal work function*
$A_{M,eff}$	*effective metal work function*
A_S	*semiconductor work function*
A_{nS}	*n-semiconductor work function*
A_{pS}	*p-semiconductor work function*
$\mathcal{A}$	*Richardson constant*
a, b, c	*lattice parameters*
D	*spacing of the diffracting plane*
d	*sample thickness*
d_{hkl}	*interplanar distance*
d_{NW}	*nanowire width*
E_0	*free electron energy*
E_C	*conductivity band*
E_{CNL}	*charge neutrality level*
E_{FM}	*Fermi level of metal*
E_{Fn}	*Fermi level of n-semiconductor*
E_{Fp}	*Fermi level of p-semiconductor*
E_g	*valence band*
E_i	*semiconductor intrinsic energy level*
E_{min}	*minimum energy of the system*
$\|F\|$	*structural factor*
$\bar{H}$	*Average height*
h_{NW}	*nanowire height*
I	*current*
I_0	*saturation current*
I_i	*initial current*
I_f	*final current*
I_F, I_R	*forward and reverse current*
I_{hkl}	*diffraction intensity of hkl plane*
k_B	*Boltzmann's constant*
L	*camera length*
l	*distance between the probe points*
m_1, m_2	*number of sites in the phase with coincidences in the opposite phase*
N	*number of measured crystallites*
N_1, N_2	*the total number of atoms in phase 1 and 2*
N_a	*carrier impurity concentration*
n_e	*electron concentration*
n	*ideality factor*
n_d	*diffraction order*
n_{ap}	*apparent ideality factor*
n_i	*semiconductor intrinsic electron concentration*
pI	*isoelectric point*
Q_{OR}	*relative orientation relationship fraction*
R	*Near-Coincidence Sites density value*
R_C	*radius of tip curvature*
R_S	*series resistance*
R_{Sh}	*shunt resistance*
r	*distance between atoms*
r_{min}	*distance at which the interaction energy of atoms turns to zero*
S	*distance between the outer probe points*
SD	*standard deviation*
s	*standard error of the mean*
S_{hkl}	*area of a diffraction peak*
T	*temperature*
V	*voltage*
V_0	*internal contact potential difference*
V_{SG}	*source-gate voltage*
V_{SD}	*source-drain voltage*
V_{VAC}	*vacuum potential*
$U(r)$	*total interaction energy of atoms*
w	*width of the Kikuchi bands*
z	*distance from the probe to the surface*
ΔI	*absolute change in current*
ΔV	*potential difference*
$\mathcal{E}_B$	*electric barrier field*
$\mathcal{E}_\infty$	*high-frequency dielectric constant*
ζ	*angle between conductivity channels of α-$FeSi_2$ and Si*
θ	*angle between incident beam and the crystallographic reflecting plane*
λ	*de Broglie wavelength*
π	*mathematical constant (3.14159)*
ρ	*resistivity*
MIGS	*metal-induced gap states*

ρ_2,ρ_3	*coefficients quantifying the voltage*
ρ_{max}	*maximum resistivity*
σ_s	*barrier inhomogeneities*
φ	*rotation angle*
φ_{ap}	*apparent barrier height*
$\overline{\varphi}_{b0}$	*mean barrier height*
φ_{Bn}	*n-semiconductor barrier*
φ_{Bp}	*p-semiconductor barrier*
χ_S	*semiconductor affinity energy*
χ	*tilting angle*
AFM	*Atomic Force Microscopy*
APTES	*(3-aminopropyl)triethoxysilane*
APTMS	*(3-Aminopropyl)trimethoxysilan*
B20	*cubic crystal structure*
BICINE	*[Bis(2-hydroxyethyl)amino]acetic acid*
BSA	*bovine serum albumin*
BSE	*Backscattered Electrons*
CAG	*catalyst-assisted growth*
CCD	*charge-coupled device*
Cmca	*C-centered monoclinic A-centered*
CMOS	*Complementary Metal-Oxide-Semiconductor*
CVD	*Chemical Vapor Deposition*
DFT	*density functional theory*
DMS	*dimethylsuberimidate dihydrochloride*
DNA	*deoxyribonucleic acid*
DPN	*Dip-Pen Nanolithography*
EBL	*Electron Beam Lithography*
EBSD	*Electron Backscatter Diffraction*
EDS	*Energy-Dispersive Spectroscopy*
fcc	*face-centered cubic*
FET	*Field-Effect Transistor*
FIB	*Focused Ion Beam*
GGA	*generalized gradient approximation*
hkl	*Miller indices*
M/S	*metal/semiconductor*
M/nS	*metal/n-semiconductor*
M/pS	*metal/p-semiconductor*
MBE	*Molecular Beam Epitaxy*
MOS	*Metal-Oxide-Semiconductor*
MOSFET	*Metal-Oxide-Semiconductor Field-Effect Transistor*
NCS	*Near-Coincidence Sites*
NW	*nanowire*
ODT	*1-octadecanethiol*
PBS	*Phosphate buffer saline*
PH	*Present Humidity*
PNA	*peptide nucleic acid*
PT	*Present Temperature*
PVD	*Physical Vapor Deposition*
RE	*Reactive Epitaxy*
RHEED	*Rapid High-Energy Electron Diffraction*
RTP	*Rapid Thermal Processing*
S/D	*source/drain*
SAG	*surfactant-assisted growth*
SB	*Schottky Barrier*
SBH	*Schottky barrier height*
SE	*Secondary Electrons*
SEM	*Scanning Electron Microscopy*
SH	*sulfhidrine (thiol) group*
Si NW	*silicon nanowire*
SME	*surfactant-mediated epitaxy*
SMG	*surfactant-mediated growth*
SOI	*silicon on insulator*
SPE	*Solid-Phase Epitaxy*
SPM	*Scanning Probe Microscopy*
SSC	*surface space-charge*
ST	*streptavidin*
TEM	*Transmission Electron Microscopy*
UHV	*ultrahigh vacuum*
uvw	*Miller-Bravais indices*
VLS	*vapor-liquid-solid*
XRD	*X-ray diffraction*

Chapter 1

Introduction

1.1 Motivation and research objectives

In the field of microelectronic devices, the metal-oxide-semiconductor (MOS) technology is one of the most important and widely used applications of silicon (Si) and Si-based devices. The MOS technology involves the fabrication of electronic devices, such as transistors, using a combination of metal, oxide, and semiconductor materials [1]. The choice of Si as the semiconductor material in MOS technology is primarily due to its exceptional electronic and tunable properties and ability to form a high-quality oxide layer, such as SiO_2, usually used as an insulating material. A thin insulating layer is sandwiched between a metal electrode and a semiconductor material. This three-layer configuration forms the basis of MOS transistors, which have been fundamental building blocks of modern integrated circuits and microprocessors for 50 years [2]. Si has a suitable energy bandgap (~1.1 eV) [3], allowing for efficient electron transport and precise control of electrical behavior. Furthermore, Si is a covalently bonded material that can be used in electronics [4] as Si-nanowires (Si NWs), which in turn demonstrate a high surface-to-volume Si ratio and a unique quasi-one-dimensional electronic structure [5].

Traditionally, the MOS technology is conducted by top-down fabrication using various lithography types, allowing outstanding control and reproducibility of such devices. As was shown in the last years in several works, Si NWs prepared by lithography are usually successfully implemented to MOS field-effect transistors (FETs) [6–8] and used for electrical detection of gases [9], nucleic acids [10], PH level [11] and cardiac biomarkers [12–14]. The important parts of a MOSFET are source (S) and drain (D) electrodes connected to both ends of Si NW. Schottky barrier MOSFETs with metallic S/D electrodes are considered as an alternative to traditional MOSFETs, in which S/D electrodes are highly doped regions of the same semiconductor material as the channel (often Si). They are connected to the channel via junctions known as *p-n* junctions, which come with their of resistance and limit the device's

performance [15]. In contrast, Schottky barrier MOSFETs use a metal-semiconductor (M/S) junction instead of a *p-n* junction for the S/D electrodes, which can reduce the parasitic resistance and capacitance of the device [16]. S/D electrodes are usually made of metals demonstrating compatibility with Si, for example, Fe, which is suitable for defect-free epitaxy on Si [17], allowing for efficient electron transfer and reduced interface resistance. Furthermore, much interest in Fe/Si-based functional materials stems from their environmental friendliness and widespread occurrence in the earth's crust, enabling a greener future with high-performance electronic devices based on these materials [18].

In this sense, Si NW FETs with Fe S/D electrodes now attract considerable attention to realizing biosensors due to simple and low-temperature processing, good suppression of short channel effects, and elimination of doping and subsequent activation steps [19,20]. Although there are many works on Si NW FET biosensors, the physical mechanisms of charge carrier transport in Si NW have not been explained in detail yet. Typically, experimental studies of detection devices based on Si NW FETs are focused on investigating the sensitivity of the fabricated device [21,22] or modifications of the Si NW surface to detect specific molecular targets [19,23].

Besides, Si often forms compounds in solid solutions or intermetallic compounds, known as silicides, usually prepared using self-assembling methods, represented by bottom-up fabrication. Silicides are compounds in which silicon combines with metals, for example, titanium silicide ($TiSi_2$) [24–26], nickel silicide (NiSi) [27–30], cobalt silicide ($CoSi_2$) [31,32], palladium silicide (PdSi) [33,34], platinum silicide (PtSi) [35,36] and tungsten silicide (WSi) [37,38], which have been extensively studied and utilized in the fabrication processes of integrated circuits.

Concerning Fe/Si-based functional materials, Si forms solid solutions with Fe in various stoichiometries, including FeSi [39], $FeSi_2$ [40], and Fe_3Si [41] phases. Among the thermodynamically stable Fe/Si compounds, metallic iron silicide α-$FeSi_2$ exhibits high thermostability and is inert up to 1200°C [42]. This phase belongs to the tetragonal crystal system (P4mmm) with lattice parameters *a, b* = 2.684 Å, *c* = 5.128 Å [43]. In this crystal structure, Fe-deficient planes are formed by iron atoms arranged into a square lattice with a Fe-Fe distance equal *to a*. These planes are denoted as α{001}. Two planes formed by Si atoms separate the Fe-deficient planes. This arrangement creates a quasi-tow-dimensional crystal

structure, where the Fe-deficient and Si planes form distinct layers. Thus, electron transport primarily occurs due to the movement of free electrons in the metal, mainly associated with the iron atoms in the crystal lattice. This characteristic leads to different conductivities along different crystallographic directions. Specifically, a higher conductivity can be expected along the {100} direction, allowing for more favorable pathways for electron movement and enhancing conductivity. On the other hand, the [001] direction may present higher to electron flow due to differences in the crystal structure [44]. Furthermore, the epitaxial relationship (orientation relationship, OR) between α-$FeSi_2$ crystals and the Si substrates on which they are grown can also influence the Schottky barrier formation. The OR determines the alignment and arrangement of the crystal structures at the interface between α-$FeSi_2$ and Si. Variations of the OR affect the electronic properties, interface quality, and the resulting Schottky barrier characteristics. Thus, in MOS technology, this phase can also be used to form Schottky barrier contacts, gate electrodes, local interconnects, and diffusion barriers since its crystal structure makes it possible to control the electron transfer from this phase into the semiconductor by changing the epitaxial alignment on Si [45]. Additionally, metallic iron silicide α-$FeSi_2$ can be used as an electrode material to silicon or semiconducting β-$FeSi_2$ phase forming ohmic contacts [46,47].

The semiconducting β-$FeSi_2$ phase [48] has an orthorhombic structure with a Cmca space group; a = 9.88 Å, b = 7.79 Å, and c = 7.83 Å, and is stable at temperatures below 950°C [49,50]. This phase can be used as active material in photonic crystals [51] and in light-emitting diodes (LED) for transmitting signals through optical fibers since it has a relatively low band gap of ∼0.87 eV favorable for optical fiber communication systems operating at 1.5-μm wavelength [51,52]. Also, in photovoltaics [53], thermoelectrics [54], and electric charge storage [55] possible applications have been discussed. However, laser diodes based on β-$FeSi_2$ are still widely unavailable on the market.

Overall, the presented overview highlights the importance of exploring new approaches in developing competitive technology for the formation of α-$FeSi_2$ and β-$FeSi_2$ crystallites on Si surfaces. Several factors must be considered, including substrate surface orientation, surface roughness, temperature, amount of deposited material, deposition rate, and the possibility of forming a set of silicides within a single technological cycle. Based on the overview, studying

functional materials based on Fe/Si formed on a silicon surface is relevant for future microelectronic devices.

The following specific research directions are of particular interest:

1. Si NW Schottky barrier field-effect transistors (SB FETs) with Fe source/drain (S/D) electrodes and their application in molecular detection, involving examining the performance of these devices for molecular sensing and detection.
2. Self-assembly and processing of metallic and semiconducting iron silicide α-$FeSi_2$ and β-$FeSi_2$ nanostructures on silicon surfaces using reactive epitaxy and molecular beam epitaxy, with control over the epitaxial relationship (OR).
3. Characterization of the morphology and determination of the preferred ORs of the fabricated iron silicide α-$FeSi_2$ and β-$FeSi_2$ crystallites considering Au-assisted growth, different substrate temperatures, and variations in the Fe or Fe/Si co-deposition process.
4. Analysis of carrier transport and the formation of Schottky barriers concerning the preferred ORs of the prepared iron silicide α-$FeSi_2$ and β-$FeSi_2$ crystallites, including studying of the electrical properties and the efficiency of charge transfer across the interface.

This comprehensive study on Fe/Si-based functional materials enables the tunability of their properties, making them highly suitable for integration into next-generation electronic devices.

The thesis is organized as follows.

Chapter 1 introduces the metal/semiconductor interface in the context of application in the metal-oxide-semiconductor (MOS) technology and introduces the Fe/Si-based functional materials properties, fabrication techniques, and application in microelectronics.

Chapter 2 provides a detailed account of the techniques employed to obtain high-quality samples of Fe/Si-based materials and the analytical equipment and experimental facilities employed to investigate the resulting structures and devices' physical, structural, and transport properties.

Chapter 3 presents a bottom-up approach to the growth of self-assembled ensembles of α-, β-$FeSi_2$ submicron- and nano- crystallites, using Au-assisted and Au-free conditions on

different p-Si substrates using molecular beam epitaxy and reactive epitaxy. The study results show that the crystals' orientation relationship (OR) with Si substrates and their morphology can be regulated using Au-assisted growth and Fe/Si atomic flux ratio variation.

Chapter 4 presents a top-down nanofabrication approach involving molecular beam epitaxy and electron beam lithography used to obtain silicon nanowire-based Indium-back-gate field-effect transistors with Schottky contacts on silicon-on-insulator substrates with Fe source and drain contact pads. Based on the source-drain current changes, the resulting devices are applied for biomolecular detection.

1.2 Metal/semiconductor interface

The essential characteristic of the metal/semiconductor (M/S) interface is the nature of the potential barrier between the Fermi level in the metal and the energy region of the main charge carriers in the semiconductor. This barrier controls current conduction and capacitive behavior. The potential barrier height is the primary characteristic of the Schottky barrier, forming a potential energy barrier for electrons at an M/S contact [56]. This potential barrier determines the performance of semiconductor devices. Thus, the M/S interface can form two types of contacts based on its characteristics [57]:

- Low-barrier Ohmic contacts exhibit moderate resistance to current flow in either direction, spanning a wide temperature range [57], as depicted in Figure 1.1. These contacts are commonly called ohmic contacts due to their conductivity adhering to Ohm's law, which states that the current is directly proportional to the voltage applied.
- High-barrier "rectifier" or Schottky contacts demonstrate a low resistance in one direction and significantly higher resistance in the opposite direction, as illustrated in Figure 1.2. These contacts derive their name from Walter Schottky, who initially elucidated the unique behavior, exhibit rectifying characteristics [58,59].

1.2.1 Low-barrier Ohmic contacts

An ohmic contact is characterized by negligibly low contact resistance compared to the total resistance of the semiconductor device. For an ohmic contact to be satisfactory, it should not significantly disrupt the operation of the device. It should allow the required current to flow with a voltage drop that is sufficiently lower when compared to the drop across the active region of the semiconductor device [60].

Minimizing the energy barriers for charge carriers at the contact interface is crucial for realizing an ohmic contact, often achieved by carefully selecting the materials and optimizing the interface to promote electrical coupling between the two materials. Controlled doping of the contact region can improve the electronic properties and facilitate Ohmic behavior [61–63] and applying heat treatment (annealing) can improve the interface and reduce contact resistance [64,65].

In the case of a metal/*n*-doped semiconductor (M/*n*S), electrons transfer from the semiconductor transfer to the metal due to the lower electron concentration in the

semiconductor compared to the metal, resulting in a partial emptying of the conduction band states in the semiconductor, causing a decrease in the Fermi energy of the semiconductor. Consequently, the Fermi energy of the *n*-doped semiconductor is below the Fermi energy of the metal (Fig. 1.1 (a.1)).

In metal/*p*-doped semiconductor (M/*p*S) contacts, electrons from the metal diffuse into the semiconductor due to their higher concentration in the metal. This electron transfer leads to a partial filling of the valence band states in the semiconductor, increasing the Fermi energy of the semiconductor. Consequently, the Fermi energy of the *p*-doped semiconductor is above that of the metal (Fig. 1.1 (b.1)).

In the case of M/S contacts, ohmic behavior is achieved when the work function of the semiconductor A_S is higher than the work function of the metal A_M: $A_{nS} > A_M$ for an M/*n*S contact (Fig. 1.1 (a.2)), or when the work function of the semiconductor A_S is smaller than the work function of the metal A_M: $A_{pS} < A_M$ for an M/*p*S contact (Fig. 1.1 (b.2)). The work function is defined as the difference between the vacuum level (E_0) and the Fermi level (E_{FM}) [60]:

$$A_M = E_0 - E_{FM}, \quad (1.1)$$

$$A_{nS} = E_0 - E_{Fn}, \quad (1.2)$$

$$A_{pS} = E_0 - E_{Fp}, \quad (1.3)$$

where E_{FM} is The Fermi level of metal and E_{Fn}, E_{Fp} – are The Fermi levels of *n*-doped and *p*-doped semiconductors respectively.

When an M/S contact is formed, electrons from the metal penetrate the semiconductor containing electrons with the intrinsic concentration n_i. After electrons from the semiconductor penetrate the metal in an M/S contact, the Fermi level alignment process occurs, reducing in the electron concentration (in the case of M/*n*S contacts) n_e in the semiconductor's contact region. This reduction follows the relation:

$$n_e = n_i \cdot exp[(E_F - E_i)/k_B T], \quad (1.4)$$

where n_i is intrinsic electron concentration, E_F – The Fermi level, E_i - intrinsic energy level of semiconductor and $k_B T$ – Boltzmann's constant multiplied by temperature in Kelvin. This decrease in concentration is a formal consequence of the decrease in the exponent.

Since the concentration of electrons is uniquely related to the position of the Fermi level, its decrease causes an "upward" bending of the energy bands for M/*n*S contacts (Fig. 1.1 (a.2))

and a "downward" bending due to the electron concentration increase for M/*p*S contacts (Fig. 1.1 (b.2)).

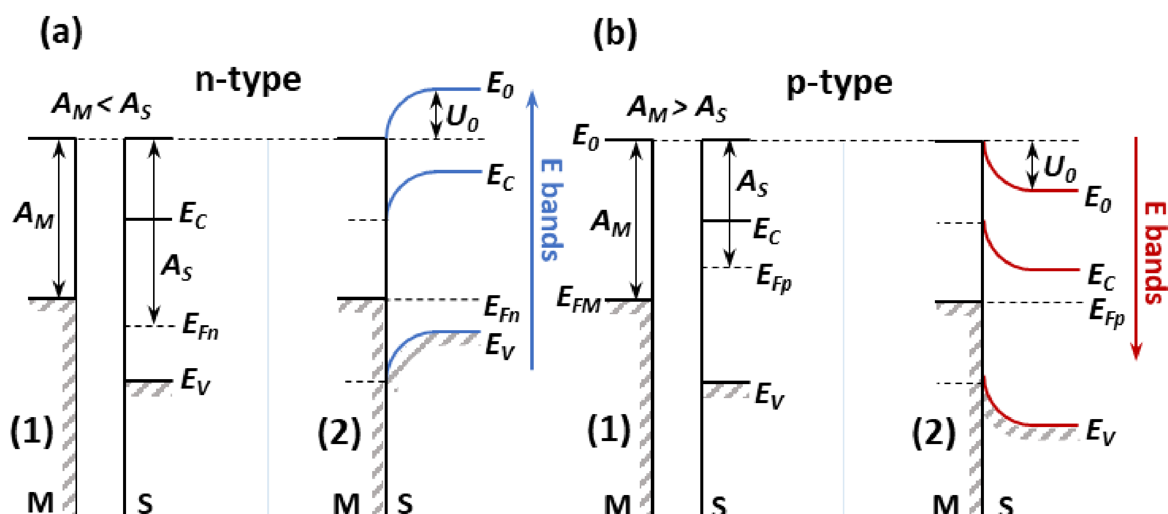

Figure 1.1. Energy diagrams of metal (M)-semiconductor (S) systems (1) isolated and (2) during ohmic contact in the case of (a) n-doped and (b) p-doped semiconductors. A_M and A_S are work functions of metal and semiconductor, respectively, E_0 – free electron energy, V_0 – internal contact potential difference, E_C and E_V – conductivity and valence band levels, E_{FM} – the Fermi level of metal, E_{Fn} and E_{Fp} – the Fermi levels of n-doped and p-doped semiconductors respectively.

The energy band diagrams for M/*n*S and M/*p*S ohmic contacts exhibit similar but inverted basic shapes due to different charge carriers and the direction of charge transfer across the interface (from metal to semiconductor for *p*-doped and from semiconductor to metal for *n*-doped).

Ohmic contacts are characterized by a low contact resistance and exhibit linear, direct, and proportional current-voltage (I-V) behavior. A high concentration of primary charge carriers in the neutral region contributes to low contact resistance. At the same time, other factors, such as barrier height, doping, and interface quality, are equally important to consider. For example, the low barrier allows for Ohmic behavior. It facilitates easy injection or extraction of charge carriers (either electrons or holes) across the interface. Doping introduces high concentrations of free charge carriers (either electrons or holes), contributing to low contact resistance.

1.2.2 High-barrier Schottky contacts

The study of Schottky barriers has been one important objective of researchers during the last decades [66,67]. Figure 1.2 (a.1, b.1) shows the energy diagrams of a metal/*n*-doped

semiconductor (M/*n*S) and metal/*p*-doped semiconductor (M/*p*S), which are isolated. When brought into contact, for instance, through an external conductive connection with a metal, charge flows from the semiconductor to the metal. It establishes thermal equilibrium in the isolated system, resulting in a bending of the energy band within the surface space charge region of the semiconductor, referred to as the depletion layer (marked as *d* in Fig. 1.1-1.2). The alignment of the Fermi levels on both sides occurs simultaneously (Fig. 1.2 (a.2, b.2)). The Fermi level of the *n*-doped semiconductor E_{Fn} decreases and the Fermi level of the *p*-doped semiconductor E_{Fp} rises above the Fermi level of the metal E_{FM} by an amount equal to the difference of the work function of the metal A_M (eq. 1.1) and semiconductor A_S (eq. 1.2-1.3). The Schottky barrier at the M/*n*S interface can be achieved when the work function of the semiconductor A_S is less than the work function of the metal A_M : $A_S < A_M$. In this case, the Fermi level of the metal is below the Fermi level of the semiconductor E_{FM} < E_{Fn} and the conduction band occupancy of the semiconductor, respectively, are higher than the occupancy of the corresponding energy levels of the metal (Fig. 1.2 (a)). Therefore, electrons move from the semiconductor to the metal through internal thermionic emission, driven by the lower work function of the semiconductor compared to that of the metal.

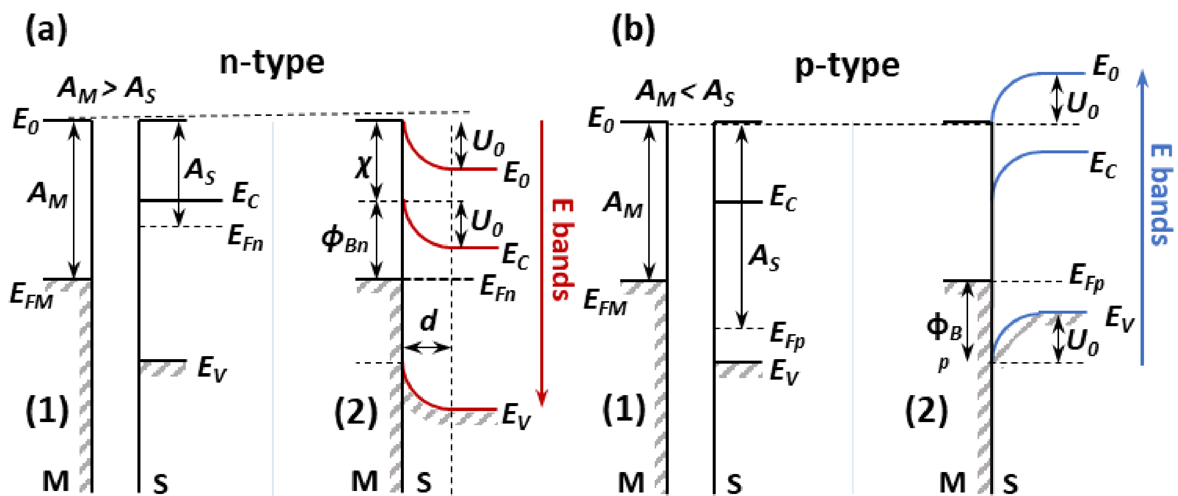

Figure 1.2. Energy diagrams of metal (M)-semiconductor (S) systems (1) isolated and (2) during Schottky contact in case of (a) n-doped and (b) p-doped semiconductors. A_M and A_S are work functions of metal and semiconductor, respectively, E_0 – free electron energy, V_0 – internal contact potential difference, E_C and E_V – conductivity and valence band levels, E_{FM} – The Fermi level of metal, E_{Fn} and E_{Fp} – the Fermi levels of n-doped and p-doped semiconductors respectively, d – depletion layer.

Thermionic emission of electrons over the potential barrier is the dominant transport mechanism for Schottky diodes on moderately doped semiconductors at room temperature

[60]. In an *n*-type semiconductor, donor impurities introduce excess electrons, creating a region with a high electron concentration. When the metal contacts the *n*-type semiconductor, the metal's work function is typically lower than the semiconductor's electron affinity χ_S, creating an energy barrier for electrons at the interface. This energy barrier forms a depletion layer (d) near the interface, where the excess electrons from the donor impurities create a region depleted of mobile charge carriers. The depletion layer establishes an electric barrier field $\mathcal{E}_B$ directed from the semiconductor to the metal. This field prevents electron emission from the semiconductor, promotes the counter emission of electrons from the metal to the semiconductor, and equalizes the electron current and the Fermi level in the system.
When the Fermi level in the system is constant $E_{FM} = E_{Fn} = E_F$ and the equality of the opposite electron emission currents from metal to semiconductor and from semiconductor to metal is achieved, the thermodynamic equilibrium is reached. In the process of Fermi level alignment, accompanied by the thermionic emission, as electrons move from the semiconductor into the metal, their concentration in the near-contact region decreases. Therefore, this decrease causes the bending of energy bands "downwards", evident from the eq. 1.4 (Fig. 1.2 (a.2)). The energy bands bend by an amount equal to the difference between the initial Fermi levels of the semiconductor and the metal, resulting in an energy potential barrier equal to the internal contact potential difference V_0. For example, in the case of the M/*n*S contact, this difference is determined as

$$V_0 = E_{Fn} - E_{FM}. \tag{1.5}$$

By incorporating the free electron energy $\pm E_0$ to the right-hand side of this relation, we determine that the contact potential difference equals the difference between the work functions of the metal and the semiconductor:

$$V_0 = (E_0 - E_{FM}) - (E_0 - E_{Fn}) = A_M - A_S. \tag{1.6}$$

Electrons entering into the semiconductor from the metal need to overcome a barrier φ_{Bn}, which is the difference between the work function of the metal and the semiconductor's electron affinity energy χ_S (independent of the doping level):

$$\varphi_{Bn} = A_M - \chi_S,\ \varphi_{Bn} = V_0 + (E_C - E_{Fn}). \tag{1.7}$$

The height of this barrier corresponds to the work function associated with the internal thermionic emission of electrons from the metal into the semiconductor [68].

For the M/*p*S case, the work function of the semiconductor A_S must be greater than the work function of the metal A_M : $A_S > A_M$. Consequently, the direction of the thermo-emission flux of electrons will initially be from the metal to the semiconductor, leading to E_{FM} > E_{Fn} (Fig. 1.2 (b)). This process is analogous to the mechanism for forming rectifying M/*n*S contacts. In this case, an energy potential barrier of holes from the semiconductor to the metal is created, equal to

$$V_0 = E_{FM} - E_{Fp} \tag{1.8}$$

and a potential barrier φ_{Bn} for the reverse current of holes from metal to semiconductor, equal to

$$\varphi_{Bp} = A_M - \chi_S = E_g - \varphi_{Bn}, \tag{1.9}$$

where E_g is the width of the semiconductor's band gap. In this case, the potential barrier for the leading charge carriers is created by the electric field of the depletion layer. It is accompanied by an “upward" bending of the energy bands (Fig. 1.2 (b-2)).

A distinctive characteristic of Schottky contacts is that charge transfer across the connection primarily involves primary carriers through thermionic emission. The energy of these carriers exceeds the corresponding potential barrier: φ_{Bn} in *n*-doped semiconductor for electrons moving from metal into semiconductor and $q(V_0 - V)$ for electrons moving from semiconductor into metal; and φ_{Bp} in *p*-doped semiconductor for holes moving from metal and $q(V_0 - V)$ for holes moving into metal. By applying an external voltage, the height of the barrier can be varied, enabling control over the thermionic emission current from metal to semiconductor.

1.2.3 Metal/semiconductor contacts in field effect transistors

Advancements in conventional silicon complementary metal-oxide semiconductor (CMOS) technology are reducing device dimensions, especially field effect transistors (FETs). A FET is an electrical device that controls current flow using an electric field. In its typical structure, it consists of an *n*- or *p*-type semiconducting channel, usually a thin layer, between two semiconducting or metallic regions, known as source (S) and drain (D) terminals [69,70]. Figure 1.3 (a) shows the typical architecture of a silicon nanowire (Si NW) based FET [9], which will be discussed further in this work. A silicon nanowire, used as the semiconducting channel, is capacitively coupled through a dielectric material, typically SiO_2 or insulators with higher dielectric permittivity, with a third terminal known as the gate (G). Applying a gate voltage (V_{SG}) turns the device on/off, and the source-drain current (I_{SD}) flowing through the channel is regulated by applying a suitable source-drain voltage (V_{SD}).

Si NW FETs are typically unipolar, exhibiting either *n*-type (Fig. 1.3 (b), green line) or *p*-type behavior (Fig. 1.3 (b), red line), based on the majority carriers being electrons or holes, respectively. However, in some cases, Si NW FETs display ambipolar behavior (Fig. 1.3 (b), black line) where carrier transport is dominated by either electrons (*n*) or holes (*p*) in different working regions of the device [71]. The transition between *n*- and *p*-type behaviors in ambipolar FETs corresponds with the minimum I_{SD} value at a specific V_{SG} value known as charge neutrality point (CNP) or Dirac point [72]. The ambipolar behavior in the Si NW FET can be classified as *n*-type dominant or *p*-type dominant, depending on the Dirac point's location concerning the gate voltage. If the Dirac point is located at $V_{SG} < 0$, it is referred to as *n*-type dominant ambipolar behavior; conversely, if the Dirac point is at $V_{SG} > 0$, it is called *p*-type dominant ambipolar behavior.

Si NW FETs can be categorized into either depletion-mode FETs or enhancement-mode FETs based on their operating characteristics. A depletion-mode FET is typically "on" and conducts current at zero-gate bias conditions ($V_{SG} = 0$). If the current at $V_{SG} = 0$ exceeds the off-current (Fig. 1.3(c), orange line), it is a normally-on depletion-mode FET. In contrast, an enhancement-mode FET is typically "off" and does not conduct current under zero-gate bias conditions ($V_{SG} = 0$). If the current at $V_{SG} = 0$ is equal to the off-current (Fig. 1.3(c), blue line), it is called a normally-off enhancement-mode FET.

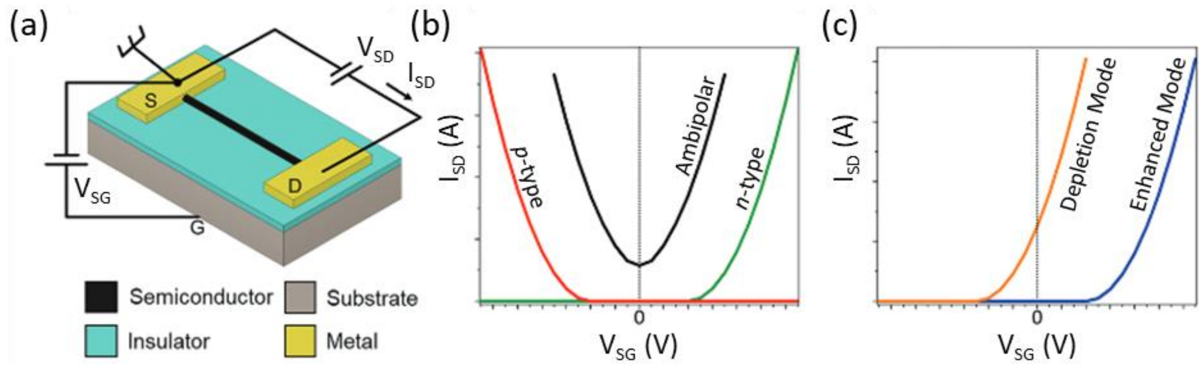

Figure 1.3. Typical architecture and bias mode (negative or positive gate voltage) of a Si NW FET, (b) transfer characteristic of p-type, n-type, and ambipolar Si NW FETs, and (c) transfer characteristic of depletion and enhanced mode n-type Si NW FETs. Reproduced from [9].

Concerning the M/S contacts in FETs, the forward-bias current through a uniform M/S interface, according to thermionic emission theory [60], can be expressed as

$$I = I_F - I_R = I_0 \left[exp\left(\frac{qV_0}{nk_BT}\right) - 1 \right], \tag{1.10}$$

where I_F and I_R are forward and reverse currents, $I_0 = A_d \mathcal{A} T^2 exp\left(\frac{-\varphi}{k_BT}\right)$ is the saturation current and φ_{ap} is the zero bias barrier height, q is the electron charge, k_B is the Boltzmann constant, T is the absolute temperature, is the forward-bias voltage, A_d is the effective diode area, $\mathcal{A}$ is the effective Richardson constant (32 A/cm^2·K^2 for p-Si [73] and 120 A/cm^2·K^2 for *n*-Si [60]). The ideality factor n, also known as *quality factor* or *emission coefficient*, typically varies from 1 to 2, depending on the fabrication process and semiconductor material. Thus, n is a parameter indicating how closely a diode follows the ideal diode I-V characteristic, and it is used in the diode equation to express the current through a diode as a function of voltage. Shockley first derived the ideal diode equation with the unity ideality factor n for *p-n* junctions in 1949 [74] and later, in 1982, Rhoderick introduced the ideality factor for Schottky contacts [75].

Direct M/S contact usually results in an energy barrier (i.e., Schottky barrier, Ch. 1.2.2) capable of inhibiting the I_{SD} flow. This effect is observed in real devices due to surface defects and interfacial traps, such as dangling bonds and impurities. In this scenario, the energy barrier is pinned to a specific level within the semiconductor bandgap, depending on the type and density of surface defects/traps. The presence of a Schottky barrier restricts the I_{SD} flowing through the FET channel, resulting in an asymmetric nonlinear behavior of the output characteristic (Fig. 1.4 (a)).

Current transport in the presence of a Schottky junction is primarily due to the majority of carriers. If Schottky barriers at the drain or source contacts have significantly different heights, transport through the device is dominated by one type of carrier, leading to FETs with unipolar behavior. When the Schottky barriers are comparable, electrons and holes are injected, leading to an ambipolar FET. To reduce surface impurities/states and enhance the Ohmic behavior of the contacts, thermal pre-annealing (before lithography steps) and reactive ion etching cleaning (after lithography steps) are commonly used. The main parameters describing the output characteristics of a real Schottky diode are the ideality factor n, the series resistance R_S and the shunt resistance R_{Sh}. The output characteristic of an ideal Schottky diode, as described by the theory of thermionic emission without considering described parameters (eq. 1.10), is shown by the blue solid line in Figure 1.4 (a).

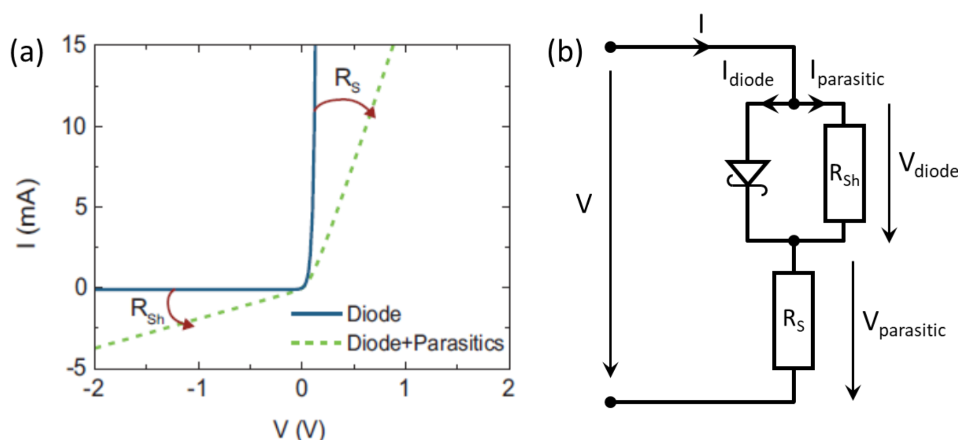

Figure 1.4. (a) The output characteristics of an ideal Schottky diode, calculated from thermionic emission theory (blue solid line) and the output characteristic of a real Schottky diode including parasitic series R_S and shunt R_{Sh} resistances (green dashed line); (b) equivalent diagram of a Schottky diode, including series R_S and shunt R_{Sh} resistances. Reproduced from [28].

However, real Schottky diodes exhibit significant deviations from this ideal output characteristic (Fig. 1.4 (a) green dotted line). On the one hand, these deviations can be attributed to the impact of the R_{Sh} shunt resistance on current flow at low forward voltages. More importantly, the output characteristic of diodes with high Schottky barrier height at reverse voltages. On the other hand, variations in the output characteristic may arise from the presence of a parasitic series resistance R_S, mainly at high voltages [33,34]. Therefore, using the equivalent diagram (Fig. 1.4 (b)), the circuit diagram of a real Schottky diode can be described as follows:

$$I = I_0\left[exp\left(\frac{q(V - R_S(T)\cdot I)}{k_B T}\right) - 1\right] + \frac{V - R_S(T)\cdot I}{R_{Sh}}. \quad (1.11)$$

Therefore, the consequential increase in parasitic resistance has become a significant limitation to the performance of nanoscale semiconductor devices [76,77]. The parasitic resistance is predominantly influenced by contact resistance.

To effectively reduce the specific contact resistance at the M/S interface, precise control and tuning of the Schottky barrier height (SBH) are important. According to the Fermi level pinning theory, in an M/S contact, electron wave functions in the metal can decay into the semiconductor band gap, creating intrinsic states known as the metal-induced gap states (MIGS) [78]. The energy level in the band gap at which the dominant character of the interface states changes from donor-like to acceptor-like is called the charge neutrality level (E_{CNL}). In the physical M/S contact, the position of the metal at the Fermi level (E_{FM}) is pinned near the E_{CNL}, due to charge transfer across the interface, creating a dipole that tends to drive the band lineup toward a position that would result in a zero dipole charge. The proximity of E_{FM} to E_{CNL} consequently creates a Schottky barrier for both electrons and holes. How strongly E_{FM} is pinned towards E_{CNL} is determined by the pinning factor (S) [79], which is defined as the rate of change in the SBH (φ_B) concerning the change in metal work function (A_M). The empirical trend is established by Mönch [80] and relates the pinning factor S to the dielectric screening of the material on which the metal the Fermi level is pinned as

$$S = \frac{\partial\varphi_B}{\partial\varphi_M} = \frac{1}{1 + 0.1(\mathcal{E}_\infty - 1)}, \quad (1.12)$$

where $\mathcal{E}_\infty$ is the high-frequency dielectric constant. Effective metal work function ($A_{M,eff}$), referred to the modified energy level of the metal at the M/S interface, influenced by the pinning of the metal Fermi level near the charge neutrality level and the resulting Schottky barrier height, is therefore given by

$$A_{M,eff} = S\cdot A_M + (1 - S)\cdot E_{CNL}. \quad (1.13)$$

Pinning can result in significant contact resistance due to a very high Schottky barrier height, irrespective of the metal used. The insertion of an ultra-thin insulating layer between the semiconductor and metal is known to reduce this barrier [81]. However, reducing the effective barrier height in *n*-doped Si is challenging because the metal tends to pin close to the valence band, leading to a large Schottky barrier height for electrons and, consequently, high contact resistance. Reducing the barrier for holes in *p*-doped Si is also important because it enables

the design of low-doped, highly conductive *p*-type contact with higher selectivity between two types of carriers [77].

Another approach to reducing contact resistance in an M/S contact is to increase the electrically active dopant density in semiconductors, which is effective for *n*-type semiconductors [76]. This method involves thinning the barrier to allow for a sufficient value of tunneling current [82]. However, it is unsuitable for *p*-type semiconductors due to insufficient electrical activation of dopants [76].

Moreover, to modulate the SBH, an additional dipole can be created at the M/S interface. Dipole manipulation is typically achieved by implanting neutral Ge or C into silicon [83]. Alternatively, the dipole charge formation can be adjusted by tuning the epitaxial alignment of the metal contact layer, where the metal exhibits anisotropy of electron wave function due to epitaxial strain or crystal structure. Metal silicides, widely used for interconnection, can produce effective barrier heights around ~0.2 eV [77], and their capabilities hold significant potential for further development in nanoscale contacts.

Additionally, as demonstrated in [84], spatially inhomogeneous SBH is assumed to model the interface of the Schottky diode. The lateral distribution of SBH can explain the decrease in the barrier height with a decrease in temperature if the barrier height has a Gaussian distribution of the barrier height values over the Schottky contact area with the mean barrier height $\overline{\varphi}_{b0}$ and standard deviation σ_s. The standard deviation is a measure of the barrier homogeneity. Thus, in the case of a Gaussian distribution of SBH, one obtains

$$\varphi_{ap} = \overline{\varphi}_{b0} - \frac{q\sigma_s^2}{2kT}, \tag{1.14}$$

where φ_{ap} is the apparent barrier height measured experimentally [85,86]. The observed variation of the ideality factor n with temperature in the model is given by [34]

$$\left(\frac{1}{n_{ap}} - 1\right) = -\rho_2 + \frac{q\rho_3}{2kT} \tag{1.15}$$

where n_{ap} is the apparent ideality factor, ρ_2 and ρ_3 are coefficients thet quantify the voltage deformation of the barrier height distribution.

1.3 Fe/Si-based materials properties and fabrication

1.3.1 Si nanowires

Silicon nanowires (Si NWs) are one-dimensional nanostructures composed of silicon, a semiconductor material with a diamond cubic crystal structure, fcc (face-centered cubic), belonging to the cubic *Fd3m* space group with lattice parameter a = 5.43 Å [87], and is presented in Fig. 1.5.

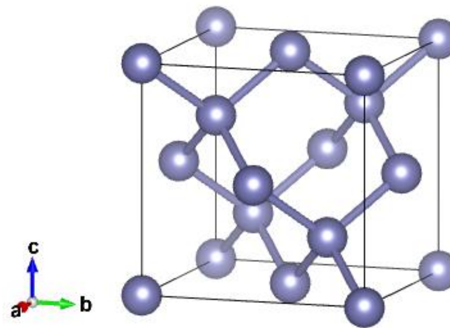

Figure 1.5. Cubic non-primitive unit cell of Si crystal in diamond structure.

The synthesis of Si NWs was first reported in 1964 by Wagner and Ellis [88]. Axial Si NWs were fabricated by vapor-liquid-solid (VLS) growth using gaseous silane (SiH_4) as a precursor and gold (Au) nanoparticles as catalysts (Fig. 1.5 (a)) [88]. Since then, Si NWs have attracted significant attention owing to their high surface-to-volume ratio, limiting electron motion to one direction along the wire axis. This confinement results in quantized energy levels, forming a series of discrete energy states known as subbands. The wire diameter determines the energy spacing between these subbands and can be tuned by controlling the nanowire dimensions [89]. As an alternative to VLS growth, the growth of epitaxial Si NWs by a metal-catalyst-free process has been reported [90]. In the process, needle-shaped Si NWs with a core-shell structure, consisting of a single-crystalline Si core and a SiO_2 surface coating, were grown on the Si(111) substrate.

In terms of applications, electronic devices based on Si NWs represent a natural extension of the downscaling semiconductor transistor based on a silicon-metal insulator [4]. However, the unique properties also enable new device concepts such as solar cells [91,92], field effect transistors [93–95], chemical [96,97], and biological [98–100] sensors. These devices can benefit from a high surface-to-volume ratio, resulting in high sensitivity.

Traditionally, the fabrication of nanostructures using a top-down approach has been widely applied to manufacture semiconductor devices. One of the most popular processes in

manufacturing is the electron beam lithography process, which produces nanostructures down to 10 nm in size [101]. The top-down approach is the preferred approach for the preparation of Si NWs. In most cases, the top-down approach is used to fabricate Si NWs when accompanied by silicon-on-insulator (SOI) lithography tools that are compatible with complementary metal-oxide-semiconductor (CMOS) technology [102–104]. Fabrication of Si NWs using lithography techniques (Fig. 1.5 (b)) offers greater flexibility and accuracy of arrangement and is much more suitable for device fabrication. SOI substrates with ultra-thin Si top layers are widely used for Si NWs fabrication. Fabrication of Si NWs using top-down technology involves the following steps: a lithography step and an etch step. In most cases, the first step in the fabrication of nanostructures is to use a bulk crystal or thin layer of material for different lithography techniques:

1. *Optical lithography:* in this process, a light-sensitive layer (mask) is exposed or irradiated using ultraviolet radiation [105]. A pre-formed mask is created based on a specially prepared template, through which the desired image is transferred to the substrate. When combined with chemical etching techniques, optical lithography can produce Si NWs with linear dimensions as small as 1 µm. This method is widely employed in producing large structures or feeder contacts in industry and research laboratories [106,107].

2. *Electron beam lithography:* this technique can produce structures with a linear size as small as 10 nm and requires sophisticated high-vacuum equipment [108]. Exposure is conducted from point to point using a focused electron beam in this process. The combination of electron beam lithography and reactive ion etching on an SOI substrate allows for precise control over the geometry and complexity of Si NWs [109,110].

3. *Dip-pen nanolithography (DPN)* [111] is one of the methods of probe nanolithography. The DPN process uses the tip of a scanning probe coated with the required material or "ink" for direct deposition with nano precision onto a substrate. In the DPN process, a mask is formed on the material's surface by transferring "ink" molecules from the scanning probe tip through the aqueous meniscus that connects the probe and the substrate. During the process, it is possible to control the speed and time of the probe's delay over the surface of the substrate. This makes it possible to produce Si NWs with different widths and lengths [112]. It is a convenient and versatile method that can use different organic and inorganic molecules as inks and create different nanostructures under ambient conditions.

The top-down approach, particularly employing lithography processes, is preferable for fabricating of Si NWs on SOI substrates. Lithography processes easily combine with chemical etching processes and allowing for selective material removal [113–115].

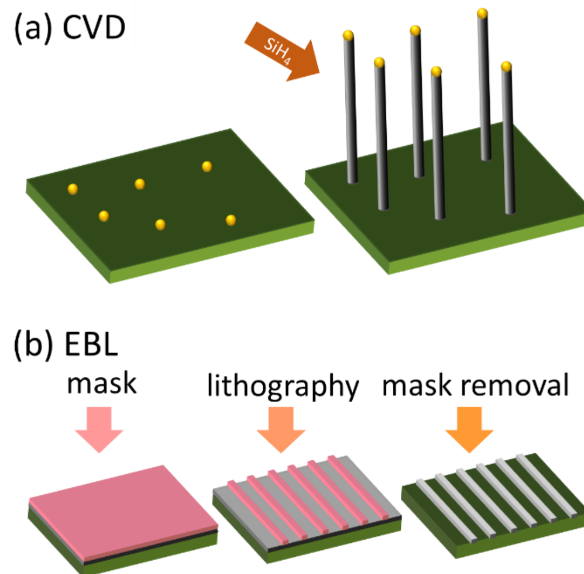

Figure 1.6. Schematic representation of Si NW fabrication approaches: (a) bottom-up, i.e. VLS-assisted chemical vapor deposition (CVD), and (b) top-down, i.e. electron-beam lithography (EBL).

1.3.2 $FeSi_2$ iron silicides

Historically iron silicides have been known since the 20th century, with the discovery of new minerals called xifengite and gupeiite in 1984 [116]. These minerals were found in meteorite dust in the Yanshan Mountains, Hebei Province, China and were identified as iron silicides with the formulas Fe_5Si_3 and Fe_3Si. The discovery of xifengite and gupeiite sparked interest in studying iron silicides, their properties and applications.

Iron silicides formation

Iron silicides' formation mechanisms and the factors influencing their growth attract special attention. Traditionally, iron silicides are produced in the process of Fe/Si solid-phase reaction [117], when the monosilicide FeSi phase is initially formed as an amorphous layer and crystallizes during thermal annealing at ~290 °C and has B20 type cubic crystal structure (P213) [39]. Other silicides such as Fe_3Si, $FeSi_2$, and Fe_5Si_3 are formed after the formation of monosilicide FeSi. The $FeSi_2$ phase exists in two thermodynamically stable phases: a tetragonal, metallic α-$FeSi_2$ phase (Fig. 1.7 (a)) and the semiconducting β-$FeSi_2$ phase, synthesized at temperatures 475-600°C (Fig. 1.7 (b)) [118,119]. The phase-transition

temperature from β-$FeSi_2$ to α-$FeSi_2$ phase is 800-950 °C [120]. A simplified iron-silicon phase diagram (Fig. 1.7 (c)) shows the various phases that occur when iron and silicon are mixed at different temperatures and Fe/Si ratios.

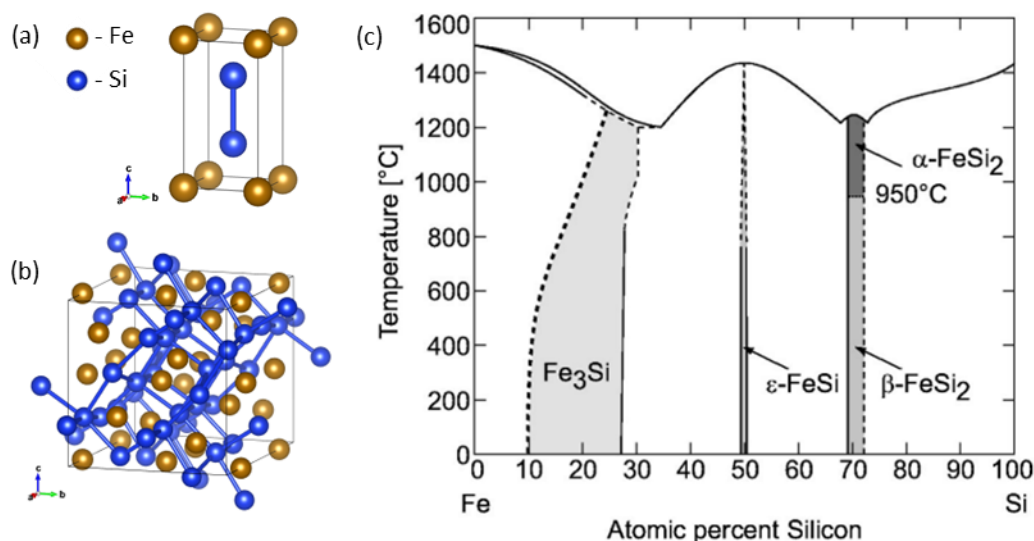

Figure 1.7. (a) α-$FeSi_2$ tetragonal unit cell, (b) β-$FeSi_2$ orthorhombic unit cell and (c) bulk phase diagram illustrating the thermodynamic behavior and phase transitions of iron-silicon compounds under different temperature and composition conditions [121].

Fig. 1.7 (a) shows the unit cell of the α-$FeSi_2$ phase belonging to the tetragonal crystal system (P4mmm) with lattice parameters *a, b* = 2.684 Å, *c* = 5.128 Å [43]. Fe-deficient planes denoted as α{001} formed by iron atoms (yellow balls) are arranged into a square lattice with a Fe-Fe distance equal *to a*. The semiconducting β-$FeSi_2$ phase, presented in Fig. 1.7 (b), has an orthorhombic structure with a Cmca space group and lattice parameters *a* = 9.88 Å, *b* = 7.79 Å, and *c* = 7.83 Å [122]. Due to such a variety of iron silicides with different properties, the synthesis conditions play a special role. The formation mechanisms and factors influencing the initial stages of iron silicide formation have been described in several works [123–125]. Some properties of α-, β-$FeSi_2$ and FeSi phases are summarized in Table 1.1.

Table 1.1. *Summary of FeSi and α-, β-$FeSi_2$ phase's crystal structure and their properties.*

Phase	Crystal structure	Lattice constant (Å)			Properties	Ref
		a	*b*	*c*		
FeSi	Cubic P213 [198]	4.467	4.467	4.467	Metallic/Semiconducting	[39]
α-$FeSi_2$	Tetragonal P4/mmm [123]	2.644	2.644	5.128	Metallic	[43]
β-$FeSi_2$	Orthorhombic Cmca [64]	9.863	7.791	7.833	Semiconducting	[122]

The substrate temperature significantly influences the formation of compounds in the Fe/Si system. Therefore, precise temperature control and a comprehensive understanding of silicide growth mechanisms, particularly at elevated temperatures, are essential.

Iron silicides fabrication techniques

The bottom-up approach involving self-assembling processes, in which nanostructures are formed from individual atoms and molecules [126], is the most common technique for the fabrication of iron silicide micro- and nanostructures. This approach is used to create functional multi-component nanostructures by the controlled assembly of atoms and molecules without developing or eliminating parts of the resulting nanostructures. In this case, a typical example is chemical methods of nanostructure fabrication [127–129]. Although some of the significant technological challenges of the bottom-up approach remain, such as surface preparation and conditions for controlled assembly of atoms, control of impurity concentration, homogeneity of the resulting nanostructures, etc., the approach is widely used to create functional nanostructures by various methods [130–132]. One of the processes of the bottom-up approach is e*pitaxy* (from Greek *epi (ἐπί)* - above, and *taxis (τάξις)* - an ordered manner) or *epitaxial growth*, which involves the nucleation of atoms on the substrate surface, followed by the growth of a crystalline layer with a specific orientation and structure [133]. In this manner, epitaxial α-$FeSi_2$ nanostructures can be produced by pulsed laser deposition [134], annealing of Fe film on Si substrates [135–137], ion implantation [138,139], polycrystalline films can be grown by radio frequency magnetron sputtering [140]. Also, α-$FeSi_2$ nanostructures can be fabricated on Si(001) substrate by chemical vapor deposition [47]. Chemical vapor deposition (CVD) is the fabrication method used in the semiconductor industry to produce high-quality nanostructures and thin films [141]. In the CVD process, the substrate is exposed to one or more volatile precursors that react and/or decompose on the surface of the substrate to produce the desired precipitate. One variation of the CVD method is the growth mechanism of one-dimensional vapor-liquid-solid (VLS) nanostructures. In the VLS growth mechanism [142], the nanostructures are formed by depositing material from the gas phase onto a substrate. This process involves the introduction of catalyst droplets onto the substrate surface. These droplets act as a bridge, absorbing the material from the gas and creating a supersaturated liquid state. The material then crystallizes onto the substrate, leading to the growth of nanostructures. Thus, it is

possible to control the physical parameters of the obtained nanostructures by changing the size and properties of the liquid alloy from which the droplets are composed. To highlight that the bottom-up approach is preferable for fabricating α-$FeSi_2$ nanostructures due to the possibility of controlling the self-assembly process it is worth mentioning work [143], where authors report on mechanochemical synthesis in a planetary ball mill in order to synthesize both α-$FeSi_2$ using elemental micron-sized Fe and Si powders as precursors.

Another process involved in the bottom-up approach is *endotaxy* (from Greek *endo (ενδο)* - inside, and *taxis (τάξις)* - an ordered manner), when one material (deposited material) grows inside another material (substrate). It involves the diffusion of atoms or molecules into the host material, followed by the growth of a new material with a specific orientation and structure [144]. Endotaxial β-$FeSi_2$ NWs (10 nm high, 30 nm wide, and 3 µm long) can be formed on Si(110) substrates by molecular beam epitaxy (MBE), especially the reactive-deposition epitaxy (RDE) method, along with annealing cubic s-phase $FeSi_2$ NWs at 800°C [145,146]. On the other hand, α-$FeSi_2$ endotaxial NWs (25 nm wide and 0.6 µm long) can be prepared by Fe deposition on Si(110) at 650°C [147] using a thermal vacuum deposition method, which is a common method of physical vapor deposition (PVD). The method employs two physical processes: evaporating heated feed material and condensation on the substrate. The quality and strength of the produced nanostructures depend, to a significant extent, on the purity of the substrate. In the study [148], authors describe the fabrication of iron silicide NWs by a different growth method in an ultrahigh vacuum (UHV) of below $5 \cdot 10^{-8}$ Pa and in a high vacuum (HV) of below $4 \cdot 10^{-4}$ Pa by solid-phase epitaxy (SPE), where Fe was deposited at room temperature followed by annealing at 600°C on a phosphorous-doped n-type Si(110) substrate and by RDE where Fe was deposited onto the Si(110) substrate held at 600°C. The resulting NWs obtained by SPE are 20-120 nm in length, 6-15 nm wide, and 1-2 nm in height, while those obtained by reactive epitaxy (RE) are 100-1000 nm in length, 15-20 nm wide and 2-4 nm in height. SPE was also used to prepare self-assembled α-$FeSi_2$ nanoislands onto vicinal Si(111) substrates, followed by thermal annealing [149]. RE combined with nitride-mediated epitaxy (NME) was used to grow self-assembled endotaxial α-$FeSi_2$ NWs on Si(100) [150]. The average length and width of NWs obtained by RDE are 160 nm and 5 nm, respectively. NWs obtained on nitride-capped Si substrates by RE at 650°C followed by prolonged annealing at the same temperature for 1.5 h were found to have significantly increased lengths up to 2 µm

and a width of 5-10 nm. The increase is attributed to the slowing down of the growth of silicide islands with an ultralow flux of Fe adatoms mediated by a thin Si_3N_4 layer.

Surfactant-mediated epitaxy (SME), also known as surfactant-mediated growth (SMG) or surfactant-assisted growth (SAG), as well as nitride-mediated epitaxy (NME), is used for controlling the growth of epitaxial thin films. SAG involves intentionally incorporating a surfactant material, such as bismuth (Bi) or antimony (Sb), into the growth process to modify the surface energy and control the morphology and growth rate of the epitaxial layer. Thus, in the study [151] the SAG method was used for high-quality β-$FeSi_2$ layers preparation on Si(111) substrate at 650°C by simultaneous exposure of the Si substrates to Fe and Sb flux. SAG involving Bi has been used to grow germanium (Ge) [152] and indium arsenide (InAs) [153] endotaxial nanowires on Si substrates.

As it was mentioned above, the fabrication process of axial semiconductor NWs is usually supported by catalyst-assisted growth (CAG) [154], which involves the use of a catalyst material, especially gold (Au), to promote the growth of NWs or other nanostructures by VLS mechanisms acting as nucleation sites [155]. The growth processes on the surface under a catalyst droplet proceed much faster than on a non-activated surface. However, several studies describing Au as a surfactant material [156,157] reveal the influence of an ultrathin Au layer on the self-assembly of Fe/Si nanostructures on Si(111). During the described SAG process, Au atoms adsorb onto the Si surface and form islands or clusters that help stabilize the FeSi phase's growth. Reducing surface energy and, at the same time, increasing its wetting properties can help to control the morphology and size of the iron silicide crystals forming on a silicon substrate. Typically, during the SAG process, the addition of a surfactant to a substrate surface can significantly reduce the size of islands and even switch the growth to layer-by-layer mode, thereby reducing the roughness of the films produced by MBE by increasing the diffusion barriers as well as reducing the specific surface energies of the growing phase and the substrate [158]. The recent study [159] describes the changes in thermodynamic equilibrium of the different forms of α-$FeSi_2$ crystallites grown under the Au layer due to changes in their surface energy. The study reveals that using Au as a surfactant previously deposited on a Si(001) substrate can change the shape of growing α-$FeSi_2$ crystallites, their crystallographic orientation, their lattice stress, and their ability to embed growth. The presence of Au as a surfactant also affects the ability of α-$FeSi_2$ crystals to grow embedded

into the substrate. These conclusions are also supported by experimental work [46], in which it is shown that the use of Au does not lead to the growth of α-$FeSi_2$ NWs, contrary to the analogy with silicon, but allows one to control the preferred orientation and morphology of the growing film. Additionally, the film changes orientation from α-$FeSi_2$(111)//Si(001) to α-$FeSi_2$(001)//Si(001) even at high synthesis temperatures, which may be useful for other technological problems [160]. Nevertheless, the literature does not present information about the Au-assisted growth of the α-$FeSi_2$ phase on Si(110) or Si(111) substrates.

Based on the presented overview, when discussing Au-assisted growth of α-$FeSi_2$ nanocrystals, it's important to consider the varying definitions and contexts used in the literature. Different authors and research groups may interpret and use terms like "surfactant" and "catalyst" differently. For example, in [161] authors describe the use of surfactants in MBE to improve the quality of strained layer semiconductor heterostructures. It was reported that Au can act as a surfactant by reducing the surface energy of the growing crystal, which promotes the formation of smooth surfaces and minimizes the formation of defects. On the other hand, the use of Au as a catalyst in MBE has been investigated in the growth of Si/Ge heterostructures and Pt/Au(111) surfaces for oxygen reduction [162,163]. It was featured that the use of Au as a catalyst could promote the growth of axial nanowire-based Si/Ge nanowires with uniform diameters and high aspect ratios [162] and can lead to the growth of high-quality crystals with controlled morphology and composition in case of Pt/Au(111) surfaces [163]. To ensure clarity, the specific definitions provided in the literature are analyzed. Thus, in the context of Au-assisted growth of α-$FeSi_2$ nanocrystals, there is a distinction between the roles of a *surfactant* and a *catalyst*:

- A *surfactant* is a substance that alters the surface properties of a material, such as wetting behavior and surface energy. It adsorbs onto surfaces or interfaces and significantly modifies their free energies [164]. In the case of α-$FeSi_2$ nanocrystal growth, Au as a surfactant reduces the surface energy of the growing α-$FeSi_2$ crystals since it has a low surface energy [165], which allows the forming of stable and well-defined islands with high adhesion to the Si substrate and better electronic properties. Thus, using Au as a surfactant makes it possible to control the size, shape, and orientation of the α-$FeSi_2$ crystal on a substrate.

- A *catalyst* is a substance that accelerates a chemical reaction without being consumed [166]. In the growth of α-$FeSi_2$ nanocrystals, the Au islands also act as catalysts. The Au-islands serve as growth centers or nucleation sites for the α-$FeSi_2$ crystals and activate the growth process, enabling the rapid formation of α-$FeSi_2$ nanocrystals on the Si substrate and enhancing the growth kinetics by facilitating the attainment of desired crystal structures. Thus, Au as a catalyst is key in determining the shape and crystallographic orientation of the α-$FeSi_2$ nanostructures.

Thus, considering both definitions, one can conclude that Au acts not only as a surfactant, but also as a catalyst in the growth of α-$FeSi_2$ and other metal silicide nano and submicron crystals. In this work, the role of Au as a surfactant and a catalyst in Au-assisted synthesis of self-assembled α-$FeSi_2$ crystallites on Si surfaces is considered to study the possibilities to control the size, shape, and orientation of the α-$FeSi_2$ phase concerning Si substrate.

1.4 Applications of Fe/Si-based materials

1.4.1 Iron silicides in electronics

Iron silicides are a group of materials that have been extensively studied for their potential applications in modern electronics. For example, the semiconducting β-$FeSi_2$ phase is the most studied material among the semiconducting silicides [167] due to a narrow bandgap of around 0.85 eV at room temperature, which is equivalent to the absorption minimum of an optical fiber at 1.5 µm [168], making it suitable for optoelectronics, which is unfeasible for pure Si due to its indirect band gap. As a result, β-$FeSi_2$ has gained attention for its potential in optoelectronic devices. Various research groups [122,169–172] have successfully developed light-emitting diodes using Si/β-$FeSi_2$ heterostructures. Furthermore, the high thermal stability and significant light absorption coefficient of β-$FeSi_2$ have led to its investigation for photovoltaics [173,174]. Undoped β-$FeSi_2$ phase is usually a *p*-type semiconductor, which can be converted to *n*-type by doping with Co, Ni, Pt or Pd [175–178] and reducing the concentration of impurities [179]. Another area of interest is the application of β-$FeSi_2$ in thermoelectrics, which was first proposed in 1964 [180]. Since then, numerous studies have been conducted on this subject, for example [181,182]. Compared to most other thermoelectric materials, β-$FeSi_2$ offers several advantages, such as its abundance, recyclability, and non-toxicity, making it a promising environmentally friendly alternative. The production of β-$FeSi_2$ devices from cast iron scrap has demonstrated the potential of this material, with devices reaching up to 90% of the figure of merit of those made using pure Fe [183]. Doping [184–186] and the reduction of thermal conductivity by nanostructuring [48,187] are promising approaches for further enhancing the thermoelectric performance of β-$FeSi_2$. For instance, C.-L. Hsin et al. [188] demonstrate that the thermal conductivity of β-$FeSi_2$ NWs with diameters of around 100 nm is significantly affected by spatial confinement. Overall, the β-$FeSi_2$ phase exhibits unique physical and electronic properties, which have attracted considerable scientific interest and research attention, making it a subject of investigation in its own right [189].

On the other hand, the bulk metallic α-$FeSi_2$ phase has been investigated as a candidate material for thermoelectric applications due to its high Seebeck coefficient and low thermal conductivity [190–192]. While the α-$FeSi_2$ phase is paramagnetic and metastable [193], it exhibits ferromagnetic properties at the nanoscale with a magnetization higher than pure iron

[149,194,195]. It is worth mentioning that according to theoretical findings by N. Zamkova and V. Zhandun, changes in the α-$FeSi_2$ lattice parameters induced by the off-stoichiometric composition or epitaxial lattice strain may lead to ferromagnetism [203,204]. Furthermore, the metallic α-$FeSi_2$ phase provides high electrical conductivity at the nanoscale and can be used as interconnects in microelectronics. Even though the electrical conductivity of bulk α-$FeSi_2$ is relatively low, which limits its use in microelectronics, α-$FeSi_2$ nano- and microstructures are used as an electrode material to silicon or β-$FeSi_2$ with good ohmic characteristics [46,47].

In the case of Schottky barrier formation, there are several works reporting on the fabrication of α-$FeSi_2$ thin films and crystallites on different Si substrates and their transport properties. In the work [196], K. Radermacher et al. report the fabrication of buried polycrystalline metallic α-$FeSi_2$ crystallites with very sharp interfaces to the Si(111) substrate, which have specific resistivities of about 250 μΩ·cm and show a relatively high Schottky barrier height of $\varphi_{Bn} \approx 0.84$ eV to *n*-type Si(111) substrates. A more recent study [197] shows that tuning the epitaxial alignment (orientation relationships) of metallic α-$FeSi_2$ crystallites on *p*-Si(001) substrate results in a difference of reverse current by two orders of magnitude due to the anisotropic structure of α-$FeSi_2$ silicide penetrating the silicon bandgap differently for the different type of the α-$FeSi_2$/Si interfaces. Thus, by varying the orientation relationships between α-$FeSi_2$ and Si substrate, we aim to create Schottky barrier contacts, gate electrodes, local interconnects, and diffusion barriers that can be easily tuned and optimized for specific device applications.

1.4.2 Si nanowires in electronics

Si NWs have a bandgap of around 1.1 eV [3], which makes them suitable for a range of applications in microelectronics, including field-effect transistors (FETs) [198], photodetectors [199], and solar cells [91,200]. Si NWs have also been investigated as building blocks for nanoelectronics due to their high surface-to-volume ratio, which can lead to improved performance and lower power consumption.

In FETs Si NWs serve as the channel region between the source and drain (S/D) electrodes. Due to their small size and high surface-to-volume ratio, Si NWs can exhibit unique electronic properties not observed in bulk silicon, for example, the ability to tune the thermal conductivity of the nanowire by varying its diameter [201], which can be achieved using top-down or bottom-up fabrication techniques [202]. The size-dependent conductivity of Si NWs offers several advantages in FET applications. First, it enables precise control over the electrical characteristics of the device, allowing for tailored performance based on specific requirements [203]. By adjusting the diameter of the Si NW, one can modulate its electronic properties, including charge carrier mobility and density, to optimize FET performance for different functionalities [204].

Moreover, the high surface-to-volume ratio of Si NWs enhances their sensitivity to surface adsorbates and charge carriers, making them excellent candidates for sensing applications [115,129,205,206]. It allows Si NW FETs to detect changes in the surrounding environment, such as the presence of biomolecules, gases, or chemical species, with high sensitivity and selectivity. In this matter, Si NW FETs can be used to detect organic materials, as will be shown below and in Ch. 4 in detail.

1.4.2.1 Biosensors based on Si NW FETs

Biomolecular detection devices, also called biosensors, consist of two main components: the biological recognition element (receptor molecule), which detects the target molecule, and the detection component, which is the device that converts biological recognition into an electrical signal [207].

The reason for the high sensitivity of Si NW biosensors is their small diameter, which allows even single molecules to influence the conductivity in a Si NW FET. Such biosensors allow the detection of tiny amounts of molecules in real-time and obtain information on the conformation of molecules and the strength of biomolecular interactions. In particular, the

binding efficiency of the receptor and analyte can be tested [208]. A typical scheme of a Si NW FET biosensor with metal (Fe) S/D and gate electrodes is shown in Fig. 1.8. A metal/semiconductor contact is formed at the interface between the metal electrodes and a Si NW. In contrast, the gate electrode modulates the conductivity within a Si NW. Thus, Si NWs serve as the sensing component of the biosensor.

To detect any biomolecule, it is necessary to functionalize the sensing element of the system, i.e., the Si NW, with a system of receptor molecules able to recognize target molecules specifically. Receptor molecules are immobilized on the surface of the Si NW. When the receptor molecules bind to target molecules carrying negative charges, the specific binding will decrease its conductivity.

The main parameter of detection devices based on Si NW FET is the surface potential induced by the gate voltage, which modulates the conductivity of the Si NW channel. Such devices are very effective sensors for changes in the surface potential, which makes them more sensitive than devices with direct potentiometric measurements (e.g., a pH meter) [209].

In an ideal Si NW FET operating at room temperature, the maximum threshold shift is determined by the Nernst equation, which predicts a shift of 59.5 mV. However, imperfections of the metal/semiconductor interface and Si NW surface roughness increase this number [210,211]. Therefore, such a device will detect any binding of molecules that changes the surface charge or surface potential due to any chemical reaction or electrostatic interaction.

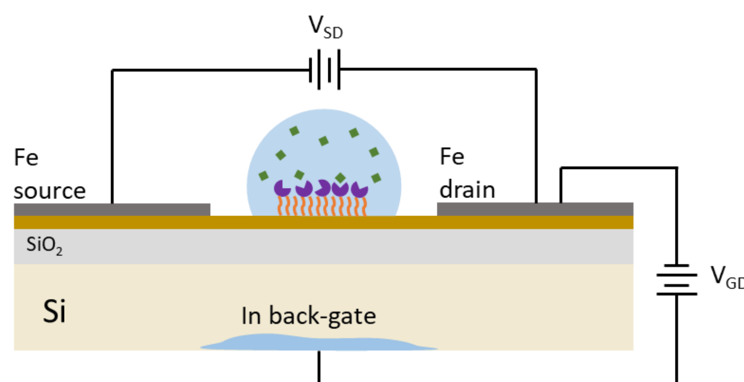

Figure 1.8. Schematic representation of a Silicon Nanowire Field-Effect Transistor (Si NW FET) with metal (Fe) source, drain, and indium back-gate electrodes. The diagram illustrates the essential components of the Si NW FET, including the silicon nanowire channel, the metal (Fe) electrodes serving as the source and drain contacts, and the back-gate electrode.

Moreover, detection devices based on Si NW FETs with Schottky contacts are being intensively investigated as an alternative to conventional transistors [212–214] due to many advantages

that Schottky field effect transistors offer, including simple low-temperature processing and the elimination of doping and subsequent activation steps [215]. These features are particularly desirable for Si NW-based devices, as they circumvent complex fabrication challenges such as precise control of the type and/or doping levels and the formation of reliable contacts at the metal/semiconductor interface. The main goal of functionalization is to reliably immobilize the recognizing molecules on the surface of the detecting element of the device, while retaining the ability to bind the receptor molecules to the target molecules specifically. One possible mechanism for immobilizing molecules on the surface of solid materials is physisorption, which is based on relatively weak interactions due to van der Waals, electrostatic or hydrophobic forces [216]. Stronger binding occurs by the chemisorption of molecules on the surface of solid materials [216].

Two approaches are used to functionalize the surface of Si NW:

- Electrostatic adsorption, in which positively or negatively charged molecules are adsorbed on an oppositely charged adsorbent, in this case, a Si NW surface [217].
- Covalent binding, which refers to chemisorption processes. Here, the receptor molecules are immobilized on the surface of the Si NW by covalent binding [217].

As Si NWs are coated with natural SiO_2, most Si NW surface functionalization methods are based on covering the oxide layer using a silanization process [218]. In the silanization process, organofunctional alkoxysilane and chlorosilane molecules self-organize on the surface; these molecules act as so-called "linkers" and are used for subsequent immobilization of the receptor molecules. The best-known molecules for the process described above are alkoxysilanes, which are suitable for covalent binding to O-terminated surfaces and typically represent metal and semiconductor oxides, including SiO_2.

The most popular alkoxysilanes are:

- (3-aminopropyl)triethoxysilane (APTES) [219–223];
- (3-Aminopropyl)trimethoxysilan (APTMS) [224,225].

These alkoxysilanes activate the Si NW surface with amino groups ($-NH_2$). They can be used for the covalent immobilization of antibody proteins due to the presence of an amino group in their chemical structure. In addition, these molecules are also used to immobilize peptide nucleic acid (PNA) and DNA to Si NW surfaces [219,226].

Well-studied molecules are used to evaluate the performances of biosensors based on Si NW FETs. For example, the system of biotin-streptavidin molecules, which has been used for many years in various applications, is most widely used to evaluate detection devices. This system is now considered a versatile independent technology with wide application in many branches of biotechnology [227]. Streptavidin is a homotetrameric protein (∼67 kDa) produced by *Streptomyces avidinii*, each subunit of which binds biotin (vitamin H), forming one of the most stable noncovalent complexes known in nature with dissociation constant ($K_d = 10^{-14}$ M) [228]. It measures of the strength of the interaction between two molecules, such as a ligand and its receptor and represents the concentration (M) at which the ligand-receptor is in equilibrium with the unbound ligand or substrate. Because of this, the streptavidin-biotin interaction is widely used in molecular biology and bionanotechnology [229]. Biotin, a vitamin H, which can be found in tiny amounts in all living cells, binds to streptavidin with high affinity. Because biotin is a relatively small molecule (∼244 Da), it can be used to functionalize many proteins without significantly altering their biological activity and function. Proteins can react with several biotin molecules, which, in turn, can bind one streptavidin molecule each. This greatly increases the sensitivity of many analytical detection schemes. The biotin-streptavidin interaction can be used to detect various targets with basic configurations explained in detail in [230–232]. Overall, of biomolecular detection devices based on Si NW FETs, the biotin-streptavidin system can be immobilized to the Si NW surface by the silanization process described above *via* covalent immobilization due to the presence of an amino group in the streptavidin structure.

Chapter 2

Experimental methods

The preparation and characterization of Fe/Si-based functional materials require various advanced technological equipment. This chapter provides a detailed account of the techniques employed to obtain high-quality samples of Fe/Si-based materials and the analytical tools and experimental facilities employed to investigate the resulting structures and devices' physical, structural, and transport properties. Specifically, a range of state-of-the-art instrumentation was utilized, including advanced deposition and lithography systems, scanning electron microscopy, transmission electron microscopy, X-ray diffraction, and setups electron transport characterization. The dip-pen nanolithography is also introduced as a tool for functionalization of silicon nanowires. These analytical tools were used to study various key properties of the Fe/Si-based nanostructures, such as crystallographic orientation, surface morphology, elemental composition, and electrical conductivity. The integration of these techniques provided a comprehensive understanding of the structure-property relationships in Fe/Si-based materials and enabled the development of high-performance devices based on these materials.

2.1 Fabrication techniques

Silicon nanowire (Si NW) Schottky barrier field-effect transistors (SB FETs) with Fe source/drain (S/D) electrodes were fabricated using a combination of electron beam lithography (EBL) with wet and dry chemical etching processes. The EBL was performed using a state-of-the-art system (VOYAGER, RAITH, Germany) capable of high-resolution patterning.

Self-assembled ensembles of $FeSi_2$ silicide crystallites were synthesized using molecular beam epitaxy (MBE) and reactive epitaxy (RE) techniques under ultrahigh vacuum (UHV) conditions. The integration of these advanced techniques enabled the development of Si NW SB FETs with Fe S/D electrodes and self-assembled ensembles of $FeSi_2$ silicide nanostructures for use in advanced electronic and optoelectronic devices.

2.1.1 Electron-beam lithography

Electron beam lithography (EBL) is a high-resolution patterning technique used to transfer a pattern onto the surface of a substrate. A thin layer of the organic film, resist, is first scanned on the surface using a tightly focused and precisely controlled electron beam. The exposure of the resist to the electron beam causes it to become either exposed or non-exposed, depending on the transferred pattern and then selectively removed in a solvent (developing). This allows for the patterning of very small features, often with submicrometer dimensions down to a few nanometers, either covering the selected surface areas by the resist or exposing otherwise resist-covered areas. The exposed areas can then be further processed for etching or thin-film deposition, while the covered parts are protected during these processes.

EBL offers the advantage of defining much smaller diffraction-limited features than photolithography due to the shorter wavelength of accelerated electrons compared to the wavelength of ultraviolet light used in photolithography. However, direct writing of patterns by scanning the electron beam is slow and results in low throughput. The technique finds widespread use in the fabrication of advanced electronic and optoelectronic devices, such as Si NW SB FETs with Fe S/D electrodes, as well as in the development of novel materials and structures for use in a variety of scientific and technological applications [233]. EBL utilizes a tightly focused and precisely controlled electron beam to transfer a pattern onto the surface of a substrate and therefore offers high resolution in the submicron range and high alignment accuracy, making it ideal for producing templates or directly forming a pattern on the wafer itself. This technique allows for the production of patterns with a resolution of < 10 nm [234], whereas conventional photolithography produces patterns of 100 nm.

Modern EBL systems (Fig. 2.1) are sophisticated and consist of fundamental parts such as an electron source, electromagnetic lenses for focusing the electron beam, beam deflectors for scanning the beam over the target, blanking apertures to deflect the beam away from the aperture hole, beam-limiting apertures to set the beam convergence angle, beam blankers to turn off or "blank" the beam, stigmator system to correct the beam shape and high-vacuum chamber in which the EBL patterning should be performed. A stage is also included, accommodating up to 300 mm of the plate, allowing movement in XYZ directions, rotation, and tilt.

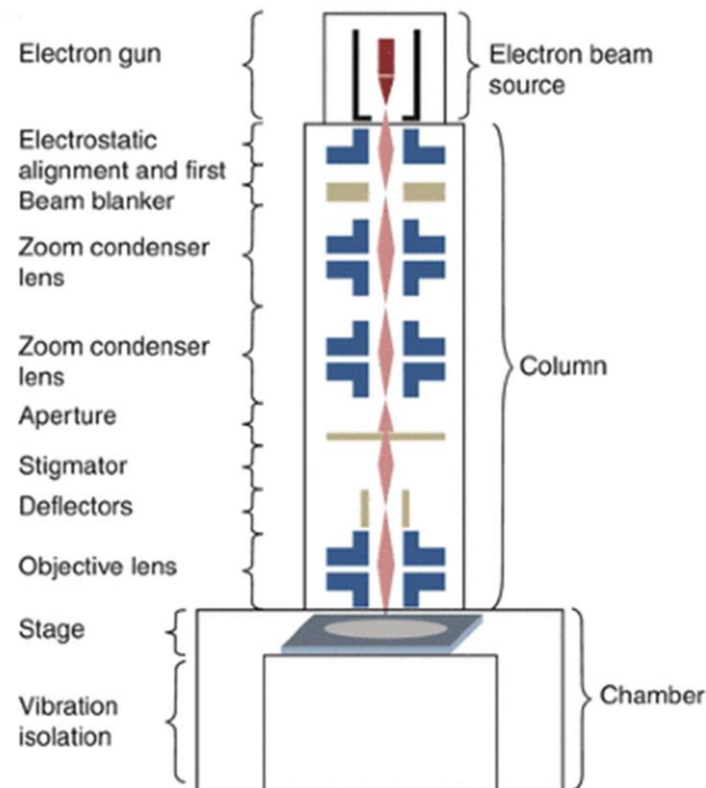

Figure 2.1. Schematic representation of a typical Electron Beam Lithography (EBL) system. The diagram highlights the key components and their interconnections within an EBL system: illustrates the electron beam source, beam shaping elements, beam deflection system, sample stage, and detectors [233].

The electron source is the most critical part of any EBL system and generates electrons that eventually reach the resist on the sample and expose it. Once the electron beam is generated, it is focused and guided through the column using lenses, apertures, and deflectors [235]. The fabrication procedure used for Si NW SB FETs with Fe S/D is described in detail in Ch. 4.1.

2.1.2 Thermal evaporation in ultrahigh vacuum

The proposed method involves the deposition of an elemental metal or alloy in ultrahigh vacuum (UHV) conditions, where the vapor of the material is condensed onto a substrate surface. The quality and strength of the resulting structures heavily rely on the purity of the substrate, which is usually cleaned before deposition. The substrate is heated during deposition to temperatures ranging between 100-300°C to minimize internal stresses in the film and improve its adhesion to the substrate. Figure 2.2 illustrates a schematic diagram of the thermal evaporation unit used in the present work designed for obtaining thin films and multilayer structures of semiconductor and magnetic materials in UHV. The ultimate vacuum in the chamber is 1×10^{-8} Pa (1×10^{-10} mbar). The design of the unit allows for 360° rotation of

the substrate to ensure precise sample positioning during in situ laser ellipsometry, rapid high-energy electron diffraction (RHEED), and mass spectrometry measurements, as well as to mechanically move the sample in the chamber, which is implemented via manipulator with five degrees of freedom (marked with arrows) with an attached substrate holder and a heating stage.

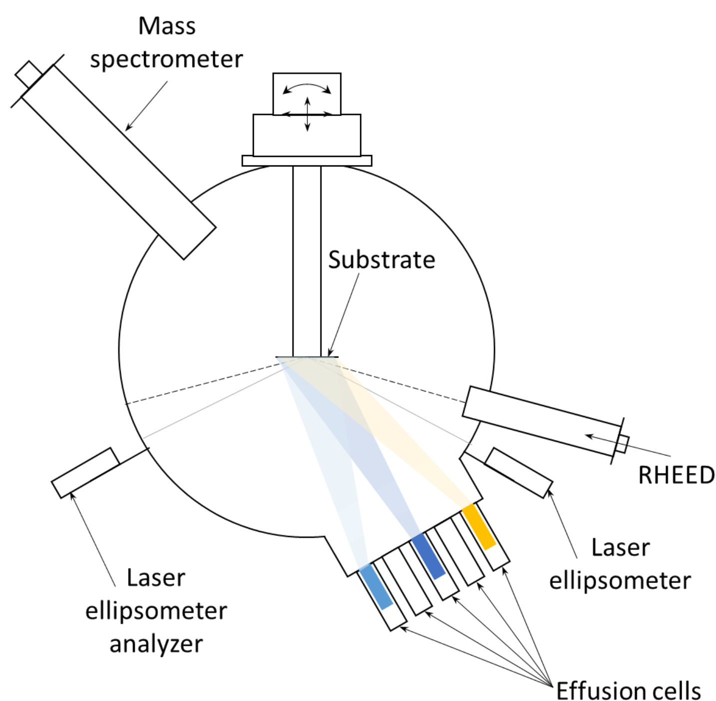

Figure 2.2. Schematic diagram illustrating the thermal evaporation unit and providing an overview of the key components and their arrangement within the thermal evaporation system unit.

The thermal evaporation process involves the heating of an effusion Knudsen cell containing the metal or alloy with an electric current until it melts and releases a vapor, which then travels to the substrate and deposits on its surface to form a thin film, also known as a vacuum condensate. During the vapor condensation process, liquid droplets crystallize, forming islands, and then further condensation of atoms leads to the growth of a continuous crystalline layer known as epitaxial growth [236]. Maintaining a vacuum pressure of approximately 10^{-6} Pa in the chamber ensures that most metal atoms have a straight trajectory toward the substrate without colliding with residual gas molecules. This is important for achieving high-quality and pure films, as collisions with gas molecules can lead to impurities and decrease the overall quality of the deposited film. Thus, thermal evaporation

in UHV allows to obtain epitaxially grown nanostructures of different sizes and shapes, which can be controlled by changing the speed or time of condensation.

There are several growth techniques to obtain epitaxially grown structures using thermal evaporation [236]:

- Solid-phase epitaxy (SPE) is a technique in which thin layers of various materials are thermally evaporated and deposited on a substrate at room temperature UHV conditions. After the deposition, the sample is heated to a high temperature (400-700°C) to form an epitaxial structure.
- Reactive epitaxy (RE) is a technique in which a thermally evaporated material is deposited immediately on a heated substrate surface. In this case, mixing the atoms of the deposited material and the substrate is faster due to very active atomic diffusion.
- Molecular beam epitaxy (MBE) is a technique in which atoms of different substances are thermally evaporated from a Knudsen cell and deposited simultaneously in a certain stoichiometric ratio onto a heated substrate surface.

The manipulation of film or nanostructure growth can be achieved through the use of *surfactants*, which are substances that can reduce surface energy and increase wetting properties [237], or *catalysts*, which accelerate a chemical reaction without being consumed in the process of crystal growth [166]. As described in Ch. 1.3.2, Au can act as a surfactant and a catalyst in the growth of $FeSi_2$ and other metal silicide crystallites. Thus, the fabrication procedure of self-assembled ensembles of $FeSi_2$ crystallites, considering Au-assisted growth using thermal evaporation in UHV conditions is described in Ch. 3.1.

2.2 Characterization techniques

The morphology of nanostructures plays a vital role in determining their physical and chemical properties. Various characterization techniques are employed to study the morphology of prepared Fe/Si-based structures. Scanning electron microscopy (SEM), transmission electron microscopy (TEM), and atomic force microscopy (AFM) are commonly used techniques for visualizing the surface morphology of nanostructures. These techniques provide information about nanostructure size, shape, and surface texture.

Structural characterization of prepared Fe/Si-based structures is equally important, as it determines the material's crystallographic orientation, defects, and interfacial quality. In the present work, X-ray diffraction (XRD) and electron backscatter diffraction (EBSD) were used for structural analysis of prepared Fe/Si-based structures.

Combining these characterization techniques provides a comprehensive understanding of the morphology and structural properties of fabricated nanostructures, which is essential for designing and optimizing their performance in various applications.

2.2.1 Characterization of morphology

Scanning Electron Microscopy (SEM)

The scanning electron microscope (SEM) is a widely used tool for investigating the surface topography of a sample. The SEM system comprises an electron column and a control console (Fig. 2.3 (a)). The vacuum in the electron column is about 10^{-4} Pa and it consists of several main components:

- an *electron gun* that generates and accelerates electrons to energies in the range of 0.1-30 keV;
- the SEM system can produce an *electron beam* with a spot size of less than 10 nm that contains enough probe current to produce an acceptable image. The beam of electrons exiting the end lens into the sample chamber interacts with the sample to a depth of about 1 µm and generates the signals used to form the image [238];
- *electron lenses* that influence the paths of electrons traveling down an evacuated tube;
- *control console,* which consists of a cathode ray tube viewing screen and the knobs and computer keyboard that controls the electron beam [239];

- *a deflection system* that deflects the electron beam as it moves along one line of the sample's surface, then along another line below the first line, and so on, until a rectangular "raster" is formed on the sample. Thus, the scanned image is formed point by point. Two pairs of electromagnetic deflection coils (scanning coils) are used to sweep the beam over the sample. One pair of coils deflects the beam away from the microscope's optical axis, and the second pair bends the beam back onto the axis at the scanning pivot point.

The magnification of the image is the ratio of the raster length on the viewing screen to the corresponding raster length on the sample. When an electron beam is exposed to a sample, many signals are generated, and any can be used for imaging. The most used signals for SEM imaging are *secondary electrons* (SE) and *backscattered electrons* (BSE). The contrast in the image occurs when the signal collected from the beam/sample interaction changes from one location to another. Both SE and BSE signals are collected when a positive voltage is applied to the collector screen in front of the detector.

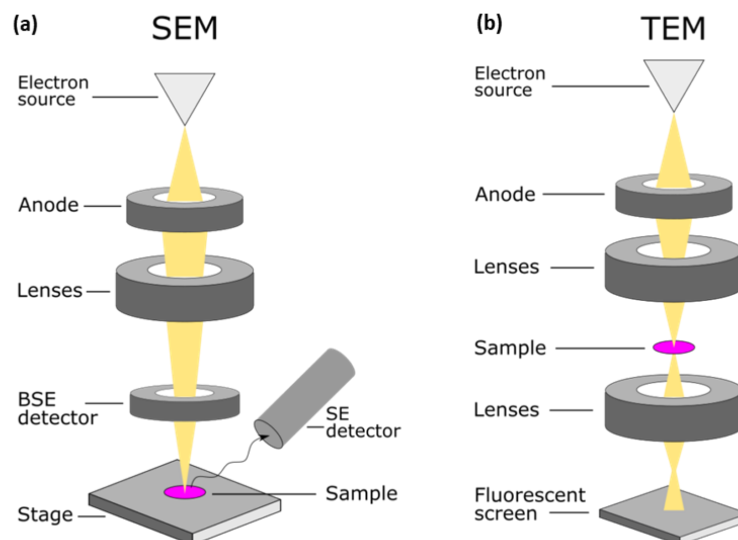

Figure 2.3. Schematic diagram illustrating the (a) Scanning Electron Microscope (SEM) and (b) Transmission Electron Microscope (TEM) columns. The diagram highlights the main components and their arrangement within the SEM and TEM systems: the electron source, lens system, specimen stage, detectors, and imaging system [240].

The quality of Fe/Si-based nanostructures prepared by means of EBL was investigated using TM3000 (Hitachi, Japan) tabletop SEM in low-vacuum mode. The morphology and quality of Fe/Si-based nanostructures prepared by MBE and RE were studied using S5500 SEM system. For the investigation, an electrically conductive coating of Au or Ag (~1 nm) was applied on the surface of the fabricated nanostructures beforehand (Chs. 3, 4).

Transmission Electron Microscopy (TEM)

Transmission electron microscopy (TEM) is one of the main direct methods of studying the structure of materials down to the atomic level [241–247]. TEM methods are based on the interaction of an electron beam with a sample as it passes through it. The result of this interaction is a range of radiation, the analysis of which allows make conclusions about a sample. Types of signals from electron beam/sample interaction are described in [247]. For example, Auger electrons are used to study the surface topography and elemental analysis (Auger spectroscopy); back-scattered electrons are used to analyze the crystal structure (scanning electron microscopy, electron backscatter diffraction). TEM image construction theory, operating principles, system construction, methods of investigation, and analysis of obtained results are described in detail in [241–247]. Generally, a TEM system consists of three main parts: the microscope column, the vacuum system, and the high-voltage transformer and power supply system. The microscope column is the most important part of a TEM system and consists of the following parts (Fig. 2.3 (b)):

- an *electron gun* in which electrons are emitted;
- a *lighting lens system* that controls the brightness and movement of the electron beam and the size of the observation area;
- a *working chamber* in which the sample is positioned and can be moved vertically/horizontally, rotated, or tilted;
- an *imaging lens system* in which the image or electron diffraction;
- an *observation camera* in which a magnified image or electron diffractogram is observed with a CCD camera.

The bright-field mode of TEM was used to confirm the quality of the prepared Fe thin film on the SOI substrate. This mode determines the quality of the resulting iron film on the substrate. The contrast on bright-field TEM images strongly depends on the atomic mass and the elastic scattering of electrons (especially when viewed in a transmitted beam). Since the atomic mass of Fe is greater than the average atomic mass of Si and SiO_2, iron films appear more contrasting (darker) in electron microscopic images compared to the substrate.

Sample preparation is crucial for high-quality TEM images. In this study, a cross-section of a Fe thin film on an SOI substrate was obtained using a focused ion beam (FIB), commonly used in the semiconductor industry and material science. FIB uses liquid gallium to ionize and focus

an ion beam on the sample. This process causes the emission of secondary electrons detected for raster point information. FIB devices can also include a facility for local material deposition, such as Pt, W, C, SiO_2, and Au, which is useful for creating masking layers and conductive contacts in micro- and nano-electronics.

A cross-section sample was prepared using FIB FB2100 (Hitachi, Japan). The sample was coated with 200-300 nm thick Ge using a thermal vacuum deposition process to protect it from ion beam degradation. Ge is atomized easily, and its film structure is close to amorphous. The preparation was carried out using an HT-7700 TEM equipped with a scanning attachment and a Bruker XFlash 6T/60 energy dispersive spectrometer (Ch. 4.2).

Atomic Force Microscopy (AFM)

Atomic force microscopy (AFM) is a type of scanning probe microscopy (SPM) that relies on the interaction between the atoms of the probe and the sample. At small distances, there is an attractive force between atoms and molecules, which is inherently quantum. This attraction arises from the correlated vibrations of electrons in both atoms. Specifically, when the electrons are shifted (polarized) in the same manner, the energy of the atom pair is slightly lower compared to a pair of non-polarized atoms. And this energy decreases with the distance between the atoms as $1/r^6$. The total interaction energy of atoms is approximated by the Lennard-Jones formula:

$$U(r) = E_{min}((r_{min}/r)^{12} - (r_{min}/r)^6), \tag{2.1}$$

where the first term is responsible for repulsion, it starts to «work» at small distances, while the second can be neglected. In this case, r is the distance between atoms, corresponding to the E_{min} minimum energy of the system, i.e. the most favorable, and r_{min} – is the distance at which the interaction energy turns to zero.

The force of a probe-sample interaction can be obtained by summing all such elementary interactions for each atom of the probe. For a probe characterized by some radius of curvature R_C ($R_C \gg z$, where z is distance from the probe to the surface, Fig. 2.4 (b)) and of an absolutely flat sample, in the continuum mechanics approximation, the force of attraction will be proportional to R_C/z^2 (Hamaker formula [248]), repulsion – about $1/z^8$.

An AFM probe, usually made of Si or Si_3N_4, is placed on the free end of an elastic cantilever and is 1-2 µm long. The smaller the radius of curvature and the angle of convergence of the

tip the smaller is its effect on the imaging of the object under study. The force acting on the probe from the surface causes the cantilever to bend (Fig. 2.5 (c)).

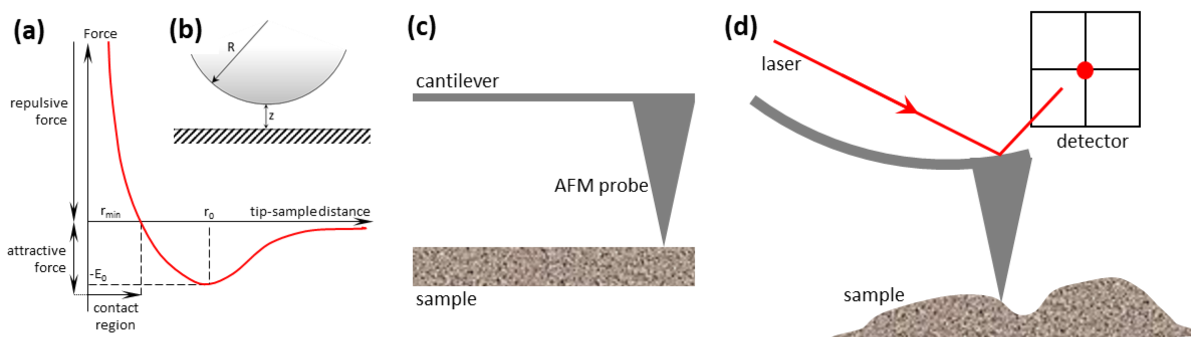

Figure 2.4. (a) Lennard-Jones potential illustrating the interaction between two atoms. The diagram demonstrates the attractive and repulsive forces involved, providing insights into the energy landscape governing the atomic interaction; (b) Schematic representation of the probe-sample interaction in an Atomic Force Microscope (AFM). The diagram illustrates the probe tip interacting with the sample surface, capturing the forces at play, such as van der Waals, electrostatic, and chemical forces; (c) the scheme of probe-cantilever design used in AFM; (d) Recording the AFM force interaction, including the laser and signal detector. The diagram outlines the components involved in detecting and measuring the deflection of the cantilever, such as the laser source, detector, and feedback mechanism, which enables accurate force mapping.

The appearance of elevations or depressions under the tip leads to a change in the force acting on the probe and, therefore, to a change in the cantilever bending value. This deflection is registered by means of the optical system, the scheme of which is shown in Fig. 2.4 (d). As the tip approaches the specimen, the forces act between them. This will be either an attraction or repulsion force, depending on how small the distance between the tip and the sample is. Hence the scanning can be performed in different modes:

- *Contact mode*, when a cantilever bend reflects repulsive force and is used directly in a feedback system or combination to display surface topography. This mode is widely used to provide detailed surface topographic information by utilizing the bending of a cantilever in response to repulsive forces.
- *Semi-contact mode*, when a cantilever can oscillate to measure the interaction force between the probe and the surface during the scanning process, in contrast to the contact scanning mode. Semi-contact mode allows visualization of surface details with high resolution.

- *Non-contact mode*, which uses changes in the amplitude *A* of cantilever oscillations caused by the interaction of the probe with the sample. The absence of repulsive forces in non-contact mode allows to analyze "soft samples".

The surface morphology of the fabricated samples was characterized using a NanoInk DPN 5000 AFM system. To prepare the samples for AFM imaging, the surface of the fabricated Si NW/Fe samples on the SOI substrate and self-assembled ensembles of $FeSi_2$ crystallites were initially cleaned using ethanol or isopropanol, followed by drying with compressed nitrogen. High-resolution silicon cantilevers of the NSG30 and VIT Pt/Ir series (TipsNano) were used, possessing a resonance frequency of 210-490 kHz, a power constant of 12-110 N/m, and a probe tip radius of 2 nm. AFM measurements were conducted in the semi-contact scanning mode, commonly called AC mode, which enables non-destructive imaging of the surface morphology with a high spatial resolution (Ch. 3.2, 4.2).

Dip-Pen Nanolithography with AFM system

Dip-Pen nanolithography (DPN) is a versatile and powerful technique for creating precise nano-scale patterns on various surfaces. The technique employs an AFM as a writing device to transfer molecules or nanoparticles from a coated AFM probe tip to a surface, creating patterns with sub-100 nm resolution (Fig. 2.5). The NanoInk DPN 5000 AFM system is a commonly used instrument for performing DPN, as it offers precise control over the movement of the AFM probe and the deposition of the "ink" onto the substrate surface.

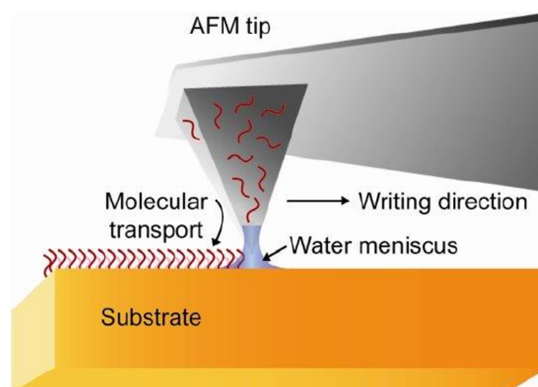

Figure 2.5. Schematic diagram illustrating the Dip Pen Nanolithography (DPN) process. The diagram provides an overview of the key components and steps involved in DPN [249].

Thus, the AFM probe in DPN is coated with a special "ink" containing the desired molecules or nanoparticles. The coated probe is then brought into contact with the surface of the substrate, and the ink is transferred to the surface as the probe moves across it. By varying the probe

speed and/or the delay time, it is possible to create lines of different widths and/or dots of different radii. Lines and dots can be combined to create complex patterns, creating highly precise and reproducible nano-scale features. The diffusion rate of molecules across the surface depends on the roughness of the substrate, present temperature (PT) and present humidity (PH) at the time of the experiment [111,250]. Regardless of the selected "ink" molecules, their diffusion onto the substrate depends on the environmental conditions [251], as well as on the probe radius and substrate roughness [250]. The present work used DPN to ensure accurate coverage of a Si NW surface with functionalizing molecules. This way, molecules were deposited onto Si NW surface using NSG30 high-resolution silicon cantilever at PT = 24.2^{o}C and PH = 52.1% (Ch. 4.4).

2.2.2 Structural characterization

Electron backscatter diffraction (EBSD)

Electron backscatter diffraction (EBSD) is a powerful technique used in materials science to characterize the crystallographic properties of a material at the micro- and nanoscale. By analyzing the diffraction pattern, EBSD can provide information about the examined material's crystal structure, orientation, and grain boundaries [252]. This non-destructive method utilizes a focused electron beam to interact with a tilted crystalline sample, causing backscattered electrons to diffract, producing a unique diffraction pattern (Fig. 2.6).

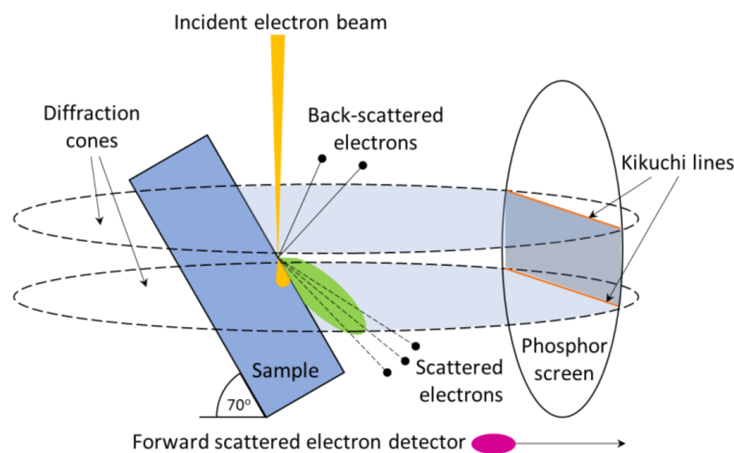

Figure 2.6. Visualization of an EBSD measurement scheme, including an incident electron source, directed onto the 70°-tilted sample, interacting with it, and causing back-scattered electrons to diffract, producing a unique diffraction Kikuchi pattern.

Backscattered electrons are generated when the primary electron beam interacts with the sample, forming a divergent source of electrons close to the sample's surface. Some of these electrons are incident on atomic lattice planes at angles that satisfy the Bragg equation [253]:

$$n_d \lambda = 2D sin\theta, \tag{2.8}$$

where n_d is diffraction order, λ is the de Broglie wavelength of the electrons, D is the spacing of the diffracting plane, and θ the angle of incidence of the electrons on the diffracting plane [252]. These electrons are diffracted to form a set of paired large-angle cones that correspond to each diffracting plane, such as the green and blue cones in Fig. 2.7 (a) corresponding to a single (110) lattice plane (red disc).

The diffraction pattern produced on the EBSD detector (usually using a phosphor screen to convert the electrons to light) contains characteristic Kikuchi bands [254], formed where the regions of enhanced electron intensity intersect the screen. The pattern imaged by the EBSD

detector is a gnomonic projection of the diffracted cone, making the band edges appear hyperbolic. The width w of the Kikuchi bands close to the pattern center is given by:

$$w \approx 2l\theta \approx \frac{n_d L\lambda}{d}, \tag{2.9}$$

where L is the camera length.

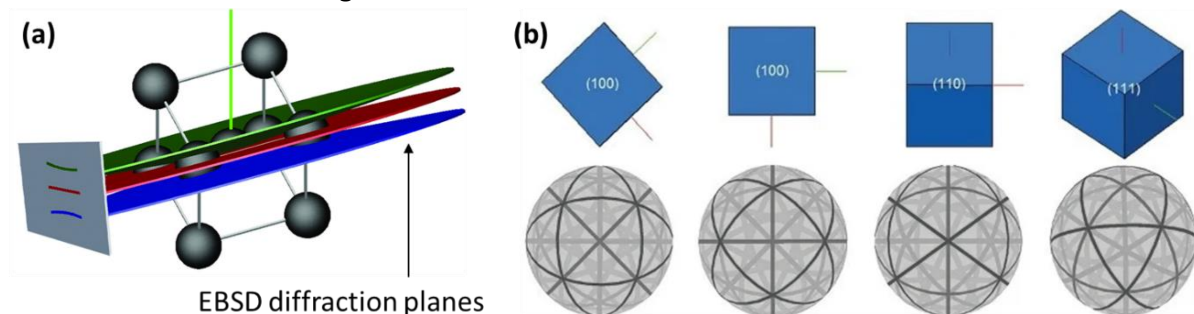

Figure 2.7. (a) Schematic illustration of a Kikuchi band formation in an EBSD pattern [252]; (b) the spherical diffraction patterns generated by different orientations of a cubic structure.

The positions of the Kikuchi bands can be used to analyze orientation relationships (OR) between crystal grains at the point where the beam interacts with the sample. The relationship between the crystal lattice orientation and the resulting diffraction patterns (Kikuchi patterns) are formed when a crystal scatters an electron beam and produces a diffraction pattern on the screen of the EBSD detector, as it is shown for spherical diffraction patterns generated by different orientations of a cubic structure (Fig. 2.7 (b)). The Kikuchi pattern is divided into various zones corresponding to different crystallographic planes of the crystal. By analyzing the positions and shapes of these zones, it is possible to determine the ORs between different grown nanocrystals and a substrate. The ORs can be used to understand the mechanisms of nanocrystal growth. The center of Kikuchi bands corresponds to the cross of the diffracting planes with the phosphor screen. Therefore, the diffracting crystal plane's Miller indices index each Kikuchi band. EBSD diffraction patterns can be automatically indexed, and the crystal orientation can be determined [255,256].

To provide the crystallographic data and in-plane epitaxial relation between a Si substrate and self-assembled ensembles of $FeSi_2$ crystallites, the Zeiss LEO 1530 SEM with Oxford Instruments Nordlys EBSD detector was used. The system allows tilting the sample to 70°, using a pre-tilted holder of the SEM. To analyze the ORs between prepared self-assembled ensembles of $FeSi_2$ crystallites and Si substrates PTCLab software package [257] was used. Obtained Kikuchi patterns were indexed by matching the observed pattern with a simulated

pattern generated for a known crystallographic orientation. This process involves identifying the Kikuchi bands in the pattern and determining their position and orientation (Ch. 3.3).

X-ray Electron Diffraction (XRD)

X-ray diffraction is a powerful analytical technique used to investigate the structure of materials. It relies on the interaction between X-rays and the crystal lattice of a sample, resulting in the scattering and diffraction of the X-rays. The X-ray diffractometer's physical principle is based on each material's unique lattice structure. Any substance in crystalline form is characterized by a certain set of interplanar distances d. When a monochromatic X-ray beam with wavelength λ hits the system of crystal planes at an angle ϑ, then constructive interference occurs according to the Bragg equation [253], resulting in a series of diffraction peaks in the X-ray diffraction pattern. In contrast to EBSD in SEM, XRD is an integral method because the information comes from a large area (several mm^2). The most common type of diffraction investigation is a qualitative and quantitative analysis of the phase composition of a sample. XRD analysis is based on the following principles [258,259]:

- the powder diffraction pattern is an individual characteristic of a crystalline substance;
- each crystalline phase always gives the same diffraction spectrum characterized by a set of interplanar d_{hkl} and the corresponding I_{hkl} line intensities only of the given crystalline phase;
- XRD spectrum from a mixture of individual phases is a superposition of their diffraction spectra;
- XRD spectrum of a mixture may be used to quantitatively estimate the ratio of the crystalline phases present in the sample, i.e. the ratio of intensities of the crystalline phases present in a particular sample is proportional to the content of these phases in the sample.

Experimentally, XRD spectra can be taken using different X-ray cameras with the registration of diffraction patterns using X-ray detectors. Modern diffractometers allow obtaining a diffraction spectrum in the range of 2θ angles from 6-8° to 140-160° with the step of Δ(2θ) = 0.1-0.05°. As a result, a diffractogram (XRD spectrum) is obtained from a diffractometer.

An X-ray diffractometer with the Bragg-Brentano geometry consists of a light source, a beam focusing system, and a system for adjusting the position and orientation of the sample, detection, and analysis systems. A schematic diagram is shown in Fig. 2.8 (a). The sample

(specimen) is placed on the stage of the goniometer (which may be rotated around its axis), and the detector is moved around the circle to focus on the sample [259].

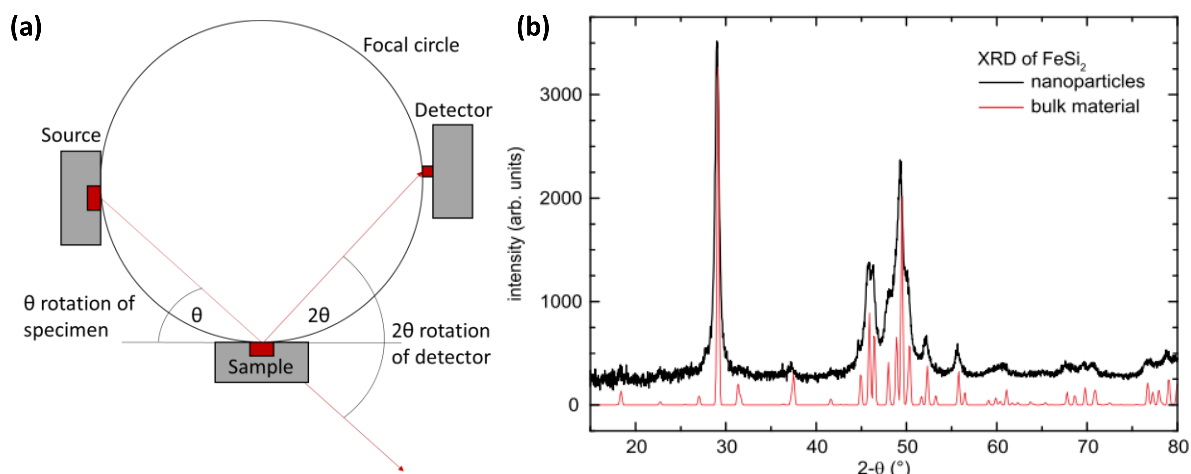

Figure 2.8. Schematic diagram of a sample mounted on a goniometer which can be rotated about one or more axis, and a detector that travels along the focusing circle in the Bragg-Brentano geometry [259], (b) XRD diffractogram of the β-$FeSi_2$ bulk material and nanoparticles, reproduced from [55].

X-rays are produced by interacting of a high-energy electron beam with a metal (usually Cu) target in a vacuum tube. Such X-ray tubes emit a wide spectrum of wavelengths above some minimum wavelength. Against a background of continuous white light, several narrow and intense peaks called *characteristic peaks* are observed. A characteristic X-ray photon is emitted when an electron crosses an empty inner shell. The brightest lines belong to the K series, consisting of the Kα1, Kα2, Kβ1, Kβ2, etc. lines. Fig. 2.8 (b) provides an example of β-$FeSi_2$ bulk material (red) and nanoparticles (black) [55].

Monochromatic radiation is generated by exciting K-radiation from a pure metal target and first filtering the beam by interposing a foil that strongly absorbs the Kβ component without appreciable reduction of the intensity of the Kα component. This can be accomplished by choosing a filter that has an absorption edge that falls exactly between the Kα and Kβ wavelengths. A good example is the use of a nickel filter ($E_{Ni\ K}$ = 0.1488 nm) with a copper target ($E_{Cu\ K}$ = 0.138 nm), transmitting the Cu Kα beam (0.154 nm) but not the Kβ (Fig. 2.9 (a)). More effective selection of a monochromatic beam can be achieved by interposing a single crystal monochromator oriented to diffract at the characteristic Kα peak. This monochromatic diffracted beam can then be used either as the source of radiation for the actual sample or to filter the diffracted signal (Fig. 2.9 (b)). The monochromator crystal can also be bent into an arc of a circle so that radiation from a line source striking any point on the arc of the crystal

will satisfy the Bragg condition, focusing a diffracted beam from the monochromator to a line at the specimen position (Fig. 2.9 (c)). The same effect can be achieved at the detector when the monochromator is placed in the beam's path diffracted from the sample.

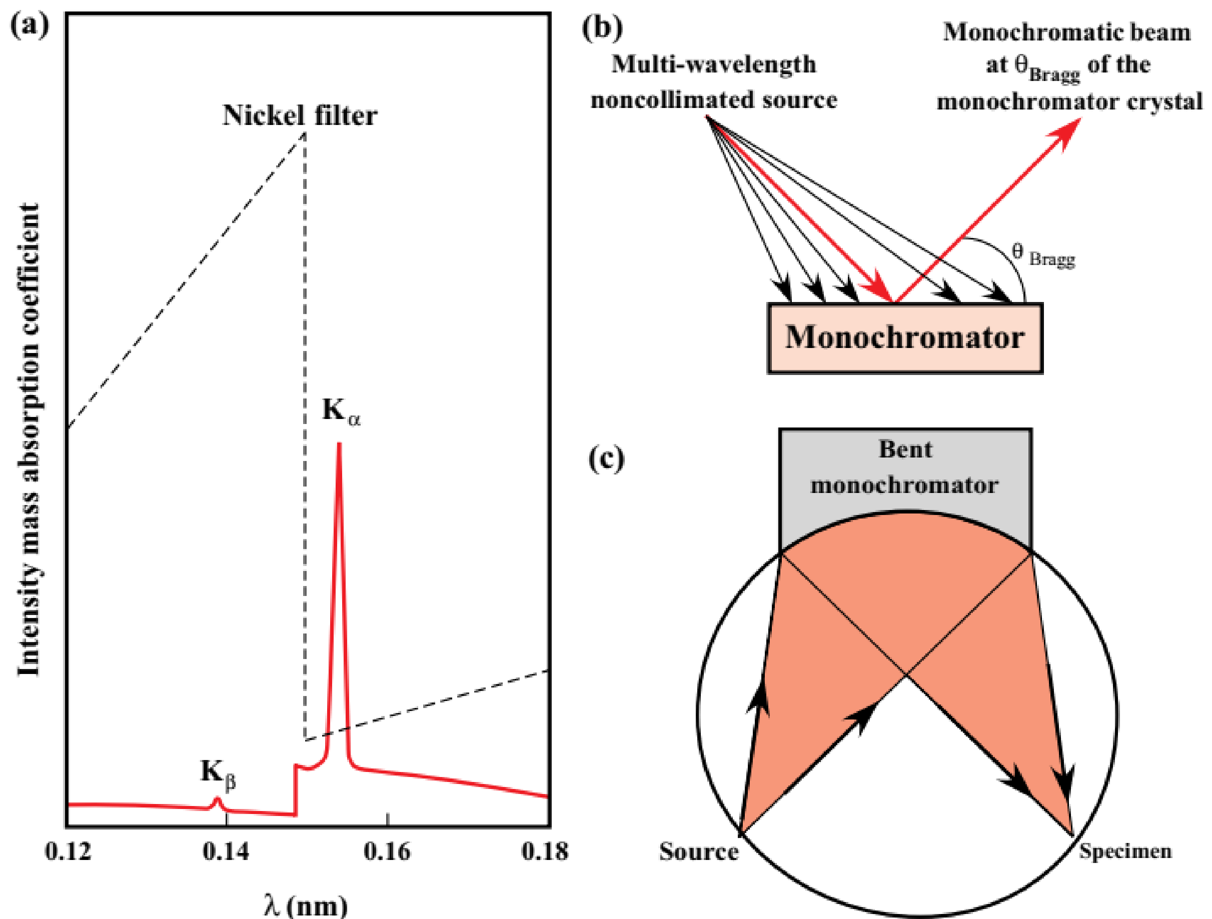

Figure 2.9. (a) Cu-K radiation filtered by a nickel foil to remove the Kβ line; (b) a monochromator crystal allows a specific wavelength to be selected from an X-ray source; (c) a fully focusing spectrometer maximizes the diffracted intensity collected at the detector [259].

An XRD spectrum is usually recorded by rotating the X-ray detector around the sample. A goniometer allows the sample to be rotated concerning one or more axes. A typical diffraction pattern of a polycrystalline sample consists of several peaks on a smooth background line. Each peak is an *n*-th order reflection from a series of planes (*hkl*) with interplanar distance d_{hkl}. Its position on the radiograph (angle θ) when recording the radiograph with wavelength λ is determined by the Bragg law [253].

Standard measurements are θ-2θ diffraction, also called as locked or symmetrical scan, since detector follows the doubled incoming angle. In this case, diffraction occurs only from crystal planes parallel to the sample surface and sometimes the substrate peaks can dominate in

intensity. This problem can be solved by recording a scan with a small offset (Δ) on θ, which is called unlocked scan in this case, since it is performed as an Ω-2θ scan, where Ω = (θ - Δ). The offset affects the diffraction conditions and reduces the peak intensity. Since the substrate is usually of better crystalline quality than a sample on it, its intensity will be reduced more effectively than the sample peaks.

XRD pole figures

In the case of a textured film exhibiting a distinct preferential alignment of grains concerning the substrate, it is reasonable that specific sets of lattice planes will never align parallel to the film's surface. Consequently, these lattice planes don't meet the diffraction criteria, resulting in their absence from the symmetrical XRD pattern. This absence of certain diffraction peaks poses a significant challenge in accurately identifying the phase present within the film. In such cases, using pole figure measurements becomes imperative to determine the observed phase and its corresponding texture uniquely.

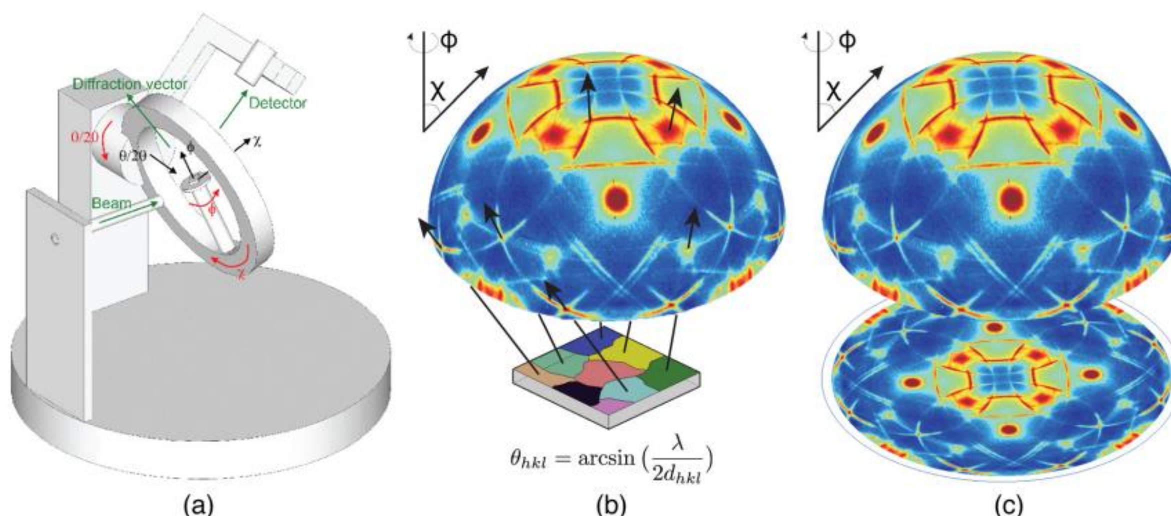

Figure 2.10. (a) Illustration of a four-circle diffractometer used in the Schulz method. The different rotation axes (χ, φ and θ) are depicted along with the corresponding rotation directions. (b) Visualization of a pole figure: the intensity distribution on the imaginary hemisphere is created by marking the intersection of the normal of the diffracting planes (those that fulfill the Bragg condition for the chosen d-spacing) with the hemisphere for each grain in the film. (c) Projection of the intensity distribution on the hemisphere onto a planar surface result in a pole figure for a specific family {hkl} of lattice planes. The data reflects the (112) pole figure of a NiSi film on Si(001). Reproduced from [260].

The Schulz method [261], introduced in 1949 and widely adopted for texture investigations in metallurgy, is a commonly used geometry for measuring pole figures through XRD. In this

method, the sample is positioned on a four-circle diffractometer, enabling precise tilting (χ angle) and rotation (φ angle) of the sample, as it is shown in Fig. 2.10 (a) [260]. Additionally, the inclination of the sample concerning the incoming X-ray beam can be chosen (θ angle). To fulfil the Bragg diffraction condition, the detector is then positioned at an angle of 2θ relative to the incoming X-ray beam. By tilting the sample around χ and rotating it around φ while measuring this diffracted intensity, it becomes possible to obtain diffraction data for the chosen family of lattice planes in all possible grain orientations, not limited to the planes parallel to the sample surface. One can imagine the sample placed at the center of a hemisphere to visualize the results. For each grain, mark the intersection between the normal to the selected lattice plane family {*hkl*} (referred to as the pole of the plane family) and the hemisphere (Fig. 10 (b)). The resulting (*hkl*) pole figure is obtained by projecting the density of these marks onto a planar surface (Fig. 2(c)). The poles' spherical coordinates (χ, φ) are converted into polar coordinates, with χ representing the radial distance and serving as the polar angle [260].

XRD unlocked scans and pole figures of self-assembled ensembles of $FeSi_2$ nanostructures were measured using Panalytical X'Pert MPD PW3040 and an Empyrean MRD device using Cu-Kα radiation (λ = 1.5406 Å). The results were analyzed using Profex [262] and PTCLab [257] software (Ch. 3.3).

2.2.3 Electron transport investigation

Silicon nanowire field-effect transistor

Silicon nanowire field-effect transistor (Si NW FET) with Fe source and drain (S/D) electrodes have been characterized in terms of electronic transport and measurement configuration for biomolecular sensing applications. Figure 2.11 schematically illustrates a Si NW FET cross-section, which has three terminals: source, drain and back-gate electrodes.

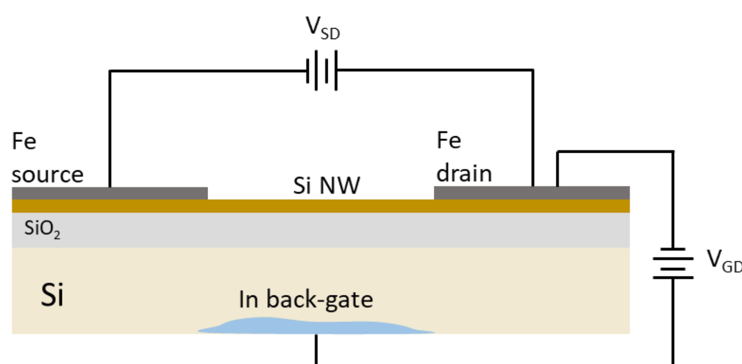

Figure 2.11. Schematic cross-section of a silicon nanowire field-effect transistor (Si NW FET). The diagram provides a visual representation of the key components and structure of the Si NW FET, containing the silicon nanowire as a part of the silicon-on-insulator (SOI) substrate, In back-gate electrode, Fe source and drain contacts.

The main characteristics of Si NW FETs can be determined from the transfer characteristics, drain current (I_{DS}) as a function of gate-source voltage at a constant source-drain voltage, and output characteristics, I_{DS} as a function of the source-drain voltage at a constant gate voltage, at room temperature. The measurements of transport characteristics of the fabricated Si NW FETs were carried out using Lakeshore EMPX-HF 2 probe station (Lake Shore Cryotronics) at room temperatures (see Ch. 4.3). The Lakeshore EMPX-HF 2 unit is comprised of several key components designed for precise and versatile measurements (Fig. 2.12 (a)). At its core, a helium cryostat is positioned between an electromagnet's poles. Inside the cryostat, four three-axis arm manipulators are mounted, allowing for precise positioning and exchangeable probes of various diameters (ranging from 6 to 50 µm) (Fig. 2.12 (b, c)). This feature enables researchers to adapt the system to different measurement requirements. This setup is placed on an anti-vibration table to mitigate the impact of vertical and horizontal vibrations during measurements, especially when the vacuum station evacuates air from the cryostat. The anti-vibration table utilizes air pads to dampen vibrations effectively. This ensures the stability and accuracy of measurements, even in challenging experimental

conditions. The sample is placed on a cooled copper holder within the cryostat and maintained under a vacuum to facilitate optimal measurement conditions. Moreover, the station supports standard electrical measurement modes and provides the flexibility to mount probes for microwave and electro-optical measurements, expanding its capabilities for various experimental techniques.

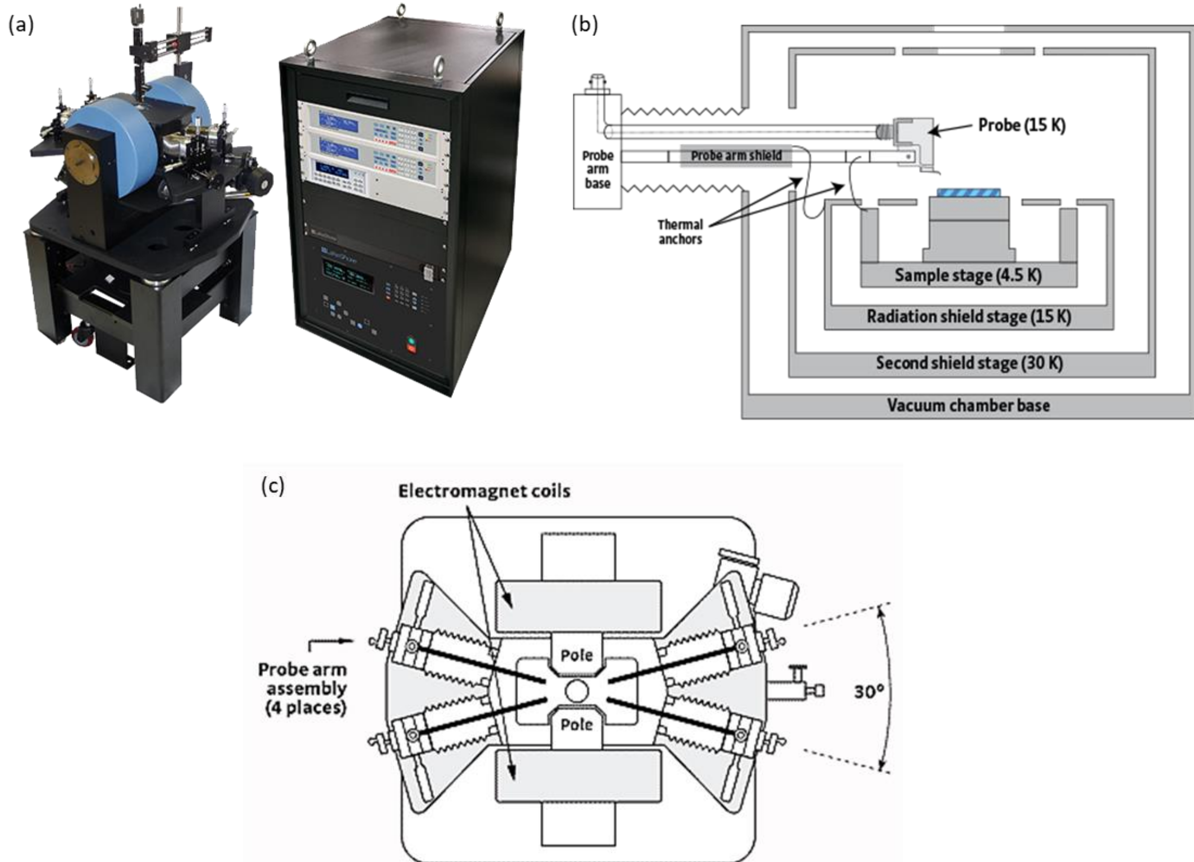

Figure 2.12. (a) General view of Lakeshore EMPX-HF 2 probe station; schemes of (b) measuring chamber and (c) micro-manipulated probe station configured with four three-axis arm manipulators, electromagnetic coils and magnetic poles [263].

Four-point probes resistivity measurements

Four-point probe stations are widespread in the semiconductor industry for measuring surface resistivity [264]. Four-point probe measurements are inherently contact measurements, so the probe points are required to make an ohmic electrical contact with the sample. The temperature dependence of resistivity for self-assembled ensembles of $FeSi_2$ crystallites are measured using the four-point probe method, two probes were used to inject the electric current I into the sample (20 µA -7 mA in this work), and the other two to measure the potential difference ΔV across the sample using a high impedance voltmeter, as it is shown

in Fig. 2.13 All four probe points were placed along one line on the flat surface of the sample (Fig. 2.13) and arranged symmetrically. The sample thickness (d) and the minimum distance from the probe points to the edge of the sample were much greater than the distance between the probe points (l) (half-space approximation). Due to this, the resistivity was determined from a simple expression [265–267]:

$$\rho = \frac{\pi \Delta V}{2I \cdot \left[\frac{1}{S-l} - \frac{1}{S+1}\right]}, \tag{2.6}$$

here I is the current flowing through the sample; S is the distance between the outermost probe points (current contacts); l is the distance between the potential contacts. The practical criterion for the applicability of this approximation is $S/d < 5$. If the electrodes are located at the same distance from each other, i.e. $S = 3l$, we get

$$\rho = \frac{2\pi l \Delta V}{I}. \tag{2.7}$$

In the other limiting case, when $d << l$ the expression (2.6) takes as follows:

$$\rho = \frac{\pi \Delta V}{2I \cdot \ln\left[\frac{S+l}{S-L}\right]}. \tag{2.8}$$

If $S = 3l$, we obtain

$$\rho = \frac{2\pi l \Delta V}{I \cdot \ln 2}. \tag{2.9}$$

This formula is applicable when $S/d > 5$.

For the apparent sample thicknesses the expression for ρ has the form of

$$\rho = \frac{2\pi l \Delta V}{2I \cdot \left\{\frac{1}{S-1} - \frac{1}{S+1} + 2\sum_{n=1}^{\infty}\left[\frac{1}{\sqrt{(S-l)^2 + (4nd)^2}} - \frac{1}{\sqrt{(S+1)^2 + (4nd)^2}}\right]\right.} \tag{2.10}$$

The four-probe method is a convenient way to determine conductivity quickly and accurately and does not require specimens to be prepared in a special geometric shape. However, the sample surface area must be large enough so that any distance (L) from the probes to the edge of the sample satisfies the condition $L_{min} > 10S$. Otherwise, the measured potential difference ΔV depends on the type of boundary and shape of the sample [268].

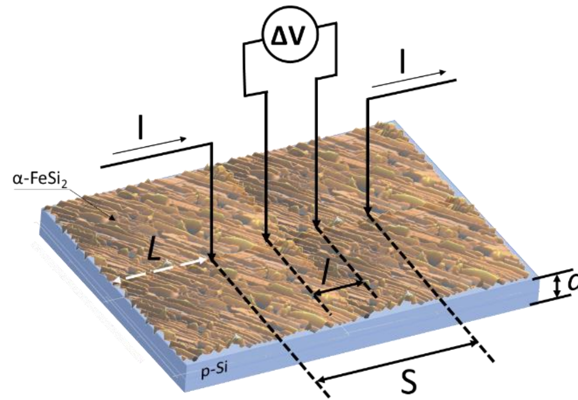

Figure 2.13. Schematic diagram illustrating the four-point probe measurement setup for in-plane electrical conductivity of α-$FeSi_2$ crystallites on p-Si substrate. The diagram showcases the arrangement of the four-point probes on the sample surface, the flow direction of electric current (I) through two outer probes, the potential difference ΔV measured from two inner probes, the sample thickness (d), the distance between the probe points (l), the distance from the probes to the edge of the sample (L).

Errors of resistivity measurement with the four-point probes method are related to inaccuracy in determining the distance between potential contacts and in determining the thickness of the sample, if the conditions of applicability of this method are fulfilled. Since the distance between the contacts is limited by the method's applicability conditions, it must be much smaller than the linear dimensions of the sample. For a typical sample with a flat surface area of 10×10 mm^2, the contact spacing should not be more than 1 mm. Under experimental conditions, the contact spacing error will be $\Delta l/l \geq$ 1%.The error in determining the thickness of the sample is, on average, of the same order. Thus, the error in determining conductivity using the four-probe method will generally be at least 2% [268].

Temperature dependencies of resistivity of self-assembled ensembles of $FeSi_2$ crystallites on *p*-Si substrates were measured using the four-probe method in the range of 100-800 K using an experimental setup for the thermopower and resistivity measurements similar to that described in [268] and in the range of 5-100 K using Physical Property Measurement System (PPMS) supplied with a configurable resistance bridge board Model 6000 PPMS Controller (Ch. 3.6.1).

Chapter 3

Self-assembled $FeSi_2$ crystallites on Si surfaces

This chapter presents a bottom-up approach for the growth of self-assembled ensembles of α-, β-$FeSi_2$ submicron- and nano- crystallites, using Au-assisted and Au-free conditions on *p*-Si(001), *p*-Si(110), and *p*-Si(111) surfaces using co-deposition of Fe and Si through molecular beam epitaxy and reactive epitaxy. This study shows that the crystals' orientation relationship (OR) with Si substrates and their morphology can be regulated using Au-assisted growth and Fe/Si atomic flux ratio variation.

3.1 Fabrication procedure

Self-assembled ensembles of α-, β-$FeSi_2$ submicron- and nanocrystallites, further in the text referred to as crystallites, were fabricated by reactive epitaxy (RE) and molecular beam epitaxy (MBE) under ultrahigh vacuum (UHV) conditions [237] using Au-assisted growth, variation of Fe/Si atomic flux ratio and substrate temperature to investigate control over the size, shape, and orientation of the α-, β-$FeSi_2$ self-assembled crystallites concerning the Si substrate.

For the $FeSi_2$ crystallites growth *p*-Si(001), *p*-Si(110), *p*-Si(111) substrates (ρ ~ 5-20 Ω·cm) (Fig. 3.1), pure (99.999 %) gold (Au) wire, pure (99.95 %) iron (Fe) wire, hydrogen peroxide (H_2O_2), and aqueous ammonia (NH_4ON) were used. Bidistilled and deionized (DI) water was used to prepare all solutions to fabricate and study samples.

The fabrication process of $FeSi_2$ crystallites on p-Si(001), p-Si(110), p-Si(111) substrates by the RE and MBE methods under UHV conditions according to the following protocol:

a. *Series of AF (Au + Fe) samples* in the following process sequence:

1) Pre-treatment of the Si surface in an aqueous solution of NH_4OH:H_2O_2:H_2O (1:1:1) and washing the DI with water to remove organic contaminations.
2) Thermal treatment of the Si substrate for 3 hours with a temperature increase to 650 °C at a rate of 4 °C min^{-1} under ultrahigh vacuum (base pressure: $1.5 \cdot 10^{-8}$ Pa) using rapid thermal processing (RTP) discussed in detail in Ch. 2.1.2.
3) Annealing the Si surface at 850-900 °C to obtain an atomically pure surface with the reconstruction (1.5×10^{-6} Pa) followed by cooling the substrate to 550°C (2.5×10^{-7} Pa).

4) Au layer (1 nm) deposition onto the Si substrate surface at a rate of 0.25 nm/min^{-1} at 550°C.
5) Increasing the substrate temperature to 740/840 °C.
6) Deposition of Fe layer ~40 nm in thickness at a rate of 0.34 nm min^{-1}.

b. *Series of AFS samples (Au + Fe + Si)* were prepared with a similar protocol. Instead of Fe deposition, the Fe/Si co-deposition was used. Thus, Fe and Si were deposited simultaneously at a rate of 0.1 and 0.34 nm min^{-1} (v_{Si}/v_{Fe} = 3.4), the Fe to Si atomic ratio being 1:2.
c. *Series of F samples (Fe) and FS samples (Fe + Si)* were prepared using a similar protocol, omitting the Au deposition.

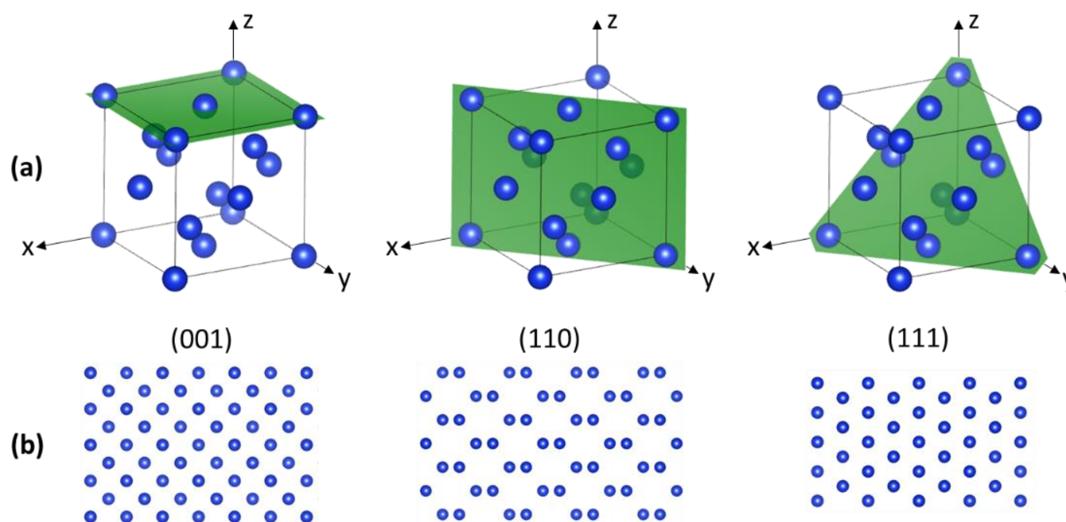

Figure 3.1. Schematic representation of (a) (001), (110) and (111) lattice planes of the non-primitive Si unit cell and (b) top view of (001), (110) and (111) lattice planes.

Three series of $FeSi_2$ samples were fabricated on *p*-Si(001), *p*-Si(110), and *p*-Si(111) substrates at 740°C and 840°C. The data on the fabricated samples are presented in Table 3.1.

Table 3.1. *Summary of samples prepared on p-Si(001), p-Si(110) and p-Si(111) substrates using Au-assisted (AF) and Au-free (F) Fe deposition, and Au-assisted (AFS) and Au-free (FS) Fe/Si co-deposition at substrate temperatures of 740 and 840 °C.*

Substrate	***p*-Si(001)**		***p*-Si(110)**		***p*-Si(111)**	
T	**740 °C**	**840 °C**	**740 °C**	**840 °C**	**740 °C**	**840 °C**
Au + Fe	AF7-001	AF8-001	AF7-110	AF8-110	AF7-111	AF8-111
Fe	F7-001	F8-001	F7-110	F8-110	F7-111	F8-111
Au + Fe + Si	AFS7-001	AFS8-001	AFS7-110	AFS8-110	AFS7-111	AFS8-111
Fe + Si	FS7-001	FS8-001	FS7-110	FS8-110	FS7-111	FS8-111

3.2 Morphology of $FeSi_2$ crystallites

The morphological characteristics, in particular influence of Au-assisted growth, temperature change and Fe/Si atomic flux ratio on the size and shape of $FeSi_2$ crystallites were studied with the help of scanning electron microscopy using S5500 SEM system (Hitachi) and atomic-force microscopy (AFM) using NanoInk DPN 5000 AFM system (Ch. 2.2.1). The average area of crystallites was calculated from SEM images by analyzing about 1000 crystallite units for each sample using ImageJ software [269]. The AFM data were processed using Gwyddion software [270].

3.2.1 $FeSi_2$ on Si(001)

The SEM images of the $FeSi_2$ crystallites prepared on Si(001) substrate are presented in Fig. 3.2 and reveal that each investigated sample exhibits unique morphological characteristics. The submicron crystals in samples AF7-001 and AF8-001 (Fig. 3.2 (a, b)), obtained using Au-assisted growth, display well-defined geometries with distinct flat facets, while maintaining a high degree of spatial separation between individual entities. Conversely, the majority of the crystals in samples F7-001 and F8-001 (Fig. 3.2 (e, f)), obtained during Au-free growth, exhibit coalescence, as evidenced by the formation of continuous films and loss of well-defined morphologies in comparison with those obtained using Au-assisted growth. Furthermore, differences in the average size and density of the crystallites are observed between the investigated samples. Notably, the crystallites obtained using Au-assisted growth are larger and sparser on the substrate surface with an average area ($\bar{A}$) of ~$69 \cdot 10^3$ nm^2 for AF7-001 and ~$180 \cdot 10^3$ nm^2 for AF8-001 when compared to those obtained without using Au-assisted growth $\bar{A}$ is ~$60 \cdot 10^3$ nm^2 for F7-001 and ~$74 \cdot 10^3$ nm^2 for F8-001 (Fig. 3.2 (d, h)) (the data on the average area of prepared crystallites on Si(001) substrate is summarized in Table 3.2). These observations suggest that the presence of Au significantly impacts the growth and aggregation behavior of the crystallites, ultimately resulting in a different morphology and size distribution.

Thus, crystallites obtained using Fe deposition using Au-assisted growth at 840 °C substrate temperature are twice larger than those obtained during Au-free growth. Au-islands are known to act as nucleation sites for metal silicide crystallites, playing an important role in determining their growth kinetics [155].

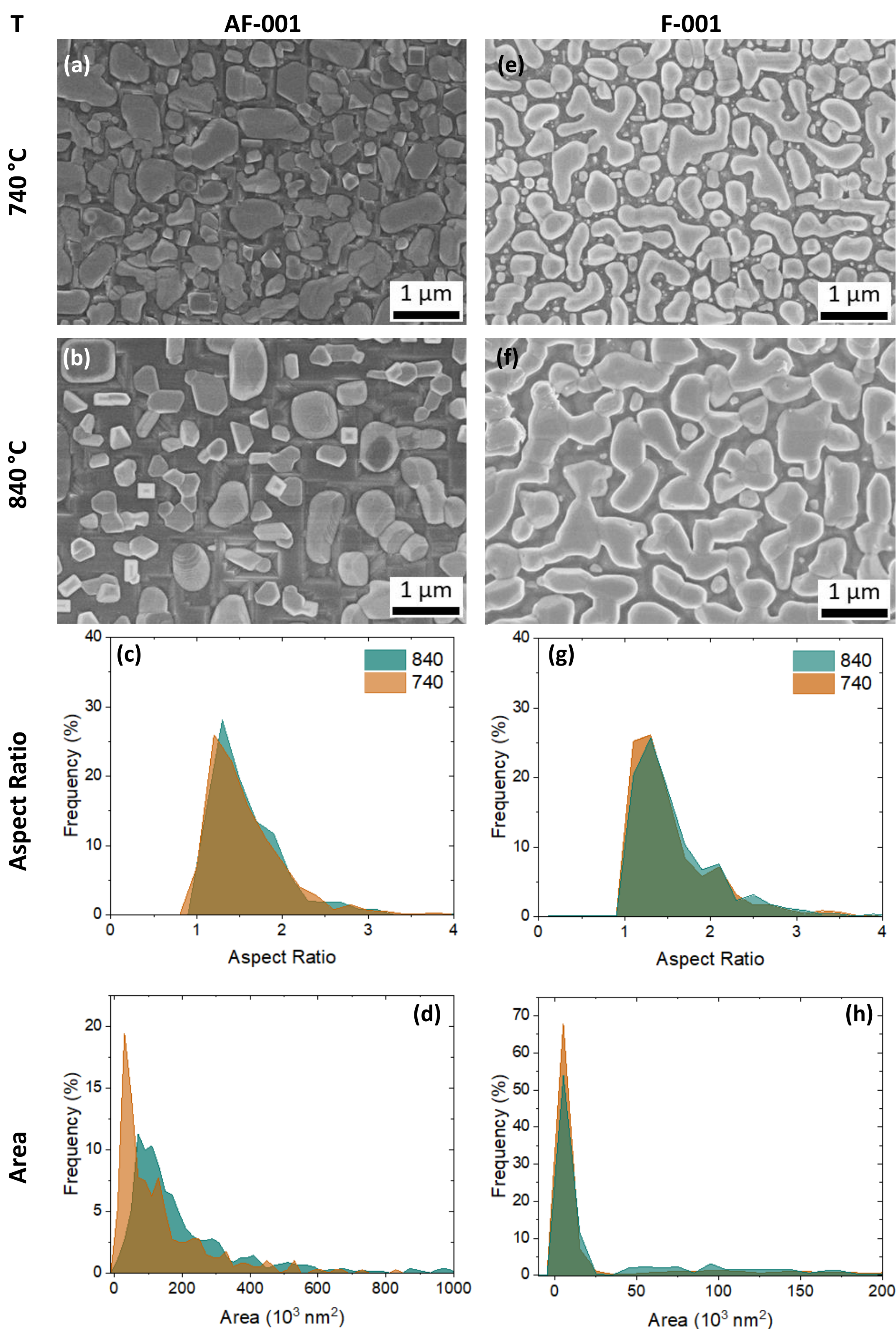

Figure 3.2. SEM-images of the $FeSi_2$ crystallites prepared on Si(001) substrates using (a-d) Au-assisted Fe deposition at (a) 740 °C (AF7-001) and (b) 840 °C (AF8-001) substrate temperature with comparison of their (c) aspect ratio and (d) area distributions, and (e-h) Au-free Fe deposition at (e) 740 °C (F7-001) and (f) 840 °C (F8-001) substrate temperature with comparison of their (g) aspect ratio and (h) area distributions.

Thus, Au-assisted growth promotes the formation of well-defined crystal facets with flat surfaces, which is observed in the AF7-001 and AF8-001 samples (Fig. 3.2 (a, b)) as well as Au-assisted Fe/Si co-deposition (Fig. 3.3 (a, b)), which can be attributed to the formation of α-$FeSi_2$(001) crystal plane parallel to the Si substrate surface, as it was calculated in [159,271]. Concerning Au-free Fe/Si co-deposition (Fig. 3.3 (e, f), the crystallites do not demonstrate a well-defined faceting, but they grow separately on the substrate surface, which is different for those obtained without Si atoms and with or without using Au-assisted growth (Fig. 3.2 (a, b, e, f)). However, Fe/Si co-deposition reduces the size of the resulting crystallites, as indicated by their area distributions (Fig. 3.3 (d, h)). The reduction in the size can be explained by decreasing the diffusion length of Fe atoms as a consequence of the formation of multiple nucleation sites due to the influence of deposited Si atoms acting together with Si atoms from the substrate. For instance, the AFS7-001 sample demonstrates crystallites smaller with $\bar{A}$ of ~$18{\cdot}10^3$ nm^2 in comparison to the AF7-001 sample and the same trend is observed for the samples AFS8-001 ~$31{\cdot}10^3$ nm^2 and AF8-001 (Fig. 3.3 (d, h)) (Table 3.2). This size reduction is consistent also for samples obtained during Au-free Fe/Si co-deposition for the FS7-001 sample has $\bar{A} \approx 19{\cdot}10^3$ nm^2 and the FS7-001 sample $\bar{A} \approx 41{\cdot}10^3$ nm^2, which are ~3 and 2 times smaller than those obtained without Fe/Si co-deposition.

The maximum aspect ratio (AR) distribution for all samples, as shown in Figs. 3.2-3.3 (c, g), is approximately 1.5, which indicates that the crystals possess an elongated shape attributed to the tetragonal crystal structure of α-$FeSi_2$.

The thickness analysis of prepared submicron $FeSi_2$ crystals was conducted using atomic force microscopy (AFM) (as described in detail in Ch. 2.2) (Fig. 3.4.). The results of the study revealed that the heights of $FeSi_2$ crystallites formed using Au-assisted growth are comparable in height for both samples AF7-001 and AF8-001 (Fig. 3.4 (a)). Thus, the average height $\bar{H}$ of crystallites of the AF7-001 sample is ~83 nm and is ~95 nm of those of the AF8-001 sample (Table 3.2).

For the $FeSi_2$ crystallites obtained using Au-free growth, the increase in height is attributed to the enhanced mobility and diffusion of atoms on the surface of the substrate at higher temperatures, allowing for more efficient incorporation of Fe and Si atoms into the growing crystals, which leads to the formation of larger and taller crystals.

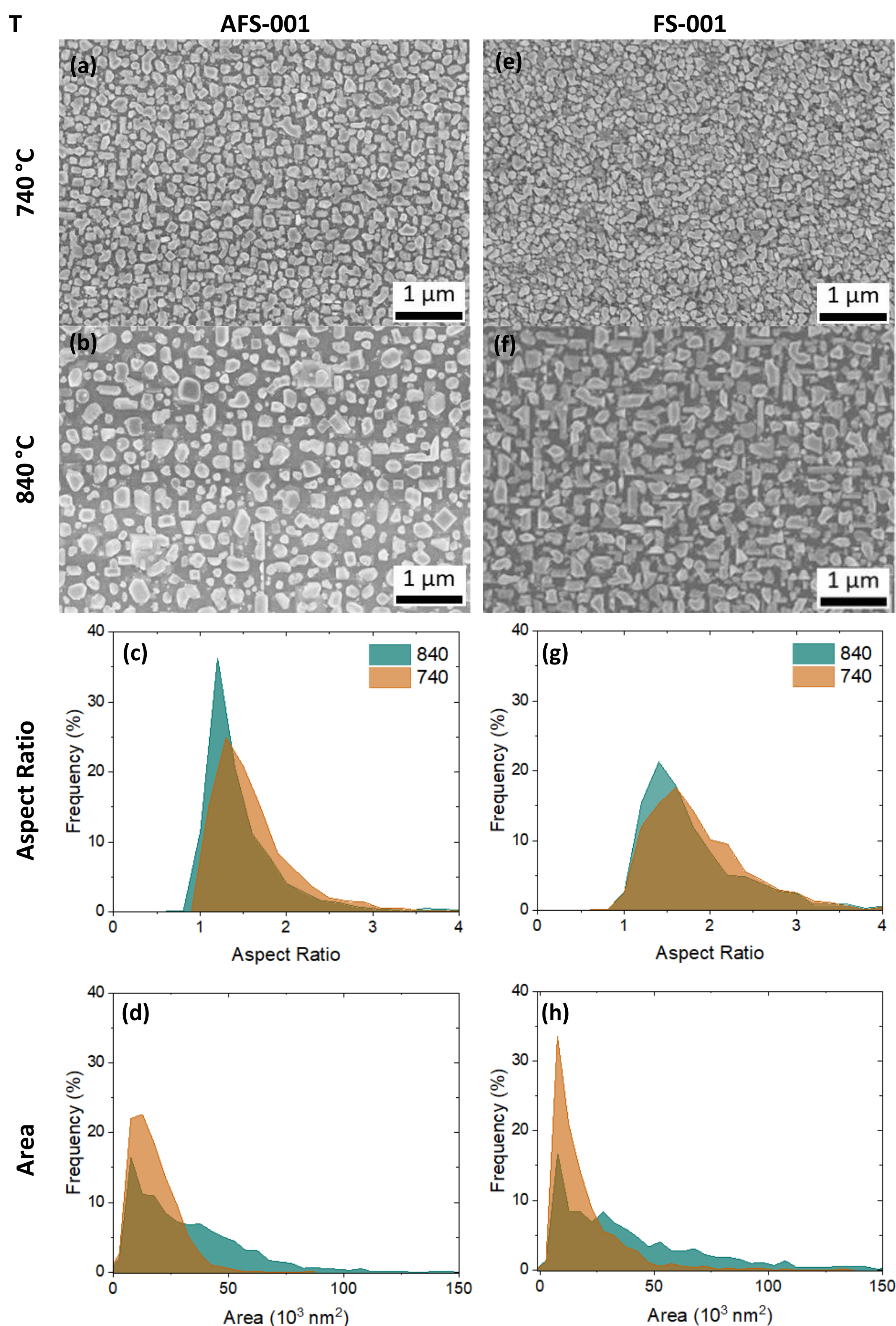

Figure 3.3. SEM-images of the $FeSi_2$ crystallites prepared on Si(001) substrates using (a-d) Au-assisted Fe/Si co-deposition at (a) 740 °C (AFS7-001) and (b) 840 °C (AFS8-001) substrate temperature with comparison of their (c) aspect ratio and (d) area distributions, and (e-h) Au-free Fe/Si co-deposition at (e) 740 °C (FS7-001) and (f) 840 °C (FS8-001) substrate temperature with comparison of their (g) aspect ratio and (h) area distributions.

Thus, the crystallites of the F8-001 sample were found to be ~2.5 higher than those of the F7-001 sample with $\bar{H}$ ~ 53 nm and $\bar{H}$~114 nm, respectively. In addition, similar behavior is observed in the case of crystallites obtained during Au-free Fe/Si co-deposition for the FS7-001 and FS8-001 samples (Fig. 3.4 (d)). Here, the increase in height with increased substrate temperature is also observed. This way, the crystallites obtained at 740ºC are ~1.5 lower with $\bar{H}$ ~ 27 nm than those obtained at 840ºC with $\bar{H}$ ~ 19 nm. In contrast, crystallites obtained during Au-assisted Fe/Si co-deposition at 740ºC substrate temperature are smaller than those obtained at 840ºC, while their $\bar{H}$ decreased with increasing substrate temperature (Fig. 3.4 (c)).

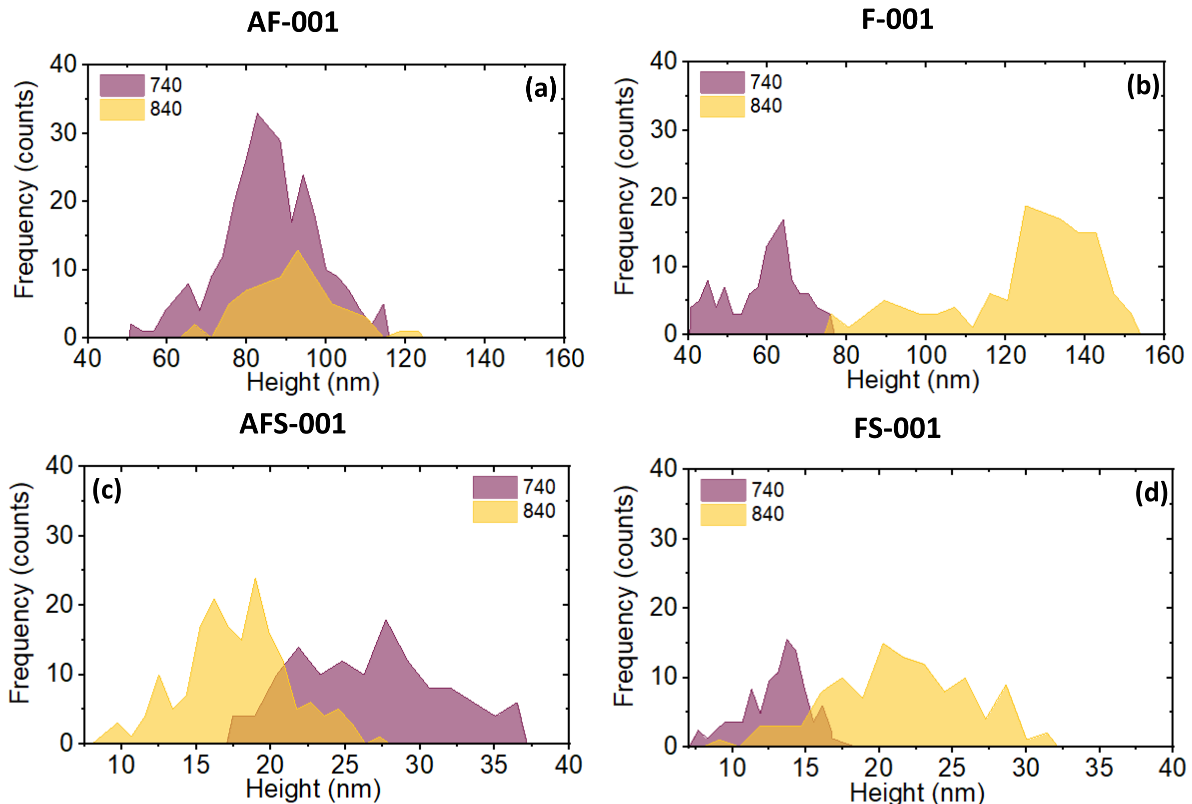

Figure 3.4. Height distributions of the $FeSi_2$ crystallites prepared on Si(001) substrates using (a) Au-assisted (AF7-001 and AF8-001) and (b) Au-free (F7-001 and F8-001) Fe deposition and using (c) Au-assisted (AFS7-001 and AFS8-001) and (b) Au-free (FS7-001 and FS8-001) Fe/Si co-deposition at 740 °C and 840 °C substrate temperatures.

Au-assisted growth promotes the height decrease, which is observed for samples AF7-001 and AF8-001 (Fig. 3.4). Moreover, the crystals in these samples are found to be buried within the silicon substrate, with voids present between the silicide facets and silicon substrate (Fig. 3.5), which is not observed in case of Au-free samples F7-001 and F8-001 (Fig. 3.2 (e, f)). The voids can exceed 50 nm in depth and 100 nm in width, indicating a significant depletion of silicon

atoms from the substrate due to high diffusion at the synthesis temperature (T = 740-840°C), which is confirmed by AFM (Fig. 3.5 (e, f)). These observations highlight the influence of Fe/Si flux ratio and Au-assisted growth in determining the morphology of iron silicide crystallites, when, during Fe deposition, the Si atoms are etched from Si substrates and iron silicide crystallites formed in 4-fold symmetry voids demonstrating lower height and larger average area in comparison with other samples.

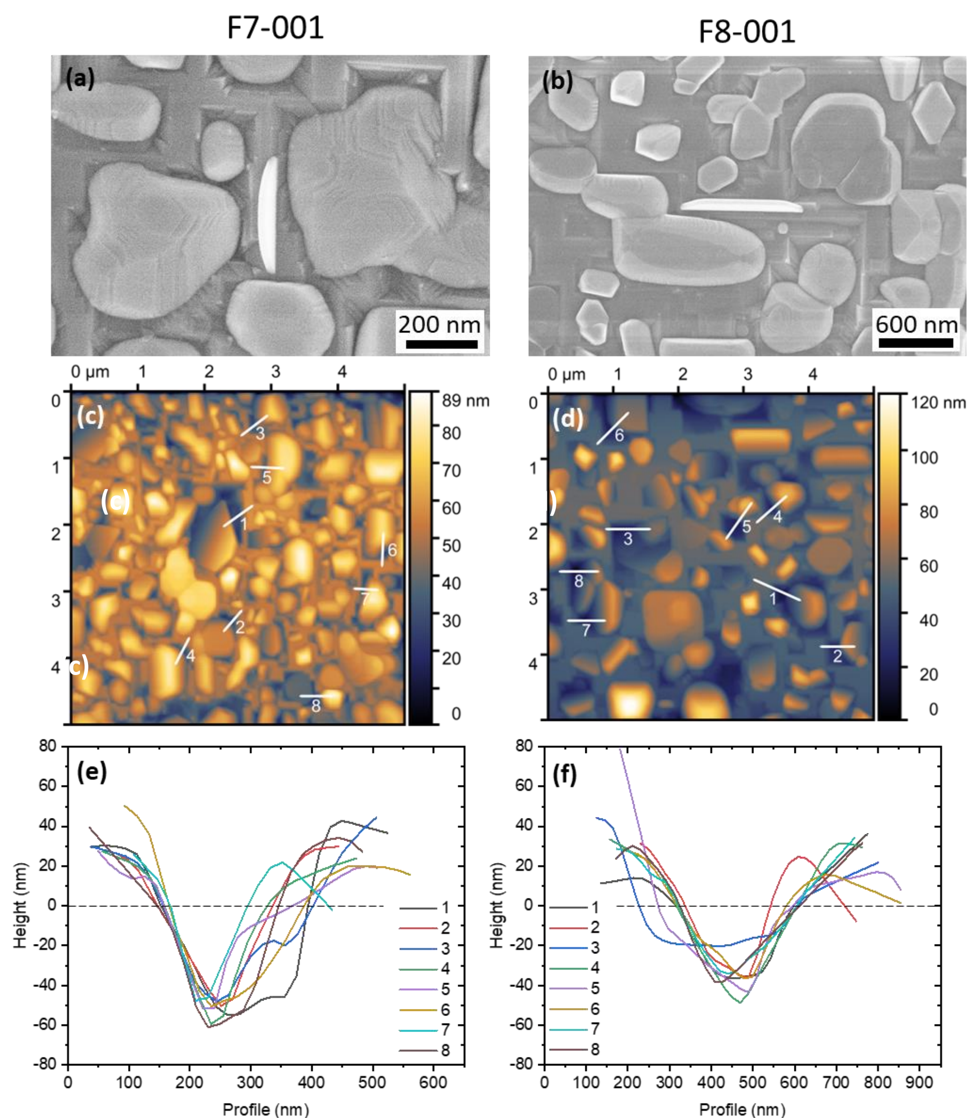

Figure 3.5. SEM- and AFM-images of the $FeSi_2$ crystallites prepared on Si(001) substrates using Au-assisted Fe deposition at (a, c) 740°C for sample AF7-001 and (b, d) 840°C for sample AF8-001 and (e, f) height profiles of voids between the silicide facets and Si substrate for these samples along the lines indicated in (c) and (d), respectively. Dashed lines indicate the level of Si substrate surface.

The average values of area and height of $FeSi_2$ crystallites prepared on *p*-Si(001) according to fabrication procedures described in Ch. 3.1 are summarized in Table 3.2. The standard error

of the mean (s) was used to estimate a sample's average crystallite area/height value [272]. The formula for SEM is equal to the ratio of the standard deviation (SD) to the square root of the sample number of measured crystallites in the sample (N)

$$s = \frac{SD}{\sqrt{N}} \tag{3.1}$$

Table 3.2. *Summary of the average area and the average height of prepared $FeSi_2$ crystallites on p-Si(001) using Au-assisted (AF) and Au-free (F) Fe deposition, Au-assisted (AFS) and Au-free (FS) Fe/Si co-deposition at of 740 and 840 °C substrate temperatures.*

	Average area $\bar{A}$, 10^3 nm^2		**Average height $\bar{H}$, nm**	
T	**740 °C**	**840 °C**	**740 °C**	**840 °C**
AF-001	69 ± 4	180 ± 6	83 ± 4	95 ± 5
F-001	57 ± 4	74 ± 8	58 ± 3	114 ± 6
AFS-001	18 ± 1	31 ± 1	27 ± 2	18 ± 1
FS-001	19 ± 1	40 ± 1	13 ± 1	20 ± 2

The crystallites observed in samples AF8-001 and AFS8-001 exhibit distinct forms, notably influenced by temperature and the use of Au-assisted growth. Understanding these specific forms and their facets holds significant importance as it provides valuable insights into these crystals' properties and potential applications. By understanding the structural characteristics of these crystals, a deeper understanding of their behavior and exploring their suitability for various practical applications can be gained. In this manner, Figure 3.6 provides a comprehensive overview of the crystallites observed in samples AF8-001 and AFS8-001, revealing several distinct shapes (marked with different colors) and characteristics:

- *Rectangular nanoplates* (blue rectangles) are present in both samples and align along <010> and <011> directions. These nanoplates exhibit dimensions of approximately 400-800 nm in length, 300-400 nm in width, and 30-70 nm in thickness.
- *Hexagonal nanoplates* (purple hexagons) are also observed in both samples, displaying irregular geometries. The lateral size of these nanoplates ranges from 300-800 nm for AF8-001 and 200-350 nm for AFS8-001.
- *Trapezoid nanoplates* (green trapezoids) are inclined at an angle of ~125° relative to the Si<001> direction and align along the Si<011> direction. The AFM analysis indicates dimensions of approximately 100 nm in height, 350 nm in width, and a thickness of ~300 nm for AF8-001. The trapezoids in AFS8-001 are smaller, with widths ranging from 50-350 nm.

- *Triangular nanoplates* (red triangles) are exclusively present in the AFS8-001 sample, exhibiting lateral sizes of ~200-250 nm. Notably, the sides of these triangular nanoplates do not align parallel to the low-index direction of the Si(001) surface. One of the sides deviates by about 14° from the Si<011> direction. The presence of triangular nanoplates may be influenced by factors such as the number of silicon atoms evaporated onto the substrate surface and the presence of Au.

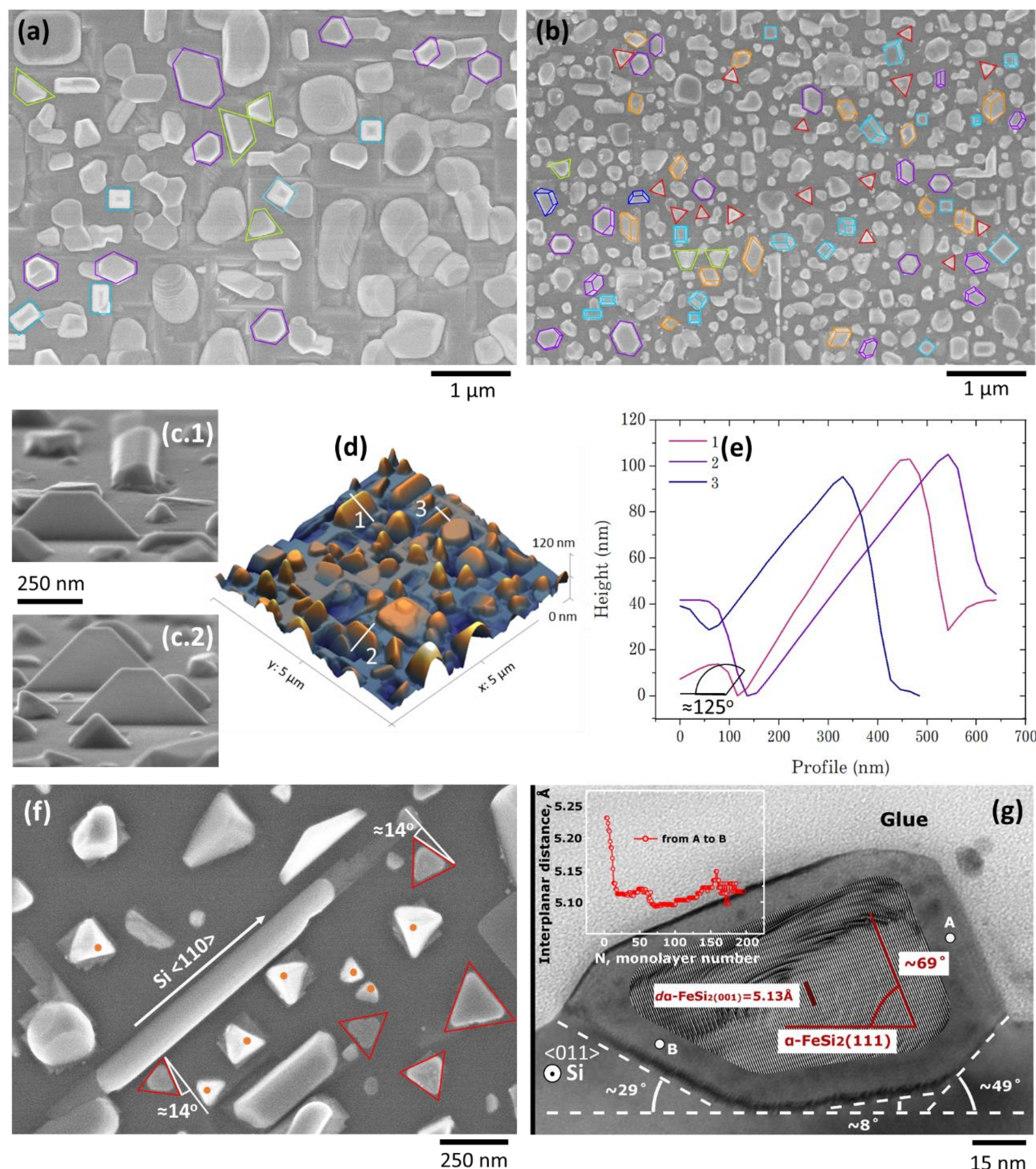

Figure 3.6. SEM-images of the $FeSi_2$ crystallites of samples (a) AF8-001 and (b) AFS8-001; (c) inclined SEM and (d) 3D AFM images with trapezoid nanoplates, and (e) 1D profiles of trapezoid nanoplates; (f) SEM-image of triangular nanoplates, tetrahedrons and with (g) cross-sectional TEM image of endotaxial polyhedral nanobar, the inset depicts the interplanar distance between (001) planes of α-$FeSi_2$ from A to B points [273].

- *Tetrahedrons* (orange dots) are observed in the AFS8-001 sample, characterized by three equal edges ranging from 80 to 300 nm. The height of these tetrahedrons varies from 16 to 170 nm, as indicated by the yellow dots in the image.
- *Polyhedral nanobars* (white arrow) align along the Si<110> direction and exhibit lengths up to ~1.5 µm, widths ranging from 100-200 nm, and 50-110 nm thicknesses. The TEM analysis (Fig. 3.6 (g)) confirms that these nanobars are endotaxial and correspond to the α-$FeSi_2$(102)[100]//Si(001)[110] orientation relationship. The (001) planes of α-$FeSi_2$ are inclined at approximately 43.7° relative to the Si(001) surface, with (102) < (001) = 43.7°.

Summary

Detailed characterization of the morphology of the $FeSi_2$ crystallites prepared on Si(001) substrate provides crucial insights into their shapes, orientations, and sizes, enabling a better understanding of their structural properties and potential applications. In particular, Au-assisted growth, temperature change and Fe/Si atomic flux ratio change.

The following results were obtained:

- *Au-assisted growth has a significant impact on the formation of $FeSi_2$ crystallites on the Si(001) surface and results in the formation of well-defined crystal facets with distinct crystal geometries during the reactive epitaxy of Fe and Fe/Si co-deposition (Fig. 3.6).*
- *Au-assisted reactive epitaxy, Fe deposition, results in preferable endotaxial growth mode. It promotes the formation of voids in Si substrates around silicide crystallites, consuming Si atoms from Si substrates and decreasing silicide crystallites' height (Fig. 3.5).*
- *Au-free conditions result in the formation of crystallites exhibiting coalescence and forming continuous films without well-defined morphologies.*
- *Change of the Fe/Si atomic flux ratio leads to a size reduction of the resulting crystallites due to a decreasing diffusion length of Fe atoms and, as a consequence, a formation of multiple nucleation sites due to the influence of deposited Si atoms acting together with Si atoms from the substrate. As a result, an increased concentration of Si atoms, due to a change in atomic Fe/Si flux ratio, leads to limited availability of Fe atoms, followed by restricted growth of individual silicide crystallites.*

Thus, the presence of Au strongly indicates the important role of Au-assisted growth of $FeSi_2$ crystals, facilitating the formation of distinct and unique crystal shapes with flat surfaces, attributed to the formation of α-$FeSi_2$(001) crystal plane parallel to the Si substrate surface.

3.2.2 $FeSi_2$ on Si(110)

The SEM images of the $FeSi_2$ crystallites prepared on Si(110) substrate are presented in Figures 3.7-3.8. Crystallite growth occurs similarly for all samples with highlighted 2-fold symmetry shape anisotropy along the Si[-110] direction (Fig. 3.7). Crystallites obtained during Au-free growth show coalescence and tend to form continuous films due to temperature changes, as observed in samples F7-110 and F8-110 (Fig. 3.7 (e, f)). At higher temperatures (F8-110 sample), the resulting crystals are larger with the average area ($\bar{A}$) of ~$863 \cdot 10^3$ nm^2 due to the increase in diffusion length of Fe atoms, occurring at high temperatures in comparison with crystallites obtained at 740°C (F7-110 sample) with $\bar{A}$ ~ $256 \cdot 10^3$ nm^2 (Fig. 3.7 (h)). The aspect ratio distribution of crystallites in samples F7-110 and F8-110 obtained using Au-free conditions is narrow (~1-5) and shows that the crystallites are slightly elongated (Fig. 3.7 (g)). In contrast, for $FeSi_2$ crystallites prepared using Au-assisted growth, specifically the AF7-110 and AF8-110 samples (Fig. 3.7 (c)), the aspect ratio distribution is wider (up to 40), which indicates the formation of long wire-like shape crystallites. Also, Au-assisted growth exhibits flat facets and sharp corners of the crystals, which are arranged in a regular pattern on the surface of a Si(110) substrate (Fig. 3.7 (a, b)). The anisotropic growth properties of $FeSi_2$ crystals cause them to nucleate and grow along the Si[-110] direction preferentially due to the orientation of the substrate, resulting in wires along the substrate surface with a rectangular cross-section (Fig. 3.11 (d)). These wires are a few hundred nanometers wide (Fig. 3.7 (d)) with $\bar{A}$ ~ $500 \cdot 10^3$ nm^2 for crystallites obtained at 740°C (AF7-110) and with $\bar{A}$ ~ $2987 \cdot 10^3$ nm^2 for crystallites of the AF8-110 sample due to the increase of diffusion length of Fe atoms at 840°C. The data on the average area of prepared crystallites on Si(110) substrate is summarized in Table 3.3.

The Fe/Si co-deposition on the Si(110) surface (Fig. 3.8) leads to a decrease in the size of the obtained crystallites, according to the area distributions (Fig. 3.8 (c, g)), in comparison to the crystallites fabricated without Fe/Si co-deposition (Fig. 3.7 (c, g)). Thus, the crystallite size is decreased from submicron- to nanoscale. In this manner, the area distributions of nanocrystals of the FS7-110 and FS8-110 samples, obtained using Au-free conditions, are comparable with the average nanocrystal area $\bar{A}$ ~ $49 \cdot 10^3$ nm^2 and $\bar{A}$ ~ $59 \cdot 10^3$ nm^2, respectively, which means that the substrate temperature during nanocrystal formation slightly influences its size and aspect ratio (Fig. 3.8 (g)).

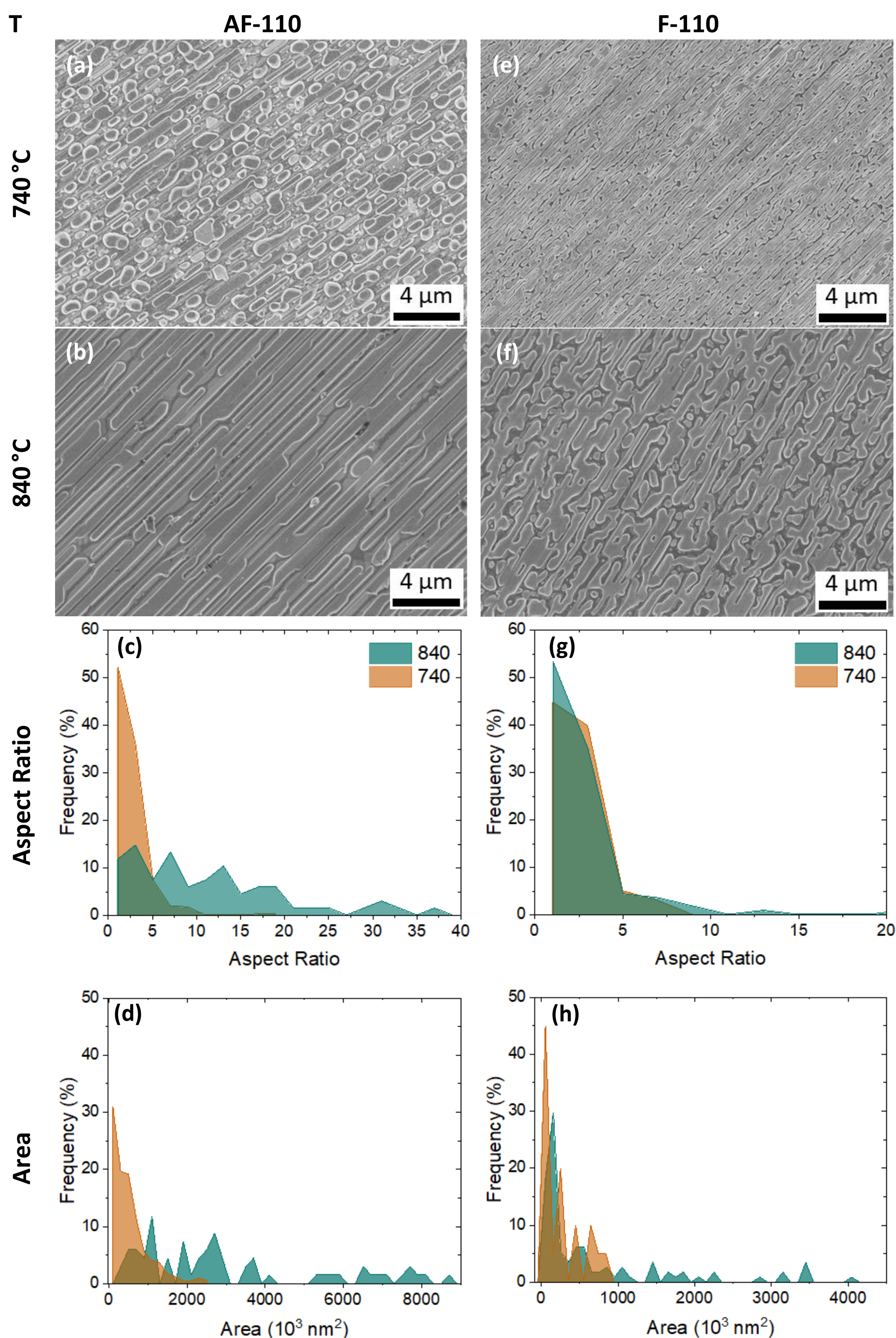

Figure 3.7. SEM-images of the $FeSi_2$ crystallites prepared on Si(110) substrates using (a-d) Au-assisted Fe deposition at (a) 740 °C (AF7-110) and (b) 840 °C (AF8-110) substrate temperature with the comparison of their (c) aspect ratio and (d) area distributions, and (e-h) Au-free Fe deposition at (e) 740 °C (F7-110) and (f) 840 °C (F8-110) substrate temperature with the comparison of their (g) aspect ratio and (h) area distributions.

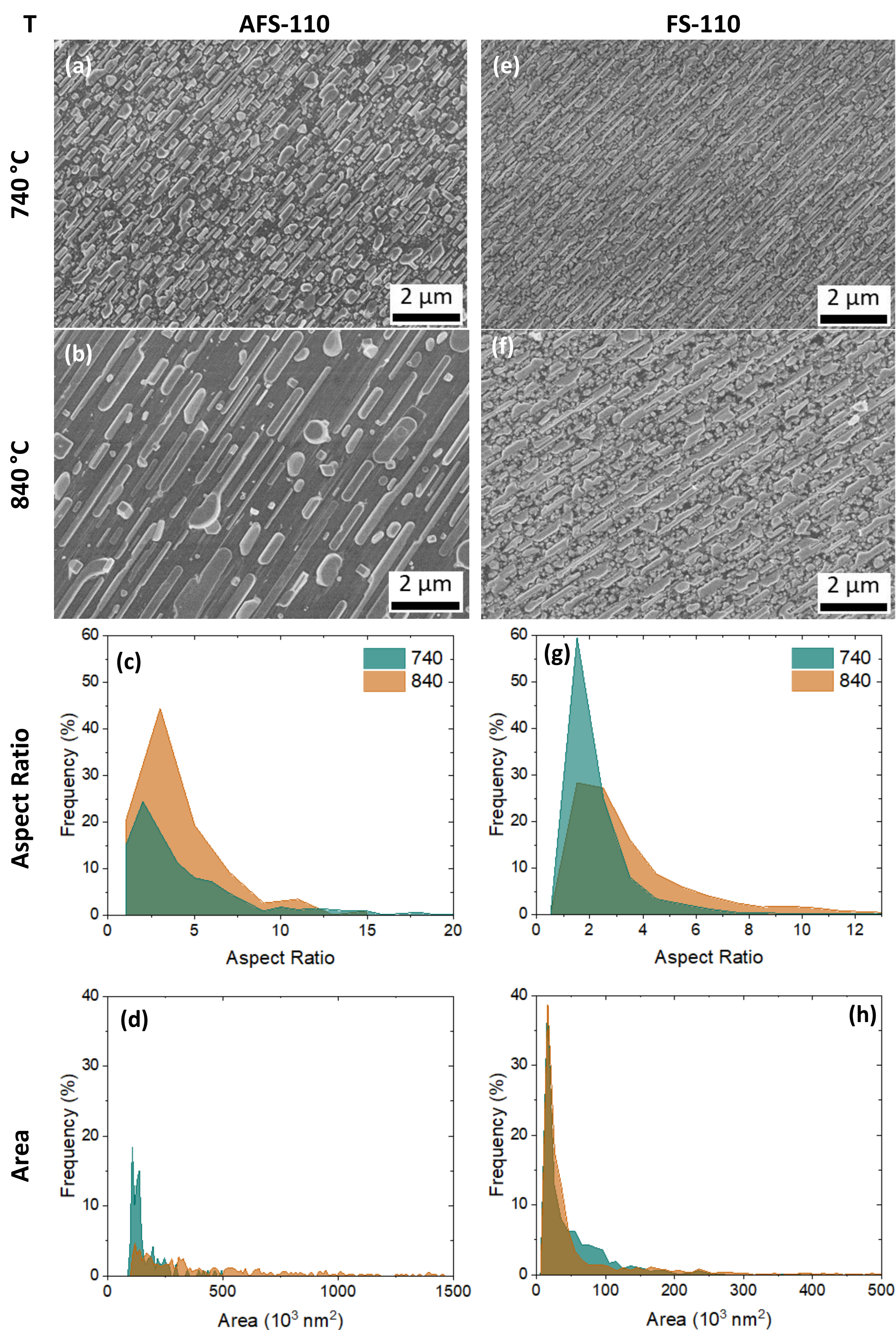

Figure 3.8. SEM-images of the $FeSi_2$ crystallites prepared on Si(110) substrates using (a-d) Au-assisted Fe/Si co-deposition at (a) 740 °C (AFS7-110) and (b) 840 °C (AFS8-110) substrate temperature with the comparison of their (c) aspect ratio and (d) area distributions, and (e-h) Au-free Fe/Si co-deposition at (e) 740 °C (FS7-110) and (f) 840 °C (FS8-110) substrate temperature with the comparison of their (g) aspect ratio and (h) area distributions.

However, the influence temperature for the growth of crystallites obtained using Au-assisted growth is obvious for the AFS8-110 sample, prepared at 840°C. Thus, the area of resultant crystallites is ~3 times (Fig. 3.8 (d)) larger with $\bar{A}$ ~ 455·10^3 nm^2 than for the crystallites of the AFS7-110 sample, grown at 740°C, with $\bar{A}$ ~ 161·10^3 nm^2 (Table 3.3). Obtained crystallites demonstrate high faceting and wire-like shape, especially on the AF8-110 sample. The aspect ratio distributions (Fig. 3.8 (c, g)) of crystallites obtained with and without Au are similar and in the range of 1-20, indicating the elongated crystal shape. Thus, increased substrate temperature increases the area of fabricated nanocrystals with the retention of their aspect ratio.

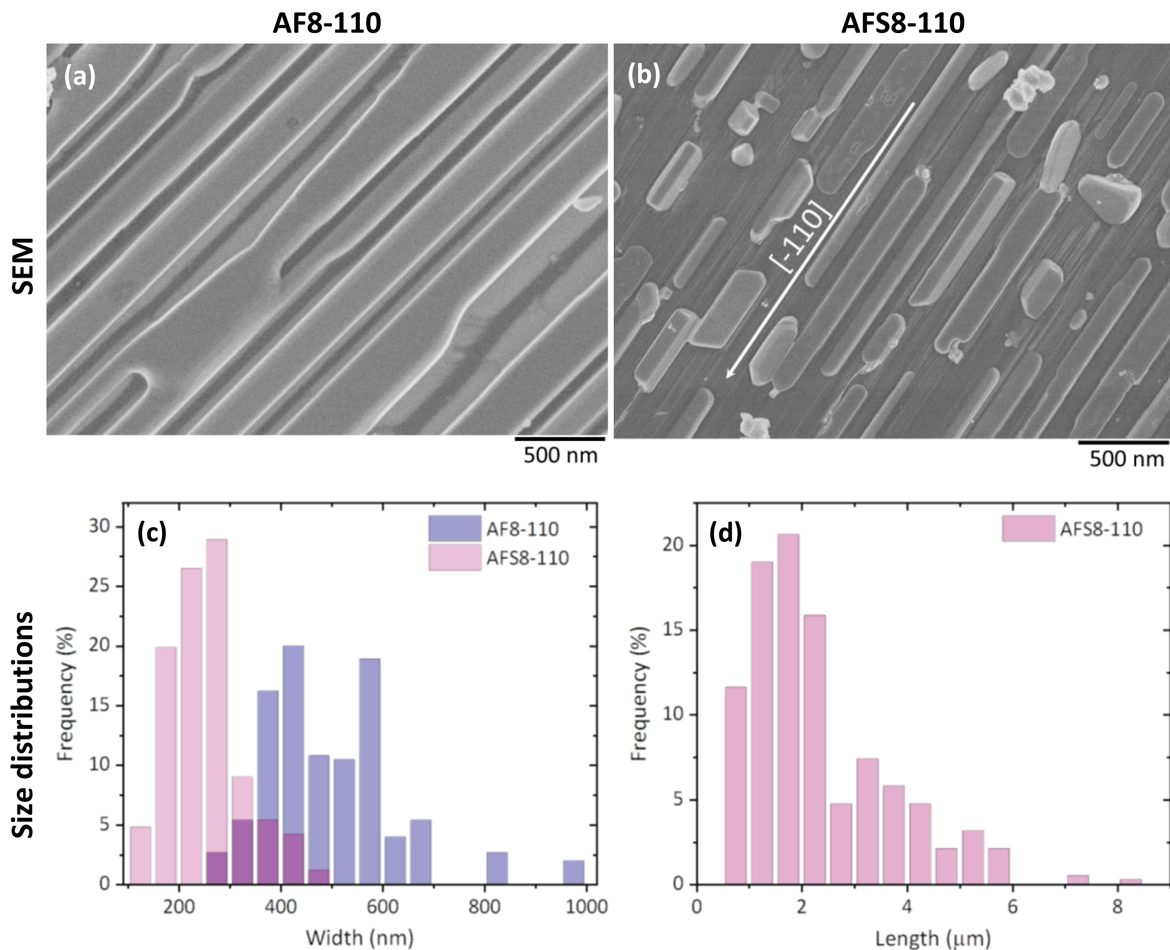

Figure 3.9. SEM-images of the $FeSi_2$ wire-like crystallites prepared on Si(110) substrates using (a) Au-assisted Fe deposition (AF8-110) and (b) Au-assisted Fe/Si co-deposition (AFS8-110) with the comparison of (c) their width and (d) AFS8-110 wire-like crystallites length distributions.

In this manner, the formation of $FeSi_2$ nanowires (NWs) with controllable lateral sizes is observed. SEM images of $FeSi_2$ NWs fabricated on the Si(110) surface using Au-assisted Fe/Si co-deposition are compared in Fig. 3.9 (a, b). The width distributions (Fig. 3.9 (c)) reveal that

the average width of NWs obtained during the Au-assisted Fe/Si co-deposition results in narrow width distribution and is about 2 times narrower than for submicron-wide wires of the sample AF8-110. Thus, the average width of submicron wires of AF8-110 is about 500 nm, while the average width of NWs of AFS8-110 is about 200 nm. Also, on the AFS8-110 sample, 100 nm wide NWs are present, which is not the case for the AF8-110 sample. The length distribution of nanowires of the AFS8-110 sample is presented in Fig. 3.9 (c), which demonstrates that the minimum length of obtained NWs is 1 μm and the maximum is 8 μm, while the average length is 2.5 nm. The length of the wires of the AF8-110 sample is not determined precisely since the continuous wires grow one into the other, forming long, continuous wire-like crystals.

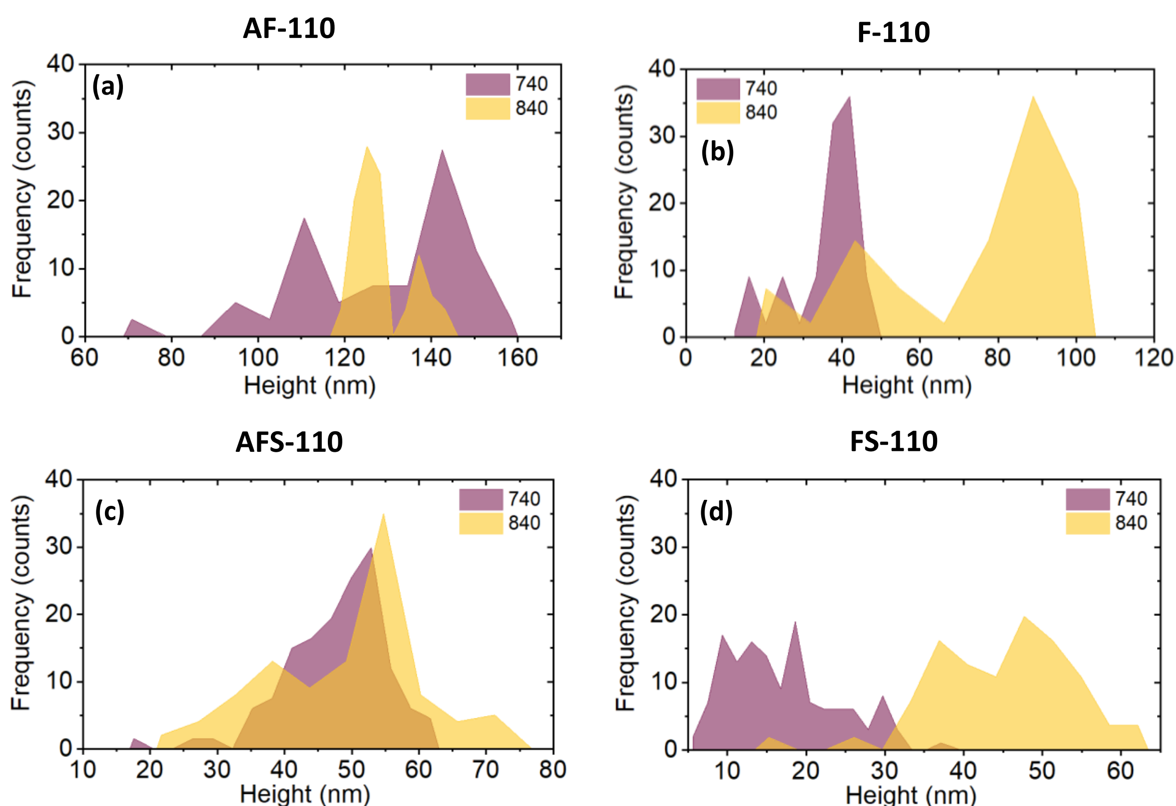

Figure 3.10. Height distributions of the $FeSi_2$ crystallites prepared on Si(110) substrates using (a) Au-assisted (AF7-110 and AF8-110) and (b) Au-free (F7-110 and F8-110) Fe deposition and using (c) Au-assisted (AFS7-110 and AFS8-110) and (d) Au-free (FS7-110 and FS8-110) Fe/Si co-deposition at 740 °C and 840 °C substrate temperatures.

Additionally, the average height of the $FeSi_2$ crystallites prepared on Si(110) substrate was investigated by AFM (Fig. 3.10). Regarding the changes in the height $\bar{H}$ distributions of the crystallites for the AF7-110 and AF8-110 samples, the higher temperature of the substrate results in narrow height distribution due to the coalescence of small and separated crystallites

into continuous wires with high faceting. Thus, the minimum height of the wires of the AF8-110 sample is 120 nm and the maximum 145 nm, while the height of the crystallites obtained on a substrate heated up to 740°C varies from 40 nm to 160 nm. In the case of crystallites obtained at Au-free Si surface, an increase in the average height with the increase of substrate temperature is observed due to increased diffusion length of Fe atoms leading to the formation of higher crystallites. Thus, the crystallites of sample F8-110 are twice higher than those obtained for the F7-110 sample.

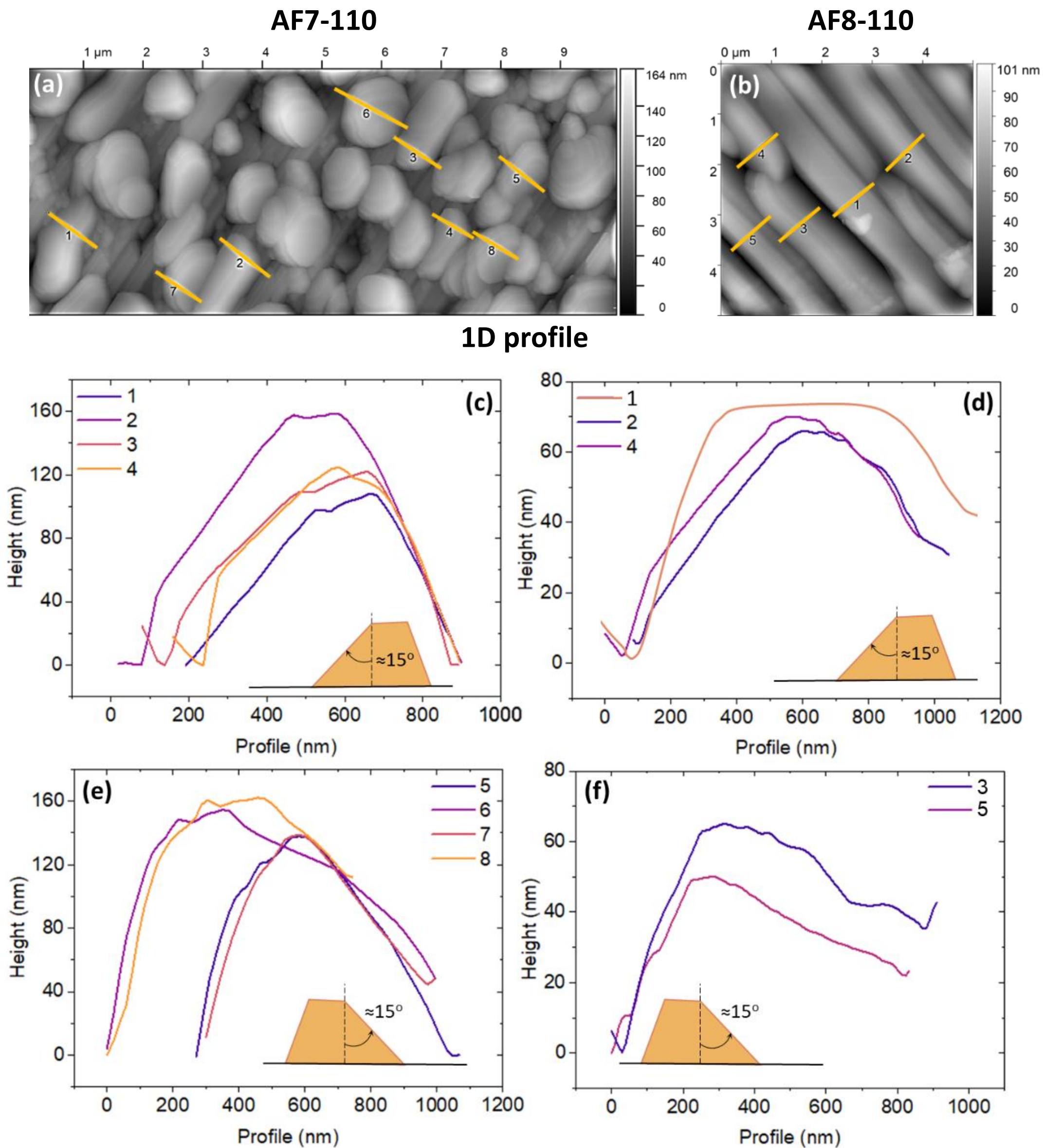

Figure 3.11. AFM-images of the $FeSi_2$ crystallites prepared on Si(110) substrates using Au-assisted Fe deposition at (a) 740°C - AF7-110 sample and (b) 840°C - AF8-110 sample and height profiles, along the lines indicated in (a) and (b), with (c, d, e, f) 2-fold inclination by ~15˚ relative to Si[-110] for samples AF7-110 and AF8-110, correspondingly; rectangular profile of not inclined elongated crystal is presented in (d) curve 1 (orange).

In the case of Fe/Si co-deposition, the height distribution of obtained crystallites of the sample AFS7-110 is narrower than one of the AFS8-110 sample, which is the opposite of the crystallites obtained at the same conditions, but without Fe/Si co-deposition. Thus, the minimum height of the crystallites of the AFS8-110 sample is ~20 nm and the maximum is ~75 nm, while the crystallites of the AFS7-110 sample demonstrate a minimum height of ~33 nm and a maximum height of ~63 nm. Nevertheless, the average height of the crystallites obtained on both samples is ~55 nm. Concerning the average height of crystallites obtained during the Au-free Fe/Si co-deposition, one can see similar situation to the previous case of Au-free conditions. Thus, the increase in the average height of the crystallites of the FS8-110 sample with the increase of substrate temperature is observed due to the increase of diffusion length of Fe atoms leading to the formation of higher crystallites ($\bar{H}$ ~ 45 nm), compared with the crystallites obtained on sample FS7-110 ($\bar{H}$ ~15 nm).

Concerning the influence of Au-assisted growth on the height of fabricated crystallites, it can be concluded that the crystallites obtained using Au-assisted growth have narrower height distributions, particularly when the substrate temperature is 840°C and in the case of 740°C are ~2 times higher than those obtained during Au-free conditions. The influence of Fe/Si co-deposition results in the lower height of obtained crystallites, which can be explained by a higher concentration of Si atoms near the surface due to a change in atomic Fe/Si flux ratio, which leads to the limited availability of Fe atoms and is followed by the decrease in crystallite lateral sizes due to formation of multiple nucleation sites influenced of deposited Si atoms acting together with Si atoms from the substrate. Furthermore, fabricated crystallites of the AF7-110 and AF8-110 samples demonstrate a 2-fold inclination by ~15˚ relative to the Si<110> direction according to 1D profiles (Fig. 3.11). In this manner, the AF7-110 sample presents two types of slightly elongated crystallites, which demonstrate 2-fold inclination by ~15˚ relative to the substrate surface. In comparison, the AF8-110 sample presents three types of submicron wires with rectangular cross-sections: parallel and with 2-fold inclination by ~15˚ relative to the substrate surface. In this case, the substrate temperature influences the formation of submicron wires and their orientation relative to the Si<110> direction. Regarding the NWs fabricated during Fe/Si co-deposition at 840°C, the inclination also occurs. The precise inclination angle was not determined in this case due to the resolution limitations of the AFM device. Despite this, Fig. 3.12 (b) demonstrates the height profiles of fabricated

NWs with two symmetrical inclination angles, assumed as a 2-fold inclination by ~15˚. Furthermore, one of the profiles (5) is not inclined and should correspond to not inclined NW with a flat surface corresponding to α(001) crystal plane parallel to the Si(110) substrate surface.

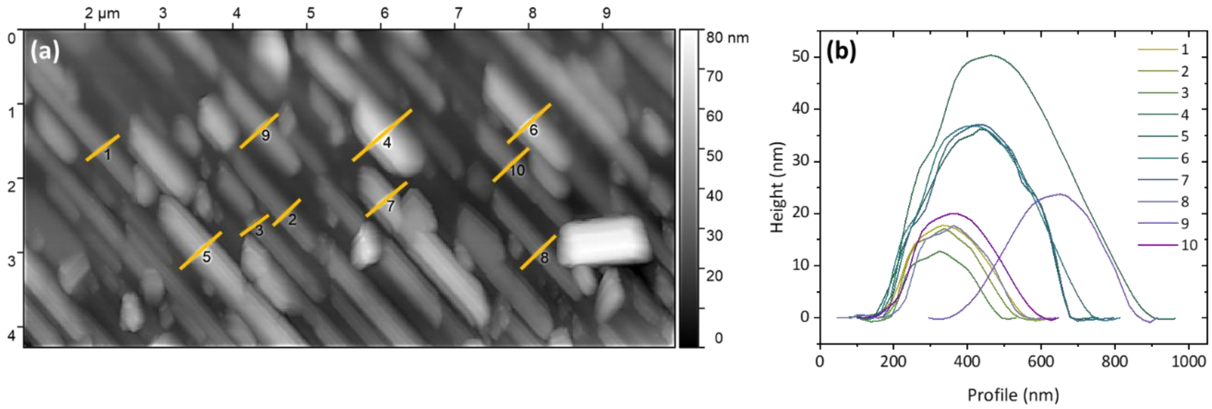

Figure 3.12. (a) AFM-image and (b) height profiles of the $FeSi_2$ NWs, along the lines indicated in (a), prepared on Si(110) substrate using Au-assisted Fe/Si co-deposition at 840°C of substrate temperature (AFS8-110). The height profile of not inclined NW is presented in (b) curve 5.

The effect of well-defined elongated crystallites observed in this study is a typical consequence of Au-assisted growth contribution. Moreover, the fabricated inclined wires are expected to be of the same phase of iron silicide as not inclined due to the shape anisotropy and lateral sizes. Such insights into the fundamental mechanisms of crystal formation and growth have significant implications for materials science and nanotechnology, where the development of novel and highly tunable materials for applications in microelectronics.

The average values of area and height with standard errors of the mean (s), calculated as explained in Ch. 3.2.1, of $FeSi_2$ crystallites prepared on *p*-Si(110) according to fabrication procedures described in Ch. 3.1, are summarized in Table 2.3.

Table 2.3. *Summary of the average area and the average height on prepared $FeSi_2$ crystallites on p-Si(110) using Au-assisted (AF) and Au-free (F) Fe deposition, Au-assisted (AFS) and Au-free (FS) Fe/Si co-deposition at of 740 and 840 °C substrate temperatures.*

	Average area $\bar{A}$, 10^3 nm^2		Average height $\bar{H}$, nm	
T	**740 °C**	**840 °C**	**740 °C**	**840 °C**
AF-110	500 ± 16	2988 ± 262	115 ± 8	132 ± 3
F-110	257 ± 22	863 ± 90	31 ± 4	61 ± 10
AFS-110	161 ± 2	455 ± 14	40 ± 4	63 ± 9
FS-110	49 ± 1	59 ± 1	22 ± 2	39 ± 5

Summary

A thorough examination of the morphology of the $FeSi_2$ crystallites fabricated on Si(110) substrates provides information about their forms, orientations, and dimensions, considering the impact of Au-assisted growth, temperature change, and Fe/Si atomic flux ratio.

Conclusions can be obtained as follows:

- *Growth on Si(110) substrate results in the formation of elongated crystallites growing along the Si[-110] direction for all prepared samples of crystallites.*
- *Au-assisted growth induces the formation of well-defined wire-shaped geometries of $FeSi_2$ crystallites on Si(110) during Fe deposition and Fe/Si co-deposition (Fig. 3.9).*
- *Au-free conditions result in the formation of crystallites exhibiting coalescence and forming continuous films without well-defined morphologies.*
- *Change in Fe/Si atomic flux ratio (Fe/Si co-deposition) results in a reduction of the wire-shaped crystallite size due to decreasing Fe atoms diffusion length and due to the influence of deposited Si atoms acting together with Si atoms from the substrate to formation of multiple nucleation sites, which leads to limited availability of Fe atoms followed by restricted growth of individual silicide crystallites following with decreased crystallite area and height.*

Thus, the introduction of Au-assisted growth strongly indicates the important role Au atoms play in the formation of $FeSi_2$ crystals on Si(110) substrates, facilitating the growth of well-defined wire-shaped crystallites with flat surfaces, which can be attributed to the formation of α-$FeSi_2$(001) crystal plane parallel to Si substrate surface.

3.2.3 $FeSi_2$ on Si(111)

The SEM images of $FeSi_2$ crystallites prepared on Si(111) substrate are presented in Fig. 3.13. Crystallite growth occurs along the three equivalent Si<110> crystallographic directions of the Si(111) substrate, exhibiting 3-fold symmetry of prepared crystallites. These directions are rotated at 54.7 degrees to the surface normal of the substrate. Crystallites obtained using Au-assisted growth (Fig. 3.13 (a, b)) at 740°C (AF7-111 sample) demonstrates the aspect ratio distribution wider (up to 10) in comparison with those obtained without at 840°C (AF8-111) due to the existence of coalesced rod-shape crystallites, which are not presented in the AF8-110 sample produced at 840°C (Fig. 3.13 (c)). Here, there is an evident effect of substrate temperature influence on the crystallite morphology. This way, the crystallites produced at 740°C are slightly coalesced and, due to that, are larger with the average area $\bar{A}$ of ~$891 \cdot 10^3$ nm^2, while those produced at 840°C have easily distinguished shapes (Fig. 3.16) and are separated on the substrate surface and have $\bar{A}$ ~ $307 \cdot 10^3$ nm^2. Also, as in the previous cases of $FeSi_2$ crystallites obtained on Si(001) and Si(110) substrates, Au-assisted growth exhibits flat facets of the obtained crystallites. In contrast, $FeSi_2$ crystallites obtained using Au-free conditions do not demonstrate high faceting and tend to form continuous films due to coalescence processes occurring during temperature changes, as observed in samples F7-111 and F8-111 (Fig. 3.13 (e, f)). At higher temperatures (840°C), due to the increased diffusion length of Fe atoms, the resulting crystals are larger (Fig. 3.13 (h)) and have $\bar{A}$ ~ $350 \cdot 10^3$ nm^2, while those obtained at 740°C have $\bar{A}$ ~ $138 \cdot 10^3$ nm^2. The aspect ratio distribution of obtained crystallites in samples F7-111 and F8-111 is ~1-4, which shows that the crystals are slightly elongated (Fig. 3.13 (g)). The crystallites obtained during Fe/Si co-deposition on the Si(111) surface (Fig. 3.14) demonstrate a decrease in the size (Fig. 3.14 (d, h)) in comparison to the crystallites obtained without Si deposition (Fig. 3.13). Thus, it was observed that the crystallite size decreased from submicron- to nanoscale. Furthermore, crystallites obtained during Au-free Fe/Si co-deposition (FS7-111 and FS8-110) do not tend to form continuous films. In this manner, the crystallite area distribution of the FS7-111 sample has the average value $\bar{A}$ ~ $16 \cdot 10^3$ nm^2. In the case of the FS8-110 sample, the area distribution has two main peaks, one of which is comparable to the area distribution of the FS7-110 sample, which means that the FS8-110 sample has two fractions of nanocrystals.

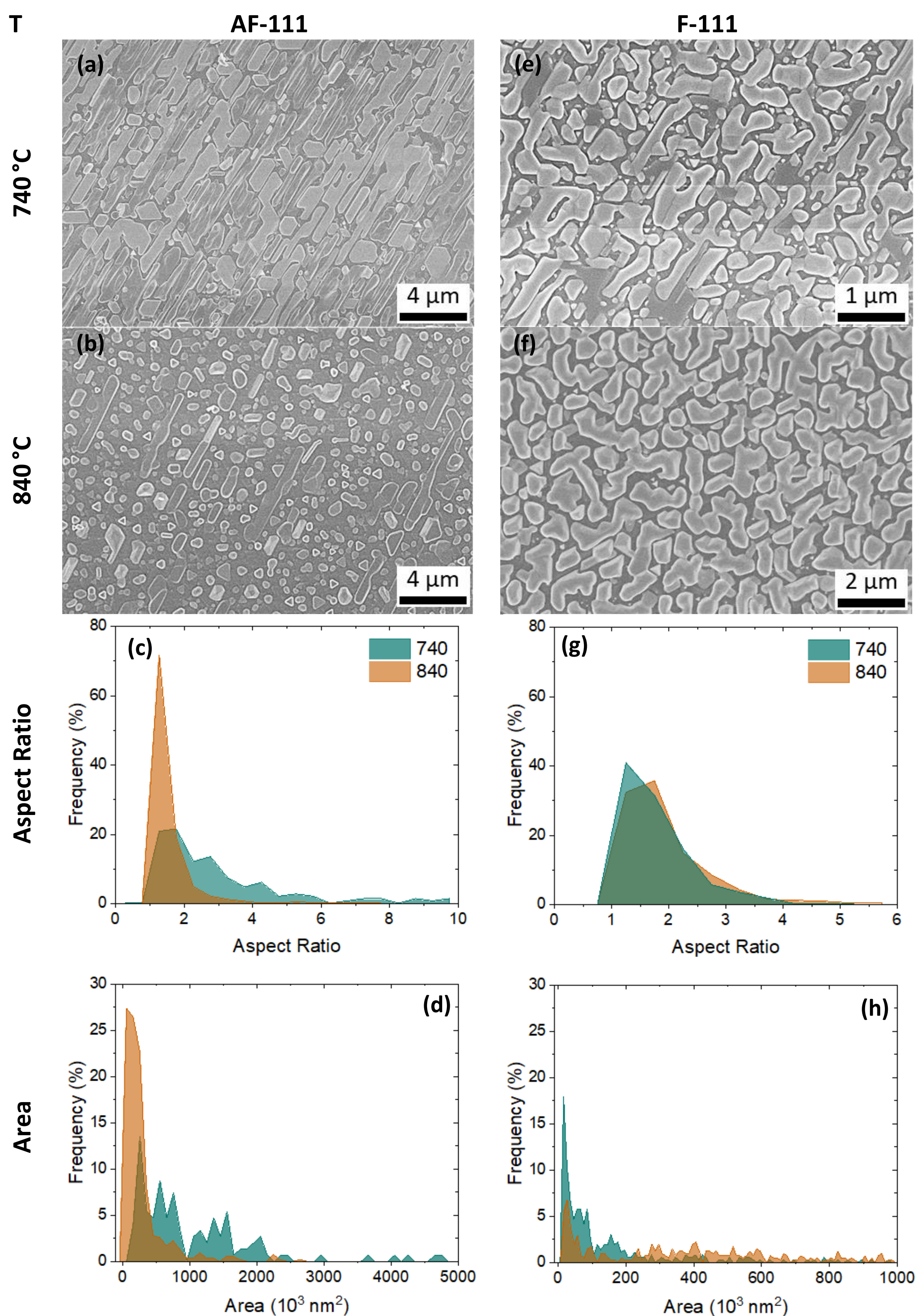

Figure 3.13. SEM-images of the $FeSi_2$ submicron crystals prepared on Si(111) substrates using (a-d) Au-assisted Fe deposition at (a) 740 °C (AF7-111) and (b) 840 °C (AF8-111) substrate temperature with the comparison of their (c) aspect ratio and (d) area distributions, and (e-h) Au-free Fe deposition at (e) 740 °C (F7-111) and (f) 840 °C (F8-111) substrate temperature with the comparison of their (g) aspect ratio and (h) area distributions.

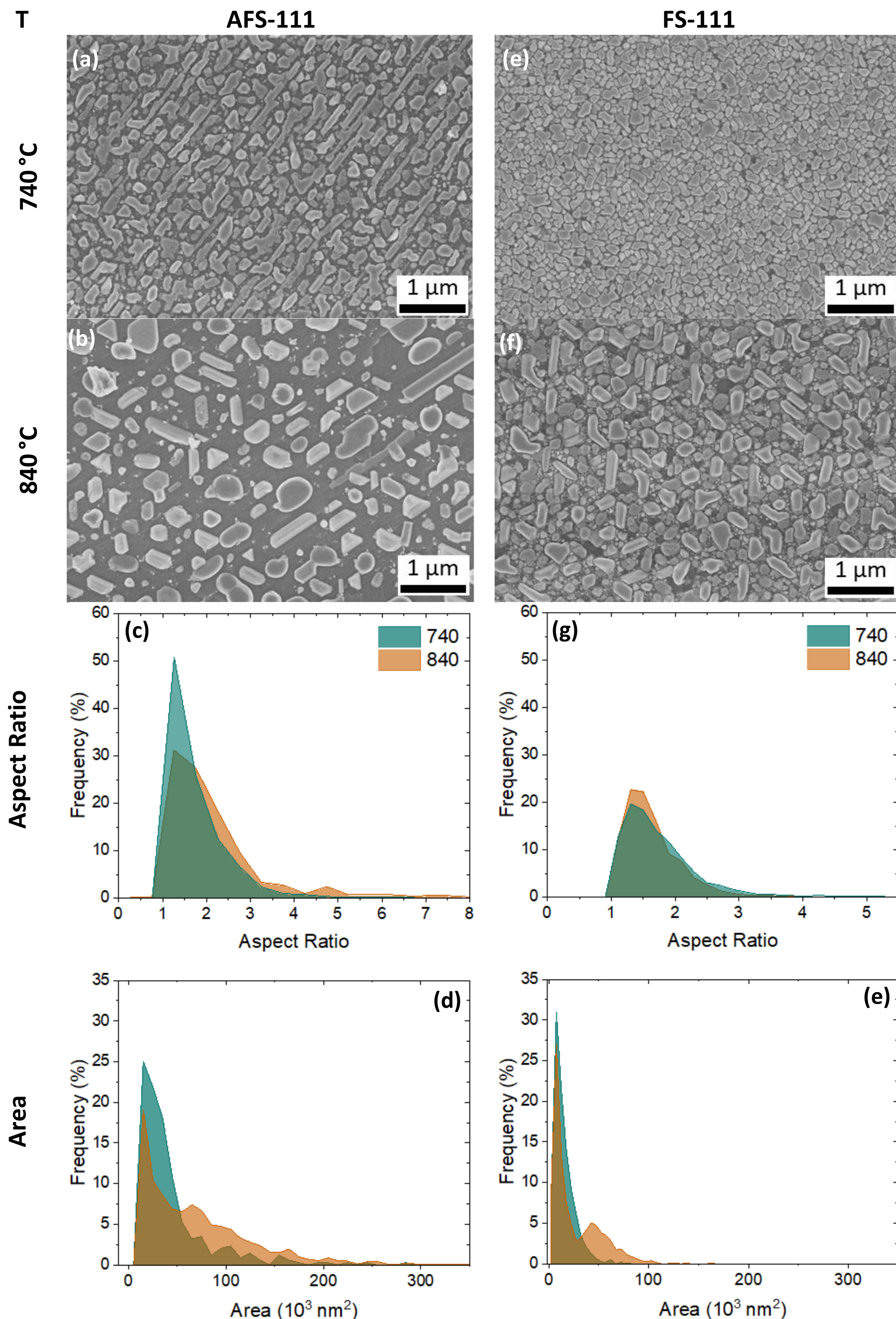

Figure 3.14. SEM-images of the $FeSi_2$ submicron crystals prepared on Si(111) substrates using (a-d) Au-assisted Fe/Si co-deposition at (a) 740 °C (AFS7-111) and (b) 840 °C (AFS8-111) substrate temperature with the comparison of their (c) aspect ratio and (d) area distributions, and (e-h) Au-free Fe/Si co-deposition at (e) 740 °C (FS7-111) and (f) 840 °C (FS8-111) substrate temperature with the comparison of their (g) aspect ratio and (h) area distributions.

This effect was caused by higher substrate temperature promoting the increase of diffusion length of Fe atoms. Thus, the second fraction of larger crystallites is formed and has $\bar{A} \sim 41 \cdot 10^3$ nm^2, while of the rest of crystallites $\bar{A} \sim 26 \cdot 10^3$ nm^2. Also, the temperature influence occurs in the case of crystallites obtained using Au-assisted growth (AFS7-111 and AFS8-111 samples) (Fig. 3.14 (a, b)). Thus, the area distribution of the AFS7-111 sample has one main peak demonstrating the average area $\bar{A} \sim 43 \cdot 10^3$ nm^2, while the area distribution of the AFS8-111 sample is more scattered with $\bar{A} \sim 72 \cdot 10^3$ nm^2. The aspect ratio distributions of nanocrystals obtained with and without Au are similar and are in the range of 1-3, indicating the similarity of crystallite shapes. Thus, the increase of substrate temperature influences the area of fabricated nanocrystals, maintaining their aspect ratio (Fig. 3.14 (c, g)).

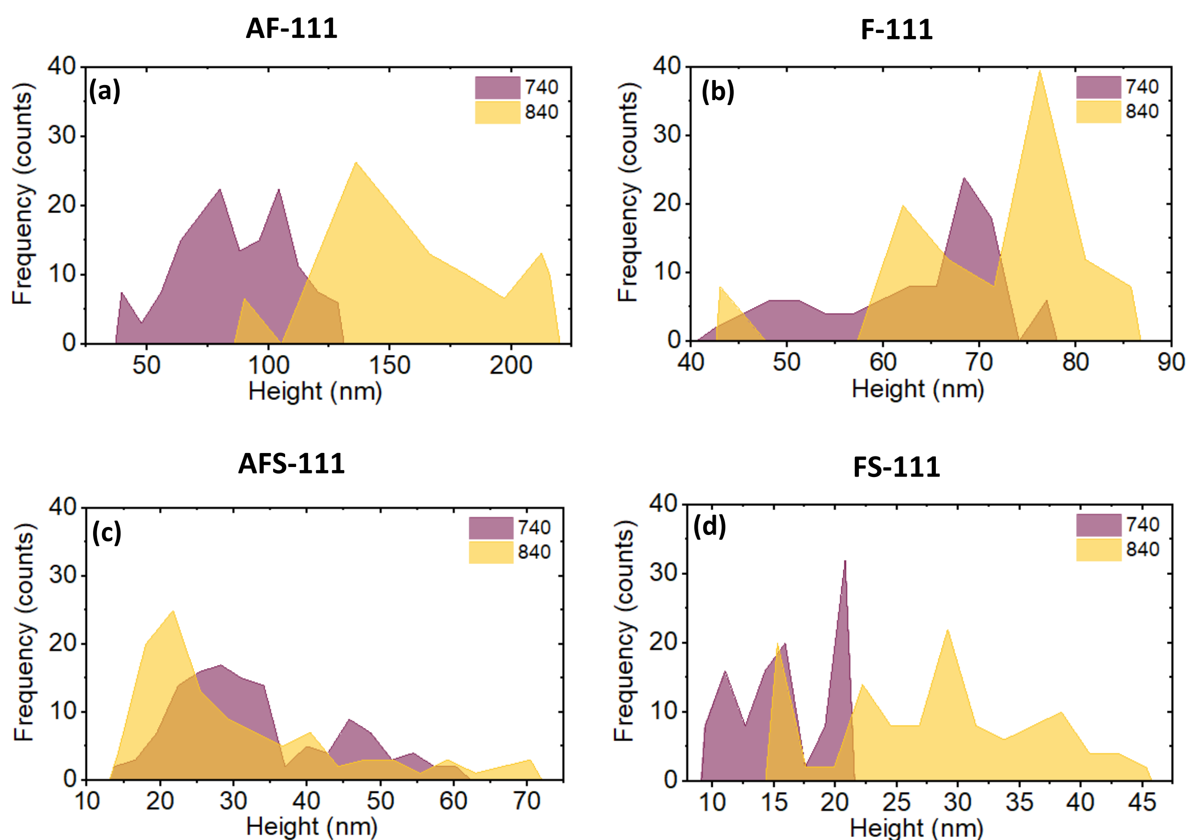

Figure 3.15. Height distributions of the $FeSi_2$ submicron crystals prepared on Si(111) substrates using (a) Au-assisted (AF7-111 and AF8-111) and (b) Au-free (F7-111 and F8-111) Fe deposition, and using (c) Au-assisted (AFS7-111 and AFS8-111) and (d) Au-free (FS7-111 and FS8-111) Fe/Si co-deposition at 740 °C and 840 °C substrate temperatures.

The average height ($\bar{H}$) of prepared $FeSi_2$ crystallites on Si(111) substrate was analyzed by AFM (Fig. 3.15) additionally. Substrate temperature influence results in the change in the average height of the crystallites obtained at 840°C of sample AF8-111, which are ~1.5 times higher with $\bar{H} \sim 157$ nm than those obtained at 740°C (AF7-111) with $\bar{H} \sim 84$ nm (Fig. 3.15 (a)).

This occurs due to the influence of Au-assisted growth at a high temperature, which exhibits the formation of faceted crystallites, increasing their surface energy and capturing incoming atoms, and increasing of Fe atoms' diffusion length. Hence, the crystallites are higher and have formed recognizable shapes at high substrate temperatures. In the case of crystallites obtained using Au-free conditions, an increase in the average height with increased substrate temperature is also observed due to the increased diffusion length of Fe atoms (Fig. 3.15 (b)). Thus, the crystallites of the F8-111 sample are approximately ~1.1 times higher with $\bar{H}$ ~ 64 nm than those of the F7-111 sample with $\bar{H}$ ~ 60 nm.

Regarding the case of Fe/Si co-deposition, the height distributions of crystallites of samples AFS7-110 and AFS8-110 obtained using Au-assisted growth are comparable, and both demonstrate the clear existence of two crystallite fractions, one of which is higher than another one (Fig. 3.15 (c)). Thus, for sample AFS7-111, the average height of one fraction $\bar{H}$ ~ 25 nm is preferable in these samples and of another fraction $\bar{H}$ ~ 45 nm. This case illustrates all three synthesis parameters: Au-assisted growth, Fe/Si co-deposition and substrate temperature influence. In that way, the formation of the second fraction of crystallites with increased lateral sizes was observed due to the change of the substrate temperature using Au-assisted Fe/Si co-deposition. In the case of crystallites obtained using Au-free conditions, the increase in height is also observed with the increase in substrate temperature. This way, the crystallites of the FS8-111 sample are ~2 times higher with $\bar{H}$ ~ 30 nm than those of the FS7-111 sample with $\bar{H}$ ~ 15 nm. The sample FS7-111 also demonstrates the presence of two fractions of crystallites with different heights of 10-15 nm and 20 nm.

Concerning the influence of Au-assisted growth on the height of obtained crystallites, it can be concluded that the average height of crystallites obtained without Au is ~2 times lower than those obtained using Au-free growth. The co-deposition of Fe/Si also influences the height of the resultant crystallites, which can be attributed to the higher concentration of Si atoms on the surface, causing a limited availability of Fe atoms and consequently leading to a reduction in the lateral size of the self-assembled $FeSi_2$ crystallites on Si(111) substrate.

The average values of area and height with standard error of the mean (SEM), calculated as explained in section 3.2.1, of $FeSi_2$ crystallites prepared on *p*-Si(111) according to fabrication procedures described in Ch. 3.1 are summarized in Table 3.4.

Table 3.4. *Summary of the average area and the average height on prepared $FeSi_2$ crystallites on p-Si(111) using Au-assisted (AF) and Au-free (F) Fe deposition, and Au-assisted (AFS) and Au-free (FS) Fe/Si co-deposition at of 740 and 840 °C substrate temperatures.*

	Average area $\bar{A}$, 10^3 nm^2		**Average height $\bar{H}$, nm**	
T	**740 °C**	**840 °C**	**740 °C**	**840 °C**
AF-111	891 ± 27	307 ± 21	84 ± 9	157 ± 15
F-111	138 ± 8	350 ± 10	60 ± 3	64 ± 4
AFS-111	43 ± 1	72 ± 1	37 ± 4	42 ± 5
FS-111	15 ± 1	26 ± 1	15 ± 2	30 ± 3

According to our observations, the crystallites obtained in the samples AF8-111 and AFS8-111 display distinctive shapes, influenced by substrate temperature and Au-assisted growth. A comprehensive understanding of these shapes and their facets can provide valuable insights into these crystals' properties and potential applications.

Thus, various submicron crystal shapes (marked with different colors) can be identified from Fig. 3.16 in the samples AF8-111 and AFS8-111:

- *triangular nanoplates* (red triangles), presented on both samples, have lateral sizes of 350-500 nm for the AF8-111 sample and ~150-200 nm for the AFS8-111 sample and are mostly exhibiting 2-fold symmetry and flat surfaces, which can be attributed to the formation of α-$FeSi_2$(001) crystal plane parallel to Si(111) substrate surface.
- *trapezium nanoplates* (purple trapeziums), presented on both samples and displaying 3-fold symmetry, with trapezium base of ~750 nm for the AF8-111 sample and ~400 nm for the AFS8-111 sample.
- *hexagon nanoplates* (orange hexagons), presented on both samples, with irregular geometry and large lateral dimensions of ~340 nm and ~570 nm for the AF8-111 and AFS8-111 samples, respectively.
- *bars* (yellow lines), presented in both samples, preferentially nucleated and grown along the Si[110] direction with a length of 1.5-4 µm and width of 300-600 nm for the AF8-111 sample and lying along <010>, <011> and <101> directions with the length of 400-800 nm and the width of 150-350 nm for the AFS8-111 sample due to the orientation of the Si substrate.
- *triangular prisms with beveled corners* (blue trapeziums), formed in both samples, with a length of ~1.5 µm and width of ~530 nm for the AF8-111 sample and a length of ~520 nm and a width of ~230 nm for the AFS8-111 sample.

- *irregular trapezoids* (pink trapeziums), presented only on the AFS8-111 sample, with the average trapezium base length of ~400 nm and the average base height of the trapezoids of ~210 nm.
- *rectangular nanoplates* (blue rectangles), presented only on the AFS8-111 sample, with a length of about 300-500 nm.

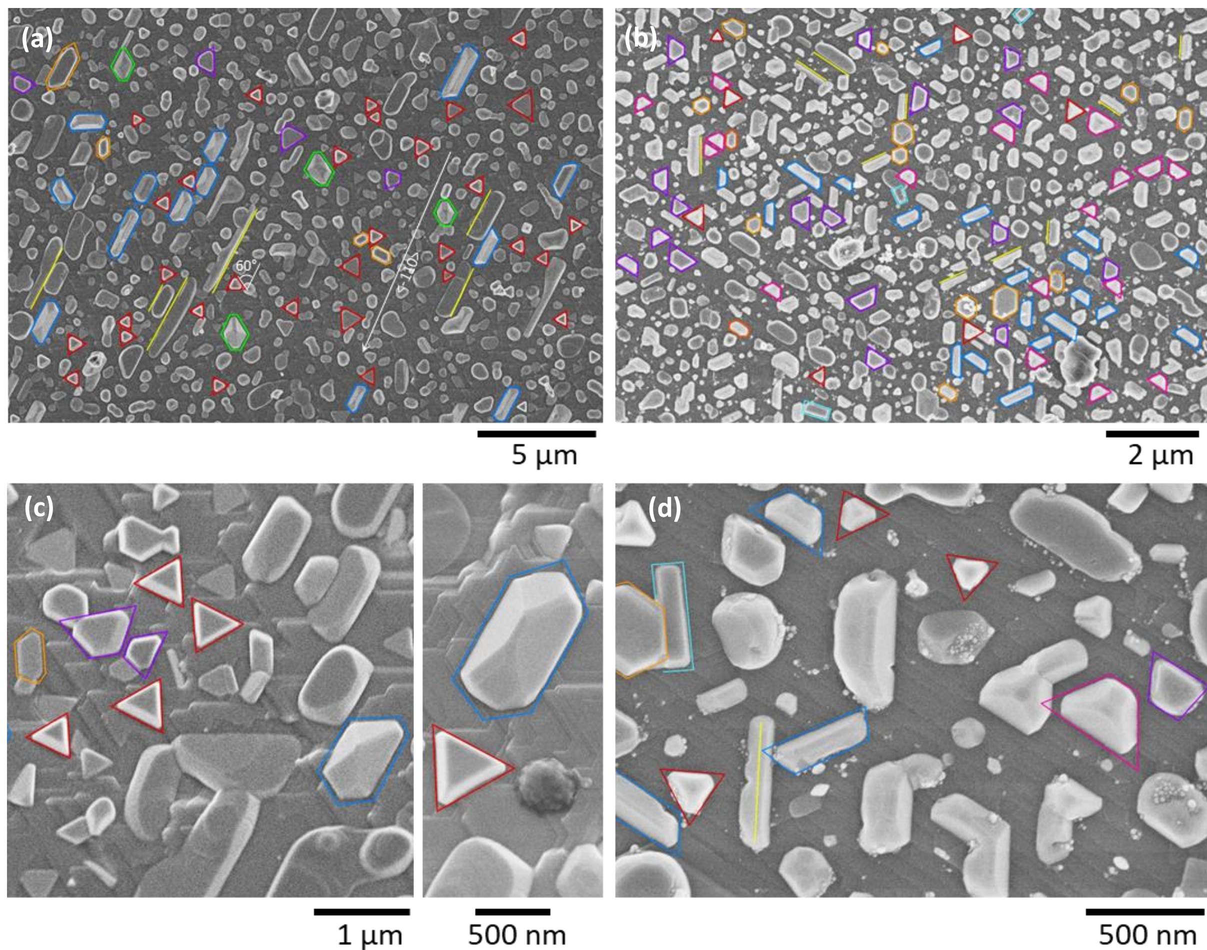

Figure 3.16. SEM-images of $FeSi_2$ crystallites of samples (a, c) AF8-111 and (b, d) AFS8-111.

The growth of the crystallites occurs along the <010>, <011> and <101> directions of Si(111) substrate. This way, the *triangular nanoplates*, the same way as the upper base of *trapezium nanoplates*, the large lateral sizes of *hexagon nanoplates*, *triangular prisms with beveled corners* and *rectangular nanoplates* are lying towards three equivalent <110> crystallographic directions. Au-assisted growth is crucial role here since the described crystal shapes are absent on the F and FS series. Thus, it can be inferred that Au-assisted growth on the silicon surface leads to the emergence of distinct forms of $FeSi_2$ silicide nano- and submicron crystals.

Summary

This description of the $FeSi_2$ crystallites prepared on Si(111) substrate morphology provides important insights into their shapes, orientations, and sizes influenced by Au-assisted growth, temperature change, and Fe/Si atomic flux ratio.

Conclusions can be obtained as follows:

- *Au-assisted growth of $FeSi_2$ crystallites on Si(111) surface leads to the formation of well-defined crystal facets with distinct crystal geometries during reactive epitaxy of Fe and Fe/Si co-deposition (Fig. 3.16).*
- *Au-free conditions result in the formation of crystallites displaying coalescence and a tendency to form continuous films without well-defined morphologies.*
- *Change in Fe/Si atomic flux ratio results in a decrease of the crystallite size due to reduced Fe atoms diffusion length and a formation of multiple nucleation sites from the combination of deposited Si atoms and Si atoms from the substrate. Consequently, the change of the atomic Fe/Si flux ratio leads to limited availability of Fe atoms and limited growth of individual silicide crystallites.*

Overall, the Au-assisted growth strongly influences the formation of $FeSi_2$ crystals, promoting the growth of clear and unique crystal shapes with flat surfaces and can be referred to as the formation of α-$FeSi_2$(001) crystal plane parallel to the Si(111) substrate surface.

3.3 Structure of fabricated $FeSi_2$ crystallites

Structure and orientation relationships of prepared α-, β-$FeSi_2$ crystallites on *p*-Si(001), *p*-Si(110) and *p*-Si(111) substrates (as explained in detail in Ch. 3.1) were studied by *ex-situ* X-ray diffraction (XRD) analysis in Bragg-Brentano geometry and by analysis of XRD pole figures. Electron backscatter diffraction (EBSD) confirmed orientation relationships defined from XRD pole figures.

Analysis of $FeSi_2$/Si orientation relationships

If $FeSi_2$ is epitaxially aligned to Si, it means that their crystallographic relationship, also known as the orientation relationship (OR), exhibits orientation of specific planes (marked with *hkl* Miller indices) and atomic rows at the interface (marked with *uvw* Miller-Bravais indices) [274]. This alignment of planes and atomic rows, representing specific crystallographic directions within a crystal lattice, is important for the epitaxial growth and the interface quality of α-$FeSi_2$/Si heterostructure. It ensures a coherent and ordered interface with minimal lattice mismatch and structural defects and determines this epitaxial system's structural integrity and electronic properties.

The Near-Coincidence Sites (NCS) method [275] can be used to assess whether it is possible to match two phases with a high-quality interface (preferable OR) and represents the value R of an NCS density, as it was shown for α-, β-$FeSi_2$‖Si phases in [159]:

$$R = \frac{1}{2}\left(\frac{m_1}{N_1} + \frac{m_2}{N_2}\right), \tag{3.2}$$

where N_1 and N_2 – is the total number of atoms in phases 1 and 2 at the interface; m_1 and m_2 are the number of sites in the phase with coincidences in the opposite phase. This approach predicted preferrable ORs for α-, β-$FeSi_2$‖Si phases (Table 3.5) [159,271]. The values of the NCS density R here play a decisive role in determining the preferable OR between the two phases. Some of the predicted ORs were reported earlier. For example, the α-$FeSi_2$(112)[021]‖Si(111)[110] OR demonstrating R = 0.9, which is the maximum value among predicted for ORs of α-, β-$FeSi_2$‖Si phases, and the α-$FeSi_2$(112)[220]‖Si(111)[110] OR with R = 0.75 were reported in [276] based on high-resolution transmission electron microscopy investigations.

Table 3.5. *Preferable orientation relationships between silicon and iron disilicide phases (*α-, β-$FeSi_2$‖Si*) and the NCS density R per interface (reproduced from [159,271]).*

Planes forming interface (hkl)‖(hkl)	**Atomic rows at the interface** [uvw]‖[uvw]	R
	α-$FeSi_2$‖Si	
α-$FeSi_2$(112)‖Si(111)	α-$FeSi_2$[0-21]‖Si[1-10]	0.90
α-$FeSi_2$(214)‖Si(113)	α-$FeSi_2$[-201]‖Si[1-10]	0.79
α-$FeSi_2$(111)‖Si(113)	α-$FeSi_2$[2-20]‖Si[1-10]	0.76
α-$FeSi_2$(001)‖Si(001)	α-$FeSi_2$[2-20]‖Si[1-10]	0.75
α-$FeSi_2$(112)‖Si(111)	α-$FeSi_2$[2-20]‖Si[1-10]	0.75
α-$FeSi_2$(100)‖Si(001)	α-$FeSi_2$[02-1]‖Si[1-10]	0.75
α-$FeSi_2$(112)‖Si(110)	α-$FeSi_2$[2-20]‖Si[1-10]	0.50
	β-$FeSi_2$‖Si	
β-$FeSi_2$(101)‖Si(111)	β-$FeSi_2$[0-10]‖Si[1-10]	0.75
β-$FeSi_2$(110)‖Si(111)	β-$FeSi_2$[00-1]‖Si[1-10]	0.75
β-$FeSi_2$(100)‖Si(001)	β-$FeSi_2$[010]‖Si[110]	0.70
β-$FeSi_2$(310)‖Si(113)	β-$FeSi_2$[00-1]‖Si[1-10]	0.57
β-$FeSi_2$(111)‖Si(210)	β-$FeSi_2$[01-1]‖Si[002]	0.54
β-$FeSi_2$(510)‖Si(115)	β-$FeSi_2$[001]‖Si[1-10]	0.51
β-$FeSi_2$(001)‖Si(110)	β-$FeSi_2$[010]‖Si[1-10]	0.48

Epitaxially grown α-$FeSi_2$ phase on Si(001) by MBE or CVD [46,160] reveals the α-$FeSi_2$(001)[220]‖Si(001)[110] OR with R = 0.75. Furthermore, a wealth of experimental studies has demonstrated that α-$FeSi_2$ exhibits a higher tendency to generate free-standing nanocrystals, which are partially embedded into a Si substrate [46,150,160,195], which also corresponds to the data presented in the previous section (Ch. 3.2).

In addition, in the case of β-$FeSi_2$, maximum values of R are found to be for Si(111) and Si(001) planes (Table 3.5). Thus, the β-$FeSi_2$(101)β[010]‖Si(111)Si[110] OR demonstrating R = 0.75 and the β-$FeSi_2$(110)β[010]‖Si(111)Si[110] OR with much lower R = 0.48, calculated by presented approach, were earlier reported in [122,147,170,277,278].

Thus, predicted ORs are expected to be formed during the growth of α-, β-$FeSi_2$ crystallites by reactive epitaxy of Fe and Fe/Si co-deposition under ultrahigh vacuum conditions using Au-assisted growth and substrate temperature change on *p*-Si(001), *p*-Si(110) and *p*-Si(111) substrates (as explained in detail in Ch. 3.1). In this study we explore basic orientations of prepared α-, β-$FeSi_2$ crystallites concerning Si(001), Si(110) and Si(111) crystallographic planes.

3.3.1 $FeSi_2$ on Si(001)

Unlocked *ex-situ* X-ray diffraction (XRD) scans of $FeSi_2$ crystallites prepared on Si(001) substrates with a miscut close to 0.1° using conditions described in Ch. 3.1 are presented in Figure 3.17 (a). Thus, samples obtained at the substrate temperature of 840°C demonstrate the presence of the α-$FeSi_2$ phase with four basic orientations: 001, 111, 110 and 211, except the F8-001 sample, which is almost mono-oriented with α-$FeSi_2$(111)//Si(001). At the same time, the samples obtained at the substrate temperature of 740°C demonstrate the formation of β-$FeSi_2$ crystallites with basic orientation β-$FeSi_2$(220)//Si(001).

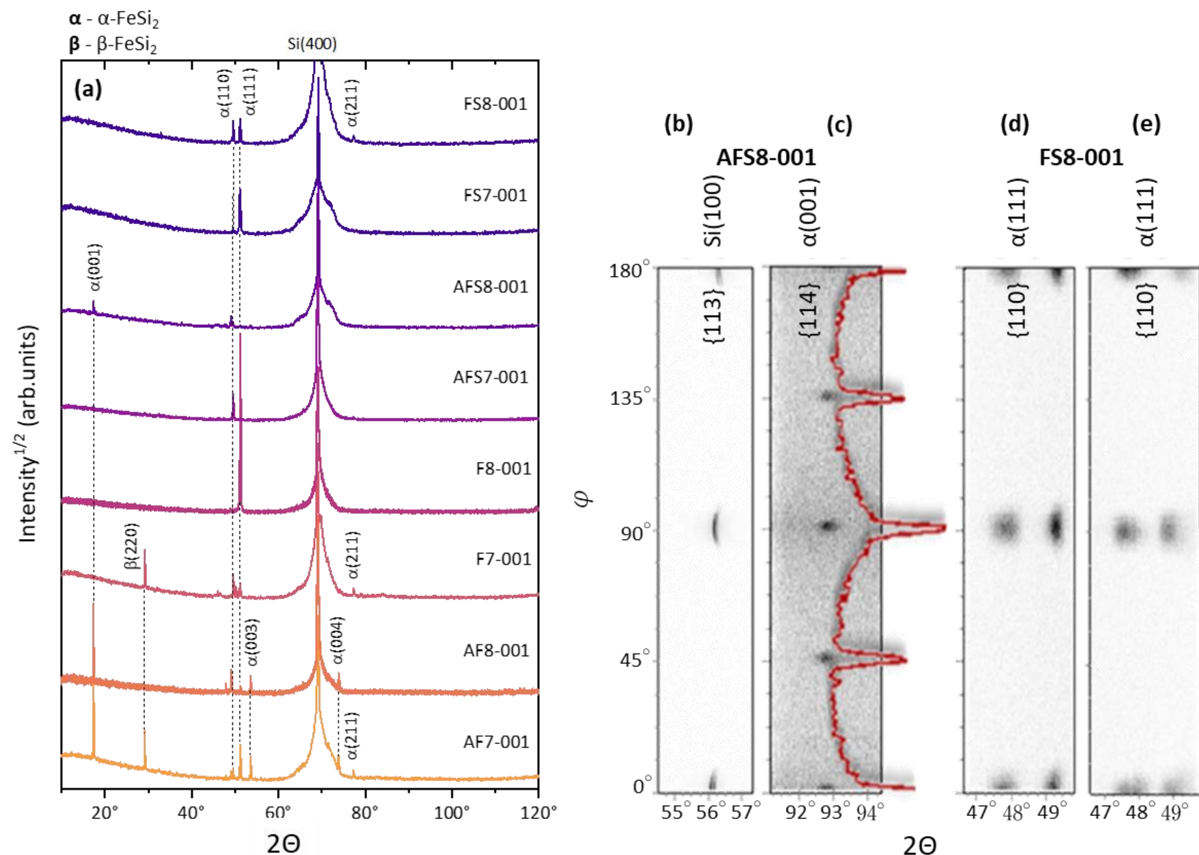

Figure 3.17. (a) XRD unlocked scans of the $FeSi_2$ crystallites prepared on Si(001) using Au-assisted (AF) and Au-free (F) Fe deposition, and Au-assisted (AFS) and Au-free (FS) Fe/Si co-deposition at substrate temperatures of 740 (7) and 840 (8) °C (plane indices are marked); images of φ-scans of sample AFS8-001 for (b) {113} reflections from Si(100) substrate, (c) {114} reflections of α-$FeSi_2$(001)//Si(100), (d) {110} reflections of α-$FeSi_2$(111)//Si(100) and (e) {110} reflections of α-$FeSi_2$(111)//Si(100) for FS8-001 sample.

The φ-scans of reflections {110} of sample AFS8-001 (Fig. 3.17 (b)) disclosed an additional orientation of α-$FeSi_2$ with the {102} planes offset by ~20.5° around the [010] (and [-110]) zone axis of the Si(001) substrate. Furthermore, the {102} planes of this additional orientation

α-$FeSi_2$(102)/20.5°/Si(001)[110] appear approximately parallel to the {110} planes of crystallites with the α-$FeSi_2$(111)//Si(100) orientation [273].

XRD pole figures of the samples F8-001 and AF8-001 were recorded for α-$FeSi_2$(001) at 2Θ ~ 17° and α-$FeSi_2$(102), β-$FeSi_2$(422) at 2Θ ~ 50° (Ch. 2.2.2) and presented in Fig. 3.18 as a function of signal intensity in logarithmic scale. Au-free growth resulted in the formation of the α-$FeSi_2$(111)[-110]//Si(001)[110] OR, observed in the unlocked scan as high-intensity peak (Fig. 3.17 (a)), and shown in Fig. 3.18 (a) as weak reflections (white dashed circles).

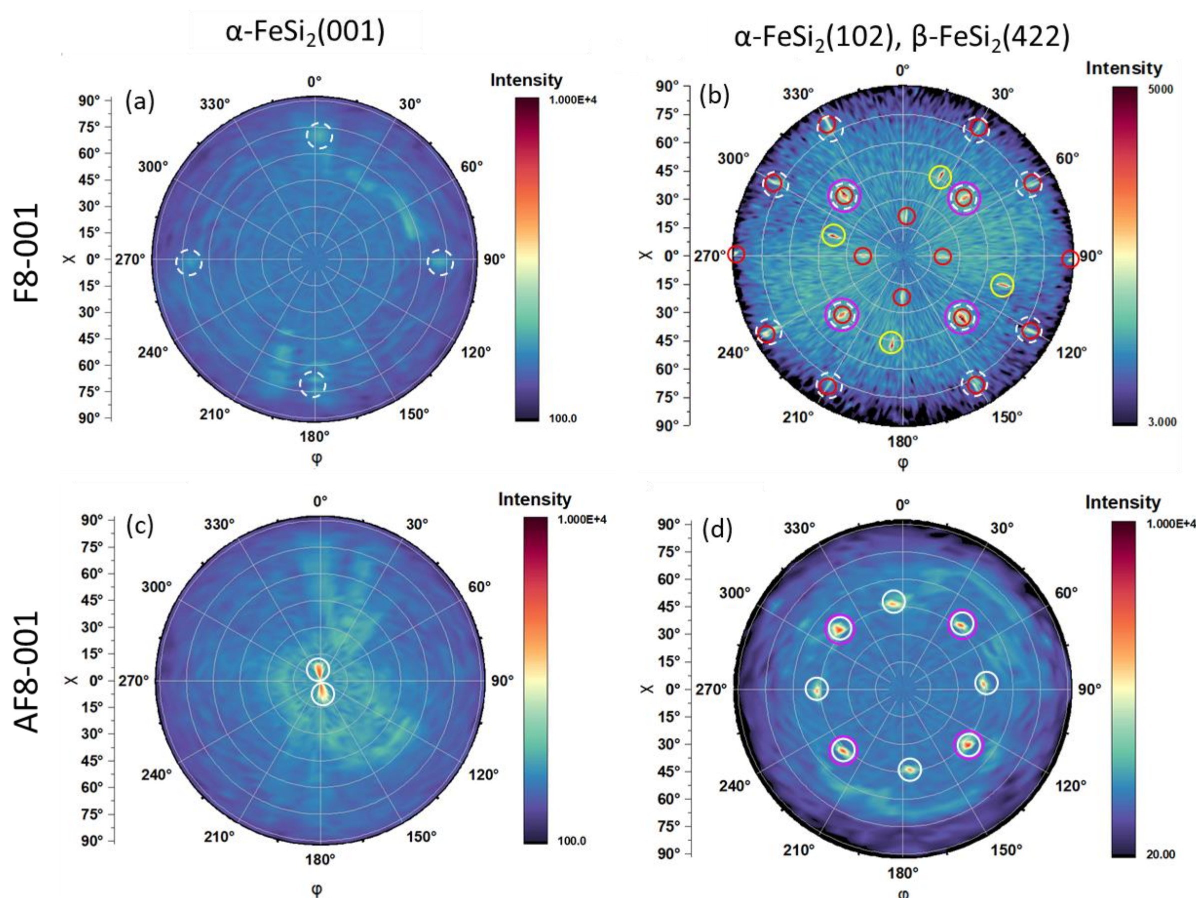

Figure 3.18. Pole figures for α-$FeSi_2$(001), α-$FeSi_2$(102) and β-$FeSi_2$(422) planes of the $FeSi_2$ crystallites prepared on Si(001) substrate (840°C) using (a, b) Au-free Fe deposition (F8-001), and (c, d) Au-assisted Fe deposition (AF8-001). Here solid white lines correspond to reflections of α-$FeSi_2$(001)[110]//Si(001)[110] and α-$FeSi_2$(001)[110]//Si(001)[100] ORs, 45 degrees azimuthal rotated in relation to previous, dashed white lines to the α-$FeSi_2$(111)[-110]// Si(001)[110] reflections, red lines to 4-fold symmetry of the β-$FeSi_2$(-2-64)[-111]//Si(1-11)[110] OR domain reflections, pink solid lines to Si(220) reflections and yellow lines correspond to reflections of the sample holder.

Furthermore, the pole figure for β-$FeSi_2$(422) plane (Fig. 3.18 (b)) demonstrates the presence of 4-fold symmetry of the β-$FeSi_2$(-2-64)[-111]//Si(1-11)[110] OR domain, which was also observed before in [279] for thin films prepared with magnetron-sputter epitaxy also at the

elevated temperatures (700°C). Reflections of the α-$FeSi_2$(111)[-110]//Si(001)[110] OR are partially overlapped with the β-$FeSi_2$(-2-64)[-111]//Si(1-11)[110] OR domain reflections (red circles). Si(220) reflections are highlighted with pink circles and are overlapped with α-$FeSi_2$(102) and β-$FeSi_2$(422) reflections at the tilting angle $\chi \sim 30°$. Yellow circles represent reflections from the sample holder.

Au-assisted growth results in formation of α-$FeSi_2$ phase with α-$FeSi_2$(001)[110]// Si(001)[110] OR and 45 degrees azimuthal rotated relative to the first one α-$FeSi_2$(001)[110]// Si(001)[100] OR for the AF8-001 sample (white circles), also presented in the unlocked scan (Fig. 3.17 (a)). Si(220) reflections are highlighted with pink circles and are overlapped with α-$FeSi_2$(102) reflections from the α-$FeSi_2$(001)[110]//Si(001)[100] OR.

To define the heteroepitaxial relationship of observed ORs on Si(001), the simulations of XRD pole figures were performed using PTCLab [257].

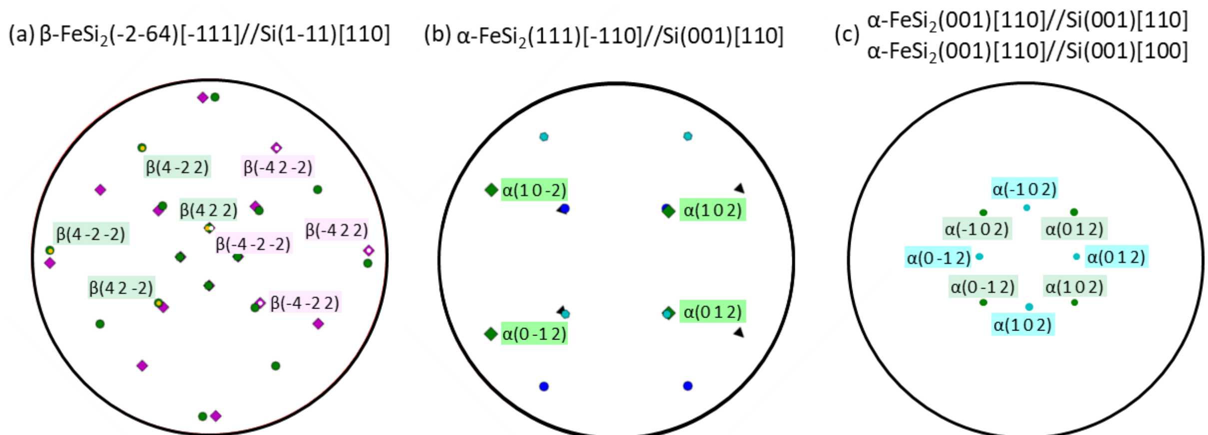

Figure 3.19. Simulation of XRD pole figures for α-$FeSi_2$(102) and β-$FeSi_2$(422) planes for (a) the β-$FeSi_2$(-2-64)[-111]//Si(1-11)[110] OR domain rotated (by steps of 90°) about its surface normal direction (yellow dotted green dots) and inversion (white dotted magenta squares) rotated (by steps of 90°) about its surface normal direction; (b) the α-$FeSi_2$(111)[-110]// Si(001)[110] OR domain rotated (by steps of 90°) about its surface normal direction; (c) the α-$FeSi_2$(001)[110]//Si(001)[110] OR (blue dots) and the α-$FeSi_2$(001)[110]//Si(001)[100] OR (green dots) reflections.

Thus, Fig. 3.19 presents the pole figures α-$FeSi_2$(102) and β-$FeSi_2$(422) crystallographic planes with the β-$FeSi_2$(-2-64)[-111]//Si(1-11)[110] OR, which represents the fitting of the diffraction peaks in pole figures of β-$FeSi_2$(422) planes for F8-001 sample, reached by the overlapping of the β-$FeSi_2$(-2-64)[-111]//Si(1-11)[110] domain followed with rotation (by steps of 90°) about its surface normal direction (yellow dotted green dots marked with *hkl* indexes) and its inversion (white dotted magenta squares marked with *hkl* indexes) also followed with rotation

(by steps of 90°) about its surface normal direction. The simulation of the pole figure for α-$FeSi_2$(102) and β-$FeSi_2$(422) planes of the α-$FeSi_2$(111)[-110]//Si(001)[110] OR for the F8-001 sample confirms, that 4-fold symmetry reflections of the α-$FeSi_2$(111)[-110]//Si(001)[110] domain are overlapped with the reflections of the 4-fold symmetry β-$FeSi_2$(-2-64)[-111]// Si(1-11)[110] OR. Fig. 3.19 (c) presents the simulation of the pole figure corresponding to the AF8-001 sample. In these reflections of α-$FeSi_2$(102) planes for the α-$FeSi_2$(001)[110]// Si(001)[110] OR (blue dots) and 45 degrees azimuthal rotated about the previous one, the α-$FeSi_2$(001)[110]//Si(001)[110] OR (green dots).

These symmetry operations correspond to the next ORs, precisely matching the measured XRD pole figures, including the peak-splitting in some of the reflections:

- 0° - β-$FeSi_2$(-2-64)[-111]//Si(1-11)[110],
- 90° - β-$FeSi_2$(-2-64)[1-1-1]//Si(111)[1-10],
- 180° - β-$FeSi_2$(26-4)[1-1-1]//Si(1-1-1)[110],
- 270° - β-$FeSi_2$(26-4)[-111]//Si(11-1)[1-10];
- α-$FeSi_2$(111)[-110]//Si(001)[110];
- α-$FeSi_2$(102)[100]//Si(001)[110];
- α-$FeSi_2$(001)[110]//Si(001)[110] and α-$FeSi_2$(001)[110]//Si(001)[110].

Overall, α- and β-$FeSi_2$ orientation relationships of the samples obtained on Si(001) substrate are revealed by the complex analysis of the unlocked XRD scans, φ-scans and pole figures of the samples prepared at 840°C substrate temperature.

One commonly used approach to estimate the relative OR fraction (%) involves integrating the raw peak data from XRD measurements and utilizing structure factors. This method provides a quantitative analysis that considers both the intensity of diffraction peaks and the crystallographic properties of the material. The structure factor $|F|$ is a complex number that quantifies the scattering properties of a crystallographic orientation. It incorporates information about the unit cell, atomic arrangement, and scattering amplitudes of the material. The structure factor is calculated using the crystallographic model and the known atomic positions [280,281]. The units of the structure factor for X-ray crystallography are multiples of the scattering unit by a single electron ($2.82 \cdot 10^{-15}$ m) [282]. Thus, to perform the integration of diffraction peaks from measured XRD pole figures, the intensity of these peaks

was plotted as a function of rotation angle φ for different tilting angles χ, as it is presented for the α-$FeSi_2$(001)[110]//Si(001)[110] OR in Figure 3.20 (a).

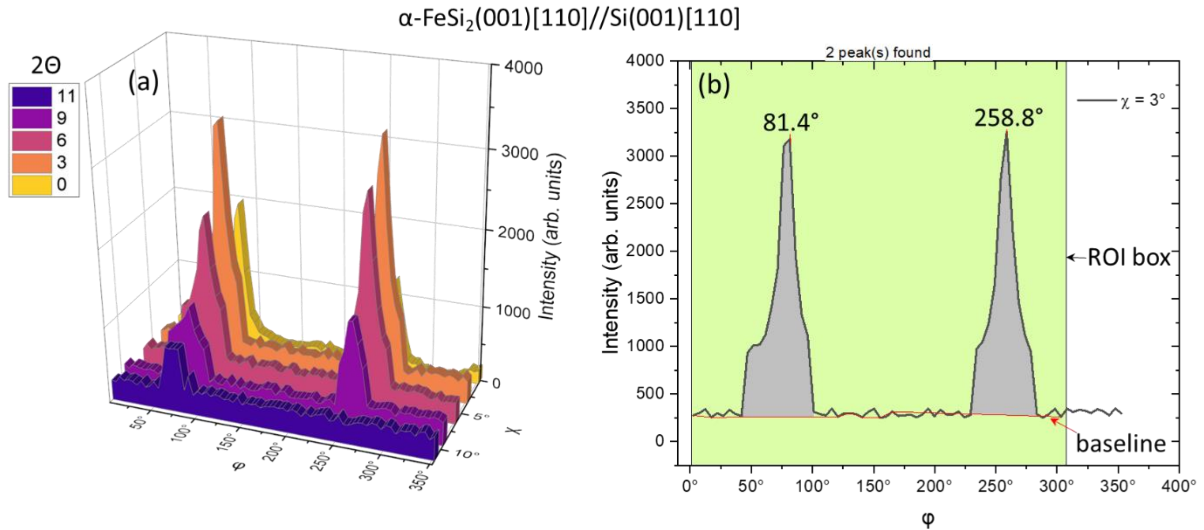

Figure 3.20. XRD pattern of the α-$FeSi_2$(001)[110]//Si(001)[110] OR plotted as a function of rotation angle φ (a) for different tilting angles χ and (b) for χ = 3° (black curve) as an example of integration of the raw peak data. The region of interest (ROI) is highlighted in green, while the baseline is marked in red. Recognized peaks are highlighted in grey, and their corresponding peak centers are also displayed.

Relative OR fraction Q_{OR} was calculated using the ratio of a peak area as a sum of the areas of the diffraction peaks S_{hkl} (as depicted in Fig. 3.20 (b)) normalized by the structural $|F|$ factor corresponding to the OR of interest (for example $\left|F_{\alpha-\mathrm{FeSi_2(001)}}\right|$ = 19.4726 × 2.82 · 10^{-15} m) to the sum of a peak area as a sum the areas of the diffraction peaks S_{hkl} normalized by the structural factor corresponding to estimated ORs in a sample.

$$Q_{OR} = \frac{S_{hkl}/|F_{hkl}|}{\sum_{n=1}^{m} S_{hkl_n}/\left|F_{hkl_n}\right|} \cdot 100\ \%, \quad (3.3)$$

where n corresponds to OR of the interest and m – to estimated ORs in a sample.

Orientation relationships of α-, β-$FeSi_2$ crystallites obtained on Si(001) substrate (840°C) using Au-free (F8-001) and Au-assisted (AF8-001) reactive deposition of Fe and also Au-free (FS8-001) and Au-assisted (AFS8-001) Fe/Si co-deposition determined from analysis of XRD pole figures and their relative orientation fractions (Q_{OR}) estimated by the presented approach are summarized in Table 3.6. For the α-$FeSi_2$(111)[-110]//Si(001)[110] OR the Q_{OR} value was determined by additional multiplying of eq. 3.3 on the counting time (for the unlocked scan - 29.845 s).

Table 3.6. *Summary of orientation relationships (OR) and relative OR fractions Q_{OR} of α-, β-$FeSi_2$ crystallites obtained on Si(001) substrate (840°C) using Au-free (F8-001) and Au-assisted (AF8-001) Fe deposition and also Au-free (FS8-001) and Au-assisted (AFS8-001) Fe/Si co-deposition.*

Sample	**F8-001**	**AF8-001**	**FS8-001**	**AFS8-001**
		Q_{OR}, %		
α-$FeSi_2$(001)[110]//Si(001)[110] α-$FeSi_2$(001)[110]//Si(001)[100]	-	99.9 ± 0.1	1.0 ± 0.1	69.0 ± 0.6
α-$FeSi_2$(111)[-110]//Si(001)[110]	69.0 ± 0.7	-	94.0 ± 0.6	25.0 ± 0.2
α-$FeSi_2$(102)[100]//Si(001)[110]	-	-	4.0 ± 0.2	5.0 ± 0.1
β-$FeSi_2$(-2-64)[-111]//Si(1-11)[110] β-$FeSi_2$(-2-64)[1-1-1]//SI(111)[1-10] β-$FeSi_2$(26-4)[1-1-1]//SI(1-1-1)[110] β-$FeSi_2$(26-4)[-111]//SI(11-1)[1-10]	31.0 ± 0.3	-	-	-

Summary

The analysis of the structure and orientation relationships of prepared α-, β-$FeSi_2$ crystallites on p-Si(001) highlights the influence of the α-$FeSi_2$ crystal growth conditions on their preferential orientation relationship. Therefore, Au-assisted growth results in the formation of preferential orientation relationships of α-$FeSi_2$(001)[110]//Si(001)[110] and 45 degrees azimuthally rotated α-$FeSi_2$(001)[110]//Si(001)[100], about the previous one, and leads to the formation of well-defined crystal facets with distinct crystallite shapes during Fe deposition and Fe/Si co-deposition for AF8-001 (99%) and AFS8-001 (69%) samples, correspondingly (Ch. 3.2.1, Fig. 3.6). During Au-free Fe/Si co-deposition (FS8-001) and Au-free Fe deposition (F8-001) the preferential α-$FeSi_2$(111)[-110]//Si(001)[110] orientation relationship is observed with relative fractions Q_{OR} of 94% and 69%, respectively.

3.3.2 $FeSi_2$ on Si(110)

In the context of the $FeSi_2$ crystallites obtained on Si(110) substrates with a miscut close to 1°-2°, XRD unlocked scans (see Fig. 3.21) demonstrate three basic orientations of α-$FeSi_2$ crystallites on the Si(110) substrate: 001, 101, and 211; and two orientations of β-$FeSi_2$ crystallites: 112 and 131.

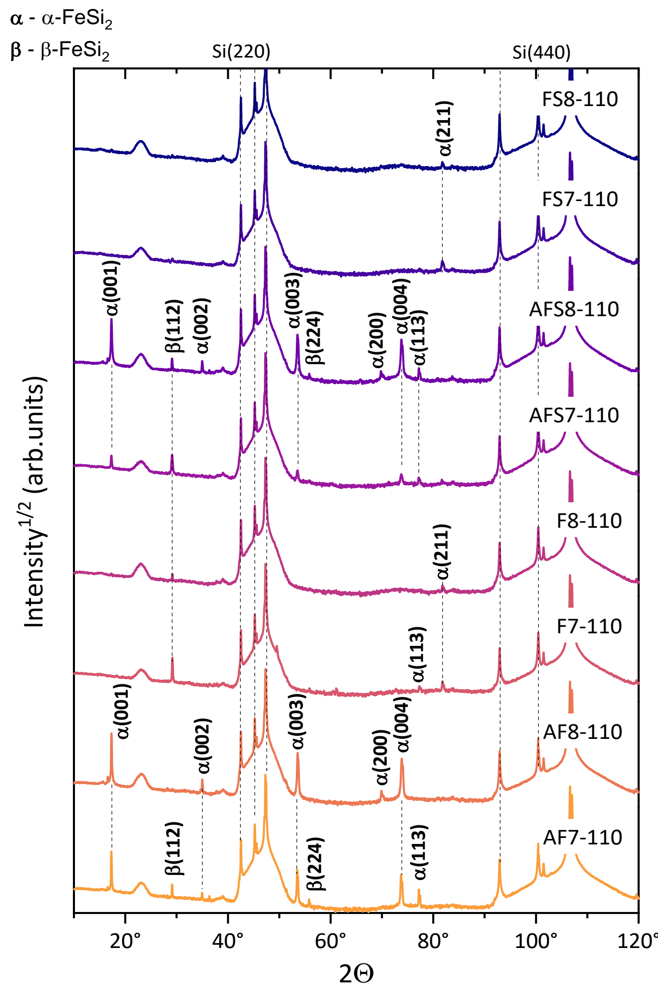

Figure 3.21. XRD unlocked scans of the $FeSi_2$ crystallites prepared on Si(110) using Au-assisted (AF) and Au-free (F) Fe deposition, and Au-assisted (AFS) and Au-free (FS) Fe/Si co-deposition at substrate temperatures of 740 (7) and 840 (8) °C (plane indices are marked).

Notably, the AF8-110 sample is almost mono-oriented with α-$FeSi_2$(001) plane, while the AF7-110 sample demonstrates weak reflections of the β-$FeSi_2$(112) planes, which is consistent with the lower formation temperature of the β-$FeSi_2$ phase (Ch. 1.3.2). In the case of samples obtained during Fe/Si co-deposition, the AFS8-110 sample indicates the formation of the α-$FeSi_2$ phase by intense reflections of the α-$FeSi_2$(001) plane. Nevertheless, weak reflections of β-$FeSi_2$(112) and α-$FeSi_2$(113) planes are also presented. At the same time, the AFS7-110 sample demonstrates the same weak peaks as the AFS8-110 sample due to the smaller

crystallite size. Samples obtained using Au-free conditions (F7-110, F8-110, FS7-110 and FS8-110) demonstrate a presence of β-$FeSi_2$(112), α-$FeSi_2$(113) and α-$FeSi_2$(211) reflections.

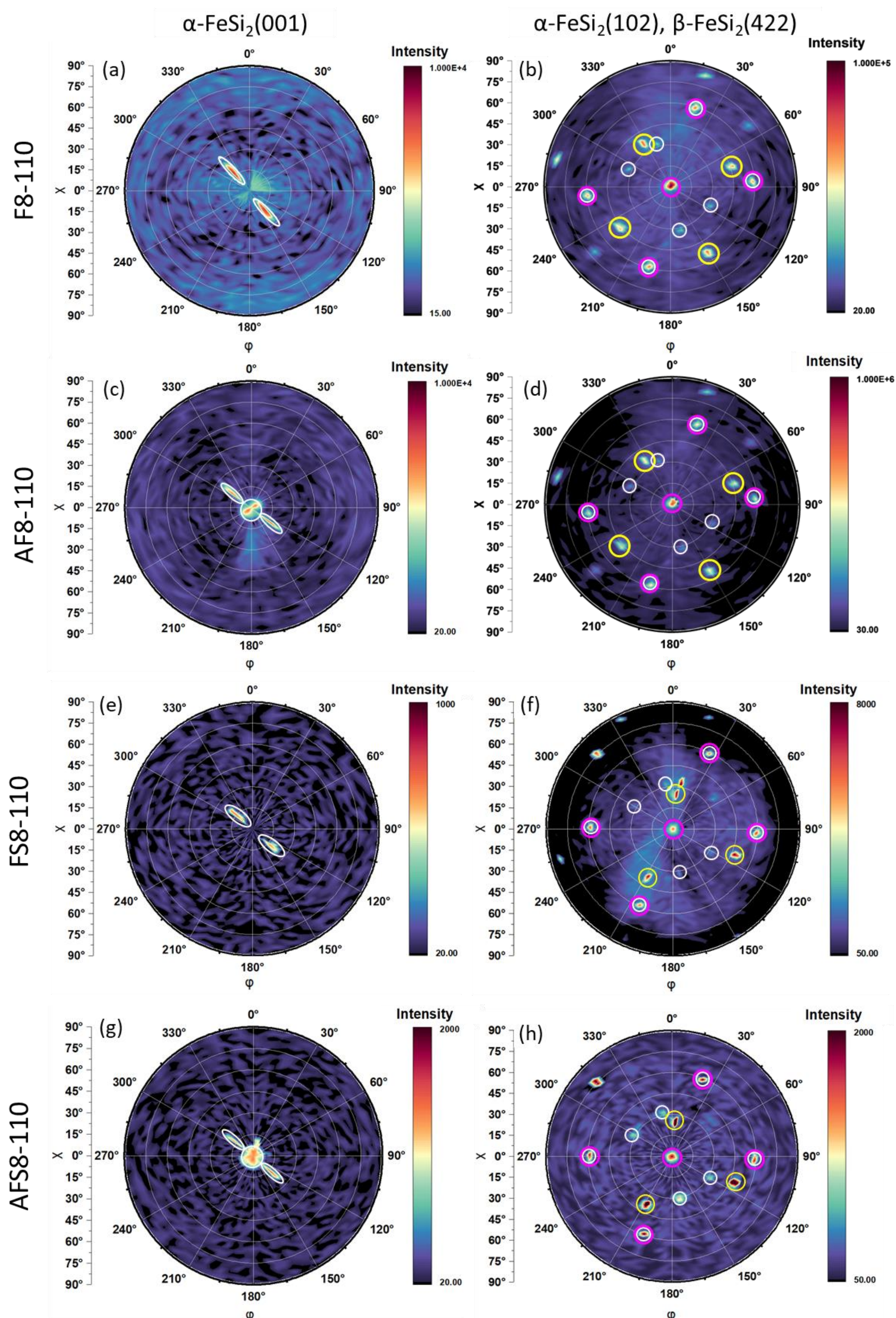

Figure 3.22. XRD pole figures recorded for α-$FeSi_2$(001), α-$FeSi_2$(102) and β-$FeSi_2$(422) planes of the $FeSi_2$ crystallites prepared on Si(110) substrate (840°C) using (a, b) Au-free (F8-110) and (c, d) Au-assisted (AF8-110) Fe deposition, and (e, f) Au-free (FS8-110) and (g, h) Au-assisted (AFS8-110) Fe/Si co-deposition. Solid white lines correspond to the α-$FeSi_2$(001)[-110]//Si(110)[-110] OR reflections (white circles) and the α-$FeSi_2$(1-12)[-110]//Si(111)[-110] with the α-$FeSi_2$(-112)[-110]//Si(11-1)[-110] ORs (white ovals), pink lines correspond to Si(220) reflections and yellow circles correspond to the sample holder reflections.

XRD pole figures presented in Fig. 3.22 as a function of signal intensity in logarithmic scale were recorded for the samples obtained at 840°C substrate temperature since these crystallites demonstrate clearer faceting in comparison with those obtained at 740°C (Ch. 3.2.2). Thus, measurements were performed for the lattice planes of α-$FeSi_2$(001) at 2Θ ~ 17° and for α-$FeSi_2$(102), β-$FeSi_2$(422) at 2Θ ~ 50° (see Ch. 2.2). The results outlined the formation of the α-$FeSi_2$(001)[-110]//Si(110)[-110] OR for the samples obtained using Au-assisted growth, while the samples obtained only with Fe deposition demonstrate the formation of 2-fold α-$FeSi_2$(001)[-110]15°//Si(110)[-110] OR symmetrically inversed in relation to Si[110] as the α-$FeSi_2$(001)[110]165°//Si(110)[-110] OR, which corresponds to the morphological analysis of obtained samples, where the 2-fold inclination by ~15˚ of elongated crystallites was observed (Ch. 3.2.2, Fig. 3.9). Observed ORs also can be written as the α-$FeSi_2$(1-12)[-110]//Si(111)[-110] and the α-$FeSi_2$(-112)[-110]//Si(11-1)[-110] to highlight the parallelism of α-$FeSi_2$(112) and Si(111) planes formed during Au-free growth, which was theoretically predicted in [159,271]. The same result was observed in [283], where authors prepared endotaxial α-$FeSi_2$ wire-shaped crystallites on Si(110) by Au-free reactive deposition epitaxy. Thus, the clear correlation between determined ORs and crystalline morphology is visible for samples AF8-110 and AFS8-110, where three types of wire-shaped crystallites are presented. All of them refer to the α-$FeSi_2$ phase: the α-$FeSi_2$(001)[-110]// Si(110)[-110] OR for those parallel to substrate surface and both the α-$FeSi_2$(1-12)[-110]// Si(111)[-110] OR and the α-$FeSi_2$(-112)[-110]//Si(11-1)[-110] OR for elongated crystallites tilted relative to the substrate, which are visible in XRD pole figures of α-$FeSi_2$(001), corresponding reflexes marked with white dashed oval lines.

This way, for $FeSi_2$ submicron crystals obtained on Si(110) substrates, the following ORs were determined:

- α-$FeSi_2$(001)[110]//Si(110)[-110],
- α-$FeSi_2$(1-12)[-110]//Si(111)[-110] (also written as α-$FeSi_2$(001)[-110]15°//Si(110)[-110]),
- α-$FeSi_2$(-112)[-110]//Si(11-1)[-110] (also written as α-$FeSi_2$(001)[110]165°//Si(110)[-110]).

Observed in unlocked scans, weak peaks of β-$FeSi_2$(112), α-$FeSi_2$(113) and α-$FeSi_2$(211) planes were not considered since they were not observed in the recorded XRD pole figures.

To find out the heteroepitaxial relationship of α- and β-$FeSi_2$ phases on Si(110), simulations of XRD pole figures for the α-$FeSi_2$(1-12)[-110]//Si(111)[-110] OR (open purple dots) and the

α-$FeSi_2$(-112)[-110]//Si(11-1)[-110] (closed purple dots) using PTCLab [257] were performed. Fig. 3.23 (a) presents the typical XRD pole figure patterns of the α-$FeSi_2$(001) plane and shows the corresponding reflections slightly shifted from the center and Fig. 23 (b) presents the α-$FeSi_2$(102) shifted reflections completely matching with experimentally observed α-$FeSi_2$ phase reflections on measured XRD pole figures at the selected angles presented in Fig. 3.22.

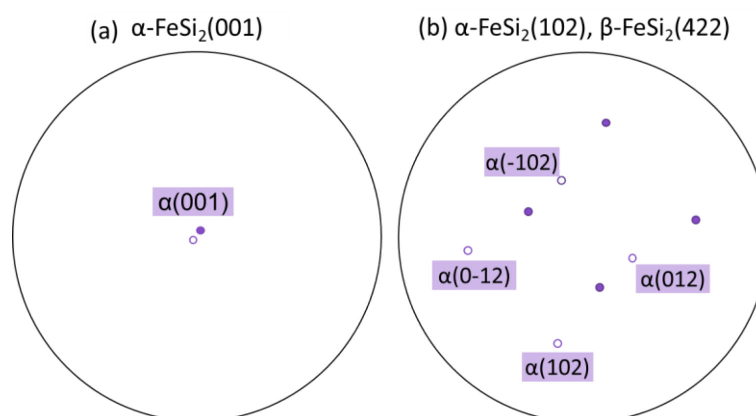

Figure 3.23. Simulation of XRD pole figures for (a) α-$FeSi_2$(001) and (b) α-$FeSi_2$(102), β-$FeSi_2$(422) planes for the α-$FeSi_2$(1-12)[-110]//Si(111)[-110] OR (open purple dots) and the α-$FeSi_2$(-112)[-110]//Si(11-1)[-110] OR (closed purple dots).

In addition, the determined ORs were confirmed by electron back-scattered diffraction (EBSD) (see Ch. 2.2.2). The measurements were performed for the obtained crystallites with the largest lateral sizes, specifically for sample AF8-110 (Fig. 3.24) at the following conditions: working voltage 20 kV, working distance 15 mm, diameter 36 mm, camera length 24 mm, sample holder tilt angle 70°. Recorded Kikuchi patterns were used to fit with simulated Kikuchi patterns in PTCLab using the experimental parameters described above. Thus, the ORs for α-$FeSi_2$ determined using XRD pole figures were also confirmed by EBSD. Figure 3.24 (a) presents the selected area with marked crystallites for the recording of Kikuchi patterns, which are displayed further in Fig. 3.24 (b) for the α-$FeSi_2$(001)[110]//Si(110)[-110] OR corresponding to the wire-like crystallite grown parallel to the substrate surface (numbered with cross 1); in Fig. 3.24 (c) for the α-$FeSi_2$(-112)[-110]//Si(11-1)[-110] OR corresponding to the wire-like crystallite grown tilted by 165° about the substrate surface (numbered with cross 2) and at Fig. 3.24 (d) for the α-$FeSi_2$(1-12)[-110]//Si(111)[-110] OR corresponding to the wire-like crystallite grown tilted by 15° about the substrate surface (numbered with cross 3).

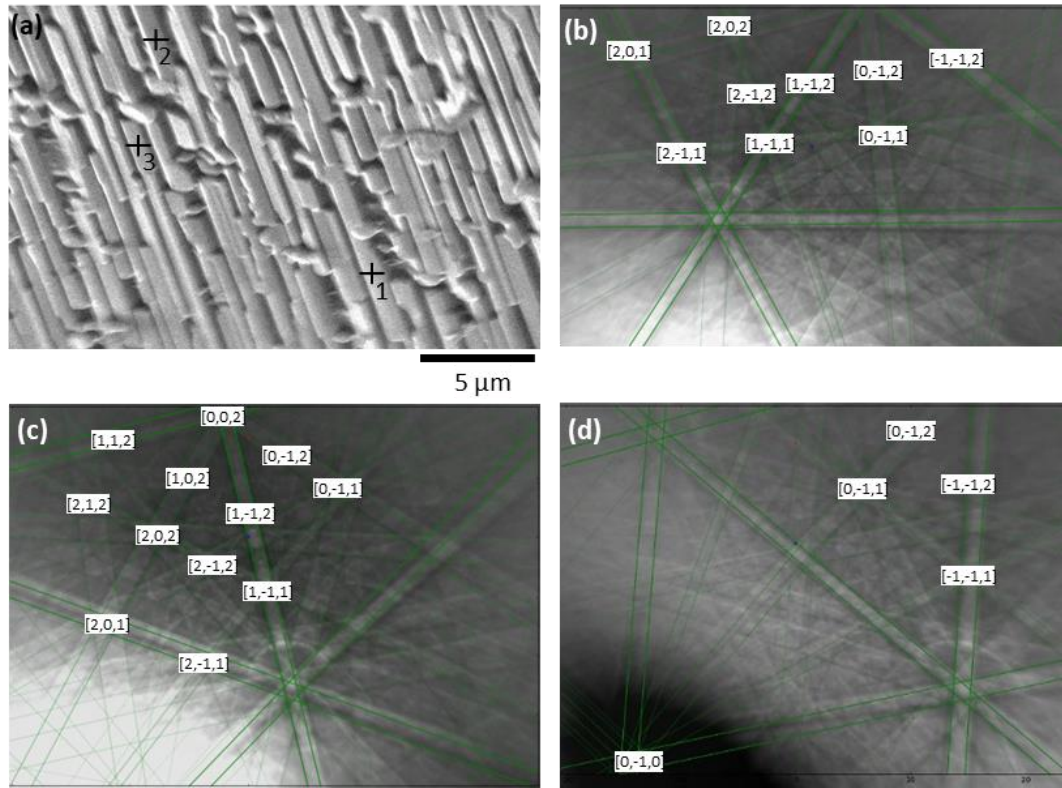

Figure 3.24. (a) SEM-image of the $FeSi_2$ crystallites prepared on Si(110) substrate (840°C) using Au-assisted (AF8-110) Fe deposition and Kikuchi patterns recorded from cross-marked crystallites (b) 1 for the α-$FeSi_2$(001)[110]//Si(110)[-110] OR, (c) 2 for the α-$FeSi_2$(-112)[-110]//Si(11-1)[-110] OR and (d) 3 for the α-$FeSi_2$(1-12)[-110]//Si(111)[-110] OR, recorded at working voltage 20 kV, working distance 15 mm, diameter 36 mm, camera length 24 mm, sample holder tilt angle 70°.

Overall, orientation relationships of α-, β-$FeSi_2$ crystallites obtained on Si(110) substrate (840°C) using Au-free (F8-110) and Au-assisted (AF8-110) reactive deposition of Fe and also Au-free (FS8-110) and Au-assisted (AFS8-110) Fe/Si co-deposition determined from XRD pole figures and their relative orientation fractions (Q_{OR}) estimated by the approach presented in Ch. 3.3.1 are summarized in Table 3.7.

Table 3.7. *Summary of orientation relationships (OR) and relative OR fractions Q_{OR} of α-, β-$FeSi_2$ crystallites obtained on Si(110) substrate (840°C) using Au-free (F8-110) and Au-assisted (AF8-110) Fe deposition and also Au-free (FS8-110) and Au-assisted (AFS8-110) Fe/Si co-deposition.*

Sample	F8-110	AF8-110	FS8-110	AFS8-110
	Q_{OR}, %			
α-$FeSi_2$(001)[110]//Si(110)[-110]	-	76.0 ± 0.2	-	65.0 ± 0.3
α-$FeSi_2$(1-12)[-110]//Si(111)[-110] α-$FeSi_2$(-112)[-110]//Si(11-1)[-110]	99.9 ± 0.1	24.0 ± 0.4	99.9 ± 0.1	35.0 ± 0.8

Summary

The analysis of structure and orientation relationships of prepared α-, β-$FeSi_2$ crystallites on p-Si(110) provides that the Au-assisted growth leads to the formation of the α-$FeSi_2$(001)[110]//Si(110)[-110] orientation relationship, preferable for both samples obtained as with Fe deposition – AF8-110 (76%), as with Fe/Si co-deposition – AFS8-110 (65%), which correspond to the formation of elongated nano and submicron wires grown perpendicularly to the Si surface normal with a flat α-$FeSi_2$(001) surface parallel to Si(110) substrate surface.

Moreover, the formation of the additional α-$FeSi_2$(1-12)[-110]//Si(111)[-110] and α-$FeSi_2$(-112)[-110]//Si(11-1)[-110] orientation relationships corresponding to 2-fold inclination by ~15˚ of elongated crystallites relative to the Si surface normal are observed for samples AF8-110 (24%) and AFS8-110 (35%) with a minor relative fraction of the orientation, and for samples F8-110 and FS8-110 as preferential orientation relationship with the relative fraction of Q_{OR} ~ 99.9%.

3.3.3 $FeSi_2$ on Si(111)

Regarding the $FeSi_2$ crystallites obtained on Si(111) substrates, XRD unlocked scans (Fig. 3.25) demonstrate two basic orientations of $FeSi_2$ crystallites on the Si(111) substrate: α-$FeSi_2$(001) and β-$FeSi_2$(002).

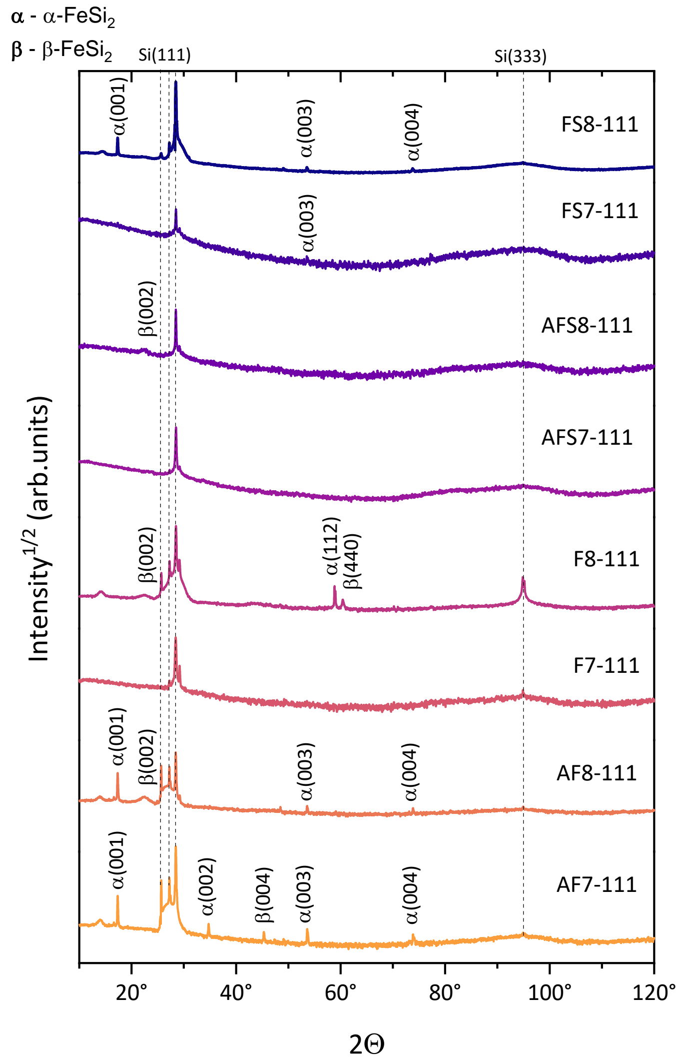

Figure 3.25. XRD unlocked scans of $FeSi_2$ crystallites prepared on Si(111) using Au-assisted (AF) and Au-free (F) Fe deposition, and Au-assisted (AFS) and Au-free (FS) Fe/Si co-deposition at substrate temperatures of 740 (7) and 840 (8) °C (plane indices are marked).

It is worth noting that the unlocked scans do not demonstrate high-intensity peaks compared to the two previous substrates, which can be explained by a Si(111) substrate miscut close to 5°-6°. Thus, high-intensity planes of prepared α- and β-$FeSi_2$ crystallites could be oriented not perpendicularly concerning the sample holder. In this case, the signal intensity from these planes is lower or undetected. In this case, XRD pole figures should show intensive reflections from α- and β-$FeSi_2$ crystal planes (see Ch. 2.2.2).

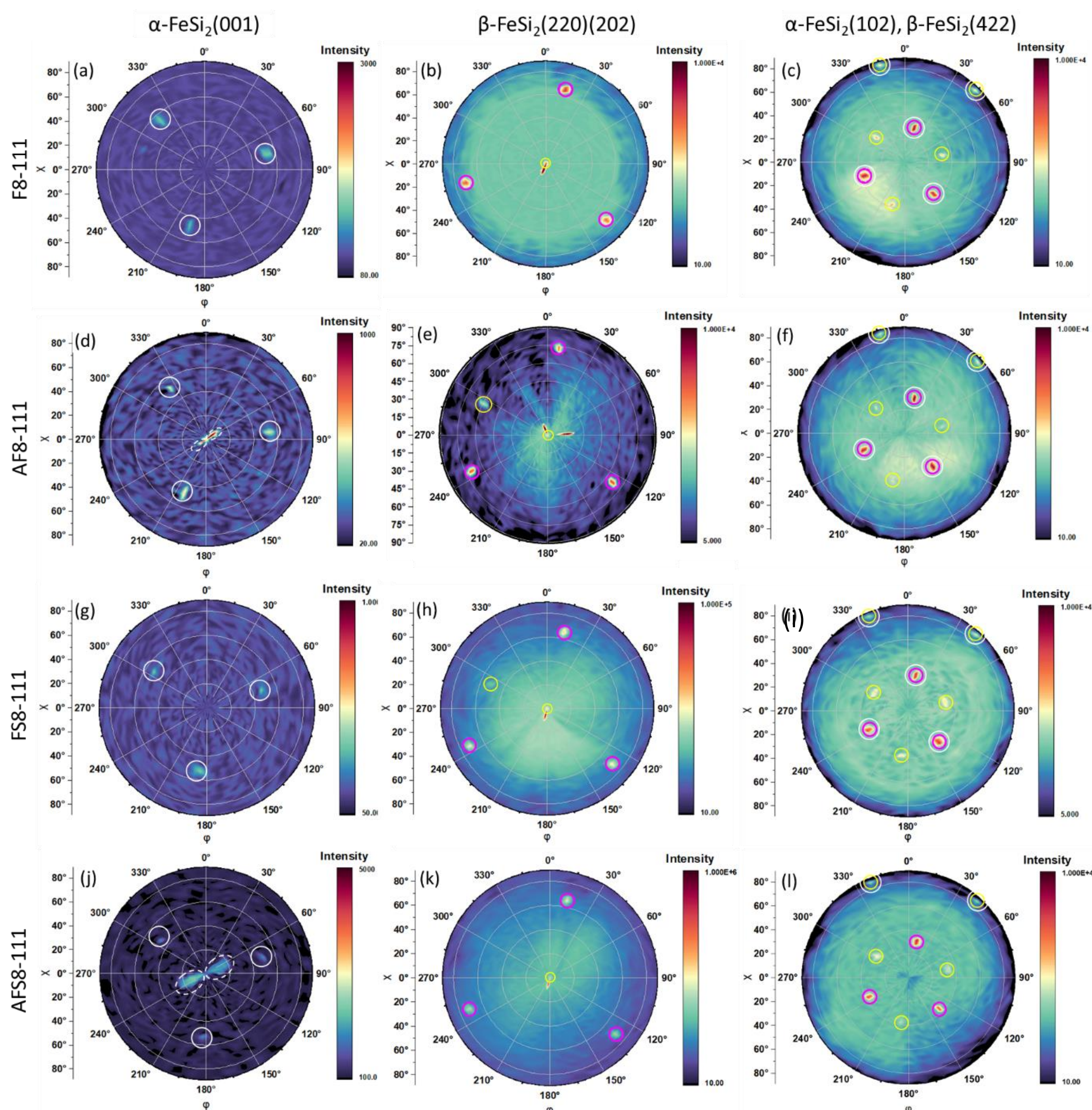

Figure 3.26. XRD pole figures recorded for α-$FeSi_2$(001), β-$FeSi_2$(220)(202), α-$FeSi_2$(102) and β-$FeSi_2$(422) planes of the $FeSi_2$ crystallites prepared on Si(111) substrate (840°C) using (a, b, c) Au-free (F8-111) and (d, e, f) Au-assisted (AF8-111) Fe deposition, and (g, h, i) Au-free (FS8-111) and (j, k, l) Au-assisted (AFS8-111) Fe/Si co-deposition. Here, solid white lines correspond to 3-fold the α-$FeSi_2$(112)[-110]//Si(111)[-110] domain rotated by 120°, dashed white lines to inversed the α-$FeSi_2$(001)[110]//Si(111)<-110> domain, yellow lines to the β-$FeSi_2$(220)(202)[001][101]//Si(111)<-110> domain rotated by steps of 120° and dashed pink lines correspond to Si reflections.

Thus, XRD pole figures presented in Fig. 3.26 as a function of signal intensity in logarithmic scale were recorded for samples prepared at the substrate temperature of 840°C, as in two previous cases. Measurements were performed for the lattice planes of α-$FeSi_2$(001) at 2Θ ~ 17°, β-$FeSi_2$(220)(202) at 2Θ ~ 29° and for α-$FeSi_2$(102), β-$FeSi_2$(422) at 2Θ ~ 50°. The results outlined the presence of the 3-fold symmetry α-$FeSi_2$(112)[-110]//Si(111)[-110]

domain rotated by 120° in all samples (Fig. 3.26 (a, d, g, j)), highlighted by the white solid line. Furthermore, recorded patterns of α-$FeSi_2$(001) reveal the formation of the inversed α-$FeSi_2$(001)[110]//Si(111)<-110> domain for the samples obtained using Au-assisted conditions (Fig. 3.26 (d, j)), highlighted by the white dashed line, while the samples obtained only with reactive epitaxy do not demonstrate the formation of this OR. Regarding formation β-$FeSi_2$ phase on Si(110) substrates, 3-fold symmetry of the β-$FeSi_2$(220)(202)[001][101]// Si(111)<-110> domain is presented on XRD pole figures for β-$FeSi_2$(220)(202) and for α-$FeSi_2$(102), β-$FeSi_2$(422) lattice planes for all samples, highlighted by the solid yellow line (Fig. 3.26 (b, e, h, k)). This way, for $FeSi_2$ crystallites obtained on Si(111) substrates the following ORs were determined:

- 0° – α-$FeSi_2$(112)[-110]//Si(111)[-110],
- 120° – α-$FeSi_2$(112)[-110]//Si(111)[10-1],
- 240° – α-$FeSi_2$(112)[-110]//Si(111)[0-11],
- α-$FeSi_2$(001)[110]//Si(111)<-110>,
- β-$FeSi_2$(220)(202)[001][101]//Si(111)<-110>.

To find out the complex heteroepitaxial relationship of α- and β-$FeSi_2$ phases on Si(111) substrate, simulations of XRD pole figures were performed using PTCLab [257] (Fig. 3.27). Typical XRD pole figures of α-$FeSi_2$(001) and α-$FeSi_2$(102), β-$FeSi_2$(422) planes (Fig. 3.27 (a, c)) present patterns of the α-$FeSi_2$(001)[110]//Si(111)<-110> domain, inversed about its surface normal direction (open magenta dots), which correspond to XRD pole figures of samples obtained using Au-assisted growth (Fig. 3.26 (d, j) for α-$FeSi_2$(001) plane and (c, i) for α-$FeSi_2$(102), β-$FeSi_2$(422) planes). Thus, Fig. 3.27 (c) demonstrates the complete pattern for the α-$FeSi_2$(112)[-110]//Si(111)[-110] OR partially overlapped with the β-$FeSi_2$(220)(202) [001][101]//Si(111)<-110> OR domains reflections (magenta dots and green squares), both rotated by steps of 120° about its surface normal direction, which is not shown on experimentally obtained XRD pole figures (Fig. 3.26 (c, f, I, l)) due to the overlapping of described ORs and the fast time of measurement (counting time 0.088 s). Also, Fig. 3.27 (b) presents the XRD pole figure simulation of β-$FeSi_2$(220)(202) reflections for the β-$FeSi_2$(220)(202)[001][101]//Si(111)<-110> OR domain rotated by steps of 120° about its surface normal direction, which correspond to the experimentally obtained XRD pole figures for β-$FeSi_2$(220)(202) planes (Fig. 3.26 (b, e, h, k)) showing three overlapped reflections of

β-$FeSi_2$(-220) planes. Thus the low intensity of obtained β-$FeSi_2$(220)(202)[001][101]// Si(111)<-110> OR, the rest of the reflections are hardly visible on the experimentally obtained XRD pole figures.

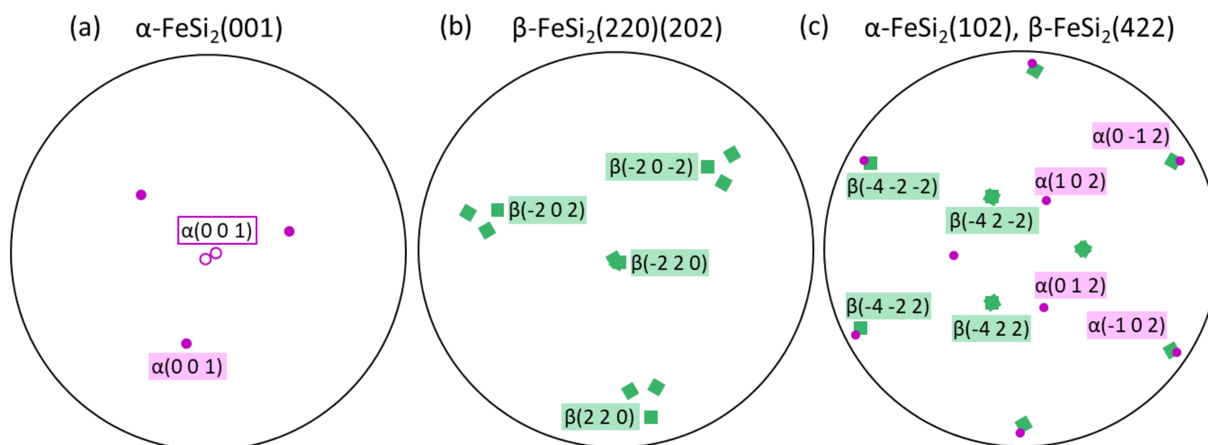

Figure 3.27. Simulation of (a) α-$FeSi_2$(001), (b) β-$FeSi_2$(220)(202) and (c) α-$FeSi_2$(102), β-$FeSi_2$(422) planes for inversed α-$FeSi_2$(001)[110]//Si(111)<-110> domain (open magenta dots), α-$FeSi_2$(112)[-110]//Si(111)[-110] domain rotated by steps of 120° about its surface normal direction (magenta dots), and β-$FeSi_2$(220)(202)[001][101]//Si(111)<-110> domain rotated by steps of 120° about its surface normal direction (green squares).

In addition, the determined ORs were confirmed by electron back-scattered diffraction (EBSD) (Ch. 2.2.2). The measurements were performed for obtained crystallites with the largest lateral sizes, specifically for samples F8-111 (Fig. 3.28 (a)) and AF8-111 (Fig. 3.28 (b)) at the following conditions: working voltage 20 kV, working distance 15 mm, diameter 36 mm, camera length 24 mm, sample holder tilt angle 70°. Recorded Kikuchi patterns were fitted with simulated Kikuchi patterns in PTCLab using the experimental parameters described above.

Thus, estimated from XRD pole figures, ORs were also confirmed by EBSD. Fig. 3.28 (c) presents the Kikuchi pattern for the α-$FeSi_2$(112)[-110]//Si(111)[-110] OR corresponding to cross-marked crystallite for F8-111 (Fig. 3.28 (a)), which according to the estimation of orientation fractions (as described in detail in 3.3.1) is preferential OR for sample F8-111. In contrast, Figure 3.28 (d) displays the Kikuchi pattern for the α-$FeSi_2$(001)[110]//Si(111)<-110> OR corresponding to the cross-marked crystallite observed in AF8-111 (Fig. 3.28 (b)). This OR, as determined by the estimation of the fractions, is preferential for sample AF8-111.

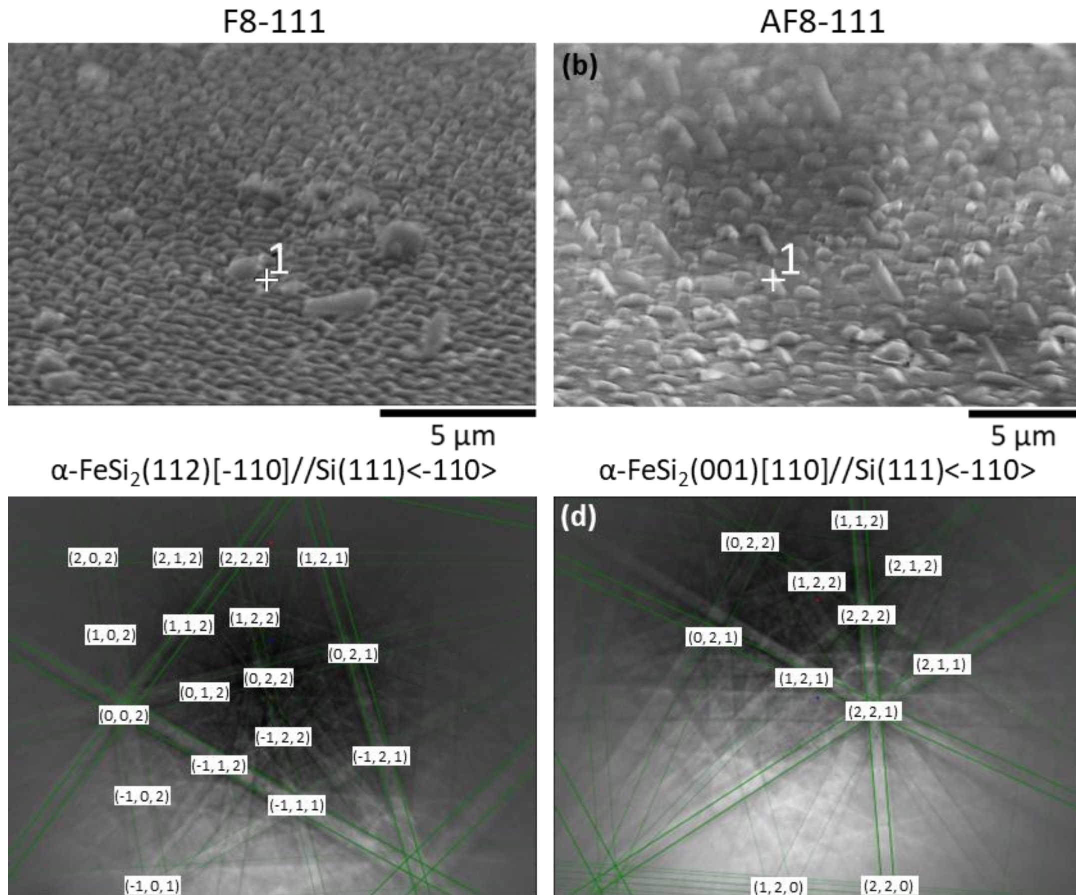

Figure 3.28. SEM-images of $FeSi_2$ crystallites prepared on Si(111) substrate (840°C) using (a) Au-free (F8-111) and (b) Au-assisted (AF8-111) reactive deposition of Fe and Kikuchi patterns recorded from cross-marked crystallites of (c) F8-111 for the α-$FeSi_2$(112)[-110]// Si(111)<-110>, (d) AF8-111 for the α-$FeSi_2$(001)[110]//Si(111)<-110> ORs, recorded at working voltage 20 kV, working distance 15 mm, diameter 36 mm, camera length 24 mm, sample holder tilt angle 70°.

Other ORs of α-, β-$FeSi_2$ crystallites prepared on Si(111) substrate (840°C) using Au-free (F8-111) and Au-assisted (AF8-111) reactive deposition of Fe and also Au-free (FS8-111) and Au-assisted (AFS8-111) Fe/Si co-deposition determined from XRD pole figures and their relative orientation fractions (Q_{OR}) estimated by the approach presented in Ch. 3.3.1 are summarized in Table 3.8.

Table 3.8. *Summary of orientation relationships (OR) and OR fractions Q_{OR} of α-, β-$FeSi_2$ crystallites obtained on Si(111) substrate (840°C) using Au-free (F8-111) and Au-assisted (AF8-111) Fe deposition and also Au-free (FS8-111) and Au-assisted (AFS8-111) Fe/Si co-deposition*

Sample	**F8-111**	**AF8-111**	**FS8-111**	**AFS8-111**
	Q_{OR}, %			
α-$FeSi_2$(112)[-110]//Si(111)[-110] α-$FeSi_2$(112)[-110]//Si(111)[10-1] α-$FeSi_2$(112)[-110]//Si(111)[0-11]	98.0 ± 0.9	29.0 ± 0.7	99.0 ± 0.4	7.0 ± 0.2
α-$FeSi_2$(001)[110]//Si(111)<-110>	-	70.0 ± 0.2	-	19.0 ± 0.7
β-$FeSi_2$(220)(202)[001][101]//Si(111)<-110>	2.0 ± 0.1	1.0 ± 0.1	1.0 ± 0.1	73.0 ± 0.1

Summary

*The analysis of structure and orientation relationships of prepared α-, β-$FeSi_2$ crystallites on p-Si(111) provides that Au-assisted growth supports the formation of the α-$FeSi_2$(001)[11**0**]//Si(111)<-110> orientation relationship, which is obtained using Fe deposition – AF8-111 (70%) and also being preferential, and using Fe/Si co-deposition – AFS8-111 (19%) corresponding to the 2-fold symmetry of triangular nanoplates demonstrating well-defined faceting and flat surfaces. Additionally, the formation of the 3-fold symmetry α-*$FeSi_2$(112)[-110]//Si(111)<-110> *domain rotated by steps of 120° is observed for all samples: F8-111 (98%), AF8-111 (29%), FS8-111 (99%) and AFS8-111 (7%), which refers to 3-fold symmetry of trapezoidal nanoplates. In this manner, Au-free growth results in the formation of almost only 3-fold symmetry α-$FeSi_2$(112)[-110]//Si(111)<-110> orientation relationship on Si(111) substrate with ~ 99% of fraction orientation Fe deposition and Fe/Si co-deposition. Furthermore, the formation of the β-$FeSi_2$ phase is observed for all samples whether Au-assisted conditions were used. Thus, the β-$FeSi_2$(220)(202)[001][101]//Si(111)<-110> orientation relationship is formed during Au-free conditions for samples F8-111 (2%) and FS8-111 (1%) and also is formed using Au-assisted growth for samples AF8-111 (1%) and AFS8-111 (73%), being preferential for the AFS8-111 sample obtained using Au-assisted Fe/Si co-deposition.*

3.4 Discussion of the growth mechanism of $FeSi_2$ crystallites on Si

During the growth process of α-$FeSi_2$ crystallites on Si substrate using reactive epitaxy (RE) and molecular beam epitaxy (MBE), the stoichiometry of $FeSi_2$ is achieved by supplying a specific number of Si atoms (as described in Ch. 3.1). The required Si atoms are provided to the developing nanostructures from the surrounding region during the Fe or Fe/Si deposition stage, as depicted in Figure 3.29. In MBE, during Fe/Si co-deposition, Si atoms contribute to the attainment of $FeSi_2$ stoichiometry. However, when Fe is deposited without Si, the Si atoms are obtained from the substrate during the RE process due to the high diffusion of Si atoms at the synthesis temperature. This diffusion process ensures the desired $FeSi_2$ stoichiometry by enabling Si atoms to diffuse from the substrate to the top of the developing nanostructure.

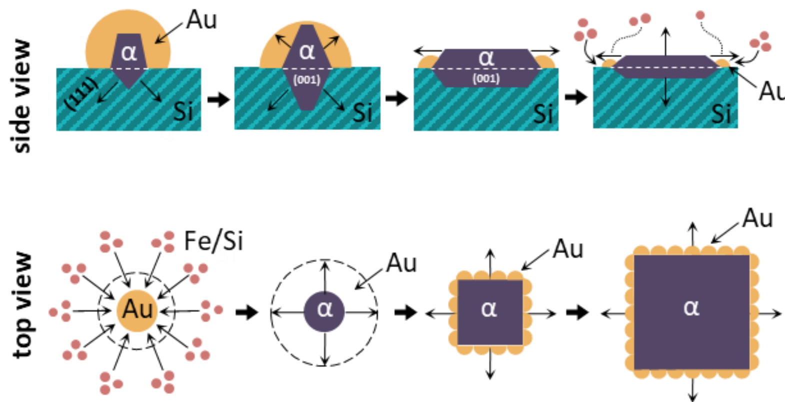

Figure 3.29. Schematic illustration of (a) top view and (b) side view of Au-assisted growth of α-$FeSi_2$ crystallites during Fe or Fe/Si co-deposition.

Furthermore, the growth of α-$FeSi_2$ crystallites on the Si substrate is supported by the Au-assisted growth, in the presence of which Au-islands act as growth centers. Here, Au acts as a *catalyst*, plays a critical role in the growth kinetics and determines the final crystallite shape. During the initial stages of growth, α-$FeSi_2$ crystallites are formed through the vapor-liquid-solid (VLS) mechanism, similar to the growth of semiconductor nanowires, when Au-islands serve as growth centers attracting incoming Fe or Si atoms. In addition, as a catalyst, Au promotes the rapid growth of α-$FeSi_2$ crystallites compared to the Au-free surface. In the case of MBE implemented in Fe/Si co-deposition, the supersaturated alloy of Si, Au, and Fe formed beneath the Au-island leads to the crystallization of α-$FeSi_2$ on the underlying surface, thereby facilitating the development of a specific orientation of a silicide crystallite. However, lateral growth outpaces vertical growth under the given conditions due to reduced diffusion flux from the substrate surface to the top of the nanostructure and increased

oversaturation on the lateral faces. As a result, the Au-islands overgrow, giving rise to the formation of new facets, as observed in the case of the crystallites obtained using Au-assisted Fe/Si co-deposition demonstrating higher faceting in comparison with those obtained using Au-free Fe/Si co-deposition.

Furthermore, Au also plays a *surfactant* role and controls the size, shape, and orientation of the α-$FeSi_2$ crystals formed on the Si substrate, as was discussed in Chs. 3.2 and 3.3. Thus, as an example, the use of Au-assisted growth in the case of α-$FeSi_2$ nanowires formation on Si(110) surface creates favorable conditions for the nucleation and growth of highly faceted and well-shaped elongated wires along Si[001] direction with the α-$FeSi_2$(001)[110]// Si(110)[-100] orientation parallel to the substrate surface. Therefore, by employing the Au-assisted conditions, it becomes possible to prepare α-$FeSi_2$ nano- and submicron crystallites with adjustable sizes ranging from 30 nm to several µm and a well-defined crystallographic orientation relationship (OR) between α-$FeSi_2$ and Si. In particular, Au-assisted growth leads to the formation of preferential orientation relationships (ORs), which differ from those formed using Au-free growth (see Tables 3.6-3.8). The prepared samples according to the protocol described in Ch. 3.1 and their preferential ORs with estimated relative fractions (Q_{OR}) are summarized in Table 3.9.

Table 3.9. *Summary of preferential orientation relationships (OR) and their relative fractions Q_{OR} for samples formed during Au-assisted (AF8 and AFS8) and Au-free (F8 and FS8) Fe deposition and Fe/Si co-deposition at substrate temperature of 840 °C under ultrahigh vacuum conditions on p-Si(001), p-Si(110) and p-Si(111) substrates.*

Sample	Preferential orientation relationship	Q_{OR}, %
AF8-001	α-$FeSi_2$(001)[110]//Si(001)[110] α-$FeSi_2$(001)[110]//Si(001)[100]	99.9 ± 0.1
F8-001	α-$FeSi_2$(111)[-110]//Si(001)[110]	69.0 ± 0.7
AFS8-001	α-$FeSi_2$(001)[110]//Si(001)[110] α-$FeSi_2$(001)[110]//Si(001)[100]	69.0 ± 0.6
FS8-001	α-$FeSi_2$(111)[-110]//Si(001)[110]	94.0 ± 0.6
AF8-110	α-$FeSi_2$(001)[110]//Si(110)[-110]	76.0 ± 0.2
F8-110	α-$FeSi_2$(1-12)[-110]//Si(111)[-110] α-$FeSi_2$(-112)[-110]//Si(11-1)[-110]	99.9 ± 0.1
AFS8-110	α-$FeSi_2$(001)[110]//Si(110)[-100]	65.0 ± 0.3
FS8-110	α-$FeSi_2$(1-12)[-110]//Si(111)[-110] α-$FeSi_2$(-112)[-110]//Si(11-1)[-110]	99.9 ± 0.1
AF8-111	α-$FeSi_2$(001)[110]//Si(111)<-110>	70.0 ± 0.2
F8-111 **FS8-111**	α-$FeSi_2$(112)[-110]//Si(111)<-110>	98.0 ± 0.9 99.0 ± 0.4
AFS8-111	β-$FeSi_2$(220)(202)[001][101]//Si(111)<-110>	73.0 ± 0.1

For the samples AF8-001, F8-001, AFS8-001, FS8-001, AF8-110, AFS8-110, AF8-111, F8-111 and FS8-111 metallic α-$FeSi_2$ phase is preferential, and estimated ORs regarding Si substrate conductivity valleys are discussed below. The conduction band of Si has six equivalent minima located on the [100] and equivalent axes. These minima are commonly called "valleys" and are labeled by the numbers 1 to 6, as shown in Fig. 3.30 (a) [284]. Thus, the conductivity valleys of Si are attributed to different crystallographic directions x||[100], y||[010], z||[001], v||[110], and w||[111] schematically shown in Figure 3.30 (b, c, d) for Si unit cell according to Si(001), Si(110) and Si(111) crystallographic planes, corresponding to orientations of used Si substrates.

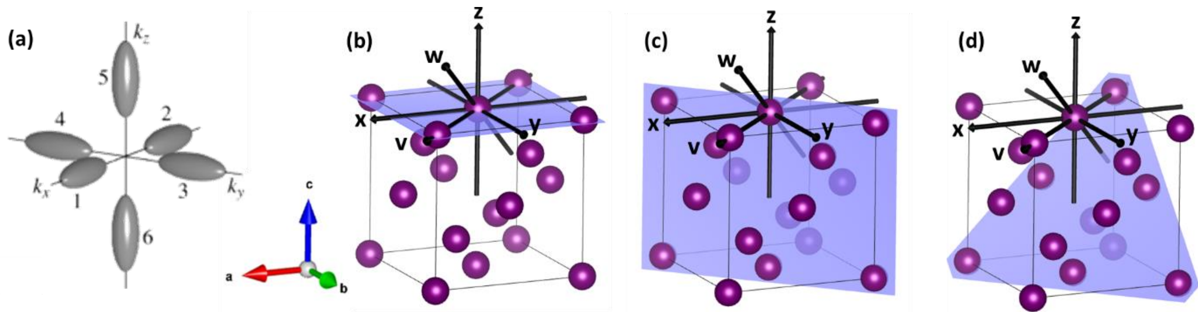

Figure 3.30. Schematic representation of the conductivity valleys of silicon as constant energy surfaces in k-space. Numbers label the six valleys, e.g., 4 represents the [0-10] direction [284]. *Si-crystal non-primitive unit cell with crystallographic directions of x||[100], y||[010], z||[001], v||[110], and w||[111] concerning (b) (001), (b) (110) and (c) (111) planes.*

The conductivity of prepared α-$FeSi_2$/Si samples can be attributed to the determined ORs and the angles between the conductivity channels of the α-$FeSi_2$ and the Si substrate, denoted in this work by the symbol ζ since the crystallographic orientation and alignment between the two materials directly influence the transport of charge carriers across the interface [285]. Thus, the conductivity channels in α-$FeSi_2$, aligned along specific crystallographic directions within the α-$FeSi_2$(001) lattice plane, provide pathways for the movement of charge carriers. On the other hand, the conductivity valleys in Si, represented by specific crystallographic directions (such as Si[100], Si[010], Si[001], Si[110], and Si[111]), determine the energy bands and states in which electrons can reside. When the α-$FeSi_2$ and Si materials are oriented to align the conductivity channels in α-$FeSi_2$ with the conductivity valleys in Si, it allows for efficient charge carrier transport across the interface. The aligned crystallographic directions and angles between the two materials create favorable conditions for the conduction of holes (for *p*-doped Si), resulting in enhanced conductivity in the α-$FeSi_2$/Si samples. The minimum angle $ζ_{min}$ indicates a closer alignment and better matching between the α-$FeSi_2$(001) lattice

plane and Si[100], Si[010], Si[001], Si[110], and Si[111] directions. It promotes more efficient charge carrier transport across the interface when close to 0.

In this way, determined preferential ORs for samples prepared on *p*-Si(001) substrate using Au-assisted (AF8-001 and AFS8-001) and Au-free (F8-001 and FS8-001) Fe deposition and Fe/Si co-deposition at the substrate temperature of 840 °C under ultrahigh vacuum conditions are schematically shown in Figure 3.31. Thus, the preferential α-$FeSi_2$(001)[110]//Si(001)[110] OR (45 degrees rotated as the α-$FeSi_2$(001)[110]//Si(001)[100] OR) for AF8-001 and AFS8-001 samples is shown in Fig. 3.32 (a, b), and α-$FeSi_2$(111)[-110]//Si(001)[110] OR preferential for F8-001 and FS8-001 samples is shown at Fig. 3.31 (c, d). The minimum angles for these ORs are ζ_{min} = 0.0° for the α-$FeSi_2$(001)[110]//Si(001)[110] OR and ζ_{min} = 48.5° for the α-$FeSi_2$(111) [-110]//Si(001)[110] OR, determined by utilizing PTCLab software [202].

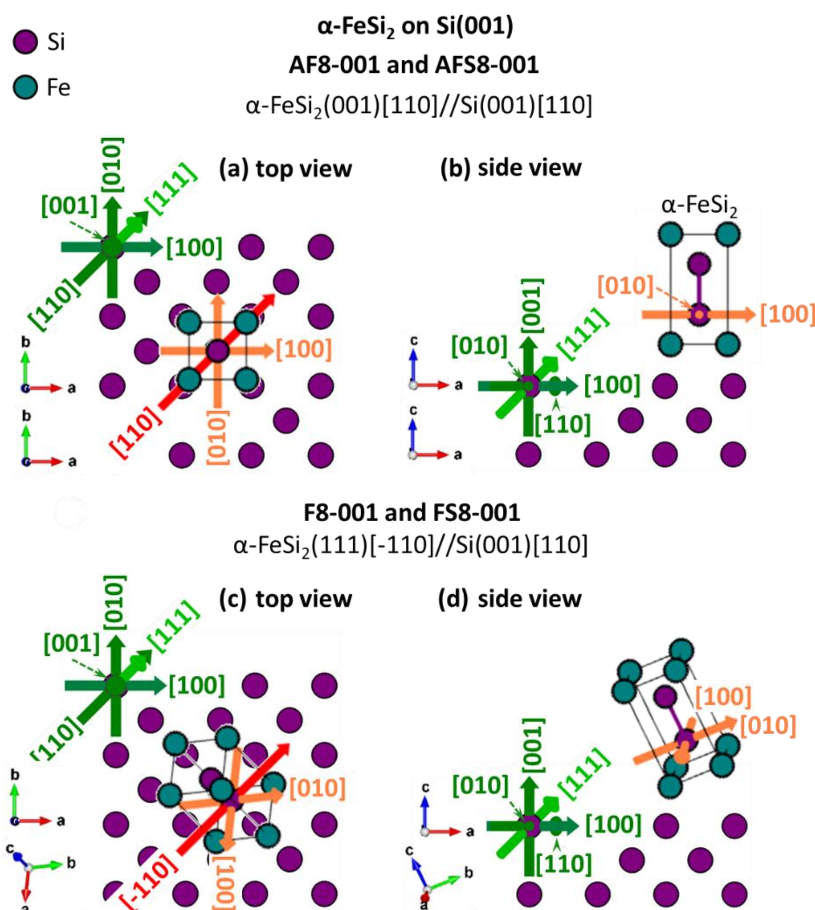

Figure 3.31. Schematic representation of preferential orientation relationships of the α-$FeSi_2$ phase to Si(001) for samples AF8-001 and AFS8-001 – α-$FeSi_2$(001)[110]//Si(001)[110] (a) top and (b) side views, and FS8-001 – α-$FeSi_2$(111)[-110]//Si(001)[110] (c) top and (d) side views concerning the conductivity valleys in Si highlighted with green arrows and in α-$FeSi_2$ highlighted with orange arrows.

Regarding the preferential ORs for samples prepared on *p*-Si(110) substrate (840 °C) α-$FeSi_2$(001)[110]//Si(110)[-110] OR is preferential for AF8-110 and AFS8-110 prepared using Au-assisted Fe deposition and Fe/Si co-deposition (Fig. 3.32 (a, b)) and 2-fold symmetry α-$FeSi_2$(1-12)[-110]//Si(111)[-110] OR or α-$FeSi_2$(001)[110]15°//Si(110)[-112] OR inversed as α-$FeSi_2$(-112)[-110]//Si(11-1)[-110] OR or α-$FeSi_2$(001)[-110]165°//Si(110)[-112] OR is preferential for F8-110 and FS8-110 samples, prepared using Au-free Fe deposition and Fe/Si co-deposition (Fig. 3.32 (c, d)). The minimum angle for both these ORs is ζ_{min} = 35.3°.

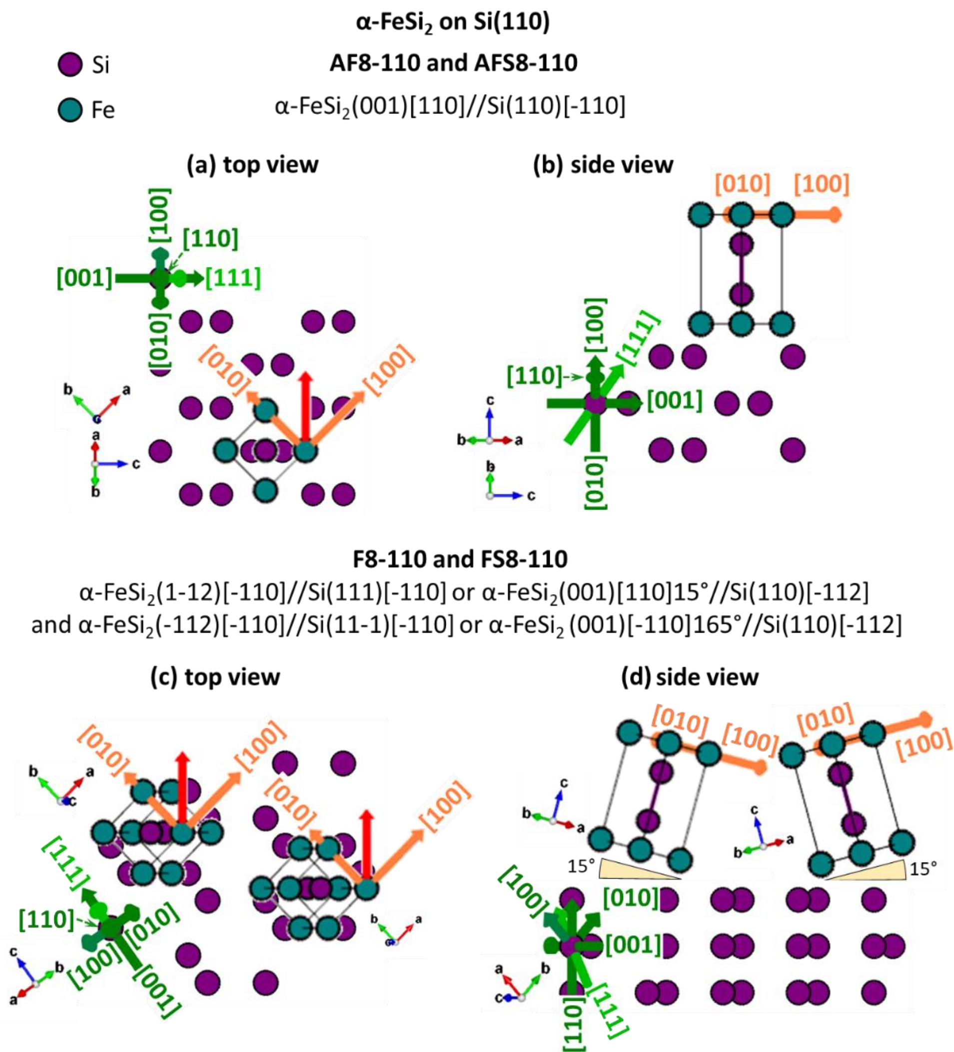

Figure 3.32. Schematic representation of preferential orientation relationships of the α-$FeSi_2$ phase to Si(110) for samples AF8-110 and AFS8-110 – α-$FeSi_2$(001)[110]//Si(110)[-110] (a) top and (b) side views, and F8-110 – 2-fold symmetry α-$FeSi_2$(1-12)[-110]//Si(111)[-110] or α-$FeSi_2$(001)[110]15°//Si(110)[-112] inversed as α-$FeSi_2$(-112)[-110]//Si(11-1)[-110] or α-$FeSi_2$ (001)[-110]165°//Si(110)[-112] (c) top and (d) side views concerning the conductivity valleys in Si highlighted with green arrows and in α-$FeSi_2$ highlighted with orange arrows.

Au-assisted Fe deposition on *p*-Si(111) substrate (840 °C) (AF8-111) results in formation of the preferential α-$FeSi_2$(001)[110]//Si(111)<-110> OR (Fig. 3.33 (a)). In contrast, Au-free Fe deposition and Fe/Si co-deposition on *p*-Si(111) substrate (840 °C) (F8-111, FS8-111) leads to the formation of 3-fold symmetry preferential α-$FeSi_2$(112)[-110]//Si(111)<-110> OR rotated about its surface normal by steps of 120° (Fig. 3.33 (b)). The minimum angles for these ORs are ζ_{min} = 0.0° for the α-$FeSi_2$(001)[110]//Si(111)<-110> OR and ζ_{min} = 1.2° for the 3-fold symmetry α-$FeSi_2$(112)[-110]//Si(111)<-110> OR.

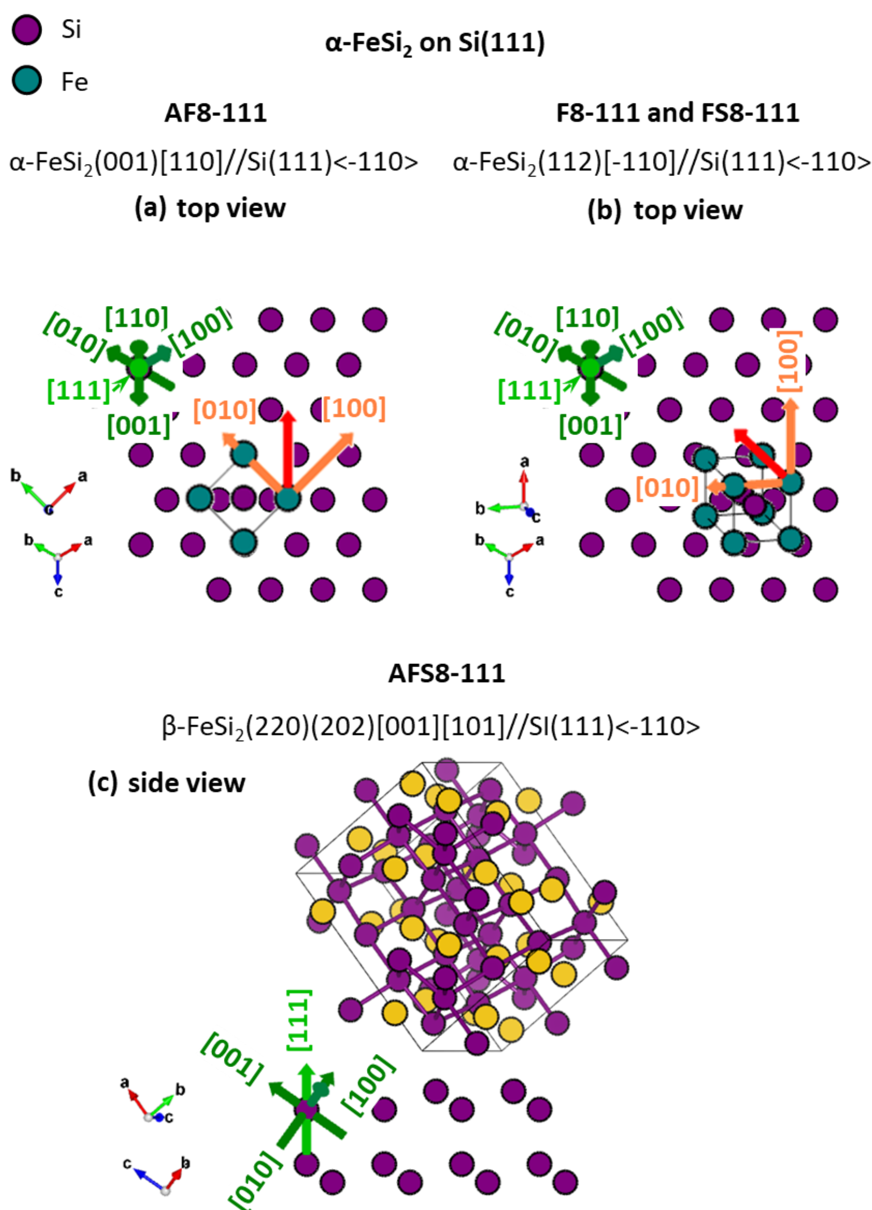

Figure 3.33. Schematic representation of preferential orientation relationships of the α-$FeSi_2$ phase to Si(111) (a) top of the α-$FeSi_2$(001)[110]//Si(111)<-110> OR (AF8-111), (b) top view of 3-fold symmetry preferential α-$FeSi_2$(112)[-110]//Si(111)<-110> OR (F8-111 and FS8-111) and (c) side view of β-$FeSi_2$(220)(202)[001][101]//Si(111)<-110> OR (AFS8-111) concerning the conductivity valleys in Si highlighted with green arrows and in α-$FeSi_2$ highlighted with orange arrows.

Additionally, for the sample AFS8-111, the semiconductor β-$FeSi_2$ phase is preferential. In this work, we study the formation of M/S contacts, and, in this manner, observed orientation relationships of the β-$FeSi_2$ phase with *p*-Si substrates were not studied further. Fig. 3.33 (c) presents the β-$FeSi_2$(220)(202)[001][101]//Si(111)<-110> OR, which was observed earlier in thin films prepared by chemical vapor deposition [286], by magnetron-sputter epitaxy [279] and investigated in terms of application in solar cells [168].

The conductivity channels in α-$FeSi_2$, attributed to [100] and [010] directions, lying in the α-$FeSi_2$(001) lattice plane, are highlighted with orange arrows, and x||[100], y||[010], z||[001], v||[110], and w||[111] crystallographic directions attributed to conductivity valleys in Si are shown with green arrows, red arrows show the orientation direction of the α-$FeSi_2$ unit cell. Si substrate and α-$FeSi_2$ unit cell's orientation is also shown with *a*, *b*, *c* vectors. The angles ζ between the α-$FeSi_2$(001) and Si[100], Si[010], Si[001], Si[110], and Si[111] directions for the different ORs are summarized in Table 3.10.

Table 3.10. *Summary of the angles between the α-$FeSi_2$(001) lattice plane and Si[100], Si[010], Si[001], Si[110], and Si[111] directions (ζ) for different orientation relationships of α-$FeSi_2$ crystallites prepared using Au-assisted (AF8 and AFS8) and Au-free (F8 and FS8) Fe deposition and Fe/Si co-deposition at substrate temperature of 840 °C under ultrahigh vacuum conditions on p-Si(001), p-Si(110) and p-Si(111) substrates.*

Sample	Orientation Relationship	ζ				
		Si[100]	Si[010]	Si[001]	Si[111]	Si[110]
AF8-001 **AFS8-001**	α-$FeSi_2$(001)[110]//Si(001)[110] α-$FeSi_2$(001)[110]//Si(001)[100]	90.0°	90.0°	0.0°	54.7°	90.0°
F8-001 **FS8-001**	α-$FeSi_2$(111)[-110]//Si(001)[110]	131.5°	48.5°	69.7°	78.4°	90.0°
AF8-110 **AFS8-110**	α-$FeSi_2$(001)[110]//Si(110)[-110]	45.0°	45.0°	90.0°	35.3°	35.3°
F8-110 **FS8-110**	α-$FeSi_2$(1-12)[-110]//Si(111)[-110] α-$FeSi_2$(-112)[-110]//Si(11-1)[-110]	45.0°	45.0°	90.0°	35.3°	35.3°
AF8-111 **AFS8-111**	α-$FeSi_2$(001)[110]//Si(111)<-110>	54.7°	54.7°	54.7°	0.0°	35.2°
F8-111 **FS8-111**	α-$FeSi_2$(112)[-110]//Si(111)<-110>	89.1°	89.1°	1.2°	52.5°	88.7°

3.5 Temperature-dependent resistance of $FeSi_2$/Si system

Electron transport of $FeSi_2$ crystallites prepared on *p*-Si(100), *p*-Si(110) and *p*-Si(111) substrates of hole conduction type with carrier concentration $N_a = 3 \cdot 10^{15}$ cm^{-3} and resistivity (ρ) is in the range of 5-15 Ω·cm was measured using of four point-probe measurements of resistivity in the range from 100 K to 800 K (Ch. 2.3.3). Prepared $FeSi_2$ crystallites on the Si substrates are considered as systems, in which the current flows through three channels, i.e., surface state ($FeSi_2$ crystallites), surface space-charge (SSC) layer [287] and bulk state [288] (Fig. 3.34 (a)). Thus, the resistance measured by the four-point probe method contains the contributions from all three channels, and it isn't easy to separate them [288]. The current flows through the Si substrate, including the SSC layer and bulk state, and occurs along different crystallographic directions x||[100], y||[010], z||[001], v||[110], and w||[111] (Fig. 3.30) attributed to 6 conductivity valleys of Si [284], as it was discussed in Ch. 3.4. Figure 3.34 (a) exemplarily demonstrates the current flowing through <100> direction parallel to the (001) cut plane of Si(001) substrate. Prepared $FeSi_2$ crystallites on Si substrates can be considered as a system of interconnected back-to-back Schottky diodes. Figure 3.34 (b) presents the equivalent electrical circuit of such $FeSi_2$/Si system, where a set of parallelly connected back-to-back Schottky diodes with different characteristics are interconnected, i.e. D^a_i and D^b_j diodes are connected in opposite directions to each other, where i and j are referred to the 1, 2, 3… diode in the set (Fig. 3.34 (b)).

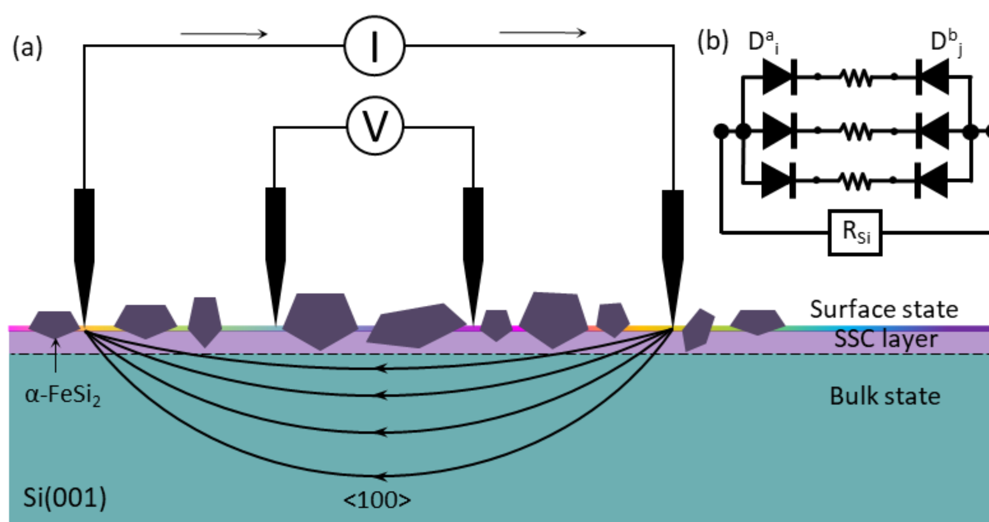

Figure 3.34. (a) Illustration of four-point probe method to measure the electrical resistivity of the α-$FeSi_2$ crystallites on Si(001) substrate, the distribution of current flowing in <100> direction of Si(001) substrate is schematically drawn. (b) Equivalent electrical circuit of the set of parallel matched interconnected back-to-back Schottky diodes, considering the Si volume resistance contribution.

In this case, we have a total current flowing through a set of diodes and two voltage drops on the individual sets of diodes, one polarized in the forward direction and one polarized in the reverse direction [289].

Fig. 3.35 demonstrates the temperature dependence of resistivity of $FeSi_2$ crystallites grown on *p*-Si(001) (Fig. 3.35 (a)), *p*-Si(110) (Fig. 3.35 (b)), *p*-Si(111) (Fig. 3.35 (c)). The Si-bulk state affects the resistivity, the same as series resistance (Ch. 1.2.3). The temperature dependence of p-Si is highlighted with a dotted black line. At the same time, samples containing $FeSi_2$ crystallites with larger interface areas, according to the morphological analysis (see Ch. 3.2), exhibited lower resistivity without a sharp increase with temperature decreasing. Here, Fig. 3.35 (a) shows the temperature dependencies of resistivity for $FeSi_2$ crystallites prepared on *p*-Si(001) substrate, among which at 100 K, the maximum of resistivity ρ_{max} of α-$FeSi_2$ crystallites of samples AFS8-001 and FS8-001, obtained during Fe/Si co-deposition with/without Au at substrate temperature of 840°C, is observed to be 4 orders of magnitude higher than for those of sample AF8-001 and F8-001 obtained at the same conditions, but using Fe reactive deposition. The same effect is specified for $FeSi_2$ crystallites prepared on *p*-Si(111) substrate (Fig. 3.35 (c)), where at

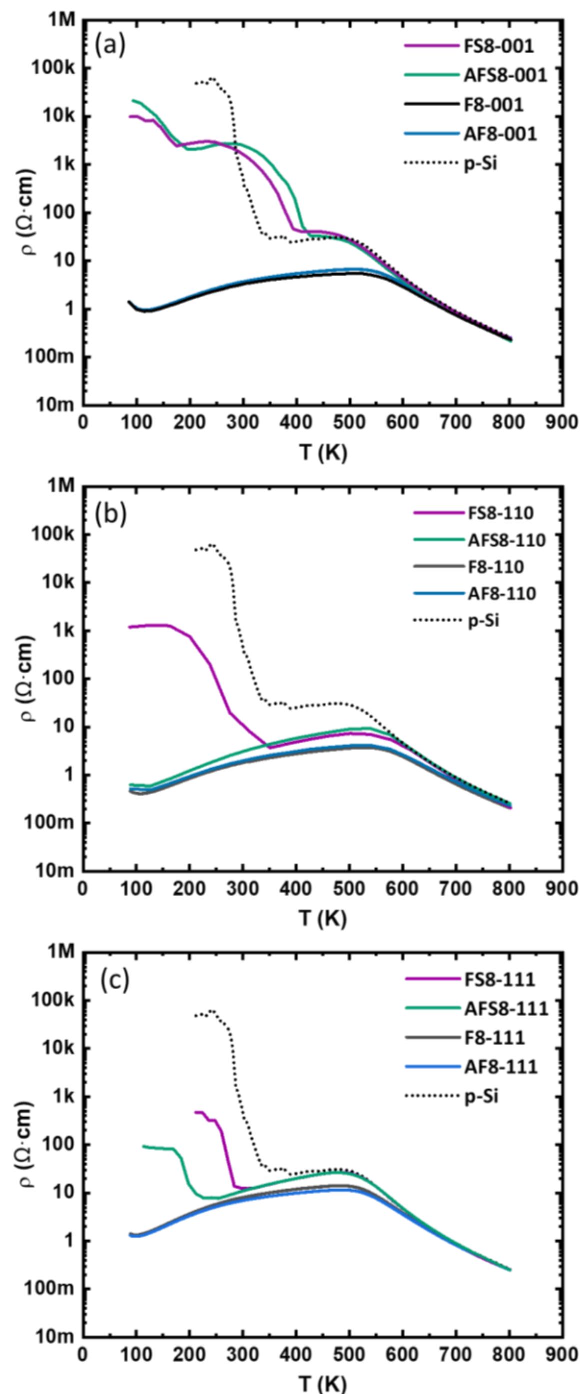

Figure 3.35. Temperature dependences of resistivity of the $FeSi_2$ crystallites prepared on (a) p-Si(001), (b) p-Si(110) and (c) p-Si(111) substrates using Au-assisted (AF) and Au-free (F) Fe deposition, and Au-assisted (AFS) and Au-free (FS) Fe/Si co-deposition at substrate temperatures 840 °C measured using a four-probe method in the range from 100 K to 800 K. Dashed black line represents temperature dependence of resistivity of p-Si substrate.

temperatures of about 100K for sample AFS8-111 and ~200K for FS8-001 sample, also obtained during Fe/Si co-deposition with/without Au at substrate temperature of 840°C, the saturated resistivity ρ_{max} is observed to be 2 and 3 orders of magnitude higher than for samples AF8-111 and F8-111 obtained using Fe reactive deposition. Regarding the $FeSi_2$ crystallites on the *p*-Si(110) substrate (Fig. 3.35 (b)), the ρ_{max} of the FS8-110 sample only is observed to be 3 orders of magnitude higher than for other samples obtained on the *p*-Si(110) substrate. Such a difference is attributable to the size of the prepared α-$FeSi_2$ crystallites and, concerning this, to the interface areas between the crystallites and the substrate surface. Thus, even though α-$FeSi_2$ crystallites of the AFS8-110 sample were also obtained during Au-assisted Fe/Si co-deposition at the substrate temperature of 840°C (Fig. 3.9 (b)), demonstrating large interface areas with Si substrate due to the wire-like shape. In this way, it was observed that the average crystal area $\bar{A}$ of sample AFS8-110 is ~7.8 times larger in comparison with the crystal area of sample FS8-110 (Ch. 3.2.2), which is attributed to the metal/semiconductor (M/S) interface area. In this manner, the difference in resistivity could be explained by the strong influence of the M/S interface area. According to the scanning electron microscopy data (Ch. 3.2.1), all samples obtained without Fe/Si co-deposition at 840°C – AF8 and F8 series – demonstrate interface area with Si about ~7.7 times larger than those obtained using Fe/Si co-deposition (see Tables 2.5, 2.6, 2.7) and therefore the formation temperature of Schottky barriers for the α-$FeSi_2$/Si system with smaller M/S interface area (less than ~$75\cdot10^3$ nm^2) is 100-400K (Fig. 3.35). This can be applicable to a field-effect transistor operating at room temperatures.

For the samples of α-$FeSi_2$ crystallites with large interface area (more than $200\cdot10^3$ nm^2) on Si(110) substrate (F7-110, F8-110 samples), the temperature dependence of resistivity was measured from 5-300 K. Fig. 3.36 (a) shows a sharp increase with the temperature decrease at ~100K for both samples, but ρ_{max} has different values Fig. 3.36 (b). Thus, for sample F7-110 with M/S interface area ~$256\cdot10^3$ nm^2 $\rho_{max} \approx 186.9$ Ω·cm and F8-110 sample, which has M/S interface area ~$863\cdot10^3$ nm^2, $\rho_{max} \approx 8.9$ Ω·cm. According to the structural analysis (Ch. 3.3.2), α-$FeSi_2$ crystallites grown on *p*-Si(110) using Au-free Fe deposition demonstrate equal preferential 2-fold symmetry α-$FeSi_2$(1-12)[-110]//Si(111)[-110] orientation relationship (OR) inversed as the α-$FeSi_2$(-112)[-110]//Si(11-1)[-110] OR for both of F7-110 and F8-110 samples. These ORs have the same minimum angle *ζ* between α-$FeSi_2$(001) and Si[100], Si[010], Si[001],

Si[110], and Si[111], introduced in Ch. 3.4, but the average crystallite area of the F7-001 sample is ~3.5 times smaller than of those for the F8-001 sample. Thus, the difference between ρ_{max} values of ~20 times originated from the ~3.5 times difference in average M/S interface area (Fig. 3.36). Similar effects were observed on GaAs-graphene and Si/Al heterostructures [290], where authors show that the area of the M/S interface strongly influences the Schottky barrier height.

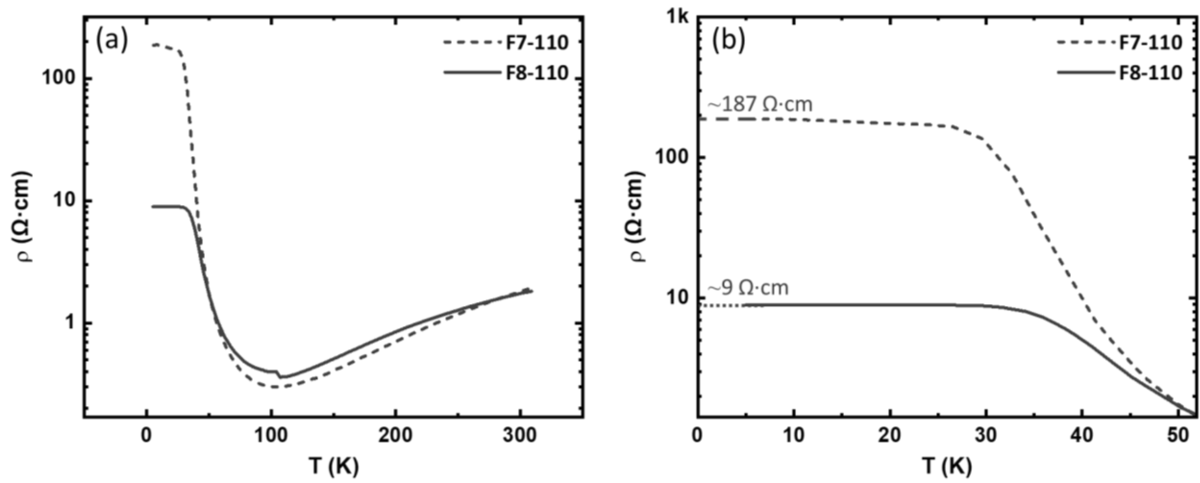

Figure 3.36. Temperature dependencies of resistivity measured using four-point probe method for α-$FeSi_2$ crystallites grown using Au-free Fe deposition on p-Si(110) at the substrate temperature of 740°C (F7-110) and 840°C (F8-110) with preferential 2-fold symmetry orientation relationship of the α-$FeSi_2$(1-12)[-110]//Si(111)[-110] OR inversed as the α-$FeSi_2$(-112)[-110]//Si(11-1)[-110] OR in the range of (a) 5 to 300 K, (b) 5 to 50 K. The difference between ρ_{max} values of about 20 times originated from the ~3.5 times difference in average M/S interface area.

Furthermore, considering the approach presented in [28], the thermionic emission theory is a generally accepted physical model of current transfer for the system of interconnected $FeSi_2$/Si back-to-back Schottky diodes. The expression for total current for an M/S interface area also called the diode area A_d, reads

$$I = I_0 \left[exp\left(\frac{qU_0}{k_B T}\right) - 1\right], \tag{3.3}$$

with

$$I_0 = A_d \mathcal{A} T^2 exp\left(-\frac{q\varphi_B}{k_B T}\right) \text{ - is the saturation current,} \tag{3.4}$$

where $\mathcal{A}$ is the Richardson constant (32 A/cm^2·K^2 for p-Si), T is the temperature in Kelvin, U_0 is applied voltage, q is the electron charge, k_B is the Boltzmann constant and φ_B is the Schottky barrier height (SBH). In this manner, the apparent φ_B can be determined using

$$\varphi_B = \frac{k_B T}{q} ln\left(\frac{I_0}{A_d \mathcal{A} T^2}\right). \quad (3.5)$$

Thus, according to the observed experimental data, the diode area A_d is inversely proportional to resistivity, which confirms the earlier introduced physical model of current transfer.

Based on structural analysis of α-$FeSi_2$ crystallites prepared on *p*-Si(001) substrate using Au-assisted and Au-free Fe/Si co-deposition at substrate temperature 840°C (AFS8-001 and FS8-001), estimated preferential ORs for AFS8-001 is the α-$FeSi_2$(001)[110]//Si(001)[110] OR (45° rotated as the α-$FeSi_2$(001)[110]//Si(001)[100] OR) with ζ = 0° and for FS8-001 is the α-$FeSi_2$(111)[-110]//Si(001)[110] OR with ζ = 48.5° for which three plateaus of resistivity and temperatures of resistivity decrease are observed (Fig. 3.37) (based on the 1st derivative of a curve). Thus, for the α-$FeSi_2$(001)[110]//Si(001)[110] OR, the first resistivity maximum is ρ_{max_1} ≈ 21265 Ω·cm and starts to decrease at T ≈ 210 K, the second is ρ_{max_2} ≈ 2741 Ω·cm and starts to decrease at T ≈ 425 K, and the third is ρ_{max_3} ≈ 33 Ω·cm influenced by Si-bulk (green curve in Fig. 3.37). A similar behavior is observed for the α-$FeSi_2$(111)[-110]// Si(001)[110] OR, which demonstrates the first maximum resistivity of ρ_{max_1}≈ 9861.2 Ω·cm, which starts to decrease at T ≈ 189 K, the second of ρ_{max_2}≈ 3070 Ω·cm decreasing at T ≈ 408 K, and the third with ρ_{max_3} ≈ 41 Ω·cm (magenta curve in Fig. 3.37).

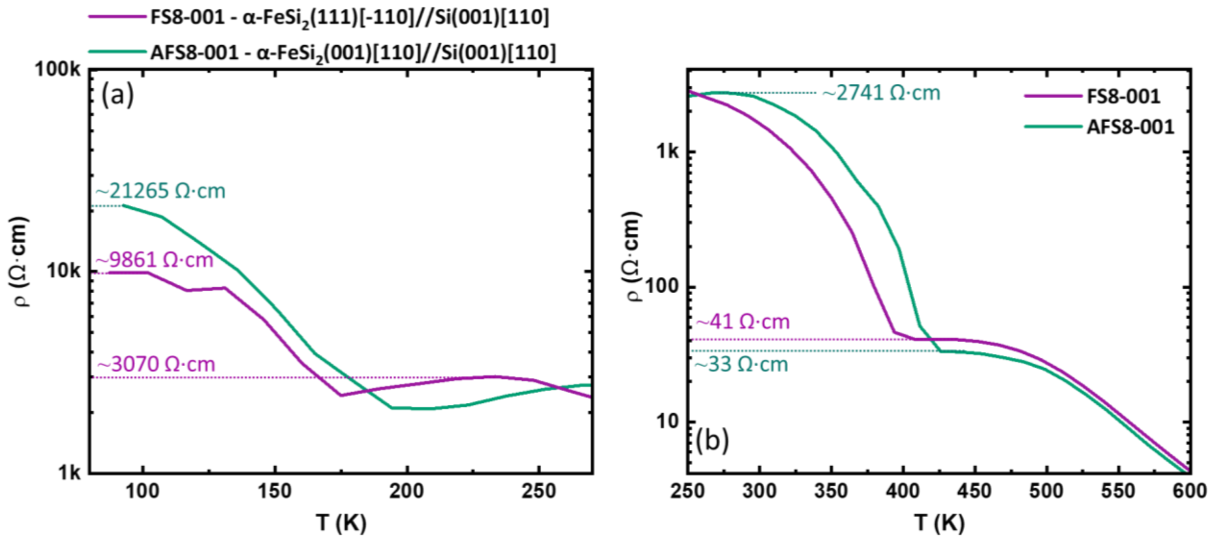

Figure 3.37. Temperature dependencies of resistivity of the $FeSi_2$ crystallites prepared on p-Si(001) using Au-assisted and Au-free Fe/Si co-deposition at substrate temperatures 840 °C (AFS8-001 and FS8-001) with preferential orientation relationships α-$FeSi_2$(001)[110]// Si(001)[110] and α-$FeSi_2$(111)[-110]//Si(001)[110], respectively, in the range of (a) 75 to 275 K, (b) 250 to 600 K.

According to the structural analysis of α-$FeSi_2$ crystallites prepared on *p*-Si(110) and *p*-Si(111) substrates using Au-assisted and Au-free Fe/Si co-deposition at substrate temperature 840°C. Sample FS8-110 demonstrates the preferential 2-fold symmetry α-$FeSi_2$(1-12)[-110]//Si(111) [-110] orientation relationship (OR) inversed as the α-$FeSi_2$(-112)[-110]//Si(11-1)[-110] OR. Figure 3.39 (a) presents this system's temperature dependence of resistivity and demonstrates the presence of two plateaus of resistivity with different temperatures of resistivity increase. Here, the first increase of resistivity shows ρ_{max_1}≈ 1197 Ω·cm and starts to decrease at T ≈ 313 K, the second has ρ_{max_2}≈ 7 Ω·cm and is comparable with one of the AFS8-110 sample, which has the α-$FeSi_2$(001)[110]//Si(110)[-110] preferential OR and shows ρ_{max} ≈ 9 Ω·cm,. Since the AFS8-110 sample demonstrated α-$FeSi_2$ crystallites with a large M/S interface area (~455·10^{-3} μm^2), the resistivity plateau should be observed at a lower temperature, as in the case of the F8-110 sample (Fig. 3.37).

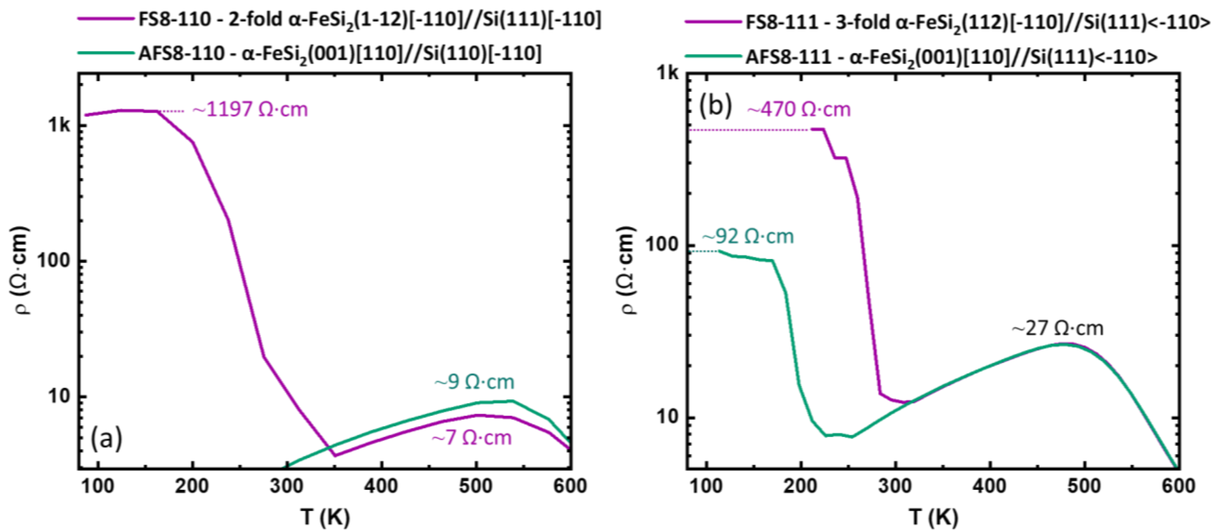

Figure 3.38. Temperature dependencies of resistivity of $FeSi_2$ crystallites prepared using Au-assisted and Au-free Fe/Si co-deposition at substrate temperatures 840 °C (a) on p-Si(110) (AFS8-110 and FS8-110) with preferential 2-fold symmetry α-$FeSi_2$(1-12)[-110]//Si(111)[-110] orientation relationship (OR) inversed as the α-$FeSi_2$(-112)[-110]//Si(11-1)[-110] OR for FS8-110 and (b) on p-Si(111) (FS8-111 and AFS8-111) with 3-fold symmetry α-$FeSi_2$(112) [-110]//Si(111)<-110> and α-$FeSi_2$(001)[110]//Si(111)<-110> preferential ORs.

Regarding the samples on *p*-Si(111) substrate (Fig. 3.38 (b)), the structural analysis shows the formation of 3-fold symmetry of preferential α-$FeSi_2$(112)[-110]//Si(111)<-110> OR rotated about its surface normal by steps of 120° for the FS8-111 sample, obtained using Au-free Fe/Si co-deposition. As in the previous two cases, the presence of two plateaus of resistivity at different temperatures of resistivity decrease is also attributable to this sample. Thus, the first

plateau of resistivity, the influence of the Si-bulk state, has ρ_{max_1} ≈ 470 Ω·cm and starts to decrease at T ≈ 225 K, the second has ρ_{max_2} ≈ 27 Ω·cm. Sample AFS8-111, obtained using Au-assisted Fe/Si co-deposition, demonstrates the presence of α-FeSi$_2$(001)[110]// Si(111)<-110>, which, according to the structural analysis is not preferential OR, and co-exists with the preferential semiconductor β-FeSi$_2$ phase (Ch. 3.3.3), as it was also shown for the FS8-110 sample (Fig. 3.39 (a)). Here, the first maximum resistivity of ρ_{max_1} ≈ 92 Ω·cm decreasing at T ≈ 295 K is observed, and the second with ρ_{max_2} ≈ 27 Ω·cm is comparable with the FS8-111 sample and influenced by Si-bulk resistivity.

Table 3.12. *Summary of preferable orientations (OR), maximum resistivity (ρ_{max}), temperature of resistivity decrease, minimum ζ angle and the average area ($\bar{A}$), for samples of the α-FeSi$_2$ crystallites prepared using Au-assisted (AF8 and AFS8) and Au-free (F8 and FS8) Fe deposition and Fe/Si co-deposition under ultrahigh vacuum conditions on p-Si(001), p-Si(110) and p-Si(111) substrates (840 °C).*

Sample	Preferential OR	ρ_{max}, Ω·cm	T, K	ζ°	$\bar{A}$, 10^3 nm^2
AFS8-001	α-FeSi$_2$(001)[110]//Si(001)[110] α-FeSi$_2$(001)[110]//Si(001)[100]	21265	237	0.0	31 ± 1
FS8-001	α-FeSi$_2$(111)[-110]//Si(001)[110]	9861	189	48.5	40 ± 1
F8-110	α-FeSi$_2$(1-12)[-110]//Si(111)[-110] α-FeSi$_2$(-112)[-110]//Si(11-1)[-110]	9	104	35.3	863 ± 90
FS8-110	α-FeSi$_2$(1-12)[-110]//Si(111)[-110] α-FeSi$_2$(-112)[-110]//Si(11-1)[-110]	1197	313	35.3	59 ± 1
AFS8-111	α-FeSi$_2$(001)[110]//Si(111)<-110>	470	225	0.0	72 ± 1
FS8-111	α-FeSi$_2$(112)[-110]//Si(111)<-110>	92	295	1.2	26 ± 1

According to the analysis of ORs and angles ζ between the α-FeSi$_2$(001) lattice plane and Si[100], Si[010], Si[001], Si[110], and Si[111] directions presented in the previous section, the conductivity of α-FeSi$_2$/Si system can be attributed to the estimated ORs and the angles between the conductivity channels of α-FeSi$_2$ and the Si substrate since the crystallographic orientation and alignment between the two materials directly influence the transport of charge carriers across the interface. Thus, the minimum ζ angle, indicating a closer alignment and better matching between the crystallographic directions of α-FeSi$_2$ and Si, was used to see the dependence between the estimated maximum resistivity ρ_{max} and estimated ORs. Figure 3.39 presents the maximum resistivity ρ_{max} as the function of the minimum ζ angle. Thus, when the crystallographic directions of the conductivity channels in α-FeSi$_2$ align more closely with the conductivity valleys in Si, i.e., the ζ between the α-FeSi$_2$(001) lattice plane and Si[100], Si[010], Si[001], Si[110], and Si[111] directions is close to 0, it promotes more efficient charge

carrier transport across the interface. This alignment allows for a smoother transition and less resistance to the movement of charge carriers between the two materials, resulting in enhanced conductivity.

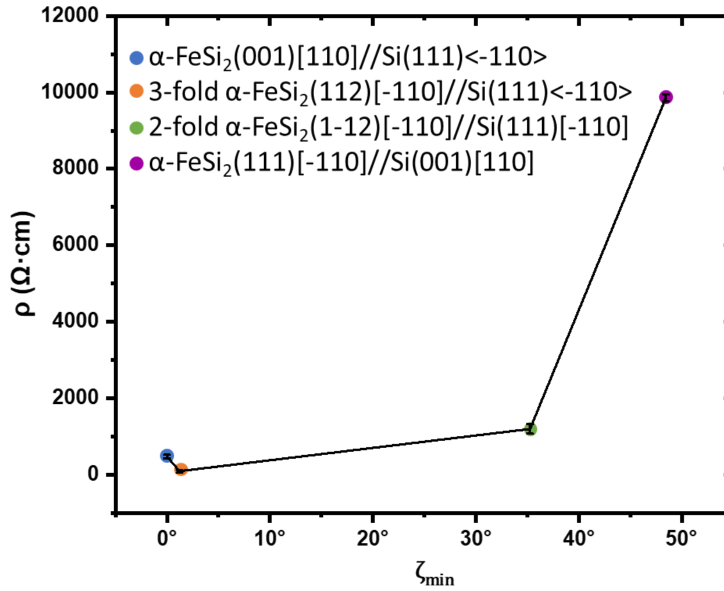

Figure 3.39. Maximum resistivity ρ_{max} as the function of minimum ζ angle, estimated from determined orientation relationships for the α-$FeSi_2$/Si system.

Here, for the α-$FeSi_2$(001)[110]//Si(111)<-110> OR and the 3-fold α-$FeSi_2$(112)[-110]// Si(111)<-110> with angles ζ equal to 0° and 1.2° the resistivity values ρ_{max} = 470 and 92 Ω·cm, which are smaller than for the 2-fold symmetry α-$FeSi_2$(1-12)[-110]//Si(111)[-110] and for the α-$FeSi_2$(111)[-110]//Si(001)[110] ORs with angles ζ equal 35.3° and 48.5° the resistivity value increases ρ_{max} = 1197 and 9861 Ω·cm.

According to the observed temperature dependencies of resistivity, in the studied $FeSi_2$/Si system, carrier transport occurs through different crystal facets that are in contact with the *p*-Si substrate since prepared crystallites are embedded in the Si substrate. As a result, several Schottky barriers impact the formation of several maximum resistivity values. To confirm this statement and to describe the observed temperature dependence of resistivity, the model of the equivalent electrical circuit of such $FeSi_2$/Si system, where a set of parallelly connected back-to-back Schottky diodes with different characteristics (Fig. 3.34 (b)) is applied in the framework of thermionic emission theory. Each set of diodes shares the same ideality factor (n), which remains constant over the entire temperature range.

The work function was calculated within the density functional theory (DFT) framework, as presented in [291]. DFT calculations were performed using the CASTEP (CAmbridge Serial Total

Energy Package) [292] plane-wave/pseudopotential code, and further used to calculate the barrier height. The exchange-correlation interactions are treated at the generalized gradient approximation (GGA) level with the density functional of Perdew, Burke and Ernzerhof (PBE) [293] using ultrasoft pseudopotentials [294]. The cut-off energy of the plane wave basis is set to 580 eV. For this scope, the α-$FeSi_2$ unit cell was used for the calculations and the average electrostatic potential along the (001), (100), (110), (101), (102), (111), (112), (214) planes of α-$FeSi_2$ [159,271] for a set of interconnected back-to-back Schottky diodes. The work function A_M was then calculated as

$$A_M = V_{VAC} - E_F, \tag{3.6}$$

where V_{VAC} is the vacuum potential and E_F is the Fermi energy for the α-$FeSi_2$ and Si structures. Using the obtained values of A_M Schottky barrier heights were calculated by

$$\varphi_{b0} = A_M - \chi_S, \tag{3.7}$$

where χ_S is the electron affinity energy of the semiconductor. For a bulk silicon value of 4.05 eV is usually used [60]. The calculated work functions and Schottky barrier heights (SBH) are presented in Table 3.11.

Table 3.11. *Calculated work function and Schottky barrier height (SBH) values within the framework of density functional theory (DFT) for (001), (100), (110), (101), (102), (111), (112), (214) lattice planes of α-$FeSi_2$ forming an interface with Si for non-optimized and optimized α-$FeSi_2$ crystal unit cell.*

non-optimized			optimized		
α-$FeSi_2$	**A_M, eV**	**SBH, eV**	**α-$FeSi_2$**	**A_M, eV**	**SBH, eV**
(110)	4.792	0.268	**(110)**	4.685	0.195
(214)	4.414	0.646	**(214)**	4.348	0.493
(111)	4.278	0.782	**(111)**	4.282	0.778
(001)	4.262	0.798	**(001)**	4.231	0.543
(112)	4.257	0.803	**(102)**	4.227	0.47
(102)	4.168	0.892	**(112)**	4.172	0.353
(101)	3.987	1.073	**(101)**	3.987	0.688
(100)	3.894	1.166	**(100)**	3.807	0.879

Thus, for one set of back-to-back Schottky diodes forming one Schottky barrier through predicted preferable (001), (100), (110), (101), (102), (111), (112), (214) planes of α-$FeSi_2$ to form an interface with silicon, according to theoretical calculations in [159,271], temperature dependencies of resistance were calculated (Fig. 3.40 (a)). The temperatures of the resistivity decrease here are observed to decrease with the increased work function value A_M. Figure

3.40 (b) presents the temperature dependencies of resistance for two sets of interconnected back-to-back Schottky diodes formed by all possible combinations for these planes (001), (100), (110), (101), (102), (111), (112), (214) of α-$FeSi_2$. Thus, several resistivity plateaus are attributed to the existence of two or more Schottky barriers. However, the presented approach does not describe several resistivity plateaus below 450 K.

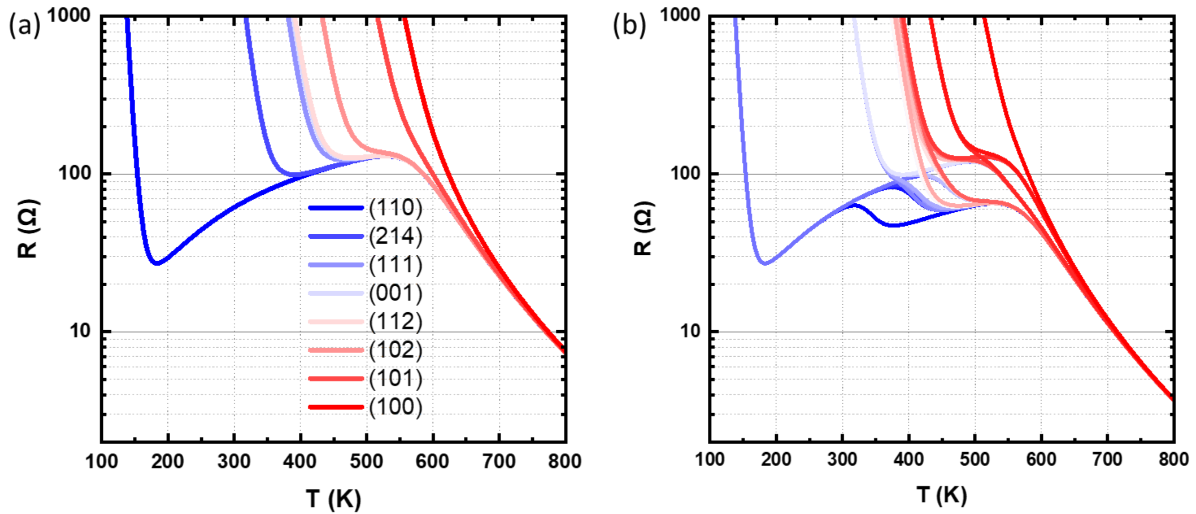

Figure 3.40. Calculated temperature dependencies of resistance for (001), (100), (110), (101), (102), (111), (112), (214) planes of α-$FeSi_2$ according to the theoretically determined work function values for (a) one set and (b) two sets of interconnected back-to-back Schottky diodes.

Thus, the complexity of the system morphology can be considered using the approach presented in [84] and described in Ch. 1.2.3. In this manner, the temperature dependencies of resistance were calculated using the barrier homogeneities as the values of standard deviation σ_s (Fig. 3.41)

$$\varphi_{ap} = \overline{\varphi}_{b0} - \frac{q\sigma_s^2}{2k_B T}, \tag{3.7}$$

where φ_{ap} is the apparent barrier height measured experimentally [85,86]. The observed variation of ideality factor n with temperature in the model is given by [34]

$$\left(\frac{1}{n_{ap}} - 1\right) = -\rho_2 + \frac{q\rho_3}{2k_B T} \tag{3.8}$$

where n_{ap} is the apparent ideality factor, ρ_2 and ρ_3 are coefficients quantifying the voltage deformation of the barrier height distribution, used in our work as -0.316 V and -0.0191 V, respectively [84].

In this manner, the obtained ideality factors (eq. 3.8) and different σ_s standard deviation values are considered to estimate the influence of the barrier inhomogeneities on the

temperature dependencies of resistivity. Figure 3.41 (a) shows calculated temperature dependencies of resistance for barrier height $\varphi_{b0} =$ 1.166 eV corresponding to the α-$FeSi_2$(100) lattice plane with $A_M = 3.894$ eV for different standard deviation values. For the homogeneous barrier $\sigma_s = 0$ eV, the resistance value is not saturated with the temperature decrease. However, when the inhomogeneity increases, the resistance decreases with the temperature. Figure 3.41 (b) presents calculated apparent barrier height φ_{ap} temperature dependencies for different standard deviation values. Here, for the homogeneous barrier $\sigma_s = 0$ eV, the barrier height φ_{b0}= 1.166 eV is constant at the whole temperature range, but with the increase of inhomogeneity values, the barrier height starts to increase with the temperature increase.

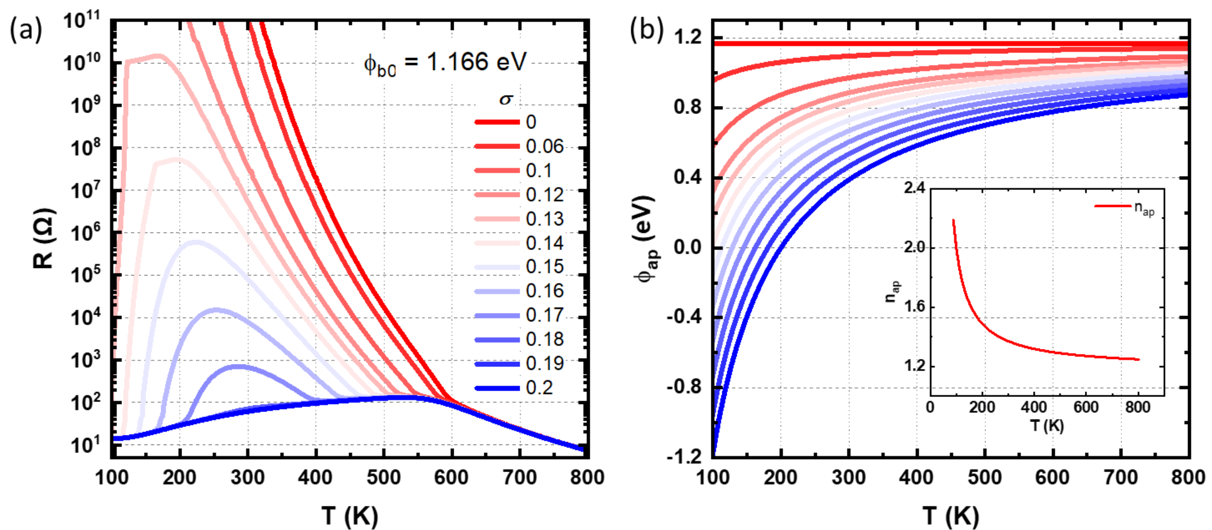

Figure 3.41. (a) Temperature dependencies of resistance for barrier height φ_{b0}= 1.166 eV, corresponding to α-$FeSi_2$(100) lattice plane with A_M = 3.894 eV, for different standard deviation values. (b) Temperature dependencies of the apparent barrier height φ_{ap} for different standard deviation values. The inset presents the temperature dependence of the ideality factor n.

Temperature dependencies of resistance calculated for two sets of interconnected back-to-back Schottky diodes with different barrier heights, considering barrier inhomogeneity σ_s, are presented in Fig. 3.42. Here, Fig. 3.42 (a) demonstrates temperature dependencies of resistance for two sets of interconnected back-to-back Schottky diodes with different barrier heights of φ^b_1 = 0.646 eV with σ_s = 0.104 eV corresponding to α-$FeSi_2$(214) plane and φ^b_2 = 1.073 eV corresponding to α-$FeSi_2$(101) plane for varied values of barrier inhomogeneity σ_s = 0-0.19 eV. The resistance value slightly increases (less than 1 order of magnitude), and resistance plateaus of low values (~30, 50 Ω) are observed at 200-500 K, and

with temperature increase, the resistance values increase before 400K and decrease after. Fig. 3.42 (b) presents the temperature dependencies of resistance for the same system. Still for the first set of diodes, barrier inhomogeneity is decreased σ_S = 0.0911 eV. Due to this, the resistance plateaus are observed at low temperatures for barrier inhomogeneity values of σ_S = 0.17, 0.19 eV for the second set of diodes.

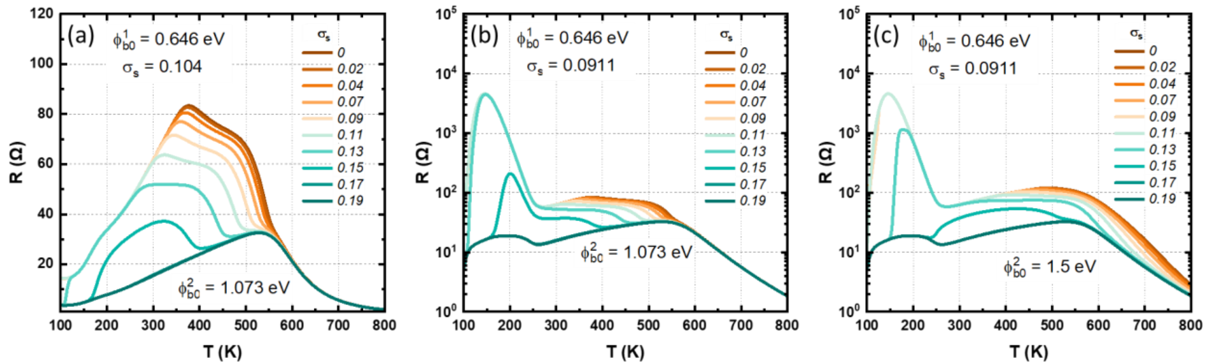

Figure 3.42. Calculated temperature dependencies of resistance for two sets of interconnected back-to-back Schottky diodes with φ^b_1 = 0.646 eV and φ^b_2 = 1.073 eV with barrier inhomogeneity σ_S = (a) 0.104 eV, (b) 0.0911 eV and with σ_S = 0-0.19 eV for the second set; and (c) for φ^b_1 = 0.646 eV and φ^b_2 = 1.5 eV with σ_S = 0.0911 for one set and with σ_S = 0-0.19 eV for the second set.

This result is similar to the experimentally observed temperature dependence of resistivity for a system of the $FeSi_2$/Si (Fig. 3.36), which, based on the presented calculations, can be qualitatively described as a system of two sets of interconnected back-to-back Schottky diodes with different inhomogeneous barrier heights. Fig. 3.42 (c) shows temperature dependencies of resistance for the same system with φ^b_1 = 0.646 eV and previously used σ_S = 0.0911 eV corresponding to α-$FeSi_2$(214) plane and φ^b_2 = 1.5 eV with varied values of barrier inhomogeneity σ_S = 0-0.19 eV. Increased barrier height of the second set of diodes leads to the increased resistance values at the 500-800 K, which qualitatively corresponds to experimentally observed temperature dependencies of resistivity for $FeSi_2$/Si(001) and $FeSi_2$/Si(111) systems (Fig. 3.35 (a, c)).

Summary

Based on the analysis of experimental and calculated data, several factors were identified as significant contributors to the temperature dependence of the electrical resistivity in the $FeSi_2$/Si system, which can be considered as a set of parallel matched interconnected back-to-back Schottky diodes:

- *The average area of $FeSi_2$ crystallites, representing the metal/semiconductor interface area and diode area (A_d), was found to have an inverse relationship with the maximum resistivity (ρ_{max}). This means that the maximum resistivity increases as the average interface area of $FeSi_2$ crystallites with Si decreases.*
- *The alignment of the crystallographic directions of conductivity channels in α-$FeSi_2$ with the conductivity valleys in Si also significantly facilitates efficient charge carrier transport across the interface. The resistivity value of the α-$FeSi_2$/Si system increases as the angle between the conductivity channels in α-$FeSi_2$ and the conductivity valleys in Si increases.*
- *The studied system exhibits multiple plateaus of resistivity attributed to two or more Schottky barriers within the system. These barriers affect the current flow and contribute to variations in resistivity. The resistivity increases with the increased barrier height.*
- *The presence of barrier inhomogeneities within the system influences its overall resistance. As the inhomogeneity increases, the resistance decreases with temperature. This suggests that when the Schottky barriers are less uniform, the resistance of the $FeSi_2$/Si system decreases as the temperature rises.*

Thus, the analysis of temperature dependencies of the $FeSi_2$/Si system revealed that the average area of the $FeSi_2$ crystallites, the presence of multiple Schottky barriers, and the level of barrier inhomogeneities all have significant impacts on the behavior of electrical resistivity in the system. Understanding these factors is important for comprehending and predicting the electrical properties of the $FeSi_2$/Si system as a set of interconnected back-to-back Schottky diodes.

3.6 Summary and discussion

Chapter 3 presented the bottom-up approach for the growth of self-assembled ensembles of α-, β-$FeSi_2$ submicron- and nano- crystallites, using Au-assisted and Au-free conditions on p-Si(001), p-Si(110), and p-Si(111) surfaces using co-deposition of Fe and Si through molecular beam epitaxy and reactive epitaxy.

Detailed characterization of the morphology of prepared $FeSi_2$ crystallites provides valuable aspects of their shapes, orientations, and sizes, which enhance the understanding of their structural properties and potential applications. Several factors, including *Au-assisted growth* and the *Fe/Si atomic flux ratio*, have been identified as important contributors to the tunable crystallite morphology and orientation about a Si substrate.

- *Au-assisted growth* significantly affects the formation of $FeSi_2$ crystallites on Si surfaces, leading to the development of well-defined crystal facets with distinct geometries during the Fe deposition and Fe/Si co-deposition. This process also promotes an endotaxial growth mode, causing the formation of voids in the Si substrate around the silicide crystallites and decreasing their height. In contrast, under Au-free conditions, the crystallites tend to exhibit coalescence, forming continuous films without well-defined morphologies.
- Changes in the *Fe/Si atomic flux ratio* result in a reduction in the size of the crystallites. This is due to a decreasing diffusion length of Fe atoms, leading to the formation of multiple nucleation sites influenced by both deposited Si atoms and Si substrate atoms. Decreasing the atomic Fe/Si flux ratio limits Fe atoms' availability and restricts individual silicide crystallites' growth. Conversely, a temperature change increases the diffusion length of Fe atoms, forming a lower number of crystallites with an increased average interface area of $FeSi_2$ crystallites with Si substrate.

The structural characterization and analysis of the orientation relationships (OR) of α-$FeSi_2$ crystallites also highlight the strong influence of Au-assisted growth on the orientation of the α-$FeSi_2$(001) lattice plane parallel to the Si substrate surface. It is obtained that:

- on *p*-Si(001) substrates, the preferential α-$FeSi_2$(001)[110]//Si(001)[110] OR, 45 degrees rotated as α-$FeSi_2$(001)[110]//Si(001)[100] OR, is observed, with relative orientation fraction of 70-99 %, and is attributed to the formation of well-defined crystal facets with flat surfaces and distinct geometries;

- on *p*-Si(110) substrates, the α-$FeSi_2$(001)[110]//Si(110)[-110] OR with relative orientation fractions of about 65-76% corresponds to the formation of elongated nano and submicron wires along the Si[-110] direction;
- on *p*-Si(111) substrates, the α-$FeSi_2$(001)[110]//Si(111)<-110> OR with relative orientation fractions of about 70% is related to the 2-fold symmetry of triangular nanoplates exhibiting well-defined faceting and flat surfaces.

The conductivity of prepared α-$FeSi_2$/Si systems is attributed to the estimated ORs and the angles between the conductivity channels of the α-$FeSi_2$ and the Si substrate since the crystallographic orientation and alignment between the two materials influence the transport of charge carriers across their interfaces. Thus, the resistivity value of the α-$FeSi_2$/Si system increases as the angle between the conductivity channels in α-$FeSi_2$ and the conductivity valleys in Si increases.

The analysis of experimental and calculated data on the temperature dependencies of resistivity identifies that the average area of the $FeSi_2$ crystallites, attributed to the metal/semiconductor interface area, has an inverse relationship with the resistivity values. The $FeSi_2$/Si system exhibits multiple resistivity plateaus attributed to two or more Schottky barriers within the system. The barrier inhomogeneities within the system influence the system's resistance. As the inhomogeneity increases, the resistance decreases with temperature.

These factors significantly contribute to the behavior of electrical resistivity in the $FeSi_2$/Si system and are important to consider for predicting the electrical properties and designing contacts in microelectronic devices.

Chapter 4

Si nanowire Schottky barrier FETs with Fe source/drain contacts

This chapter presents a top-down nanofabrication approach involving molecular beam epitaxy and electron beam lithography used to obtain silicon nanowire-based Indium-back-gate field-effect transistors with Schottky contacts on silicon-on-insulator substrates with Fe source and drain contact pads. The technological procedure was modified by omission of the second lithography step and increasing the time of wet chemical etching of Fe film. The resulting devices are applied for biomolecular detection based on the source-drain current changes.

4.1 Fabrication procedure

The nanofabrication process of silicon nanowire-based Indium-back-gate field-effect transistors (SiNW FETs) with Schottky contacts on silicon-on-insulator (SOI) with Fe source and drain (S/D) contact pads using the top-down approach represents a multistep process involving thermal evaporation in ultra-high vacuum and electron beam lithography (EBL) described in detail in Ch. 2.1. In this manner, Si NW FETs with Fe S/D contacts were fabricated by EBL combined with wet and dry chemical etching processes on a boron-doped SOI (SIMOX) substrate with a specific resistance of 18 Ω·cm (boron impurity concentration of 10^{15} cm^{-3}), a 100 nm Si(100) layer and a 200 nm thick SiO_2 layer using AZ 2035 nLof negative photoresist (Microchemicals, Germany) and PP-051MS developer (NIOPIK, Russia). Hydrogen peroxide (H_2O_2) and aqueous ammonia (NH_4OH) were used to remove organic impurities and natural oxide from the SOI substrate. Fluorine-containing plasma from CF_4 gas was used for the reactive ion etching (RIE) process. HCl solution (5%) was used for wet chemical etching. A pure (99,95%) iron (Fe) wire was used to prepare S and D contact pads. Deionized distilled (DI) water was used to prepare all solutions for the fabrication process. The lithography template was developed with the help of LayoutEditor software [295] (Fig. 4.1 (a)). Fig. 4.1. (b) presents the optical image of the fabricated nanostructures. Circles (d = 70 μm) represent the contact pads, and the lines between them are the Si NWs. The width of the Si NWs with rectangular contact pads within the row varies from 300 nm to 2 μm and the length of 48 μm is fixed.

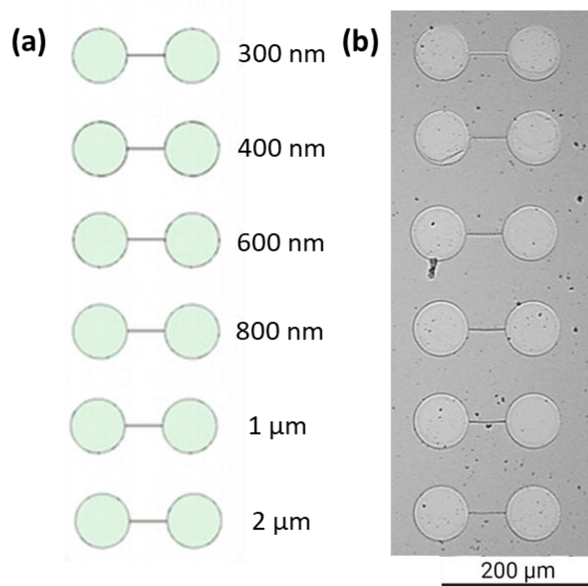

Figure 4.1. (a) Part of the lithography template, designed in the LayoutEditor program, and (b) electron image of the fabricated nanostructures. Here, circles represent the contact pads, and the lines between them are the silicon nanowires with varied widths from 300 nm to 2 µm, and a fixed length of 48 µm.

The process of fabrication of Si NW FETs with different Si NW widths on SOI substrate has the following steps (Fig. 4.2):

1. Cleaning the SOI substrate (Fig. 4.2 (a)) from organic impurities and natural oxide using a solution of NH_4OH:H_2O_2:H_2O (1:1:1) at 80 °C for 2-3 minutes and further rinse with DI water.
2. Fabrication of contact pads (S and D) from a thin Fe layer by EBL:
   1) Fe layer deposition by thermal evaporation in ultra-high vacuum (10^{-8} Pa) at T = 750 °C (Ch. 2.1.2) (Fig. 4.2 (b)).
   2) Spin-coating of a 300 nm thick AZ 2035 nLof negative photoresist (PR) mask on the obtained Fe thin layer surface by centrifugation followed by heat treatment at T ≈ 112°C for 1.5 min.
   3) Exposing the PR-mask with an electron beam according to the template (Fig. 4.1), followed by heat treatment of the mask at 112°C for 1.5 min to activate the polymerization process, and next to remove unexposed areas of the PR-mask in developer PP-051MS (Fig. 4.2 (c)).
   4) Etching of obtained sample in an aqueous HCl solution (5%) for 50 s to remove Fe film in the regions unprotected by the PR-mask. During this time, the isotropic acid penetration under the PR-mask to a depth of about 1 µm was achieved. This method

allowed the dissolving of Fe film in the nanowire area while preserving it on the contact pads (Fig. 4.2 (d)).

3. Reactive ion etching (RIE) with CF_4 plasma generated by the RIE-1701 system (Nordson MARCH) to remove the Si layer uncovered with PR-mask (Fig. 4.2(e)).
4. Indium (In) rubbing [296] into the back side of the SOI substrate to form the back-bottom gate of the FET (Fig. 4.2 (e)).

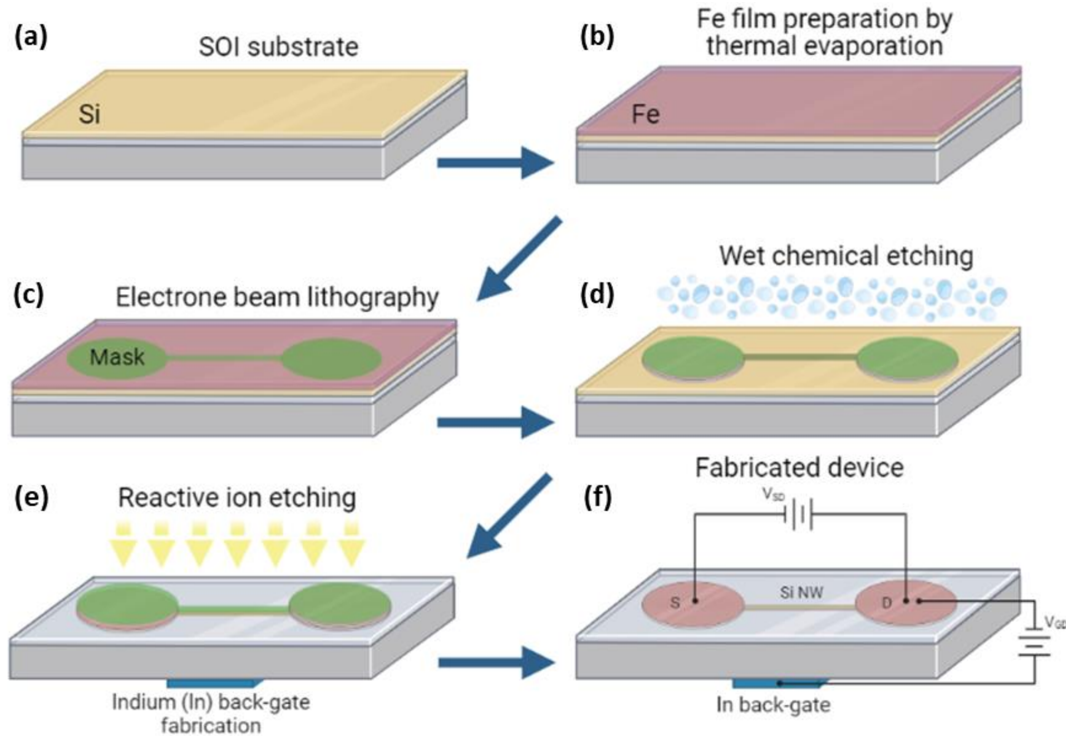

Figure 4.2. The multistep fabrication process of Si NW FET with Fe S/D contact pads using (a) cleaned SOI substrate for (b) Fe layer deposition by thermal evaporation with further (c) spin-coting of photoresist mask for S/D contact pads preparation using electron-beam lithography followed by (d) wet chemical etching to remove Fe film in the regions uncovered with photoresist mask and in nanowire area, and (e) reactive ion etching to remove the Si layer uncovered with photoresist mask with next Indium-doping of back side of the SOI substrate to form back-bottom gate of the (f) fabricated Si NW FET.

Summary

A top-down nanofabrication approach involving thermal evaporation in ultra-high vacuum, electron beam lithography and wet and dry chemical etching was used to prepare Si NW FETs with varied Si NW widths. As a result, the second lithography step, for example, optical lithography, usually used for the fabrication of Si NW FETs, was not required for the preparation of Si NWs due to the modified process of wet chemical etching, which was enough to continue with the anisotropic dry etching step and remove the top Si layer from the exposed areas using CF_4 reactive plasma. Due to this, the Fe/Si contact area was formed under Fe film.

4.2 Morphology of Si NWs and Fe contact pads

The morphology of fabricated silicon nanowires (Si NWs) was investigated using scanning electron microscopy with S5500 SEM system (Hitachi) and atomic force microscopy (AFM) using NanoInk DPN 5000 AFM system. The thickness and morphological homogeneity of the Fe contact pads were analyzed by transmission electron microscopy (TEM) using an S-5500 transmission electron microscope (Hitachi) (Ch. 2.2). TEM cross-section image shows the sharp interface between prepared ~14 nm thick Fe film and the 100 nm Si(100) device layer on the SOI substrate (Fig. 4.3 (a)).

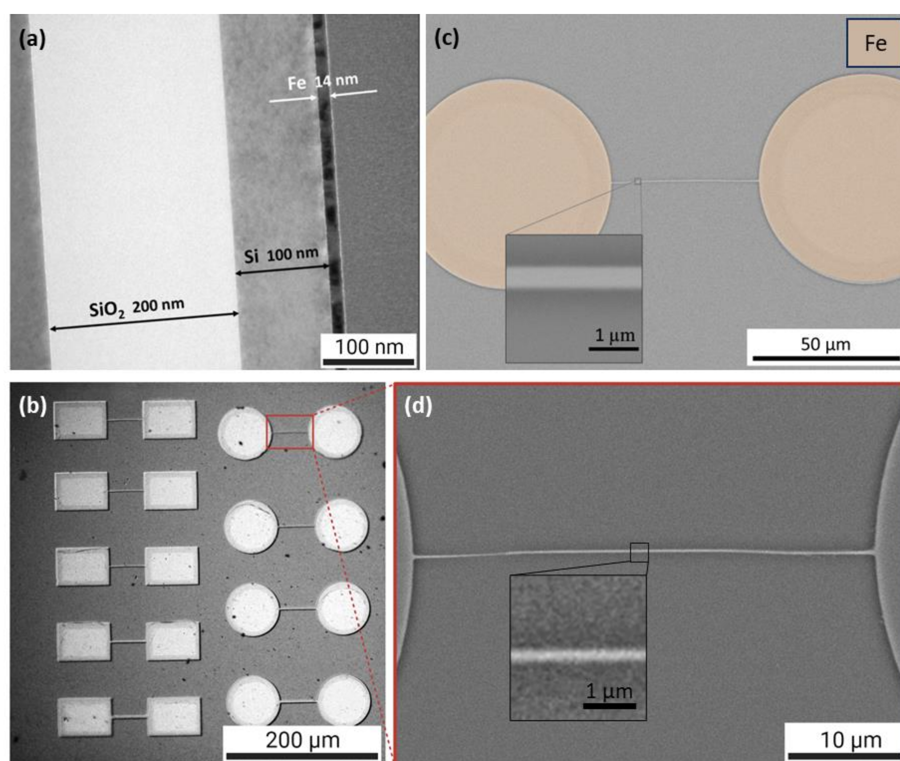

Figure 4.3. (a) TEM cross-section image of the fabricated ~14 nm thick Fe film on the SOI substrate with ~100 nm Si and ~200 nm SiO_2 layers; (b) SEM-image of fabricated Si NWs with contact pads according to the lithography template; (c) SEM-image of Si NW with nominal width of 800 nm in EDS mode highlighting Fe S/D contact pads and (d) SEM-image of Si NW with nominal width of 400 nm.

Figure 4.3 (b) shows SEM-image of the fabricated well-defined Si NWs with contact pads according to the lithography template (Fig. 4.1 (a)). Figure 4.3 (c) presents the SEM-image of fabricated Si NW with a nominal width of 800 nm in energy dispersive spectroscopy (EDS) mode, demonstrating that S/D contact pads are made of Fe and confirms the quality of wet chemical and reactive ion etching processes. Highlighted red rectangle in Fig. 4.3 (b) corresponds to Fig. 4.3 (d) magnified SEM-image of Si NW with a nominal width of 400 nm

demonstrating slightly non-homogeneous thickness along the whole length due to overexposure in HCl acid for isotropic penetration under the photoresist mask to a depth of about 1 μm to dissolve Fe film under the Si NW surface.

The thickness and surface morphology of the fabricated Si NWs were investigated in more detail and compared with the lithography template by atomic force microscopy (AFM) using a DPN 5000 scanning probe microscope (Nanoink Ink., USA). For the AFM study, the surface of the fabricated Si NW FETs on the SOI substrate was preliminarily cleaned with ethanol or isopropanol, followed by nitrogen drying. The AFM measurements were performed in a semi-contact scanning mode (AC mode), as explained in detail in Ch. 2.2. The AFM results (Fig. 4.4) were processed using the Gwyddion software [270]. Experimental widths were measured by taking 1D profiles along the numbered lines on AFM scans. 3D profiles demonstrate surface inhomogeneities and the maximum height of prepared Si NWs.

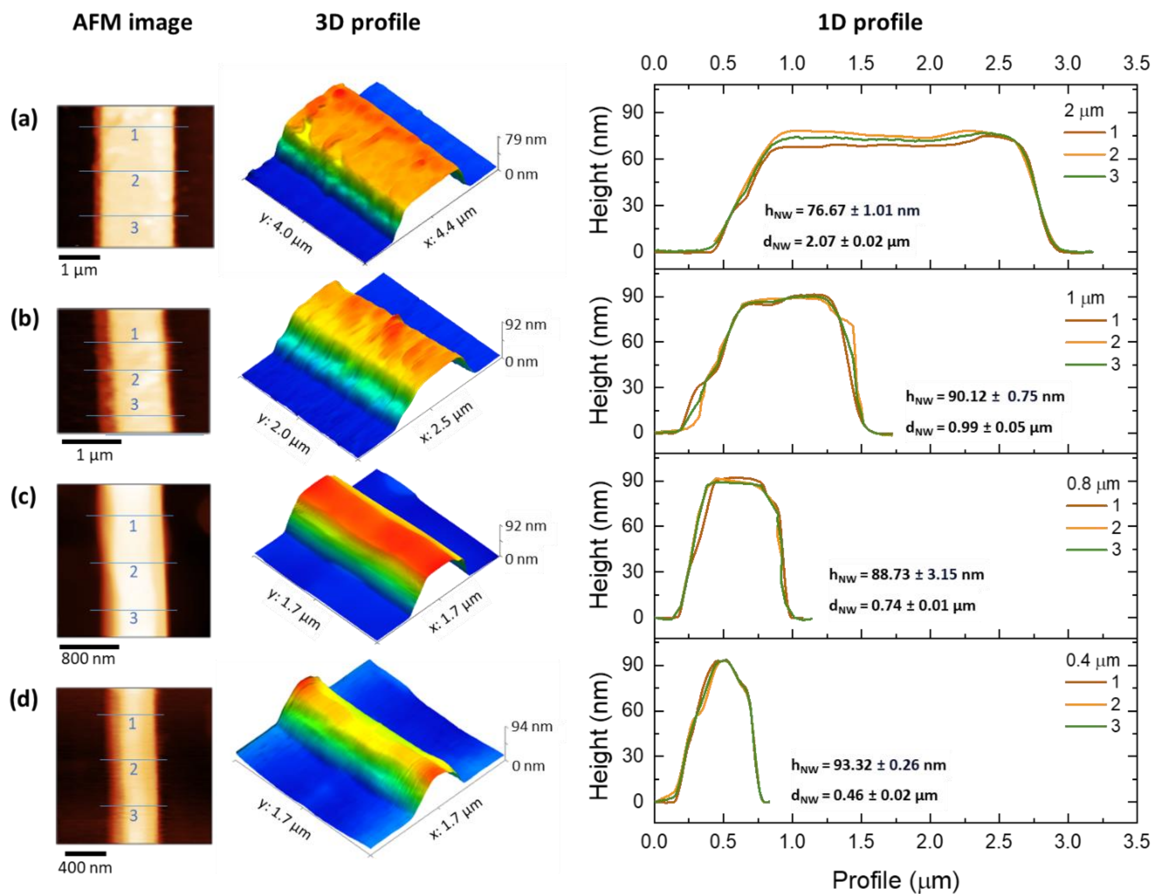

Figure 4.4. AFM images, 3D profiles and 1D profiles of Si NWs with determined width of (a) ~2 μm, (b) ~1 μm, (c) ~0.8 μm, (d) ~0.4 μm respectively. Here, 1D profiles were taken along the numbered lines on AFM images. The average height and width are shown for every nanowire.

The experimentally measured widths of prepared Si NWs differ from the nominally set values by no more than 5%, except for Si NW with a nominal width of 0.8 μm experimentally measured as ~0.74 μm. The height of prepared Si NWs does not correspond to the initial thickness of the Si layer (~100 nm), which is explained by the isotropic HCl (5%) acid penetration under the photoresist mask to dissolve Fe film in the nanowire region, which was successfully achieved according to SEM EDS measurements (Fig. 4.3 (c)). However, it should be noted that the etching process also led to a reduction in the thickness of the Si layer. The average height (h_{NW}) and width (d_{NW}) of prepared Si NWs are summarized in Table 4.1. The error is determined as a standard deviation.

Table 4.1. *AFM determined summary of the average height (h_{NW}) and width (d_{NW}) of prepared Si NWs.*

Si NW, µm	h_{NW}, nm	d_{NW}, µm
0.4	93.33 ± 0.26	0.46 ± 0.02
0.8	88.74 ± 3.16	0.74 ± 0.01
1.0	90.13 ± 0.75	0.99 ± 0.05
2.0	76.67 ± 1.02	2.07 ± 0.02

Summary

Presented morphological characterization highlights that the simplified fabrication procedure by the omission of the second lithography step, described earlier (Ch. 4.1), allowed the successful preparation of Si NW FETs with varied Si NW widths (~0.4, ~0.8, ~1 and ~2 µm) due to modified process of wet chemical etching, which also resulted in the reduction of the height of prepared Si NWs.

4.3 Electron transport in Si NW FETs

Electron transport in prepared silicon nanowire-based Indium-back-gate field-effect transistors (Si NW FETs) with Schottky contacts with Fe source and drain (S/D) contact pads (Fig. 4.5) were investigated by measuring the source-drain current (I_{SD}) versus gate-drain (V_{GD}) voltage (transfer) and source-drain voltage (V_{SD}) (output) characteristics at room temperature. The measurements of transport characteristics were carried out using the Lakeshore EMPX-HF 2 probe station (Lake Shore Cryotronics) (Ch. 2.3.2).

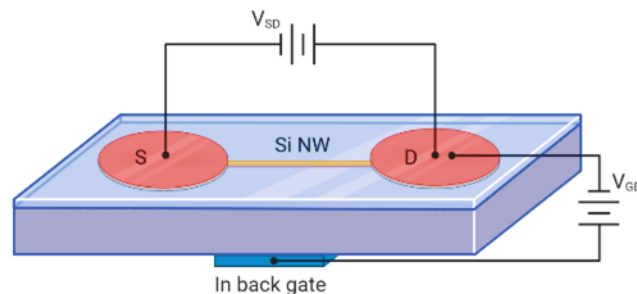

Figure 4.5. Schematic representation of prepared silicon nanowire-based Indium-back-gate field-effect transistor (Si NW FET) with Schottky contacts with Fe source and drain (S/D) contact pads and measurement scheme of source-drain current (I_{SD}) versus gate-drain (V_{GD}) voltage (transfer) and source-drain voltage (V_{SD}) (output) characteristics.

The room-temperature gate-drain (transfer) characteristics for prepared Si NW FETs with varied Si NW widths ~0.4 µm (Fig. 4.8 (a)), ~0.8 µm (Fig. 4.8 (b)), ~1 µm (Fig. 4.8 (c)) and ~2 µm (Fig. 4.8 (d)) demonstrate an asymmetric behavior at positive (forward) and negative (reverse) source-drain bias V_{SD}.

Increasing the gate voltage (V_{GD}) results in a sharp increase in the current flowing through the I_{SD} channel, indicating the "opening" of the transistor. The maximum current ratio between the "on" and "off" states of the transistor varies with the Si NW width (shown as an example in Fig. 4.8 (a)), ranging from 6 orders of magnitude for d_{NW} ~ 0.4, 0.8, and 1 µm and 3 orders of magnitude for d_{NW} ~ 2 µm. Therefore, the prepared devices exhibit ambipolar characteristics, supporting the realization of both *n*-type and *p*-type conduction types. This means that at the negative V_{GD}, hole accumulation occurs, and at the positive V_{GD}, the inversion mode is switched on, i.e., electrons are accumulated.

At zero gate voltage, the current in the transistor's channel is extremely low, less than 10^{-10} A for all samples, due to the drain and source acting as back-to-back Schottky diodes, where the inverse branch of the diode determines the current. Additionally, the asymmetry of the

transfer characteristics, observed for all samples, indicates the presence of a Schottky barrier at the Fe/Si interface.

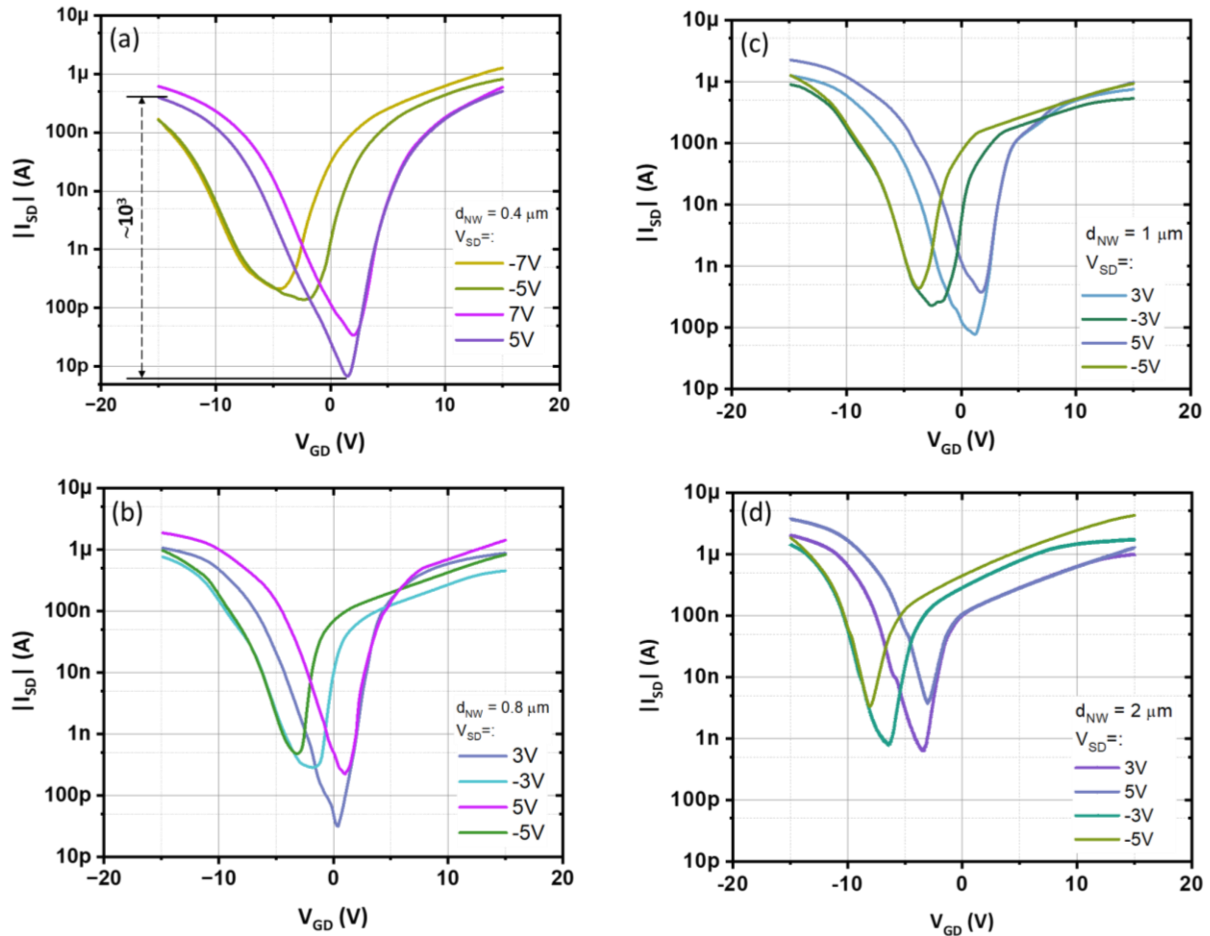

Figure 4.6. Transfer characteristics of prepared Si NW FETs with d_{NW} =: (a) ~ 0.4, (b) ~ 0.8, (c) ~ 1 and (d) ~ 2 µm at positive (forward) and negative (reverse) source-drain bias V_{SD}.

According to the thermionic emission transport theory of the Schottky barrier diode, the Schottky barrier height (SBH) the apparent φ_B was determined using the following equation

$$\varphi_B = \frac{k_B T}{q} ln\left(\frac{I_0}{A_d \mathcal{A} T^2}\right), \tag{4.1}$$

where I_0 is the saturation current, k_B is the Boltzmann constant, and T is the room temperature (293 K), A_d is the diode area (M\S interface area) calculated as the area of Fe contact pads (~$3.84 \cdot 10^3$ µm^2), $\mathcal{A}$ is the Richardson constant (32 A/cm^2·K^2 for p-Si) and q is the electron charge.

Saturation current values I_0 were obtained by an extrapolation of I_{SD} versus V_{GD} = 0 V at forward bias (Fig. 4.7). SBH values estimated at V_{SD} = 5V are summarized in Table 4.2 and shown in Fig. 4.7 (b) as a function of nanowire width d_{NW}.

Table 4.2. *Summary of saturation current values I_0 and apparent Schottky barrier heights φ_B of prepared Si NW FETs with d_{NW} = ~0.4, ~0.8, ~1 and ~2 µm.*

Si NW, µm	I_0, µA	φ_B, eV
0.4	0.032 ± 0.26	0.105 ± 0.02
0.8	0.148 ± 3.16	0.067 ± 0.01
1.0	0.163 ± 0.75	0.065 ± 0.05
2.0	0.291 ± 1.02	0.051 ± 0.02

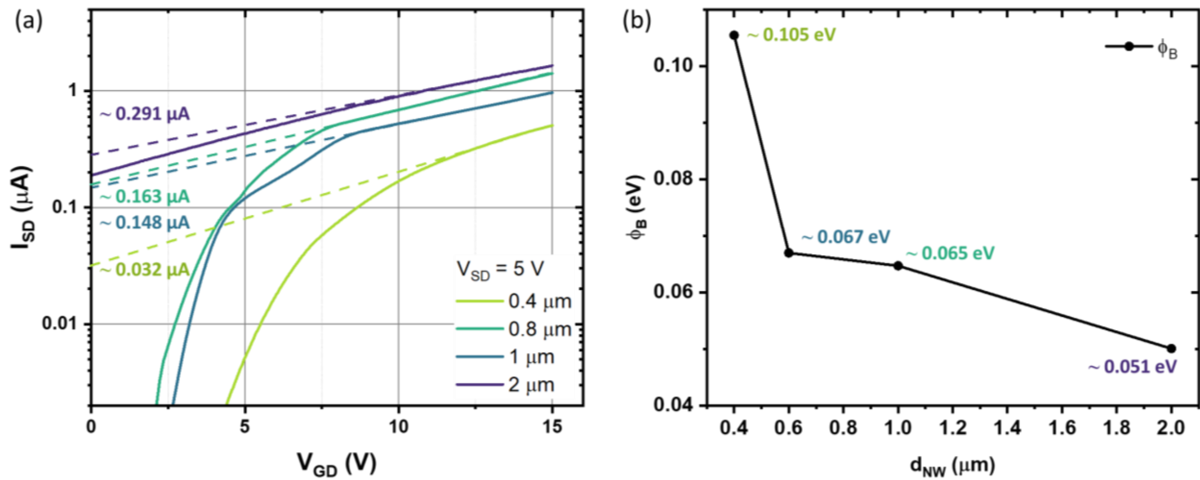

Figure 4.7. Estimated (a) saturation current values from extrapolation of I_{SD} versus V_{GD} = 0 V at forward bias and (b) Schottky barrier heights φ_B as the function of nanowire width d_{NW} of prepared Si NW FETs with d_{NW} = ~0.4, ~0.8, ~1 and ~2 µm.

Summary

Analysis of the room-temperature gate-drain characteristics of the Si NW FETs indicates the presence of a Schottky barrier at the Fe/Si interface. The devices exhibit ambipolar behavior independent of the gate polarity, and the current is influenced by the back-to-back Schottky diodes formed by the source and drain. Prepared devices demonstrate relatively low apparent Schottky barrier heights of 0.05-0.1 eV compared with the values from the literature. This is consistent with the large Fe\Si interface area formed due to the omission of the second lithography step in the fabrication procedure described earlier (Ch. 4.1).

Furthermore, simplified device geometry and realization of the gate on the back side of the substrate leave the current channel of the transistor open and allow the Si NW FETs to be used as a biosensor and will be discussed in the next section.

4.4 Si NW surface functionalization

Functionalization of the Si NW surface is necessary to evaluate the performance of manufactured devices. There are two main options to functionalize the Si NW surface properly with the required molecules and to provide a reliable attachment.

Firstly, *electrostatic adsorption* was used to immobilize positively charged molecules on the negatively charged Si NW surface, covered with the native SiO_2, in a liquid medium. Functionalization was carried out by dip-pen nanolithography (DPN) (explained in detail in Ch. 2.2) using 1-octadecanethiol (ODT) dissolved in acetonitrile first for Si NW of ~0.4 and ~0.8 µm in width. 1-octadecanethiol is a polymer that consists of two parts: the first part (CH_3-$(CH_2)_{17}$) is an organic substituent and the second part (SH) is the positively charged thiol group, which covalently binds to the Au surface [111]. The ODT-polymer is usually used as an ink for Au-covered surfaces in the DPN process [297]. In this work, ODT-molecules dissolved in acetonitrile (0.1 mM) are used to confirm the possibility of molecule deposition on the Si NW surface by the DPN method [298]. During the deposition by the DPN method, ODT-molecules diffuse through the liquid meniscus on the SiO_2-covered Si NW surface and form a self-assembled monolayer [111] due to Van der Waals interactions [299].

The second option is the *covalent binding* of molecules to the Si NW surface. For this purpose, molecules of (3-Aminopropyl)triethoxysilane (APTES) were deposited on the Si NWs of ~1 and ~2 µm in width by the DPN process to ensure a sufficiently strong interaction (Si-O-Si) [300] and further precise immobilization of receptor-molecules. For this purpose, first, dimethylsuberimidate dihydrochloride (DMS) was immobilized on APTES-covered Si NW surface as a linker-molecule [301] during incubation in a Petri dish for 20 min. Then, the homotetrameric streptavidin (ST) protein produced by *Streptomyces avidinii*, each subunit of which binds biotin (vitamin H), forming one of the most stable non-covalent complexes known in nature with the dissociation constant $K_d = 10^{-14}$ M [228], (see Ch. 1.4.2) was then immobilized to APTES-DMS-functionalized Si NW surface as a receptor-molecule. The biotinylated bovine serum albumin (biotin-BSA) complex was used as a target molecule [302]. Phosphate buffer saline (PBS) (pH = 8.5), prepared as 1×NaP_i mixed with 138 mM NaCl and 2.7 mM KCl, was used to prepare molecule solutions and [Bis(2-hydroxyethyl)amino]acetic acid (BICINE) buffer solution (pH = 8.5) and was used to remove the unbound molecules after each step of the modification process.

After each Si NW surface functionalization stage, the current-voltage (I-V) characteristics of Si NW FETs were measured. The results are discussed in the next section.

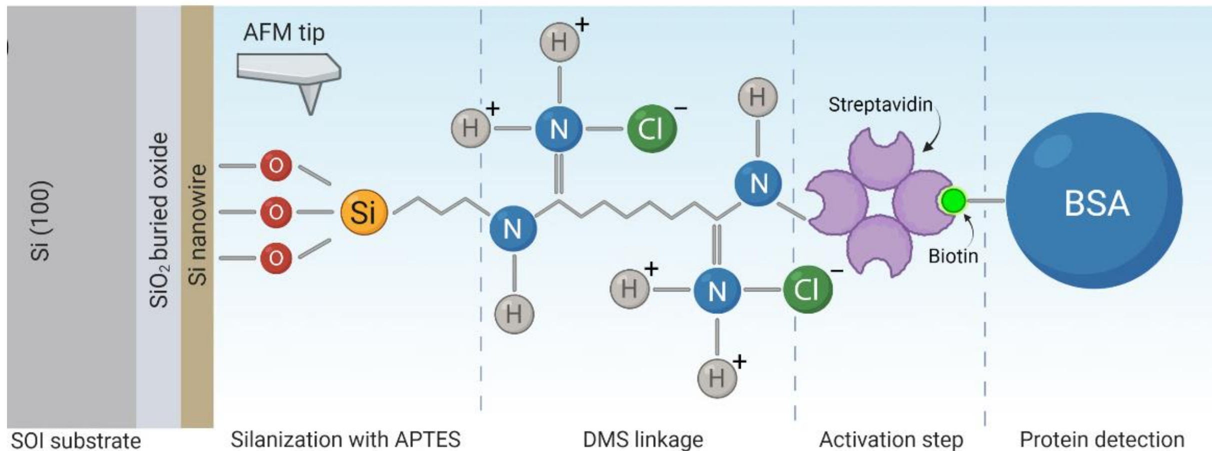

Figure 4.8. Scheme of multistep Si NW surface functionalization procedure. Here, APTES-molecules are deposited using the DPN method first (silanization step), DMS linkage is used to provide NH_2-terminated groups for further binding of streptavidin molecules (activation step), and final immobilization of biotin-BSA complex (protein detection) through streptavidin-biotin interaction [302].

The detailed multistep Si NW surface functionalization procedure is described below and schematically presented in Figure 4.8:

1. Modification of the Si NW surface is performed by 50% aqueous solution of APTES, in which molecules covalently bind to the Si surface due to the formation of siloxane bonds (Si-O-Si), which leads to the activation of the Si NW surface by amino groups (NH_2) for further covalent immobilization and recognition of molecules.
2. To ensure accurate coverage of the Si NW surface, APTES-molecules were applied to the Si NW surface using an AFM probe (DPN method) at temperature T = 24.2^{o}C and humidity H = 52.1%. The Si NW surface was washed with 0.1 M BICINE solution (pH = 8.5) to remove unbound APTES-molecules from the Si NW surface.
3. Activation of the Si NW surface was carried out by incubating ST (2 µl, 1 mg/ml) and crosslinking agent DMS (0.5 µl, 50 mg/ml) dissolved in 0.1 M BICINE solution with pH = 8.5 on the APTES-modified Si NW surface in a Petri dish for 20 min. Thus, ST molecules were covalently attached to the NH_2-activated Si NW surface using an excess of DMS crosslinking agent. The Si NW surface was washed with 0.1 M BICINE solution (pH = 8.5) to remove the unbound ST molecules.

4. Immobilization of biotin-BSA molecules (2 µl, 0.1 M in PBS with pH = 8.5) took place on the activated Si NW surface by incubation in a Petri dish for 20 min. Then the Si NW surface was washed with 0.1 M BICINE solution (pH = 8.5) to remove unbound biotin-BSA molecules.

4.5 Biosensing performance

The measurements of transport characteristics of silicon nanowire-based Indium-back-gate field-effect transistors (Si NW FETs) with Schottky contacts with Fe source and drain (S/D) contact pads after Si NW surface functionalization were carried out at room temperature using Lakeshore EMPX-HF 2 probe station (Lake Shore Cryotronics) (Ch. 2.3.2).

Source-drain current (I_{SD}) versus gate-drain (V_{GD}) voltage (transfer) characteristics of Si NW FET with d_{NW} = ~0.4 µm before and after functionalization with 1-octadecanethiol (ODT) molecules are presented in Figure 4.9 (a). The deposition of ODT-molecules affects transfer characteristics, resulting in the shift toward the positive bias and equally reducing I_{SD} at V_{SD} = -3, -5 and -7 V. This effect is attributed to the influence of ODT molecules on the transport properties of the Si NW, resulting in the presence of an additional constant positive surface charge, which is caused by the thiol terminal (SH) groups in the ODT molecules [111].

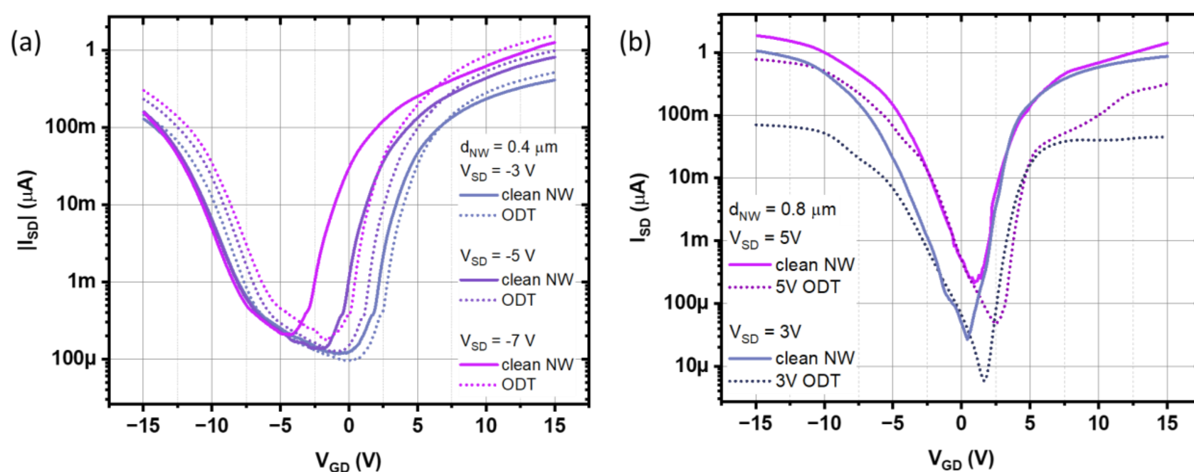

Figure 4.9. Transfer characteristics of Si NW FET with d_{NW} =: (a) ~0.4 µm and (b) ~0.8 µm at different V_{SD} for a clean Si NW and with deposited ODT-molecules.

Figure 4.9 (b) presents source-drain current (I_{SD}) versus gate-drain (V_{GD}) voltage (transfer) characteristics of Si NW FET with d_{NW} = ~0.8 µm before and after functionalization with ODT-molecules. The deposition of ODT-molecules causes the shift of transfer characteristics towards positive bias, while the shape of the graph is almost unchanged, which is also the case for Si NW FET with d_{NW} = ~0.4 µm. The effect of I_{SD} decrease after deposition of ODT-molecules

is typical for negative and positive V_{GD}, which is consistent with constant positive surface charge caused by the SH-group of ODT-molecules [298].

Sensitivity of biosensor

The term sensitivity includes two components: measuring of a specific response and its dependence upon analyte concentration (according to the IUPAC definition). Nevertheless, in some works, the sensitivity of a biosensor was evaluated using the absolute change in current (*ΔI*) or the change in current divided by the initial current (4.1) [303,304]. Here, I_{norm} relates to the normalized change in the current:

$$I_{norm} = \frac{I_f - I_i}{I_i} = \frac{\Delta I}{I_i} \tag{4.1}$$

where I_i and I_f are initial and final (after molecule deposition) values of the I_{SD} current, respectively. The results show I_{norm} as a function of gate-drain voltage (V_{GD}) for Si NW FET with d_{NW} = ~0.8 µm and ~0.4 µm (Fig. 4.10) at various source-drain voltage (V_{SD}).

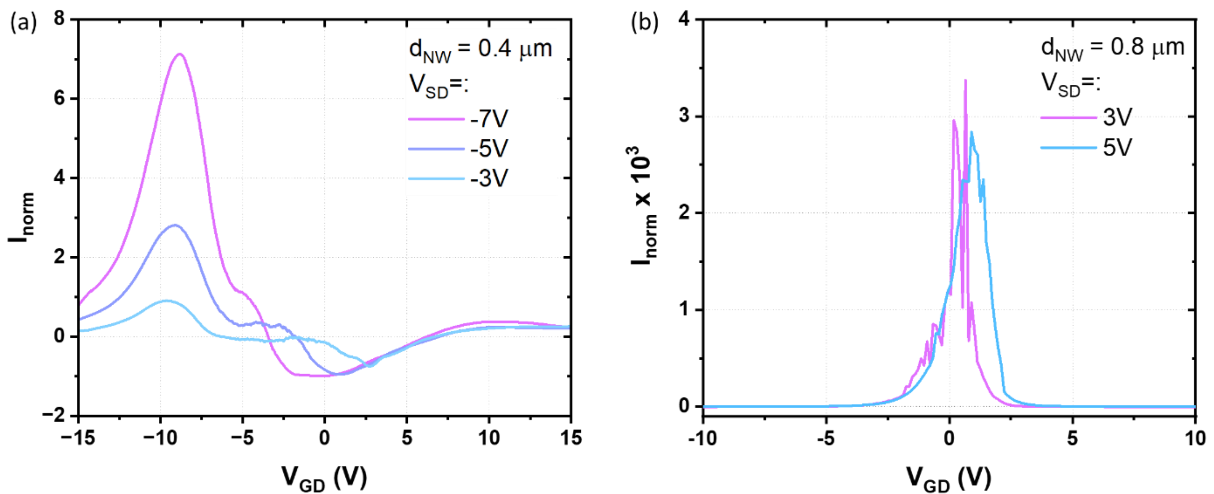

Figure 4.10. Sensitivity of fabricated Si NW FETs as I_{norm} after deposition of ODT molecules for d_{NW} =: (a) 0.4 µm and (b) 0.6 µm at various V_{SD}.

For Si NW FETs with d_{NW} = ~0.4 µm (Fig. 4.10 (a)) the maximum I_{norm} value is noted at V_{SD} = -7V and is ~10^3 times less in comparison with the maximum for Si NW FETs with d_{NW} = ~0.8 µm (Fig. 4.10 (b)). This fact is explained by the area of ODT-molecules deposition, which means that on Si NW with d_{NW} = ~0.4 µm, there are ~1.5 times less amount of ODT-molecules deposited then on Si NW with d_{NW} = ~0.8 µm.

Thus, the functionalization of the Si NW surface using the dip-pen nanolithography (DPN) method results in precise deposition of ODT-molecules, which creates a positive surface charge caused by the terminal SH-group and causes the positive shift of the I-V curve and I_{SD}

current decrease. However, ODT-molecules didn't drastically influence the operating modes of Si NW FETs, which means that the main physical mechanisms of the charge carrier transport in Si NW were unaffected. Overall, as a conclusion for this part, it was shown that ODT-molecules could be used for to functionalize Si NW as a sensitive part of a Si NW FET-based biosensor using the DPN method, which can be used for other thiol-containing molecules.

Isoelectric points of deposited molecules

The functionalization of the Si NW surface by covalently bonded APTES molecules and further multistep functionalization for biotin-BSA complex detection entails considering of the isoelectric points of molecules in use. The net charge of a molecule depends on the pH value of the used buffer solution. This value is called a molecule's *isoelectric point* (pI) and is defined for every molecular compound as a pH value in which its net charge equals zero [305]. The isoelectric points pI of molecules, especially proteins, depend on seven charged amino acids: glutamate, aspartate, cysteine, tyrosine, histidine, lysine and arginine [306]. Furthermore, the charge of protein terminal groups should also be considered since each has its unique acid dissociation constant. Thus, the protein's net charge is closely related to the pH of the buffer solution. In this way, the Henderson-Hasselbach equation is used to calculate protein charge in a certain solution [307].

In this work, the pIs of ST and BSA, biotin and APTES molecules, and the pH of the buffer solution, which maintains the stability of the molecules, are considered (Table 4.3). The composition, concentration, and ratios of ions in the buffer solution significantly affect a biosensor's sensitivity. Phosphate buffer saline (PBS) with pH = 8.5 was used to prepare solutions of ST, biotin-BSA and APTES molecules.

Table 4.3. *Summary of isoelectric points pIs and resulted net charge of APTES, streptavidin, biotin and bovine serum albumin molecules considering the pH value of the buffer solution used.*

Molecule	pI	pH of buffer	net charge
APTES	6.2	8.5	negative
Streptavidin	8.1	8.5	negative
Biotin	6.2	8.5	negative
Bovine serum albumin (BSA)	5.6	8.5	negative

The isoelectric points pIs of ST and BSA, biotin and APTES molecules are also presented in Figure 4.11 (a) as functions of molecular weight. The net charge of a molecule is determined by the presence and distribution of charged groups, such as amino or carboxyl groups, within the molecule. Larger molecules, such as BSA, tend to have more charged groups than smaller molecules, such as APTES and biotin, which can affect their net charge [308].

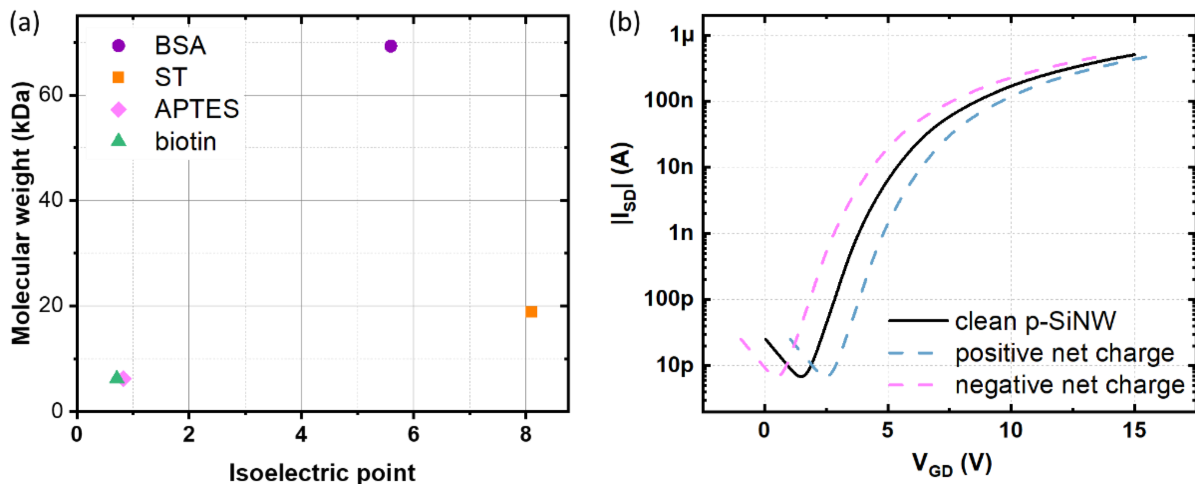

Figure 4.11. (a) Isoelectric points of APTES, streptavidin, biotin and bovine serum albumin molecules as a function of molecular weight and (b) shift of transfer characteristics of p-Si NW FET according to a net charge of the deposited molecule.

Depending on the Si NW doping type, the net charge of a detected molecule causes the shift in transfer characteristics toward negative or positive bias, as demonstrated for *n*-doped Si NWs in [309]. This work shows that in the case of *p*-doped Si NWs, the transfer characteristic shifts towards positive bias in the case of positive charge density on the Si NW surface and towards negative in the opposite case (Fig. 4.11 (b)).

In the case of biotin-BSA detection, transfer characteristics of Si NW FET were measured after each step of the Si NW surface modification (Fig. 4.12 – Fig. 4.14). The functionalization of the Si NW surface with APTES molecules (Ch. 4.4) causes the shift of transfer characteristic towards the negative bias and a decrease in I_{SD} current (Fig. 4.12 (a, b), green dashed lines), which is consistent with the negative pI creating a negative surface charge. Here, it can be concluded that the DPN method is suitable for the deposition of APTES molecules. The current decrease and voltage shift is similar for both Si NW FETs with d_{NW} = ~1 µm and ~2 µm at V_{SD} = -3V, -5V (Fig. 4.12 (a, b), green dashed lines).

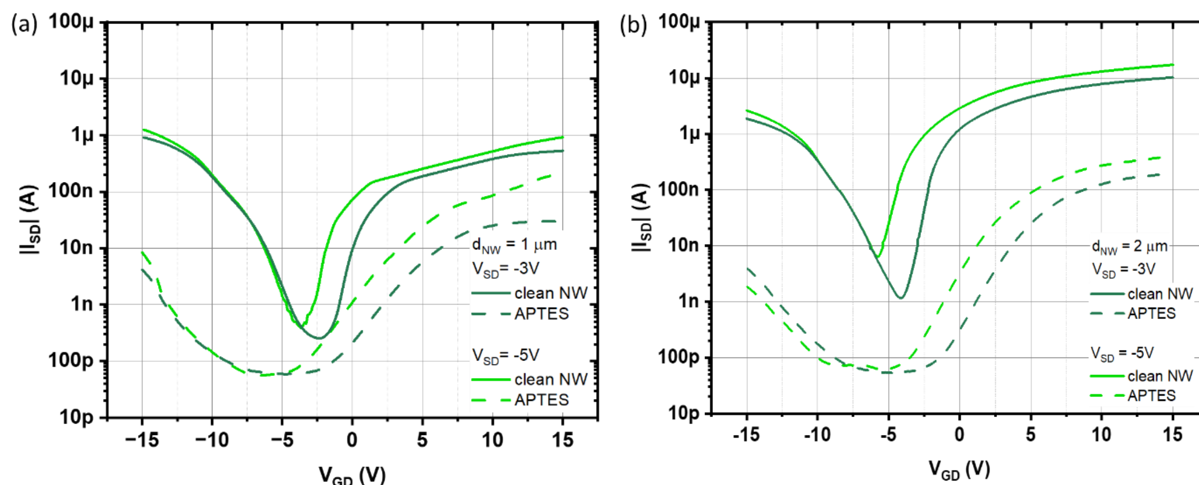

Figure 4.12. Transfer characteristics of Si NW FETs with d_{NW} =: (a) ~1 and (b) ~2 μm before (solid green lines) and after functionalization with APTES molecules (dashed line) at varied V_{SD}.

Transfer characteristics of Si NW FET measured after Si NW surface functionalization with streptavidin molecules and further immobilization of the biotin-BSA complex are presented in Figure 4.13. Streptavidin and biotin-BSA are proteins with a negative net charge, acting as a floating charged gate. Indeed, the net charges of streptavidin and BSA in PBS with pH = 8.5 are negative because the isoelectric points of streptavidin and BSA are 8.1 and 5.6, respectively (Table 4.3). In this case, a negative charge density appears on the Si NW surface and shifts transfer characteristic towards the negative bias (Fig. 4.13, dashed blue lines).

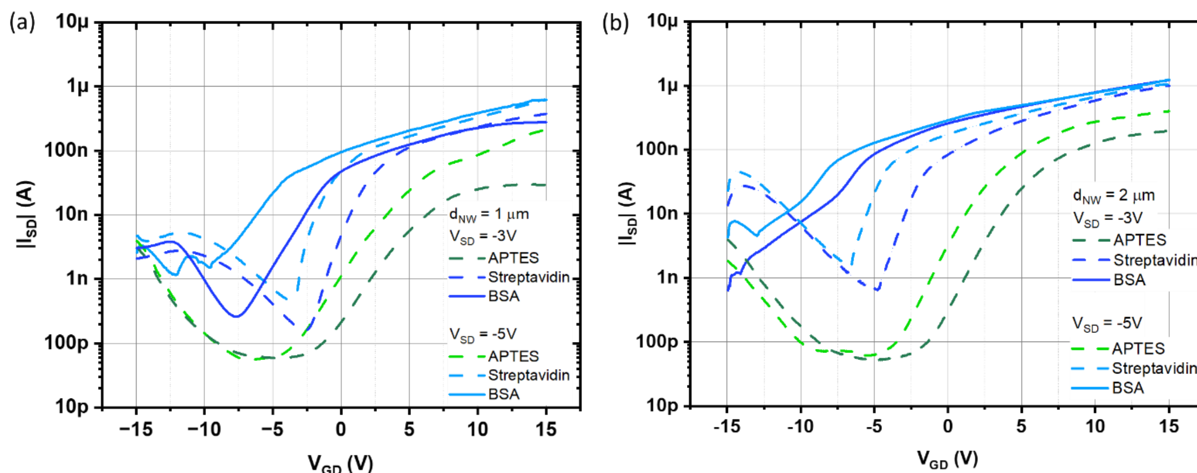

Figure 4.13. Transfer characteristics of Si NW FETs with d_{NW} =: (a) ~1 and (b) ~2 μm after functionalization with streptavidin (dashed blue lines) and further immobilization of the biotin-BSA complex (solid blue lines) in comparison with transfer characteristics after functionalization with APTES molecules (dashed green lines) at varied V_{SD}.

The immobilization of biotin-BSA molecules results in a significant shift of I_{SD}-V_{GD} characteristic towards the negative bias for both Si NW FETs with d_{NW} = ~1 μm and ~2 μm, which is consistent with the net negative charge of the biotin-BSA complex [310].

Figure 4.14 compares transfer characteristics of Si NW FETs with d_{NW} = ~1 µm and ~2 µm for clean Si NW and after immobilization of the biotin-BSA complex at various V_{SD}. The sharp decrease of I_{SD} current in saturation region in negative V_{GD} is observed: more than by 2 orders of magnitude at V_{GD} = -7V and -15V compared to clean Si NW with d_{NW} = ~1 µm at V_{SD} = -5V and -3V (Fig. 4.14 (a), solid blue lines) and more than by 3 orders of magnitude at V_{GD} = -15V compared to clean Si NW with d_{NW} = ~2 µm for V_{SD} = -5V (Fig. 4.14 (b), solid blue lines). Thus, when *p*-doped Si NWs are used, the negative surface charge density causes the transfer characteristics to shift toward negative bias.

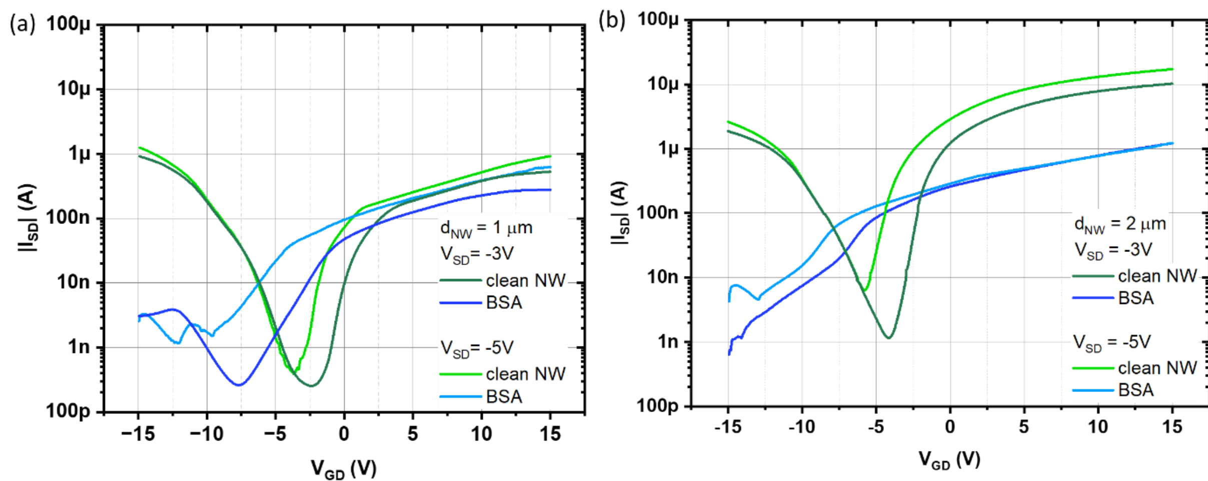

Figure 4.14. Transfer characteristics of Si NW FETs with d_{NW} =: (a) ~1 and (b) ~2 µm for clean Si NW and after immobilization of the biotin-BSA complex at varied V_{SD}.

The determined sensitivity as I_{norm} for Si NW FET with d_{NW} = ~1 µm and ~2 µm is presented in Figure 4.15. The results demonstrate the maximum value of I_{norm} after immobilization of the biotin-BSA complex is observed at V_{SD} = -5V for both Si NW FET with d_{NW} = ~1 µm and ~2 µm. Thus, the I_{norm} observed after the biotin-BSA complex immobilization is ~100 times higher than after streptavidin (ST) deposition in the case of Si NW FET with d_{NW} = ~1 µm for V_{SD} = -5V, -3V (Fig. 4.15 (a, b)). This observation is consistent with the net charge of the biotin-BSA complex. Also, streptavidin exhibits tetravalent binding to biotin, according to [228], meaning it can bind four biotin molecules. Thus, the tetravalent streptavidin-biotin interaction can explain the ~100 times difference in I_{norm}.

A similar behavior is observed for a Si NW FET with d_{NW} = ~2 µm for V_{SD} = -5V, -3V (Fig. 4.15 (c, d)). In this case, the value of I_{norm} after biotin-BSA complex immobilization is ~20 times higher than that for the Si NW FET with d_{NW} = ~1 µm. This difference is consistent with the

approximately 2 times larger area of molecule deposition and the tetravalent binding between biotin and streptavidin.

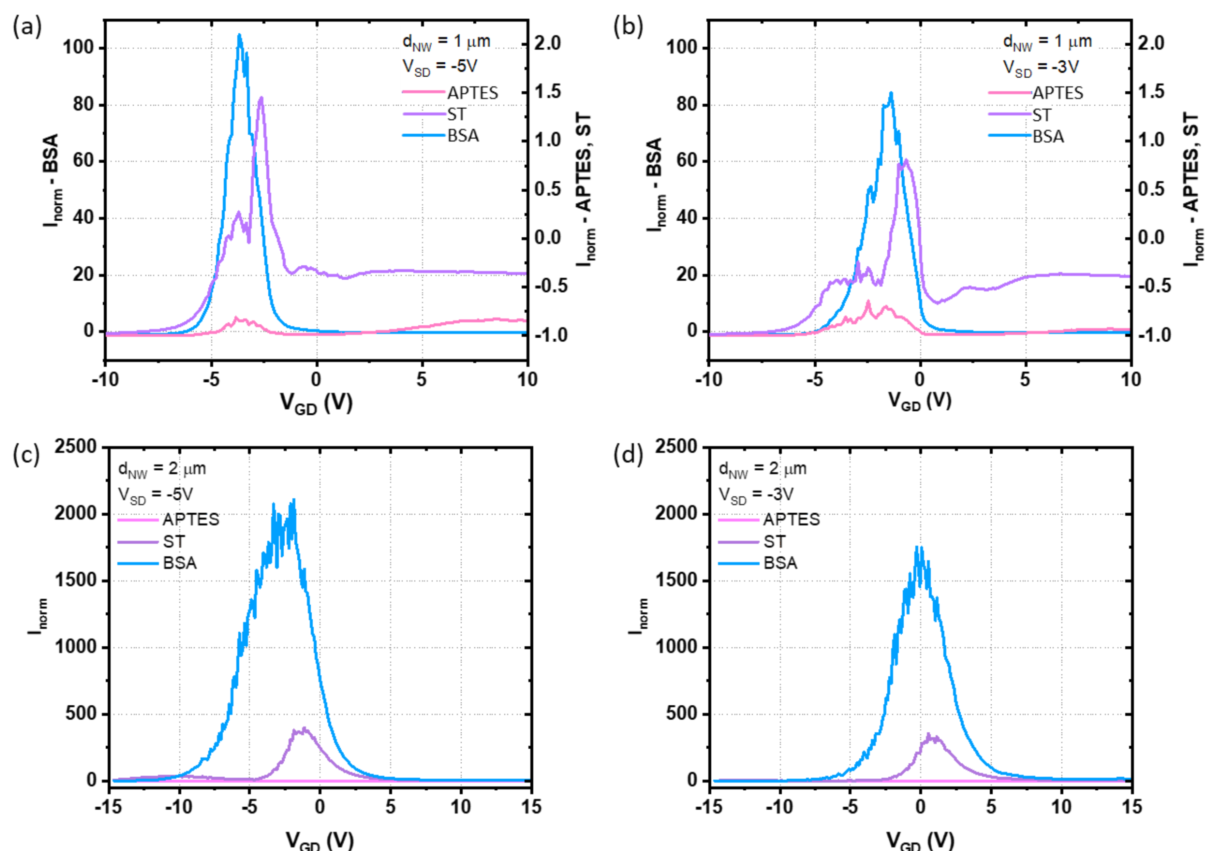

Figure 4.15. Sensitivity as I_{norm} of Si NW FETs after modification with APTES, streptavidin (ST) and immobilization of biotin-BSA (BSA) for d_{NW} = ~1 µm at varied V_{SD} =: (a) -5 V and (b) -3 V, and for d_{NW} = ~2 µm at V_{SD} =: (a) -5 V and (b) -3 V.

Based on the observed results, as the Si NW surface acquires a negative charge due to protein attachment, the bending of the energy bands is modulated by this additional surface charge (N_{surf}), slightly shifting the bands upward.

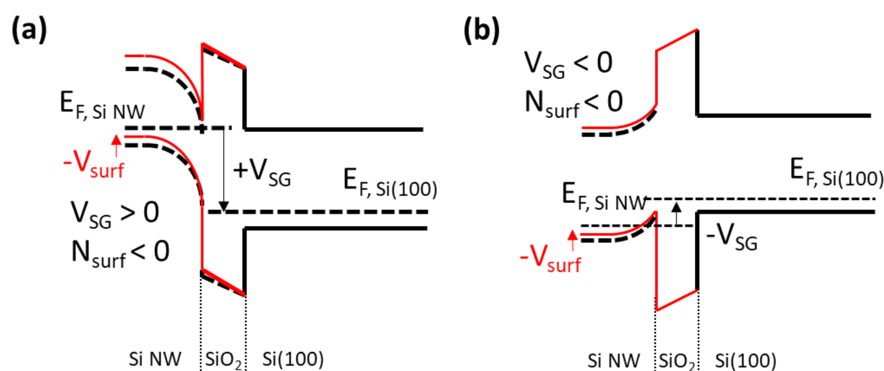

Figure 4.16. Band diagrams of (a) inversion and (b) accumulation modes of Si NW FET in the presence of negative surface charge N_{surf}. Here, $E_{F, Si NW}$ is the Fermi level of Si nanowire and $E_{F, Si(100)}$ is the Fermi level of Si(100) bulk.

This upward shift leads to a decrease in current in the transistor inversion mode ($V_{SG} > 0$) as the edge of the conduction band at the Si/SiO_2 interface moves further away from the Fermi level and the 2D electron gas concentration decreases (Fig. 4.16 (a)). Alternatively, the hole current increases in the accumulation mode ($V_{SG} < 0$) as the edge of the valence band at the Si/SiO_2 boundary moves deeper below the Fermi level of the holes, increasing in the 2D hole gas concentration (Fig. 4.16 (b)). Thus, the combined effect of the two mechanisms mentioned above is an effective positive shift of the transistor's current-voltage characteristics and the associated device threshold voltage.

Summary

Fabricated Si NW FETs with varied Si NW widths were used for molecular detection based on the source-drain current (I_{SD}) changes. Si NW surface was functionalized with ODT and APTES molecules using dip-pen nanolithography (DPN).

ODT-molecules didn't drastically influence the operating modes of Si NW FETs. They could be used for the functionalization of Si NW surface using the DPN method, which can be used for other thiol-containing molecules.

APTES-functionalized Si NW surface was further modified with streptavidin molecules, enabling the covalent binding of biotinylated bovine serum albumin (biotin-BSA) molecules. After the biotin-BSA detection, a decrease in I_{SD} current was observed. This decrease is attributed to the appearance of a negative charge density on the Si NW surface.

The normalized change in I_{SD} current I_{norm} was used to evaluate the sensitivity of a Si NW FET-based biosensor. The I_{norm} observed for Si NW FETs with d_{NW} = ~1 and ~2 µm after the biotin-BSA complex detection is ~100 times higher than after streptavidin deposition, which is consistent with the net charge of the biotin-BSA complex and with tetravalent binding to biotin.

The proposed version of the detection device, characterized by a simple manufacturing method, a well-reproducible functionalization scheme, and a clear electrical detection mechanism, is a promising prototype for the realization of detectors and sensors for biological compounds.

4.6 Summary and discussion

Silicon nanowire-based Indium-back-gate field-effect transistors (Si NW FETs) with Schottky contacts on silicon-on-insulator substrates with Fe source and drain contact pads with varied Si NW widths were prepared using a top-down nanofabrication approach involving thermal evaporation in ultra-high vacuum, electron beam lithography, wet and dry chemical etching. The fabrication procedure was modified by omission of the second lithography step, usually used for the fabrication of Si NW FETs and increasing the time of wet chemical etching. Due to this Fe/Si contact area was formed under Fe film.

The room-temperature gate-drain characteristics of the Si NW FETs indicate the presence of a Schottky barrier at the Fe/Si interface. The devices exhibit ambipolar behavior regardless of the gate polarity, indicating the presence of both electron and hole conduction, and the current is influenced by the back-to-back Schottky diodes formed by the drain and source.

The simplified device geometry allowed to the use of the prepared devices for molecular detection based on the source-drain current (I_{SD}) changes. For that purpose, a multistep procedure for functionalizing the Si NW surface with ODT and APTES molecules has been performed using the dip-pen nanolithography method to confirm the possibility of Si NW surface functionalization by the electrostatic adsorption, in the case of ODT molecules and the covalent binding, in the case of APTES molecules.

Functionalization with ODT-molecules results in the presence of a positive surface charge caused by the terminal SH-group, leading to the positive shift of the I-V curve and I_{SD} current decrease. However, ODT-molecules didn’t drastically influence the operating modes of Si NW FETs.

Thus, it was shown that ODT-molecules could be used to functionalize of Si NW as a sensitive part of a Si NW FET-based biosensor using the DPN method, which can be used for other thiol-containing molecules.

APTES functionalized Si NW surface causes the shift of transfer characteristic towards the negative bias and a decrease in I_{SD} current, consistent with the negative pI creating a negative surface charge. Subsequent immobilization of streptavidin enables the covalent binding of biotinylated bovine serum albumin (biotin-BSA) molecules. After biotin-BSA detection, a

decrease in source-drain current was observed. This decrease is attributed to the appearance of a negative charge density on the Si NW surface.

To assess the sensitivity of a Si NW FET-based biosensor, the normalized change in source-drain current I_{norm} was utilized. Si NW FETs with Si NW widths d_{NW} = ∼1 and ∼2 μm were investigated. The observed I_{norm} values after the biotin-BSA complex detection were approximately 100 times higher than those after streptavidin deposition. This result aligns with the overall charge of the biotin-BSA complex and its tetravalent binding to biotin.

The proposed version of the detection device, based on Si NW FET, is characterized by a simple manufacturing method, a well-reproducible functionalization scheme, and a clear electrical detection mechanism, it is a promising prototype for the realization of detectors and sensors for biological compounds.

5. Conclusions and outlook

In metal-oxide-semiconductor (MOS) technology, new materials and device architectures are required to control and improve device performance. The present thesis presented the preparation of Fe/Si nanostructures using bottom-up and top-down nanofabrication approaches. For this purpose, reactive epitaxy and molecular beam epitaxy under ultrahigh vacuum conditions were used to prepare the self-assembled ensembles of metallic α-$FeSi_2$ and semiconducting β-$FeSi_2$ iron silicide nano- and submicron crystallites. Then, electron-beam lithography was used to prepare silicon nanowire (Si NW)-based field-effect transistors (FET) with Schottky contacts on silicon-on-insulator (SOI) substrates with Fe source and drain contact pads and varied Si NW widths.

The major results of this thesis work are summarized below:

An experimental study of the $FeSi_2$/Si system prepared on gold-activated and gold-free Si(001), Si(110), Si(111) surfaces at different Si/Fe flux ratios and different substrate temperatures reveals that the utilization of gold-assisted growth regulates the morphology of the resulting crystallites and preferred orientation relationship (OR). Thus, the α-$FeSi_2$(001) lattice plane is oriented parallel to the Si substrate surface during gold-assisted growth. In this manner, preferential α-$FeSi_2$(001)[110]//Si(001)[110] OR, also 45 degrees rotated as α-$FeSi_2$(001)[110]//Si(001)[100] OR, is observed on *p*-Si(001) substrates, which is attributed to the formation of well-defined crystal facets with flat surfaces. On *p*-Si(110) substrates, the α-$FeSi_2$(001)[110]//Si(110)[-110] OR corresponds to the formation of elongated nano and submicron wires along the Si[-110] direction. For *p*-Si(111) substrates, the α-$FeSi_2$(001)[110]// Si(111)<-110> OR is preferential and is related to the 2-fold symmetry of triangular nanoplates exhibiting well-defined faceting and flat surfaces.

The resistivity of the α-$FeSi_2$/Si system increases as the angle between the conductivity channels in α-$FeSi_2$ and the conductivity valleys in Si increases. The prepared $FeSi_2$/Si system can be considered as a system of back-to-back connected Schottky diodes and used when in the ohmic contact may be substituted by another Schottky contact with lower-barrier height in semiconductor devices. The analysis of experimental and calculated data on the temperature dependencies of resistivity identifies that the average area of the $FeSi_2$ crystallites, attributed to the metal/semiconductor interface area, has an inverse relationship with the resistivity values. The $FeSi_2$/Si system exhibits multiple resistivity plateaus attributed

to two or more Schottky barriers within the system. The barrier inhomogeneities within the system influence the system's resistance. As the inhomogeneity increases, the resistance decreases with temperature. This suggests that when the Schottky barriers are less uniform, the resistance of the $FeSi_2$/Si system decreases as the temperature rises.

A modified approach involving thermal evaporation in ultra-high vacuum, electron beam lithography, wet and dry chemical etching, and increasing time of wet chemical etching was used to prepare Si NW-based Indium-back-gate FETs with Schottky contacts on SOI substrates with Fe source and drain contact pads and varied Si NW widths. Due to this, a Fe/Si contact area was formed under Fe film, which leads to relatively low apparent Schottky barrier heights of 0.05-0.1 eV. The room-temperature gate-drain characteristics of the Si NW FETs indicate the presence of a Schottky barrier at the Fe/Si interface. The devices exhibit ambipolar behavior regardless of the gate polarity, indicating the presence of both electron and hole conduction, and the current is influenced by the back-to-back Schottky diodes formed by source and drain electrodes. Based on the source-drain current changes, the resulting devices are applied for biomolecular detection. The functionalization of the Si NW surface was performed using the dip-pen nanolithography process. For that purpose, a multistep procedure for functionalizing the Si NW surface with 1-octadecanethiol (ODT) and (3-Aminopropyl)triethoxysilane (APTES) molecules has been performed using dip-pen nanolithography method to confirm the possibility of Si NW surface functionalization by the electrostatic adsorption, in the case of ODT molecules, and the covalent binding, in the case of APTES molecules.
The functionalization with ODT-molecules resulted in the presence of a positive surface charge and decrease in the I_{SD} current. APTES functionalization resulted in a negative shift and a decrease in the I_{SD} current caused by the negative net surface charge. Subsequent immobilization of streptavidin enables the covalent binding of biotinylated bovine serum albumin (biotin-BSA) molecules. The sensitivity of a Si NW FET-based biosensor was assessed using the normalized change in source-drain current I_{norm}. Si NW FETs with Si NW widths d_{NW} = ~1 µm and ~2 µm were investigated. The observed I_{norm} values after the biotin-BSA complex detection were approximately 100 times higher than those after streptavidin deposition. This result can be explained by the overall charge of the biotin-BSA complex and its tetravalent binding to biotin.

Conclusions and outlook

This study discusses the factors significantly contributing to the electrical resistivity in the $FeSi_2$/Si system, which allows for the prediction of the electrical properties and designing contacts in microelectronic devices. The proposed design of a Si NW FET with Fe S/D contacts is a promising prototype for the detection of biomolecules in room temperature conditions.

As an outlook, two important topics deserve further investigation in the future. Firstly, the preparation of Si NW FET with α-$FeSi_2$ S/D contacts, prepared using the presented simplified fabrication procedure, is worth to be investigated since the α-$FeSi_2$/Si system allows an increase in the height of the Schottky barrier, which may enable better control and modulation of the high-performance Si NW FETs with improved switching characteristics, reduced power consumption, and enhanced overall device efficiency. The compatibility of the α-$FeSi_2$ with silicon technology ensures seamless integration into existing CMOS processes, making it an attractive material for future nanoelectronic applications.

Secondly, the detection limit of biosensors based on Si NW FET with both Fe and α-$FeSi_2$ S/D contacts needs to be investigated by varying the concentration of target molecules, which can be performed by implementing a microfluidic channel. Using a microfluidic channel provides a controlled environment for manipulating the concentration of target molecules in a precise and repeatable manner. This allows for a thorough assessment of the Si NW FET biosensor's response to varying analyte concentrations, enabling the determination of its detection limit with high accuracy and defining the sensitivity of the biosensor in real-world applications.

List of publications

- I.A. Tarasov, **T.E. Smolyarova**, I.V. Nemtsev, et al., Tailoring the preferable orientation relationship and shape of α-$FeSi_2$ nanocrystals on Si(001): The impact of gold and the Si/Fe flux ratio, and the origin of α/Si boundaries, CrystEngComm. 22 (2020). [273]

- **T.E. Smolyarova**, A. V. Lukyanenko, A.S. Tarasov, et al., Biosensors based on nanowire field effect transistors with Schottky contacts, in: J. Phys. Conf. Ser., (2019). [298]

- **T.E. Smolyarova**, L.V. Shanidze, A.V. Lukyanenko, et al., Protein biosensor based on Schottky barrier nanowire field effect transistor, Talanta. 239 (2022). [302]

List of conference contributions

- "Modern problems of radio electronics", Krasnoyarsk, Russia (2017), talk.
- "Nanostructures: Physics and Technology", St. Petersburg, Russia (2017), poster.
- Moscow International Symposium on Magnetism (MISM), Moscow, Russia (2017), poster.
- "Digital Controlled Drugs at the Interface of Sciences", Krasnoyarsk, Russia (2018), talk.
- "Scanning Probe Microscopy", Ekaterinburg, Russia, (2018), poster.
- Asian School-Conference on Physics and Technology of Nanostructured Materials (ASCO-Nanomat), Vladivostok, Russia (2018), poster.
- International school-conference on optoelectronics, photonics, engineering and nanostructures "Saint Peterburg-OPEN", Saint Petersburg, Russia (2019), poster.
- International Baltic conference on magnetism (IBCM), Kaliningrad, Russia (2019, 2021), posters.
- Euro-Asian Symposium on Trends in Magnetism (EASTMAG), Ekaterinburg, Russia (2019), poster.
- International Conference on Magnetic and Superconducting Materials (MSM22), Duisburg, Germany (2022), poster.
- DPG Spring Meeting (SKM), Regensburg, Germany (2022), poster.
- Lüscher-Wassermann-Seminar, Klosters, Switzerland (2023), poster.
- DPG Spring Meeting (SKM), Dresden, Germany (2023), talk.

Acknowledgments

This thesis presents the research work I started at the Kirensky Institute of Physics, Krasnoyarsk, Russia, and finished at the University of Duisburg-Essen (UDE), Duisburg, Germany, due to certain circumstances that happened to me during this period. I want to thank everybody who contributed to this thesis through engagement, assistance, advice, or various other ways.

First, I would like to thank my supervisor, Prof. Dr. Ulf Wiedwald, for accepting me as a Ph.D. student at UDE. Thanks a lot for your feedback, support, patience, and encouragement to finish this thesis and the communication skills I learned from you, which are certainly helpful in my life.

I am grateful for the financial support of the CRC/TRR HoMMage 270 research project, which allowed me to stay in Germany and continue my research and scientific career.

I want to thank to Prof. Dr. Michael Farle for the support, helpful advice, motivation, and opportunity to complete this thesis in his research group.

Many thanks go to Dr. Detlef Spoddig for your assistance with EBSD measurements and to Dr. Anna Semisalova, thank you for your valuable help at the last steps of writing, your constant motivation and good suggestions in my research and everyday life in Duisburg.

I would also like to thank Prof. Dr. Doru Lupascu and M.Sc. Merlin Schmuck for providing the equipment for the measurement of XRD pole figures.

I want to acknowledge my colleagues from the Kirensky Institute of Physics, Dr. Anna Lukyanenko, for the help with Si NW FETs preparation, your guidance at my first steps with AFM measurements, and for being my officemate for several years. I would also thank M.Sc. Lev Shanidze for your assistance with electron transport measurement, Dr. Vasilisa Krasitskaya for your help with the development of Si NW functionalization scheme, Dr. Filipp Baron for fruitful discussions and your guidance with Si NW FETs publications, Dr. Ivan Yakovlev for your help with $FeSi_2$/Si sample preparation, Dr. Ivan Nemtsev and Dr. Michail Volochaev for providing SEM and TEM measurements, Dr. Leonid Solovyov for assistance with XRD measurements.

I want to thank Dr. Anton Tarasov for allowing me to start this research in your group and for your guidance at all steps in the investigation of Si nanowire-based filed-effect transistors.

Many thanks go to Elisavet Papadopoulou and Inci Nur Sahin for supporting my mental health and creating a friendly environment during the last stage of this thesis preparation.

Finally, special thanks are given to Dr. Ivan Tarasov. Without your help, I could hardly finish this thesis. I am grateful for your infinite patience and support during this period.

And last but not least, I am deeply grateful to my family for their constant support ♡.

Thank you all!

Tatiana Smoliarova

Duisburg, 1.08.2023

Bibliography

[1] A.C. Arias, J.D. MacKenzie, I. McCulloch, J. Rivnay, A. Salleo, Materials and applications for large area electronics: Solution-based approaches, Chem. Rev. 110 (2010) 3–24.

[2] L.L. Vadasz, A.S. Grove, T.A. Rowe, G.E. Moore, Silicon-gate technology, IEEE Spectr. 6 (1969) 28–35. https://doi.org/10.1109/MSPEC.1969.5214116.

[3] F. Fabbri, E. Rotunno, L. Lazzarini, D. Cavalcoli, A. Castaldini, N. Fukata, K. Sato, G. Salviati, A. Cavallini, Preparing the Way for Doping Wurtzite Silicon Nanowires while Retaining the Phase, Nano Lett. 13 (2013) 5900–5906.

[4] T. Mikolajick, A. Heinzig, J. Trommer, S. Pregl, M. Grube, G. Cuniberti, W.M. Weber, Silicon nanowires - a versatile technology platform, Phys. Status Solidi - Rapid Res. Lett. 7 (2013) 793–799.

[5] M. Menon, E. Richter, Are Quasi-One Dimensional Structures of Si Stable?, Phys. Rev. Lett. 83 (1999) 792–795.

[6] Y. Cui, Q. Wei, H. Park, C.M. Lieber, Nanowire Nanosensors for Highly Sensitive and Selective Detection of Biological and Chemical Species, Science (80). 293 (2001) 1289–1292.

[7] F. Patolsky, G. Zheng, O. Hayden, M. Lakadamyali, X. Zhuang, C.M. Lieber, Electrical detection of single viruses, Proc. Natl. Acad. Sci. 101 (2004) 14017–14022.

[8] G. Zheng, F. Patolsky, Y. Cui, W.U. Wang, C.M. Lieber, Multiplexed electrical detection of cancer markers with nanowire sensor arrays, Nat. Biotechnol. 23 (2005) 1294–1301.

[9] A. Paghi, S. Mariani, G. Barillaro, 1D and 2D Field Effect Transistors in Gas Sensing: A Comprehensive Review, Small. 19 (2023).

[10] A. Gao, S. Chen, Y. Wang, T. Li, Silicon Nanowire Field-effect-transistor-based Biosensor for Biomedical Applications, Sensors Mater. 30 (2018) 1619.

[11] K. Zhou, Z. Zhao, L. Pan, Z. Wang, Silicon nanowire pH sensors fabricated with CMOS compatible sidewall mask technology, Sensors Actuators B Chem. 279 (2019) 111–121.

[12] M.D. Prakash, B.V. Krsihna, B.V. V. Satyanarayana, N.A. Vignesh, A.K. Panigrahy, S. Ahmadsaidulu, A Study of an Ultrasensitive Label Free Silicon Nanowire FET Biosensor for Cardiac Troponin I Detection, Silicon. 14 (2022) 5683–5690.

[13] Y. Kutovyi, I. Zadorozhnyi, H. Hlukhova, V. Handziuk, M. Petrychuk, A. Ivanchuk, S. Vitusevich, Origin of noise in liquid-gated Si nanowire troponin biosensors, Nanotechnology. 29 (2018) 175202.

[14] J. Li, Y. Kutovyi, I. Zadorozhnyi, N. Boichuk, S. Vitusevich, Monitoring of Dynamic Processes during Detection of Cardiac Biomarkers Using Silicon Nanowire Field-Effect Transistors, Adv. Mater. Interfaces. 7 (2020) 2000508.

[15] J. Kedzierski, P. Xuan, E.H. Anderson, J. Bokor, Tsu-Jae King, Chenming Hu, Complementary silicide source/drain thin-body MOSFETs for the 20 nm gate length regime, in: Int. Electron Devices Meet. 2000. Tech. Dig. IEDM (Cat. No.00CH37138), IEEE, 2000: pp. 57–60.

[16] J.M. Larson, J.P. Snyder, Overview and status of metal S/D Schottky-barrier MOSFET technology, IEEE Trans. Electron Devices. 53 (2006) 1048–1058.

[17] M. Itakura, N. Kishikawa, R. Kawashita, N. Kuwano, Epitaxial orientation and morphology of β-$FeSi_2$ produced on a flat and a patterned Si(001) substrates, Thin Solid Films. 515 (2007) 8169–8174.

[18] F. Zhang, A.R. Oganov, Iron silicides at pressures of the Earth's inner core, Geophys. Res. Lett. 37 (2010) n/a-n/a.

[19] S.M. Koo, M.D. Edelstein, Q. Li, C.A. Richter, E.M. Vogel, Silicon nanowires as enhancement-mode Schottky barrier field-effect transistors, Nanotechnology. 16 (2005).

[20] S. Veeraraghavan, J.G. Fossum, Short-channel effects in SOI MOSFETs, IEEE Trans. Electron Devices. 36 (1989) 522–528.

[21] G. Jayakumar, M. Östling, Pixel-based biosensor for enhanced control: silicon nanowires monolithically integrated with field-effect transistors in fully depleted silicon on insulator technology, Nanotechnology. 30 (2019) 225502.

[22] M. Kaisti, Detection principles of biological and chemical FET sensors, Biosens. Bioelectron. 98 (2017) 437–448.

[23] S. Kim, R. Lee, D. Kwon, T.-H. Kim, T.J. Park, S.-J. Choi, H.-S. Mo, D.H. Kim, B.-G. Park, Multiplexed Silicon Nanowire Tunnel FET-Based Biosensors With Optimized Multi-Sensing Currents, IEEE Sens. J. 21 (2021) 8839–8846.

[24] F. Runovc, H. Norström, R. Buchta, P. Wiklund, S. Petersson, Titanium Disilicide in MOS Technology, Phys. Scr. 26 (1982) 108–112.

[25] T.E. Tang, Che-Chia Wei, R.A. Haken, T.C. Holloway, L.R. Hite, T.G.W. Blake, Titanium nitride local interconnect technology for VLSI, IEEE Trans. Electron Devices. 34 (1987) 682–688.

[26] D.B. Scott, R.A. Chapman, Che-Chia Wei, S.S. Mahant-Shetti, R.A. Haken, T.C. Holloway, Titanium disilicide contact resistivity and its impact on 1-μm CMOS circuit performance, IEEE Trans. Electron Devices. 34 (1987) 562–574.

[27] M. Qin, V.M.C. Poon, S.C.H. Ho, Investigation of Polycrystalline Nickel Silicide Films as a Gate Material, J. Electrochem. Soc. 148 (2001) G271.

[28] C.J. Urban, DC and RF characterization of NiSi Schottky barrier MOSFETs with dopant segregation, Forschungszentrum Jülich, 2010.

[29] K. Yamamoto, T. Nakamura, K. Fujimoto, R. Tamura, K. Nishio, Preparation of $NiSi_2$ and application to thermoelectric silicide elements used as electrodes, MRS Adv. 3 (2018)

[30] O. Nakatsuka, K. Okubo, A. Sakai, M. Ogawa, Y. Yasuda, S. Zaima, Improvement in NiSi/Si contact properties with C-implantation, Microelectron. Eng. 82 (2005) 479–484.

[31] L. Van den hove, R. Wolters, K. Maex, R.F. De Keersmaecker, G.J. Declerck, A self-aligned $CoSi_2$ interconnection and contact technology for VLSI applications, IEEE Trans. Electron Devices. 34 (1987) 554–561.

[32] V.I. Rudakov, Y.I. Denisenko, V. V. Naumov, S.G. Simakin, Control of the formation of ultrathin $CoSi_2$ layers during the rapid thermal annealing of Ti/Co/Ti/Si(100) structures, Russ. Microelectron. 40 (2011) 389–394.

[33] P. Butvin, P. Duhaj, The hall effect in PdSi-based amorphous alloys containing Co., Czechoslov. J. Phys. 26 (1976) 208–214.

[34] S. Chand, J. Kumar, Current-voltage characteristics and barrier parameters of Pd_2Si/p-Si(111) Schottky diodes in a wide temperature range, Semicond. Sci. Technol. 10 (1995) 1680–1688.

[35] M. Denda, M. Kimata, N. Yutani, N. Tsubouchi, S. Uematsu, A PtSi Schottky-barrier infrared MOS area imager with large fill factor, in: 1983 Int. Electron Devices Meet., IRE, 1983: pp. 722–725.

[36] S. Zollner, P. Grudowski, A. Thean, D. Jawarani, G. Karve, T. White, S. Bolton, H. Desjardins, M. Chowdhury, K. Chang, M. Jahanbani, R. Noble, L. Lovejoy, M. Rossow, D. Denning, D. Goedeke, S. Filipiak, R. Garcia, M. Raymond, V. Dhandapani, Da Zhang, L. Kang, P. Crabtree, X. Zhu, M.L. Kottke, R. Gregory, P. Fejes, X.-D. Wang, D. Theodore,

W.J. Taylor, B.-Y. Nguyen, Dual Silicide SOI CMOS Integration with Low-Resistance PtSi PMOS Contacts, in: 2007 IEEE Int. SOI Conf., IEEE, 2007: pp. 75–76.

[37] C.Y. Ting, B. Davari, Gate materials consideration for submicron CMOS, Appl. Surf. Sci. 38 (1989) 416–428.

[38] J.-W. Hoon, K.-Y. Chan, J. Krishnasamy, S.A.B. Kamaruddin, H.-Y. Wong, T. Tou, Electrical properties of sputtered deposited tungsten silicide films, in: 2010 IEEE Int. Conf. Semicond. Electron., IEEE, 2010: pp. 5–7.

[39] A.I. Al-Sharif, M. Abu-Jafar, A. Qteish, Structural and electronic structure properties of FeSi: The driving force behind the stability of the B20 phase, J. Phys. Condens. Matter. 13 (2001) 2807–2815.

[40] C.A. Dimitriadis, J.H. Werner, S. Logothetidis, M. Stutzmann, J. Weber, R. Nesper, Electronic properties of semiconducting $FeSi_2$ films, J. Appl. Phys. 68 (1990) 1726–1734.

[41] Y. Zhang, D.G. Ivey, Fe3Si formation in Fe–Si diffusion couples, J. Mater. Sci. 33 (1998) 3131–3135.

[42] F. ZHANG, S. SAXENA, Phase stability and thermal expansion property of $FeSi_2$, Scr. Mater. 54 (2006) 1375–1377.

[43] B. Aronsson, D.H. Templeton, S. Rundqvist, E. Varde, G. Westin, A Note on the Compositions and Crystal Structures of MnB_2, Mn_3Si, Mn_5Si_3, and $FeSi_2$., Acta Chem. Scand. 14 (1960) 1414–1418.

[44] I. Sandalov, N. Zamkova, V. Zhandun, I. Tarasov, S. Varnakov, I. Yakovlev, L. Solovyov, S. Ovchinnikov, Effect of electron correlations on the Fe_3Si and α−$FeSi_2$ band structure, Phys. Rev. B. 92 (2015) 205129.

[45] N.G. Galkin, D.L. Goroshko, E.A. Chusovitin, K.N. Galkin, S.A. Dotsenko, Silicon-silicide quasi-zero dimensional heterostructures for silicon based photonics, opto- and thermoelectronics, Phys. Status Solidi Curr. Top. Solid State Phys. 10 (2013) 1670–1676.

[46] I.A. Tarasov, I.A. Yakovlev, M.S. Molokeev, M.. Rautskii, I.V. Nemtsev, S.N. Varnakov, S.G. Ovchinnikov, Growth of α-$FeSi_2$ nanocrystals on Si(100) with Au catalyst, Mater. Lett. 168 (2016) 90–94.

[47] B.-X. Xu, Y. Zhang, H.-S. Zhu, D.-Z. Shen, J.-L. Wu, Fabrication and mechanism of α-$FeSi_2$ nanobars on (001) silicon wafer, Mater. Lett. 59 (2005) 833–837.

[48] K. Watanabe, T. Taniguchi, S. Sakane, S. Aoki, T. Suzuki, T. Fujita, Y. Nakamura, Thermoelectric properties of epitaxial β-$FeSi_2$ thin films grown on Si(111) substrates with various film qualities, Jpn. J. Appl. Phys. 56 (2017) 05DC04.

[49] R.L. Maltez, L. Amaral, M. Behar, Mossbauer study of the magnetic character and ordering process of the cubic gamma-$FeSi_2$ phase obtained by Fe implantation into a Si(100) matrix, Phys. Rev. B. 54 (1996) 659–665.

[50] M. Fanciulli, C. Rosenblad, G. Weyer, A. Svane, N.E. Christensen, Conversion Electron Mossbauer Spectroscopy Study of Epitaxial β-$FeSi_2$, Phys. Rev. Lett. 75 (1995) 1642–1645.

[51] H. Tokushige, T. Endo, K. Hiidome, K. Saiki, S. Kitamura, T. Katsuyama, N. Ikeda, Y. Sugimoto, Y. Maeda, Photonic crystals composed of β-FeSi 2 with amorphous Si cladding layers, Jpn. J. Appl. Phys. 54 (2015) 07JB03.

[52] D. Leong, M. Harry, K.J. Reeson, K.P. Homewood, A silicon/iron-disilicide light-emitting diode operating at a wavelength of 1.5 μm, Nature. 387 (1997) 686–688.

[53] Z. Liu, S. Wang, N. Otogawa, Y. Suzuki, M. Osamura, Y. Fukuzawa, T. Ootsuka, Y. Nakayama, H. Tanoue, Y. Makita, A thin-film solar cell of high-quality β-$FeSi_2$/Si heterojunction prepared by sputtering, Sol. Energy Mater. Sol. Cells. 90 (2006) 276–

282.

[54] M. Mohebali, Y. Liu, L. Tayebi, J.S. Krasinski, D. Vashaee, Thermoelectric figure of merit of bulk $FeSi_2$–$Si_{0.8}Ge_{0.2}$ nanocomposite and a comparison with β-$FeSi_2$, Renew. Energy. 74 (2015) 940–947.

[55] J. Theis, R. Bywalez, S. Küpper, A. Lorke, H. Wiggers, Charge storage in β-$FeSi_2$ nanoparticles, J. Appl. Phys. 117 (2015).

[56] W. Monch, On the physics of metal-semiconductor interfaces, Reports Prog. Phys. 53 (1990) 221–278.

[57] L. BRILLSON, The structure and properties of metal-semiconductor interfaces, Surf. Sci. Rep. 2 (1982) 123–326.

[58] W. Schottky, Vereinfachte und erweiterte Theorie der Randschicht-gleichrichter, Zeitschrift Für Phys. 118 (1942) 539–592.

[59] W. Schottky, Zur Halbleitertheorie der Sperrschicht- und Spitzengleichrichter, Zeitschrift Für Phys. 113 (1939) 367–414.

[60] S.M. Sze, K.K. Ng, Physics of Semiconductor Devices, Wiley, 2006.

[61] S. Ruffell, K. Sears, A.P. Knights, J.E. Bradby, J.S. Williams, Experimental evidence for semiconducting behavior of Si-XII, Phys. Rev. B. 83 (2011) 075316.

[62] P.S. Yun, J. Koike, Metal Reaction Doping and Ohmic Contact with Cu-Mn Electrode on Amorphous In-Ga-Zn-O Semiconductor, J. Electrochem. Soc. 158 (2011) H1034.

[63] J. Chen, W.D. Brewer, Ohmic Contacts on p-GaN, Adv. Electron. Mater. 1 (2015) 1500113.

[64] J. Zhang, S. Huang, Q. Bao, X. Wang, K. Wei, Y. Zheng, Y. Li, C. Zhao, X. Liu, Q. Zhou, W. Chen, B. Zhang, Mechanism of Ti/Al/Ti/W Au-free ohmic contacts to AlGaN/GaN heterostructures via pre-ohmic recess etching and low temperature annealing, Appl. Phys. Lett. 107 (2015) 262109.

[65] C.-F. Lo, L. Liu, C.Y. Chang, F. Ren, V. Craciun, S.J. Pearton, Y.W. Heo, O. Laboutin, J.W. Johnson, Annealing temperature dependence of Ohmic contact resistance and morphology on InAlN/GaN high electron mobility transistor structures, J. Vac. Sci. Technol. B, Nanotechnol. Microelectron. Mater. Process. Meas. Phenom. 29 (2011) 021002.

[66] R.T. Tung, The physics and chemistry of the Schottky barrier height, Appl. Phys. Rev. 1 (2014).

[67] Metal-Semiconductor Schottky Barrier Junctions and Their Applications, 1984.

[68] B.G. Shinkarenko, Semiconductor devices, MIPT, Moscow, 2011.

[69] S. Matsumoto, I.-J. Kim, T. Sakai, T. Fukumitsu, T.Y. Toshiaki Yachi, Switching Characteristics of a Thin Film SOI Power MOSFET, Jpn. J. Appl. Phys. 34 (1995) 817.

[70] C.H. Wann, K. Noda, T. Tanaka, M. Yoshida, Chenming Hu, A comparative study of advanced MOSFET concepts, IEEE Trans. Electron Devices. 43 (1996) 1742–1753.

[71] S.Z. Bisri, C. Piliego, J. Gao, M.A. Loi, Outlook and Emerging Semiconducting Materials for Ambipolar Transistors, Adv. Mater. 26 (2014) 1176–1199.

[72] Z. Jiang, Y. Zhang, H.L. Stormer, P. Kim, Quantum Hall States near the Charge-Neutral Dirac Point in Graphene, Phys. Rev. Lett. 99 (2007) 106802.

[73] F.D. Shepherd, R.W. Taylor, L.H. Skolnik, B.R. Capone, S.A. Roosild, W.F. Kosonocky, E.S. Kohn, Schottky IRCCD Thermal Imaging, in: Adv. Electron. Electron Phys., 1980: pp. 495–512.

[74] W. Shockley, The Theory of p-n Junctions in Semiconductors and p-n Junction Transistors, Bell Syst. Tech. J. 28 (1949) 435–489.

[75] E.H. Rhoderick, METAL-SEMICONDUCTOR CONTACTS., IEE Proc. I Solid State Electron Devices. 129 (1982).
[76] G. Shine, K.C. Saraswat, Analysis of Atomistic Dopant Variation and Fermi Level Depinning in Nanoscale Contacts, IEEE Trans. Electron Devices. 64 (2017) 3768–3774.
[77] R. Islam, G. Shine, K.C. Saraswat, Schottky barrier height reduction for holes by Fermi level depinning using metal/nickel oxide/silicon contacts, Appl. Phys. Lett. 105 (2014) 182103.
[78] V. Heine, Theory of Surface States, Phys. Rev. 138 (1965) A1689–A1696.
[79] A. Agrawal, J. Lin, M. Barth, R. White, B. Zheng, S. Chopra, S. Gupta, K. Wang, J. Gelatos, S.E. Mohney, S. Datta, Fermi level depinning and contact resistivity reduction using a reduced titania interlayer in n-silicon metal-insulator-semiconductor ohmic contacts, Appl. Phys. Lett. 104 (2014) 112101.
[80] W. Mönch, Role of Virtual Gap States and Defects in Metal-Semiconductor Contacts, in: Electron. Struct. Semicond. Heterojunctions, Springer Netherlands, 1988: pp. 307–310.
[81] D. Connelly, C. Faulkner, P.A. Clifton, D.E. Grupp, Fermi-level depinning for low-barrier Schottky source/drain transistors, Appl. Phys. Lett. 88 (2006) 012105.
[82] A. Baraskar, A.C. Gossard, M.J.W. Rodwell, Lower limits to metal-semiconductor contact resistance: Theoretical models and experimental data, J. Appl. Phys. 114 (2013) 154516.
[83] D.P. Brunco, B. De Jaeger, G. Eneman, J. Mitard, G. Hellings, A. Satta, V. Terzieva, L. Souriau, F.E. Leys, G. Pourtois, M. Houssa, G. Winderickx, E. Vrancken, S. Sioncke, K. Opsomer, G. Nicholas, M. Caymax, A. Stesmans, J. Van Steenbergen, P.W. Mertens, M. Meuris, M.M. Heyns, Germanium MOSFET Devices: Advances in Materials Understanding, Process Development, and Electrical Performance, J. Electrochem. Soc. 155 (2008) H552.
[84] S. Doğan, S. Duman, B. Gürbulak, S. Tüzemen, H. Morkoç, Temperature variation of current–voltage characteristics of Au/Ni/n-GaN Schottky diodes, Phys. E Low-Dimensional Syst. Nanostructures. 41 (2009) 646–651.
[85] Y.P. Song, R.L. Van Meirhaeghe, W.H. Laflère, F. Cardon, On the difference in apparent barrier height as obtained from capacitance-voltage and current-voltage-temperature measurements on Al/p-InP Schottky barriers, Solid. State. Electron. 29 (1986) 633–638.
[86] J.H. Werner, H.H. Güttler, Barrier inhomogeneities at Schottky contacts, J. Appl. Phys. 69 (1991) 1522–1533.
[87] A. Navrotsky, Physics and Chemistry of Earth Materials, 6th ed., Cambridge University Press, 1994.
[88] R.S. Wagner, W.C. Ellis, VAPOR-LIQUID-SOLID MECHANISM OF SINGLE CRYSTAL GROWTH, Appl. Phys. Lett. 4 (1964) 89–90. https://doi.org/10.1063/1.1753975.
[89] M. Hasan, M.F. Huq, Z.H. Mahmood, A review on electronic and optical properties of silicon nanowire and its different growth techniques, Springerplus. 2 (2013) 151.
[90] T. Ishiyama, S. Nakagawa, T. Wakamatsu, Growth of epitaxial silicon nanowires on a Si substrate by a metal-catalyst-free process, Sci. Rep. 6 (2016) 30608.
[91] L. Tsakalakos, J. Balch, J. Fronheiser, B.A. Korevaar, O. Sulima, J. Rand, Silicon nanowire solar cells, Appl. Phys. Lett. 91 (2007) 233117. https://doi.org/10.1063/1.2821113.
[92] E. Garnett, P. Yang, Light Trapping in Silicon Nanowire Solar Cells, Nano Lett. 10 (2010) 1082–1087.
[93] N. Singh, W.W. Fang, S.C. Rustagi, K.D. Budharaju, S.H.G. Teo, S. Mohanraj, G.Q. Lo, N. Balasubramanian, D.-L. Kwong, Observation of Metal-Layer Stress on Si Nanowires in

Gate-All-Around High-Metal-Gate Device Structures, IEEE Electron Device Lett. 28 (2007) 558–561.

[94] J. Fu, K.D. Buddharaju, S.H.G. Teo, C. Zhu, M.B. Yu, N. Singh, G.Q. Lo, N. Balasubramanian, D.L. Kwong, Trap Layer Engineered Gate-All-Around Vertically Stacked Twin Si-Nanowire Nonvolatile Memory, in: 2007 IEEE Int. Electron Devices Meet., IEEE, 2007: pp. 79–82.

[95] K.E. Moselund, P. Dobrosz, S. Olsen, V. Pott, L. De Michielis, D. Tsamados, D. Bouvet, A. O'Neill, A.M. Ionescu, Bended Gate-All-Around Nanowire MOSFET: a device with enhanced carrier mobility due to oxidation-induced tensile stress, in: 2007 IEEE Int. Electron Devices Meet., IEEE, 2007: pp. 191–194.

[96] A.A. Talin, L.L. Hunter, F. Léonard, B. Rokad, Large area, dense silicon nanowire array chemical sensors, Appl. Phys. Lett. 89 (2006) 153102.

[97] X.T. Zhou, J.Q. Hu, C.P. Li, D.D.D. Ma, C.S. Lee, S.T. Lee, Silicon nanowires as chemical sensors, Chem. Phys. Lett. 369 (2003) 220–224.

[98] G. Zheng, X.P.A. Gao, C.M. Lieber, Frequency Domain Detection of Biomolecules Using Silicon Nanowire Biosensors, Nano Lett. 10 (2010) 3179–3183.

[99] E. Stern, J.F. Klemic, D.A. Routenberg, P.N. Wyrembak, D.B. Turner-Evans, A.D. Hamilton, D.A. LaVan, T.M. Fahmy, M.A. Reed, Label-free immunodetection with CMOS-compatible semiconducting nanowires, Nature. 445 (2007) 519–522.

[100] Y.L. Bunimovich, Y.S. Shin, W.-S. Yeo, M. Amori, G. Kwong, J.R. Heath, Quantitative Real-Time Measurements of DNA Hybridization with Alkylated Nonoxidized Silicon Nanowires in Electrolyte Solution, J. Am. Chem. Soc. 128 (2006) 16323–16331.

[101] The Future of Semiconductor Lithography? Look to Flash, J. Micro/Nanolithography, MEMS, MOEMS. 12 (2013) 030101.

[102] M.N. M. N, U. Hashim, M.K. Md Arshad, A.R. Ruslinda, S.F.A. Rahman, M.F.M. Fathil, M.H. Ismail, Top-Down Nanofabrication and Characterization of 20 nm Silicon Nanowires for Biosensing Applications, PLoS One. 11 (2016) e0152318.

[103] R.A. Minamisawa, M.J. Süess, R. Spolenak, J. Faist, C. David, J. Gobrecht, K.K. Bourdelle, H. Sigg, Top-down fabricated silicon nanowires under tensile elastic strain up to 4.5%, Nat. Commun. 3 (2012) 1096.

[104] I. Park, Z. Li, A.P. Pisano, R.S. Williams, Top-down fabricated silicon nanowire sensors for real-time chemical detection, Nanotechnology. 21 (2010) 015501.

[105] N.F. Za'bah, K.S.K. Kwa, L. Bowen, B. Mendis, A. O'Neill, Top-down fabrication of single crystal silicon nanowire using optical lithography, J. Appl. Phys. 112 (2012) 024309.

[106] H.D. Tong, S. Chen, W.G. van der Wiel, E.T. Carlen, A. van den Berg, Novel Top-Down Wafer-Scale Fabrication of Single Crystal Silicon Nanowires, Nano Lett. 9 (2009) 1015–1022.

[107] S. Chen, J.G. Bomer, W.G. van der Wiel, E.T. Carlen, A. van den Berg, Top-Down Fabrication of Sub-30 nm Monocrystalline Silicon Nanowires Using Conventional Microfabrication, ACS Nano. 3 (2009) 3485–3492.

[108] R. Juhasz, N. Elfström, J. Linnros, Controlled Fabrication of Silicon Nanowires by Electron Beam Lithography and Electrochemical Size Reduction, Nano Lett. 5 (2005) 275–280.

[109] T. Barwicz, L. Klein, S.J. Koester, H. Hamann, Silicon nanowire piezoresistance: Impact of surface crystallographic orientation, Appl. Phys. Lett. 97 (2010) 023110.

[110] A. Koumela, D. Mercier, C. Dupré, G. Jourdan, C. Marcoux, E. Ollier, S.T. Purcell, L. Duraffourg, Piezoresistance of top-down suspended Si nanowires, Nanotechnology. 22 (2011) 395701.

[111] R.D. Piner, J. Zhu, F. Xu, S. Hong, C.A. Mirkin, “Dip-Pen” Nanolithography, Science (80-.). 283 (1999) 661–663.
[112] B. Basnar, Y. Weizmann, Z. Cheglakov, I. Willner, Synthesis of Nanowires Using Dip-Pen Nanolithography and Biocatalytic Inks, Adv. Mater. 18 (2006) 713–718.
[113] T.E. Smolyarova, A. V Lukyanenko, A.S. Tarasov, L. V Shanidze, F.A. Baron, F. V Zelenov, I.A. Yakovlev, N. V Volkov, Biosensors based on nanowire field effect transistors with Schottky contacts, J. Phys. Conf. Ser. 1410 (2019) 012013.
[114] A. Solanki, H. Um, Top-Down Etching of Si Nanowires, in: Semicond. Semimetals, 2018: pp. 71–149.
[115] P.-C. Su, B.-H. Chen, Y.-C. Lee, Y.-S. Yang, Silicon Nanowire Field-Effect Transistor as Biosensing Platforms for Post-Translational Modification, Biosensors. 10 (2020) 213.
[116] Z. Yu, Two new minerals gupeiite and xifengite in cosmic dusts from Yanshan, Acta Petrol. Mineral. Anal. 3 (1984) 231–238.
[117] T. NOVET, D.C. JOHNSON, New Synthetic Approach to Extended Solids: Selective Synthesis of Iron Silicides via the Amorphous State., ChemInform. 22 (2010) 3398–3403.
[118] Y. Dusausoy, J. Protas, R. Wandji, B. Roques, Structure cristalline du disiliciure de fer, $FeSi_2\beta$, Acta Crystallogr. Sect. B Struct. Crystallogr. Cryst. Chem. 27 (1971) 1209–1218.
[119] N.G. Galkin, D.L. Goroshko, V.O. Polar, E.A. Chusovitin, A.K. Gutakovsky, A. V Latyshev, Y. Khang, Formation, crystal structure and properties of silicon with embedded iron disilicide nanocrystallites on Si(100) substrates, Semiconductors. 2 (2007) 1085–1092.
[120] M.E. Schlesinger, Thermodynamics of Solid Transition-Metal Silicides, Chem. Rev. 90 (1990) 607–628.
[121] M. Hansen, K. Anderko, H.W. Salzberg, Constitution of binary alloys, J. Electrochem. Soc. 105 (1959) 260C.
[122] D.Z. Chi, Semiconducting beta-phase $FeSi_2$ for light emitting diode applications: Recent developments, challenges, and solutions, Thin Solid Films. 537 (2013) 1–22.
[123] J. Alvarez, A.L. Vázquez de Parga, J.J. Hinarejos, J. de la Figuera, E.G. Michel, C. Ocal, R. Miranda, Geometric and electronic structure of epitaxial iron silicides, J. Vac. Sci. Technol. A Vacuum, Surfaces, Film. 11 (1993).
[124] B. Balashev, B. Korobtsov, Study of ultrathin iron silicide films grown by solid-phase epitaxy on Si (001) surface, Phys. Solid State. (2010) 370–376.
[125] S.N. Varnakov, I.A. Yakovlev, S.A. Lyashchenko, S.G. Ovchinnikov, G. V. Bondarenko, Comparison of iron silicides obtained by molecular-beam and solid-phase epitaxy methods, Sib. Aerosp. J. (2013) 45–51.
[126] M. Shimomura, T. Sawadaishi, Bottom-up strategy of materials fabrication: a new trend in nanotechnology of soft materials, Curr. Opin. Colloid Interface Sci. 6 (2001) 11–16.
[127] N.A. Taranova, V.D. Slobodenuyk, A. V. Zherdev, B.B. Dzantiev, Network of gold conjugates for enhanced sensitive immunochromatographic assays of troponins, RSC Adv. 11 (2021) 16445–16452.
[128] A.S. Tarasov, A. V. Lukyanenko, I.A. Bondarev, M. V. Rautskii, F.A. Baron, T.E. Smolyarova, I.A. Yakovlev, S.N. Varnakov, S.G. Ovchinnikov, N. V. Volkov, Fabrication and DC/AC Characterization of 3-Terminal Ferromagnet/Silicon Spintronics Devices, Semiconductors. 52 (2018) 1875–1878.
[129] D. Tran, T. Pham, B. Wolfrum, A. Offenhäusser, B. Thierry, CMOS-Compatible Silicon Nanowire Field-Effect Transistor Biosensor: Technology Development toward Commercialization, Materials (Basel). 11 (2018) 785.
[130] G.M. Whitesides, J.P. Mathias, C.T. Seto, Molecular Self-Assembly and Nanochemistry:

a Chemical Strategy for the Synthesis of Nanostructures, Science (80-.). 254 (1991) 1312–1319.
[131] J.-M. Lehn, Perspectives in Supramolecular Chemistry—From Molecular Recognition towards Molecular Information Processing and Self-Organization, Angew. Chemie Int. Ed. English. 29 (1990) 1304–1319.
[132] T. Kunitake, Synthetic Bilayer Membranes: Molecular Design, Self-Organization, and Application, Angew. Chemie Int. Ed. English. 31 (1992) 709–726.
[133] A.Y. Cho, Morphology of Epitaxial Growth of GaAs by a Molecular Beam Method: The Observation of Surface Structures, J. Appl. Phys. 41 (1970) 2780–2786.
[134] G. Cao, D.J. Singh, X.-G. Zhang, G. Samolyuk, L. Qiao, C. Parish, K. Jin, Y. Zhang, H. Guo, S. Tang, W. Wang, J. Yi, C. Cantoni, W. Siemons, E.A. Payzant, M. Biegalski, T.Z. Ward, D. Mandrus, G.M. Stocks, Z. Gai, Ferromagnetism and Nonmetallic Transport of Thin-Film α-$FeSi_2$: A Stabilized Metastable Material, Phys. Rev. Lett. 114 (2015) 147202.
[135] C. Detavernier, C. Lavoie, J. Jordan-Sweet, A.S. Özcan, Texture of tetragonal α-$FeSi_2$ films on Si(001), Phys. Rev. B. 69 (2004) 174106.
[136] N. Jedrecy, A. Waldhauer, M. Sauvage-Simkin, R. Pinchaux, Y. Zheng, Structural characterization of epitaxial α-derived $FeSi_2$ on Si(111), Phys. Rev. B. 49 (1994) 4725–4730.
[137] J. Chevrier, P. Stocker, L.T. Vinh, J.M. Gay, J. Derrien, Epitaxial Growth of α-$FeSi_2$ on Si(111) at Low Temperature, Europhys. Lett. 22 (1993) 449–454.
[138] X.W. Lin, M. Behar, J. Desimoni, H. Bernas, J. Washburn, Z. Liliental-Weber, Low-temperature ion-induced epitaxial growth of α-$FeSi_2$ and cubic $FeSi_2$ in Si, Appl. Phys. Lett. 63 (1993) 105–107.
[139] Y. Gao, G. Shao, R.S. Chen, Y.T. Chong, Q. Li, TEM study of self-assembled $FeSi_2$ nanostructures by ion beam implantation, Solid State Commun. 149 (2009) 97–100.
[140] S.S. Pan, C. Ye, X.M. Teng, H.T. Fan, G.H. Li, Controllable growth of α- And β-$FeSi_2$ thin films on Si(100) by facing-target sputtering, Phys. Status Solidi Appl. Mater. Sci. 204 (2007) 3316–3320.
[141] N. binti Hamzan, C.Y. Bin Ng, R. Sadri, M.K. Lee, L.-J. Chang, M. Tripathi, A. Dalton, B.T. Goh, Controlled physical properties and growth mechanism of manganese silicide nanorods, J. Alloys Compd. 851 (2021) 156693.
[142] X. Xu, X. Liu, Y. Li, Y. Ying, A simple and rapid optical biosensor for detection of aflatoxin B1 based on competitive dispersion of gold nanorods, Biosens. Bioelectron. 47 (2013) 361–367.
[143] M. Ruttert, V. Siozios, M. Winter, T. Placke, Mechanochemical Synthesis of Fe-Si-Based Anode Materials for High-Energy Lithium Ion Full-Cells, ACS Appl. Energy Mater. 3 (2020) 743–758.
[144] W. Braun, A. Trampert, V.M. Kaganer, B. Jenichen, D.K. Satapathy, K.H. Ploog, Endotaxy of MnSb into GaSb, J. Cryst. Growth. 301–302 (2007) 50–53.
[145] S. Liang, R. Islam, D.J. Smith, P.A. Bennett, Phase transformation in $FeSi_2$ nanowires, J. Cryst. Growth. 295 (2006) 166–171.
[146] S. Liang, R. Islam, D.J. Smith, P.A. Bennett, J.R. O'Brien, B. Taylor, Magnetic iron silicide nanowires on Si(110), Appl. Phys. Lett. 88 (2006) 1–3.
[147] Z.-Q. Zou, X. Li, X.-Y. Liu, K.-J. Shi, X.-Q. Guo, Thermal stability of iron silicide nanowires epitaxially grown on Si(110) substrates, Appl. Surf. Sci. 399 (2017) 200–204.
[148] Y. Ohira, T. Tanji, M. Yoshimura, K. Ueda, Iron nanowire formation in Si(110), Jpn. J. Appl. Phys. 47 (2008) 6138–6141.

[149] J.K. Tripathi, M. Garbrecht, W.D. Kaplan, G. Markovich, I. Goldfarb, The effect of Fe-coverage on the structure, morphology and magnetic properties of α-$FeSi_2$ nanoislands, Nanotechnology. 23 (2012) 495603.
[150] S.Y. Chen, H.C. Chen, L.J. Chen, Self-assembled endotaxial α-$FeSi_2$ nanowires with length tunability mediated by a thin nitride layer on Si(001), Appl. Phys. Lett. 88 (2006) 2–5.
[151] T. Koga, H. Tatsuoka, H. Kuwabara, Epitaxial growth of high quality β-$FeSi_2$ layers on Si(111) under the presence of an Sb flux, Appl. Surf. Sci. 169–170 (2001) 310–314.
[152] K. Romanyuk, J. Mysliveček, V. Cherepanov, T. Sekiguchi, S. Yoshida, K.M. Itoh, B. Voigtländer, Optimized Ge nanowire arrays on Si by modified surfactant mediated epitaxy, Phys. Rev. B. 75 (2007) 241309.
[153] S. Saleem, A. Maryam, K. Fatima, H. Noor, F. Javed, M. Asghar, Phase Control Growth of InAs Nanowires by Using Bi Surfactant, Coatings. 12 (2022) 250.
[154] V.G. Dubrovskii, Nucleation Theory and Growth of Nanostructures, Springer, 2014.
[155] V.G. Dubrovskii, N. V. Sibirev, G.E. Cirlin, M. Tchernycheva, J.C. Harmand, V.M. Ustinov, Shape modification of III-V nanowires: The role of nucleation on sidewalls, Phys. Rev. E. 77 (2008) 031606.
[156] K. Paredis, D. Smeets, A. Vantomme, Iron silicide nanostructure formation on Au induced superstructures on Si(111), Nanotechnology. 20 (2009) 075607.
[157] K. Paredis, D. Smeets, A. Vantomme, The Influence of an Adsorbate Layer on Adatom Diffusion and Island Nucleation: Fe on Si(111)-√3 x √3-Au, Nanoscale Res. Lett. 4 (2009) 1447.
[158] M. Copel, M.C. Reuter, E. Kaxiras, R.M. Tromp, Surfactants in epitaxial growth, Phys. Rev. Lett. 63 (1989) 632–635.
[159] M.A. Vysotin, Modelling the structure and properties of compounds of silicon with iron, manganese and lithium, Ph. D. Thesis. (2021).
[160] R.V. Pushkarev, N.I. Fainer, H. Katsui, V.V. Kaichev, T. Goto, Structural features and surface composition of epitaxial α-$FeSi_2$ films obtained by CVD, Mater. Des. 137 (2018) 422–429.
[161] E. Tournié, K.H. Ploog, Surfactant-mediated molecular beam epitaxy of strained layer semiconductor heterostructures, Thin Solid Films. 231 (1993) 43–60.
[162] A. Wolfsteller, N. Geyer, T.-K. Nguyen-Duc, P. Das Kanungo, N.D. Zakharov, M. Reiche, W. Erfurth, H. Blumtritt, S. Kalem, P. Werner, U. Gösele, Comparison of the top-down and bottom-up approach to fabricate nanowire-based silicon/germanium heterostructures, Thin Solid Films. 518 (2010) 2555–2561.
[163] Y. Iijima, Y. Takahashi, K. Matsumoto, T. Hayashi, N. Todoroki, T. Wadayama, Oxygen reduction reaction activities of Pt/Au(111) surfaces prepared by molecular beam epitaxy, J. Electroanal. Chem. 685 (2012) 79–85.
[164] M.J. Rosen, J.T. Kunjappu, Surfactants and Interfacial Phenomena: Fourth Edition, 2012.
[165] G. Abadias, B. Gilles, A. Marty, A relation between the Au-surfactant effect and the chemical mixing during the epitaxial growth of Ni on Au(0 0 1), Appl. Surf. Sci. 177 (2001) 273–281.
[166] G. Ertl, H.-J. Freund, Catalysis and Surface Science, Phys. Today. 52 (1999) 32–38.
[167] L. Ivanenko, V. Shaposhnikov, A. Filonov, A. Krivosheeva, V. Borisenko, D. Migas, L. Miglio, G. Behr, J. Schumann, Electronic properties of semiconducting silicides: fundamentals and recent predictions, Thin Solid Films. 461 (2004) 141–147.
[168] Y. Makita, T. Ootsuka, Y. Fukuzawa, N. Otogawa, H. Abe, Z. Liu, Y. Nakayama, β-$FeSi_2$ as a Kankyo (environmentally friendly) semiconductor for solar cells in the space

application, in: A. Gombert (Ed.), Photonics Sol. Energy Syst., 2006: p. 61970O.
[169] T. Suemasu, Y. Negishi, K. Takakura, F. Hasegawa, T. Chikyow, Influence of Si growth temperature for embedding β-$FeSi_2$ and resultant strain in β-$FeSi_2$ on light emission from p-Si/β-$FeSi_2$ particles/n-Si light-emitting diodes, Appl. Phys. Lett. 79 (2001) 1804–1806.
[170] T. Suemasu, K. Takakura, C. Li, Y. Ozawa, Y. Kumagai, F. Hasegawa, Epitaxial growth of semiconducting β-$FeSi_2$ and its application to light-emitting diodes, Thin Solid Films. 461 (2004) 209–218.
[171] A. V. Shevlyagin, D.L. Goroshko, E.A. Chusovitin, K.N. Galkin, N.G. Galkin, A.K. Gutakovskii, Enhancement of the Si p-n diode NIR photoresponse by embedding β-$FeSi_2$ nanocrystallites, Sci. Rep. 5 (2015) 1–9.
[172] A. Shevlyagin, A. Gutakovskii, D. Goroshko, E. Chusovitin, S. Dotsenko, N. Galkin, Embedding of iron silicide nanocrystals into monocrystalline silicon: suppression of emersion effect, Asia-Pacific Conf. Fundam. Probl. Opto-and Microelectron. (2019) 1102402.
[173] Y. Okuhara, T. Kuroyama, D. Yokoe, T. Kato, M. Takata, T. Tsutsui, K. Noritake, Thermal durability of solar selective absorbers consisting of β-$FeSi_2$ with low emissive Ag layers on stainless steel, Sol. Energy Mater. Sol. Cells. 206 (2020) 110304.
[174] Y. Okuhara, D. Yokoe, T. Kato, S. Suda, M. Takata, K. Noritake, A. Sato, Solar-selective absorbers based on semiconducting β-$FeSi_2$ for efficient photothermal conversion at high temperature, Sol. Energy Mater. Sol. Cells. 161 (2017) 240–246.
[175] J. Tani, H. Kido, Electrical properties of Co-doped and Ni-doped β-$FeSi_2$, J. Appl. Phys. 84 (1998) 1408–1411.
[176] M. Komabayashi, K.H. Ido, Effects of Some Additives on Thermoelectric Properties of FeSi 2 Thin Films, Jpn. J. Appl. Phys. 30 (1991) 331.
[177] T. Kojima, Semiconducting and Thermoelectric Properties of Sintered Iron Disilicide, Phys. Status Solidi. 111 (1989) 233–242.
[178] U. Birkholz, J. Schelm, Mechanism of Electrical Conduction in β-$FeSi_2$, Phys. Status Solidi. 27 (1968) 413–425.
[179] A. Heinrich, A. Burkov, C. Gladun, G. Behr, K. Herz, J. Schumann, H. Powalla, Thermopower and electrical resistivity of undoped and co-doped β-$FeSi_2$ single crystals and β-$FeSi_{2+x}$ thin films, in: Fifteenth Int. Conf. Thermoelectr. Proc. ICT '96, IEEE, 1996: pp. 57–61.
[180] R.M. Ware, D.J. McNeill, Iron disilicide as a thermoelectric generator material, Proc. Inst. Electr. Eng. 111 (1964) 178.
[181] Priyanka, S. Muthiah, Process-structure-properties relationship in low-cost thermoelectric iron silicide synthesis, Ceram. Int. 48 (2022) 29366–29371.
[182] M.I. Fedorov, G.N. Isachenko, Silicides: Materials for thermoelectric energy conversion, Jpn. J. Appl. Phys. 54 (2015) 07JA05.
[183] A. Laila, M. Nanko, M. Takeda, Preparation of Eco-Friendly Fe_2VAl-Based Thermoelectric Materials Using Cast Iron Scrap Chips as a Source Material, Mater. Trans. 61 (2020) 2216–2221.
[184] J. Tani, H. Kido, Thermoelectric Properties of β-$Fe_{1-x}Co_xSi_2$ Semiconductors, Jpn. J. Appl. Phys. 40 (2001) 3236.
[185] H.Y. Chen, X.B. Zhao, T.J. Zhu, J.Z. Jiang, C. Stiewe, C. Lathe, E. Mueller, In situ energy dispersive X-ray diffraction study of iron disilicide thermoelectric materials, J. Phys. Chem. Solids. 69 (2008) 2013–2018.

[186] X. Du, P. Qiu, J. Chai, T. Mao, P. Hu, J. Yang, Y.-Y. Sun, X. Shi, L. Chen, Doubled Thermoelectric Figure of Merit in p-Type β-$FeSi_2$ via Synergistically Optimizing Electrical and Thermal Transports, ACS Appl. Mater. Interfaces. 12 (2020) 12901–12909.
[187] T. Taniguchi, S. Sakane, S. Aoki, R. Okuhata, T. Ishibe, K. Watanabe, T. Suzuki, T. Fujita, K. Sawano, Y. Nakamura, Thermoelectric Properties of Epitaxial β-$FeSi_2$ Thin Films on Si(111) and Approach for Their Enhancement, J. Electron. Mater. 46 (2017) 3235–3241.
[188] C.-L. Hsin, Y.-T. Liu, Y.-Y. Tsai, Suppressed Umklapp scattering of β-$FeSi_2$ thin film and single crystalline nanowires, Nanotechnology. 28 (2017) 485702.
[189] J. Kalt, M. Sternik, I. Sergeev, M. Mikolasek, D. Bessas, J. Göttlicher, B. Krause, T. Vitova, R. Steininger, O. Sikora, P.T. Jochym, O. Leupold, H.C. Wille, A.I. Chumakov, P. Piekarz, K. Parlinski, T. Baumbach, S. Stankov, Lattice dynamics of beta-$FeSi_2$ nanorods, Phys. Rev. B. 106 (2022) 1–13.
[190] D. Platzek, G. Karpinski, C. Drasar, E. Müller, Seebeck Scanning Microprobe for Thermoelectric FGM, Mater. Sci. Forum. 492–493 (2005) 587–592.
[191] R.M. Ware, D.J. McNeill, Iron disilicide as a thermoelectric generator material, Proc. Inst. Electr. Eng. 111 (1964) 178.
[192] U. Stohrer, U. Birkholz, E. Grop, Polycrystalline Iron Disilicide as a Thermoelectric Generator Material, in: Handb. Thermoelectr., CRC Press, 1995: pp. 287–298.
[193] W. Miiller, J.M. Tomczak, J.W. Simonson, G. Smith, G. Kotliar, M.C. Aronson, Protected Fe valence in quasi-two-dimensional α-$FeSi_2$, J. Phys. Condens. Matter. 27 (2015) 175601.
[194] J.K. Tripathi, R. Levy, Y. Camus, M. Dascalu, F. Cesura, R. Chalasani, A. Kohn, G. Markovich, I. Goldfarb, Self-organized growth and magnetic properties of epitaxial silicide nanoislands, Appl. Surf. Sci. 391 (2017) 24–32.
[195] J.K. Tripathi, G. Markovich, I. Goldfarb, Self-ordered magnetic α-$FeSi_2$ nano-stripes on Si(111), Appl. Phys. Lett. 102 (2013). https://doi.org/10.1063/1.4812239.
[196] K. Radermacher, S. Mantl, C. Dieker, H. Lüth, Ion beam synthesis of buried α-$FeSi_2$ and β-$FeSi_2$ layers, Appl. Phys. Lett. 59 (1991) 2145–2147.
[197] I.A. Tarasov, M. V. Rautskii, I.A. Yakovlev, M.N. Volochaev, Effect of Epitaxial Alignment on Electron Transport from Quasi-Two-Dimensional Iron Silicide α-$FeSi_2$ Nanocrystals Into p-Si(001), Semiconductors. 52 (2018) 654–659.
[198] Y. Cui, X. Duan, J. Hu, C.M. Lieber, Doping and Electrical Transport in Silicon Nanowires, J. Phys. Chem. B. 104 (2000) 5213–5216. https://doi.org/10.1021/jp0009305.
[199] P. Servati, A. Colli, S. Hofmann, Y.Q. Fu, P. Beecher, Z.A.K. Durrani, A.C. Ferrari, A.J. Flewitt, J. Robertson, W.I. Milne, Scalable silicon nanowire photodetectors, Phys. E Low-Dimensional Syst. Nanostructures. 38 (2007) 64–66.
[200] T. Stelzner, M. Pietsch, G. Andrä, F. Falk, E. Ose, S. Christiansen, Silicon nanowire-based solar cells, Nanotechnology. 19 (2008) 295203.
[201] Y. Chen, D. Li, J.R. Lukes, A. Majumdar, Monte Carlo Simulation of Silicon Nanowire Thermal Conductivity, J. Heat Transfer. 127 (2005) 1129–1137.
[202] T. Mikolajick, W.M. Weber, Silicon Nanowires: Fabrication and Applications, in: Nanosci. Technol., 2015: pp. 1–25.
[203] X.F. Hu, S.J. Li, J. Wang, Z.M. Jiang, X.J. Yang, Investigating Size-Dependent Conductive Properties on Individual Si Nanowires, Nanoscale Res. Lett. 15 (2020) 52.
[204] L. Baraban, B. Ibarlucea, E. Baek, G. Cuniberti, Hybrid Silicon Nanowire Devices and Their Functional Diversity, Adv. Sci. 6 (2019) 1900522.
[205] T. Adam, U. Hashim, Highly sensitive silicon nanowire biosensor with novel liquid gate

control for detection of specific single-stranded DNA molecules, Biosens. Bioelectron. 67 (2015).

[206] J.H. Lee, E.J. Chae, S. jeong Park, J.W. Choi, Label-free detection of γ-aminobutyric acid based on silicon nanowire biosensor, Nano Converg. 6 (2019).

[207] G.-J. Zhang, Y. Ning, Silicon nanowire biosensor and its applications in disease diagnostics: A review, Anal. Chim. Acta. 749 (2012) 1–15.

[208] Z. Li, Y. Chen, X. Li, T.I. Kamins, K. Nauka, R.S. Williams, Sequence-Specific Label-Free DNA Sensors Based on Silicon Nanowires, Nano Lett. 4 (2004) 245–247.

[209] P. Bergveld, Development of an Ion-Sensitive Solid-State Device for Neurophysiological Measurements, IEEE Trans. Biomed. Eng. BME-17 (1970) 70–71.

[210] O. Knopfmacher, A. Tarasov, W. Fu, M. Wipf, B. Niesen, M. Calame, C. Schönenberger, Nernst Limit in Dual-Gated Si-Nanowire FET Sensors, Nano Lett. 10 (2010) 2268–2274.

[211] S. Pregl, W.M. Weber, D. Nozaki, J. Kunstmann, L. Baraban, J. Opitz, T. Mikolajick, G. Cuniberti, Parallel arrays of Schottky barrier nanowire field effect transistors: Nanoscopic effects for macroscopic current output, Nano Res. 6 (2013) 381–388.

[212] C.-Y. Hsiao, C.-H. Lin, C.-H. Hung, C.-J. Su, Y.-R. Lo, C.-C. Lee, H.-C. Lin, F.-H. Ko, T.-Y. Huang, Y.-S. Yang, Novel poly-silicon nanowire field effect transistor for biosensing application, Biosens. Bioelectron. 24 (2009) 1223–1229.

[213] G.A.M. Hurkx, D.B.M. Klaassen, M.P.G. Knuvers, A new recombination model for device simulation including tunneling, IEEE Trans. Electron Devices. 39 (1992) 331–338.

[214] F. Iacopi, P.M. Vereecken, M. Schaekers, M. Caymax, N. Moelans, B. Blanpain, O. Richard, C. Detavernier, H. Griffiths, Plasma-enhanced chemical vapour deposition growth of Si nanowires with low melting point metal catalysts: an effective alternative to Au-mediated growth, Nanotechnology. 18 (2007) 505307.

[215] M.H. Jakob, B. Dong, S. Gutsch, C. Chatelle, A. Krishnaraja, W. Weber, M. Zacharias, Label-free SnO_2 nanowire FET biosensor for protein detection, Nanotechnology. 28 (2017) 245503.

[216] P. Zucca, E. Sanjust, Inorganic Materials as Supports for Covalent Enzyme Immobilization: Methods and Mechanisms, Molecules. 19 (2014) 14139–14194.

[217] S. Ebnesajjad, Introduction and Adhesion Theories, in: Handb. Adhes. Surf. Prep., Elsevier, 2011: pp. 3–13.

[218] X. Duan, L. Mu, S.D. Sawtelle, N.K. Rajan, Z. Han, Y. Wang, H. Qu, M.A. Reed, Functionalized Polyelectrolytes Assembling on Nano-BioFETs for Biosensing Applications, Adv. Funct. Mater. 25 (2015) 2279–2286.

[219] N. Aissaoui, L. Bergaoui, J. Landoulsi, J.-F. Lambert, S. Boujday, Silane Layers on Silicon Surfaces: Mechanism of Interaction, Stability, and Influence on Protein Adsorption, Langmuir. 28 (2012) 656–665.

[220] T. Adam, A.M. Mohammed, T.S. Dhahi, N.F.B.N. Azua, N. Azizah, U. Hashim, S.C.B. Gopinath, Semiconductor nanowires biosensors for highly selective and multiplexed detection of biomolecules, J. Telecommun. Electron. Comput. Eng. 10 (2018).

[221] N.A.K.H. Ehfaed, T. Adam, M. Mohammed, O.S. Dahham, U. Hashim, N.Z. Noriman, A.R. Rabia, Functionalization of Si Nanowire Surfaces to Create Interactive Mechanism for Heavy Metals Detection Application, in: IOP Conf. Ser. Mater. Sci. Eng., 2018.

[222] M.F.M. Fathil, M.K. Md Arshad, A.R. Ruslinda, S.C.B. Gopinath, M.M.N. Nuzaihan, R. Adzhri, U. Hashim, H.Y. Lam, Substrate-gate coupling in ZnO-FET biosensor for cardiac troponin I detection, Sensors Actuators, B Chem. 242 (2017).

[223] Y. Liang, J. Huang, P. Zang, J. Kim, W. Hu, Molecular layer deposition of APTES on silicon

nanowire biosensors: Surface characterization, stability and pH response, Appl. Surf. Sci. 322 (2014) 202–208.
[224] B.-R. Li, C.-W. Chen, W.-L. Yang, T.-Y. Lin, C.-Y. Pan, Y.-T. Chen, Biomolecular recognition with a sensitivity-enhanced nanowire transistor biosensor, Biosens. Bioelectron. 45 (2013) 252–259.
[225] M.-Y. Shen, B.-R. Li, Y.-K. Li, Silicon nanowire field-effect-transistor based biosensors: From sensitive to ultra-sensitive, Biosens. Bioelectron. 60 (2014) 101–111.
[226] X.T. Vu, R. GhoshMoulick, J.F. Eschermann, R. Stockmann, A. Offenhäusser, S. Ingebrandt, Fabrication and application of silicon nanowire transistor arrays for biomolecular detection, Sensors Actuators B Chem. 144 (2010) 354–360.
[227] E.P. Diamandis, T.K. Christopoulos, The biotin-(strept)avidin system: principles and applications in biotechnology, Clin. Chem. 37 (1991) 625–636.
[228] N. Michael Green, Avidin and streptavidin, in: Methods Enzymol., 1990: pp. 51–67.
[229] C.M. Dundas, D. Demonte, S. Park, Streptavidin–biotin technology: improvements and innovations in chemical and biological applications, Appl. Microbiol. Biotechnol. 97 (2013) 9343–9353.
[230] E. Fehskens, M.W. Burgett, Measurement of serum chorionic gonadotropin by a biotin-avidin labeled enzyme immunoassay, Ann. Clin. Lab. Sci. 15 (1985) 241–245.
[231] J.L. Guesdon, T. Ternynck, S. Avrameas, The use of avidin-biotin interaction in immunoenzymatic techniques, J. Histochem. Cytochem. 27 (1979).
[232] C.M. Preissner, G.G. Klee, C.J. Krco, Nonisotopic “sandwich” immunoassay of thyroglobulin in serum by the biotin-streptavidin technique: evaluation and comparison with an immunoradiometric assay., Clin. Chem. 34 (1988) 1794–1798.
[233] N. Pala, M. Karabiyik, Electron Beam Lithography (EBL), in: Encycl. Nanotechnol., Springer Netherlands, Dordrecht, 2016: pp. 1033–1057.
[234] D.W.M. Arrigan, Nanoelectrode arrays for electroanalysis, in: Front. Nanosci., 2021: pp. 49–86.
[235] D.R. HERRIOTT, G.R. BREWER, Electron-beam lithography machines, in: Electron-Beam Technol. Microelectron. Fabr., Elsevier, 1980: pp. 141–216.
[236] K. Oura, V.G. Lifshits, A.A. Saranin, A.V. Zotov, M. Katayama, Surface science: an introduction, Nauka, Moscow, 2005.
[237] V.G. Kazakov, Thin magnetic films, Soros Educ. J. 1 (1997) 107–114.
[238] J. Pawley, The development of field-emission scanning electron microscopy for imaging biological surfaces, in: SCANNING-NEW YORK Bad. Bad. THEN MAHWAH, 1997: pp. 324–336.
[239] J.I. Goldstein, D.E. Newbury, J.R. Michael, N.W.M. Ritchie, J.H.J. Scott, D.C. Joy, Scanning Electron Microscopy and X-Ray Microanalysis, Springer New York, New York, NY, 2018.
[240] AnaPath, ELECTRON MICROSCOPY, (n.d.). https://anapath.ch/electron-microscopy-2/.
[241] Utevsky L. M., Diffraction Electron Microscopy in Metallurgy. Moscow, Metallurgy, 1973.
[242] O.W. Richards, R.D. Heidenreich, Fundamentals of Transmission Electron Microscopy, Trans. Am. Microsc. Soc. 84 (1965) 295.
[243] P.B. Hirsch, A. Howie, R.B. Nicholson, D.W. Pashley, M.J. Whelan, L. Marton, Electron Microscopy of Thin Crystals, Phys. Today. 19 (1966).
[244] M.J. Goringe, Applications Of High Voltage Electron Microscopy In Materials Science, in: L.R. Baker (Ed.), Microsc. Tech. Capab., 1983: pp. 41–49.
[245] D. Shindo, T. Oikawa, Analytical Electron Microscopy for Materials Science, Springer

Japan, Tokyo, 2013.
[246] B. Fultz, J.M. Howe, Transmission Electron Microscopy and Diffractometry of Materials, Springer Berlin Heidelberg, Berlin, Heidelberg, 2012.
[247] D.B. Williams, C.B. Carter, Transmission Electron Microscopy, Springer US, Boston, MA, 2009.
[248] H.C. Hamaker, The London-van der Waals attraction between spherical particles, Physica. 4 (1937) 1058–1072.
[249] C. Maedler, H. Graaf, S. Chada, M. Yan, A. La Rosa, Nanostructure formation driven by local protonation of polymer thin films, Nanotechnol. IV. 7364 (2009) 736409.
[250] J. Haaheim, R. Eby, M. Nelson, J. Fragala, B. Rosner, H. Zhang, G. Athas, Dip Pen Nanolithography (DPN): process and instrument performance with NanoInk's Nscriptor system, Ultramicroscopy. 103 (2005) 117–132.
[251] L.M. Demers, D.S. Ginger, S.-J. Park, Z. Li, S.-W. Chung, C.A. Mirkin, Direct Patterning of Modified Oligonucleotides on Metals and Insulators by Dip-Pen Nanolithography, Science (80-.). 296 (2002) 1836–1838. https://doi.org/10.1126/science.1071480.
[252] Oxford Instruments, EBSD: Electron Backscatter Diffraction, (n.d.). https://nano.oxinst.com/.
[253] W.H. Bragg, The reflection of X-rays by crystals [3], Nature. 91 (1913).
[254] S. NISHIKAWA, S. KIKUCHI, Diffraction of Cathode Rays by Mica, Nature. 121 (1928) 1019–1020.
[255] R.O. Duda, P.E. Hart, Use of the Hough transformation to detect lines and curves in pictures, Commun. ACM. 15 (1972) 11–15.
[256] E.J. Kirkland, Advanced Computing in Electron Microscopy, 1998.
[257] X.-F. Gu, T. Furuhara, W.-Z. Zhang, PTCLab : free and open-source software for calculating phase transformation crystallography, J. Appl. Crystallogr. 49 (2016) 1099–1106.
[258] G.A. Kuznetsova, Qualitative X-ray diffraction analysis, Irkutsk, 2005.
[259] D. Brandon, W.D. Kaplan, Microstructural Characterization of Materials, Wiley, 2013.
[260] B. De Schutter, K. De Keyser, C. Lavoie, C. Detavernier, Texture in Thin Film Silicides and Germanides: A Review, Appl. Phys. Rev. 47 (2016) 031302.
[261] L.G. Schulz, A Direct Method of Determining Preferred Orientation of a Flat Reflection Sample Using a Geiger Counter X-Ray Spectrometer, J. Appl. Phys. 20 (1949) 1030–1033.
[262] N. Doebelin, R. Kleeberg, Profex : a graphical user interface for the Rietveld refinement program BGMN, J. Appl. Crystallogr. 48 (2015) 1573–1580.
[263] Web-page, Model EMPX-HF Cryogenic Probe Station, (n.d.). www.lakeshore.com.
[264] D.K. Schroder, M.S. Fung, R.L. Verkuil, S. Pandey, W.H. Howland, M. Kleefstra, CORONA-OXIDE-SEMICONDUCTOR device CHARACTERIZATION, Solid. State. Electron. 42 (1998) 505–512.
[265] N. Bowler, Theory of Four-Point Direct-Current Potential Drop Measurements on a Metal Plate, Res. Nondestruct. Eval. 17 (2006) 29–48.
[266] N. Bowler, Four-point potential drop measurements for materials characterization, Meas. Sci. Technol. 22 (2011) 012001.
[267] Pavlov L. P., Methods for measuring the parameters of semiconductor materials, in: Vyss. Shkola, Moscow, 1987: p. 10.
[268] A.T. Burkov, A.I. Fedotov, A.A. Kasyanov, R.I. Panteleev, T. Nakama, Methods and technique of thermopower and electrical conductivity measurements of thermoelectric

materials at high temperatures, Sci. Tech. J. Inf. Technol. Mech. Opt. (2015) 173–195.

[269] C.T. Rueden, J. Schindelin, M.C. Hiner, B.E. DeZonia, A.E. Walter, E.T. Arena, K.W. Eliceiri, ImageJ2: ImageJ for the next generation of scientific image data, BMC Bioinformatics. 18 (2017) 529.

[270] D. Nečas, P. Klapetek, Gwyddion: an open-source software for SPM data analysis, Open Phys. 10 (2012) 181–188.

[271] M.A. Visotin, I.A. Tarasov, A.S. Fedorov, S.N. Varnakov, S.G. Ovchinnikov, Prediction of orientation relationships and interface structures between α-, β-, γ-$FeSi_2$ and Si phases, Acta Crystallogr. Sect. B Struct. Sci. Cryst. Eng. Mater. 76 (2020) 469–482.

[272] D.K. Lee, J. In, S. Lee, Standard deviation and standard error of the mean, Korean J. Anesthesiol. 68 (2015) 220.

[273] I.A. Tarasov, T.E. Smolyarova, I.V. Nemtsev, I.A. Yakovlev, M.N. Volochaev, L.A. Solovyov, S.N. Varnakov, S.G. Ovchinnikov, Tailoring the preferable orientation relationship and shape of α-$FeSi_2$ nanocrystals on Si(001): The impact of gold and the Si/Fe flux ratio, and the origin of α/Si boundaries, CrystEngComm. 22 (2020).

[274] J.. Nie, Crystallography and migration mechanisms of planar interphase boundaries, Acta Mater. 52 (2004) 795–807.

[275] Q. Liang, W.T. Reynolds, Determining interphase boundary orientations from near-coincidence sites, Metall. Mater. Trans. A. 29 (1998) 2059–2072.

[276] I. Berbezier, J. Chevrier, J. Derrien, High-resolution electron microscopy study of α-$FeSi_2$ heteroepitaxy on Si(111), Surf. Sci. 315 (1994) 27–39.

[277] J.E. Mahan, V. Le Thanh, J. Chevrier, I. Berbezier, J. Derrien, R.G. Long, Surface electron-diffraction patterns of β-$FeSi_2$ films epitaxially grown on silicon, J. Appl. Phys. 74 (1993) 1747–1761.

[278] K. Konuma, J. Vrijmoeth, P.M. Zagwijn, J.W.M. Frenken, E. Vlieg, J.F. van der Veen, Formation of epitaxial β-$FeSi_2$ films on Si(001) as studied by medium-energy ion scattering, J. Appl. Phys. 73 (1993) 1104–1109.

[279] H. Liu, C. Tan, D. Chi, Magnetron-sputter epitaxy of β-$FeSi_2$(220)/Si(111) and β-$FeSi_2$ (431)/Si(001) thin films at elevated temperatures, J. Vac. Sci. Technol. A Vacuum, Surfaces, Film. 30 (2012) 041516.

[280] International Tables for Crystallography, J. Appl. Crystallogr. 16 (1983) 284–284.

[281] The reflection of X-rays by crystals, Proc. R. Soc. London. Ser. A, Contain. Pap. a Math. Phys. Character. 88 (1913) 428–438.

[282] J.C.H. Spence, On the accurate measurement of structure-factor amplitudes and phases by electron diffraction, Acta Crystallogr. Sect. A Found. Crystallogr. 49 (1993) 231–260.

[283] J. Kalt, M. Sternik, B. Krause, I. Sergueev, M. Mikolasek, D. Merkel, D. Bessas, O. Sikora, T. Vitova, J. Göttlicher, R. Steininger, P.T. Jochym, A. Ptok, O. Leupold, H.-C. Wille, A.I. Chumakov, P. Piekarz, K. Parlinski, T. Baumbach, S. Stankov, Lattice dynamics of endotaxial silicide nanowires, Phys. Rev. B. 102 (2020) 195414.

[284] G.D.J. Smit, S. Rogge, J. Caro, T.M. Klapwijk, Stark effect in shallow impurities in Si, Phys. Rev. B. 70 (2004) 035206.

[285] J. Nomoto, K. Inaba, S. Kobayashi, T. Watanabe, H. Makino, T. Yamamoto, Characteristics of Carrier Transport and Crystallographic Orientation Distribution of Transparent Conductive Al-Doped ZnO Polycrystalline Films Deposited by Radio-Frequency, Direct-Current, and Radio-Frequency-Superimposed Direct-Current Magnetron Sputter, Materials (Basel). 10 (2017) 916.

[286] I. Berbezier, J.L. Regolini, C. D'Anterroches, Epitaxial orientation of β-$FeSi_2$/Si

heterojunctions obtained by RTP chemical vapor deposition, Microsc. Microanal. Microstruct. 4 (1993) 5–21.

[287] M. HENZLER, Electronic Transport at Surfaces, in: J.M. BLAKELY (Ed.), Surf. Phys. Mater., Elsevier, 1975: pp. 241–278. https://doi.org/10.1016/B978-0-12-103801-4.50011-2.

[288] S. Hasegawa, I. Shiraki, T. Tanikawa, C.L. Petersen, T.M. Hansen, P. Boggild, F. Grey, Direct measurement of surface-state conductance by microscopic four-point probe method, J. Phys. Condens. Matter. 14 (2002) 8379–8392.

[289] J. Osvald, Back-to-back connected asymmetric Schottky diodes with series resistance as a single diode, Phys. Status Solidi. 212 (2015) 2754–2758.

[290] D. Skachkov, S.-L. Liu, Y. Wang, X.-G. Zhang, H.-P. Cheng, First-principles theory for Schottky barrier physics, Phys. Rev. B. 104 (2021) 045429.

[291] N. Kelaidis, S. Bousiadi, M. Zervos, A. Chroneos, N.N. Lathiotakis, Electronic properties of the $Sn_{1-x}Pb_xO$ alloy and band alignment of the SnO/PbO system: a DFT study, Sci. Rep. 10 (2020) 16828.

[292] M.D. Segall, P.J.D. Lindan, M.J. Probert, C.J. Pickard, P.J. Hasnip, S.J. Clark, M.C. Payne, First-principles simulation: ideas, illustrations and the CASTEP code, J. Phys. Condens. Matter. 14 (2002) 2717–2744.

[293] J.P. Perdew, K. Burke, M. Ernzerhof, Generalized Gradient Approximation Made Simple, Phys. Rev. Lett. 77 (1996) 3865–3868.

[294] D. Vanderbilt, Soft self-consistent pseudopotentials in a generalized eigenvalue formalism, Phys. Rev. B. 41 (1990) 7892–7895.

[295] Juspertor, LayoutEditor, (n.d.). https://www.layouteditor.org/.

[296] D.W. Lee, E.M. Kim, G.S. Heo, D.H. Kim, J.Y. Oh, D. Bin Yang, J.I. Jang, H. Jeong, D. Seo, Inducement of an Anisotropic One-dimensional Surface of Solution-derived Indium Gallium Oxide Film via Imprint Lithography for Liquid Crystal Alignment, ChemNanoMat. 8 (2022) e202200367.

[297] J.-H. Lim, C.A. Mirkin, Electrostatically Driven Dip-Pen Nanolithography of Conducting Polymers, Adv. Mater. 14 (2002) 1474–1477.

[298] T.E. Smolyarova, A. V. Lukyanenko, A.S. Tarasov, L. V. Shanidze, F.A. Baron, F. V. Zelenov, I.A. Yakovlev, N. V. Volkov, Biosensors based on nanowire field effect transistors with Schottky contacts, in: J. Phys. Conf. Ser., 2019.

[299] A. Kaifer, M. Gómez-Kaifer, Supramolecular Electrochemistry, Wiley, 1999.

[300] S. Grabowsky, M.F. Hesse, C. Paulmann, P. Luger, J. Beckmann, How to Make the Ionic Si-O Bond More Covalent and the Si-O-Si Linkage a Better Acceptor for Hydrogen Bonding, Inorg. Chem. 48 (2009) 4384–4393.

[301] N.S. Green, E. Reisler, K.N. Houk, Quantitative evaluation of the lengths of homobifunctional protein cross-linking reagents used as molecular rulers, Protein Sci. 10 (2008) 1293–1304.

[302] T.E. Smolyarova, L.V. Shanidze, A.V. Lukyanenko, F.A. Baron, V.V. Krasitskaya, A.S. Kichkailo, A.S. Tarasov, N. Volkov, Protein biosensor based on Schottky barrier nanowire field effect transistor, Talanta. 239 (2022).

[303] S.N. Das, J.P. Kar, J.-H. Choi, T. Il Lee, K.-J. Moon, J.-M. Myoung, Fabrication and Characterization of ZnO Single Nanowire-Based Hydrogen Sensor, J. Phys. Chem. C. 114 (2010) 1689–1693.

[304] S.N. Das, A.K. Pal, Hydrogen sensor based on thin film nanocrystalline n-GaN/Pd Schottky diode, J. Phys. D. Appl. Phys. 40 (2007) 7291–7297.

[305] S. Pihlasalo, L. Auranen, P. Hänninen, H. Härmä, Method for Estimation of Protein

Isoelectric Point, Anal. Chem. 84 (2012) 8253–8258.

[306] A. Soult, Chemistry for Allied Health, in: Encycl. Glob. Warm. Clim. Chang., SAGE Publications, Inc., 2455 Teller Road, Thousand Oaks California 91320 United States, 2008.

[307] R. De Levie, The Henderson-Hasselbalch equation: Its history and limitations, J. Chem. Educ. 80 (2003).

[308] J.M. Freire, A.S. Veiga, T.M. Conceição, W. Kowalczyk, R. Mohana-Borges, D. Andreu, N.C. Santos, A.T. Da Poian, M.A.R.B. Castanho, Intracellular Nucleic Acid Delivery by the Supercharged Dengue Virus Capsid Protein, PLoS One. 8 (2013) e81450.

[309] O. V. Naumova, B.I. Fomin, D.A. Nasimov, N. V. Dudchenko, S.F. Devyatova, E.D. Zhanaev, V.P. Popov, A. V. Latyshev, A.L. Aseev, Y.D. Ivanov, A.I. Archakov, SOI nanowires as sensors for charge detection, Semicond. Sci. Technol. 25 (2010) 055004.

[310] A. V. Pawar, S.S. Kanapally, A.P. Chougule, P.P. Waifalkar, K. V. More, R.K. Kamat, T.D. Dongale, Simulation Study of Field-effect Transistor Based Cylindrical Silicon Nanowire Biosensor: Effect of Length and Radius of the Nanowire, J. Nano- Electron. Phys. 11 (2019) 01005-1-01005–5.

DuEPublico

Duisburg-Essen Publications online

UNIVERSITÄT DUISBURG ESSEN

Offen im Denken

ub | universitäts bibliothek

Diese Dissertation wird via DuEPublico, dem Dokumenten- und Publikationsserver der Universität Duisburg-Essen, zur Verfügung gestellt und liegt auch als Print-Version vor.

DOI: 10.17185/duepublico/81444

URN: urn:nbn:de:hbz:465-20240126-075304-3

Alle Rechte vorbehalten.